EXPERIMENTAL AND NUMERICAL INVESTIGATION OF THE QUANTIFICATION OF CORROSION DAMAGE IN REINFORCED CONCRETE

Victor Saye Gilayeneh

A research report submitted to the Faculty of Engineering and the Built Environment, University of the Witwatersrand, Johannesburg, in partial fulfilment of the requirements for the degree of Master of Science in Engineering.

February, 2019

Johannesburg

DECLARATION

I declare that this research report is my own unaided work. It is being submitted for the Degree of Master of Science in Engineering to the University of the Witwatersrand, Johannesburg. It has not been submitted before for any degree or examination to any other university.

……

7th day of February 2019

ABSTRACT

Steel corrosion in concrete is the dominant variable contributing to the reduced service life of concrete structures. Corrosion reduces the cross-section of the rebar, weakens the steel-concrete bond, develops cracks and spalls concrete covers, and some instances, it may increase deflection and buckling. Safety is a major concern of corroding concrete structures, and to minimise the risk; appropriate measures are to be taken in deciding when and how to implement maintenance. The influential factor that governs or informs such decisions is the corrosion damage quantification. However, the current non-destructive methods of corrosion damage quantification often lead to ambiguity, and most do not evaluate corrosion damage in terms of rebar cross-section loss, which is the primary effect of steel corrosion in concrete.

Consequently, this study presents a non-destructive model for quantifying corrosion damage in reinforced concrete structures using the corrosion-induced crack width. This model is effective, less complicated, applicable to structures in service, and permits the evaluation of the corrosion damage in terms of the residual cross-section. Moreover, the derived model requires input parameters that are easily attainable both in the laboratory and the field. This model was derived based on experimental and numerical investigation of the relationship between the corrosion-induced crack width and the rebar cross-section loss. The derived model was tested against the author's experimental data and data from the literature which include natural and accelerated corrosion as well as loading conditions, and the results correlate well with these data.

ACKNOWLEDGEMENTS

Firstly, I would like to thank my supervisor, Professor Sunday Nwaubani, for his excellent guidance through this research. His mentorship has afforded me the opportunity to develop my potential further.

Also, I would like to express appreciation to all my lecturers at the University of Witwatersrand, the knowledge imparted was beneficial in my research.

I express my sincere thanks and gratitude to my dear brother, Mr Kidia Kaddy Kalima, without him, the completion of my study would have been impossible.

I would also like to express my appreciation to Serina Trading (Pty) Ltd for the donation of metakaolin towards this study.

Furthermore, I express the most profound appreciation to my sponsors, the Ministry of Public Works of the Republic of Liberia and its partner, the African Development Bank (ADB).

Finally, to my family and friends, I express my profound gratitude for their unwavering supports and continuous encouragement throughout my years of study.

DEDICATION

To the glory of the almighty God, I dedicate this work.

TABLE OF CONTENTS

LIST OF FIGURES

LIST OF TABLES

LIST OF SYMBOLS

x_p: Radius loss to corrosion

Δr_b: Maximum radius loss

r_b: Original radius of the rebar

R_{rb}: Residual radius of the rebar

V_S: Volume of steel loss to corrosion

V_{rust}: Volume of free rust expansion

CV_{rust}:Compressed volume of rust

n: Volume expansion ratio

B_{rust}: Bulk modulus of the rust

E_{rust}: Elastic modulus of the rust

v: Poisson's ratio

ε_{rust}: Volumetric strain of the rust

K_{rust}: Stiffness of the compressed layer of the rust

P: Pressure exerted by the corrosion product (rust)

$r_{CV_{rust}}$:Radius of the compressed rust volume

1 INTRODUCTION

1.1 BACKGROUND INFORMATION

Reinforced concrete is the most widely used type of structural concrete. It is versatile and very economical as compared to other building materials, requiring very little maintenance during its service life. When properly constructed and depending on the exposure conditions, reinforced concrete is durable and sustainable, exhibiting excellent resistance to both static and cyclic loading. However, reinforced concrete is not immune from attacks (physical and chemical) which may result in the premature deterioration of the structures and some instances loss of its functionality. Reinforced concrete may suffer several forms of attacks as results of aggressive environment, poor design considerations and materials selection, as well as substandard construction practices.

The most common deterioration mechanism or durability problem associated with reinforced concrete is the corrosion of its reinforcing steel (Angst, 2018). Corrosion is a form of chemical attack on reinforced concrete that affects the embedded steel and is the most dominant cause of premature degradation of reinforced concrete structures (Du et al., 2013). Corrosion of reinforcement in concrete poses severe structural and economic problems. Structural-wise, corrosion reduces the cross-section of the rebar, attenuates the steel-concrete bond, develops cracks and spalls concrete covers, and in some cases, it may increase deflection and buckling as a direct consequence of loss in load-carrying capacity. Corrosion of steel in concrete has created a multi-billion-dollar infrastructure deficit (Poursaee, 2016), for example, the repair cost of corrosion has become a prominent part of many industrialised countries' budget. Globally, billions of dollars are spent every year in maintaining and replacing corrosion-damaged concrete structures (Broomfield, 2006). In the United States alone, the direct cost of corrosion in 1998 as reported by National Association of Corrosion Engineers (NACE) was 276 billion dollars, approximately 3.1% of the gross domestic product (Nwaubani and Katsanos, 2014). The structural damages and economic losses caused by the corrosion of steel in concrete makes it perhaps the largest single infrastructure problem facing industrialised countries (Ferreira, 2004; Broomfield, 2006). Corrosion prevention, damage evaluation, and maintenance of corroding concrete structures are a major challenge to engineers (Ferreira, 2004; Broomfield, 2006).

Corrosion of reinforcement in concrete is an electrochemical reaction between the environment and the embedded steel, as the steel seeks to transform to a more stable state. This process results in the deterioration of both the embedded steel and the concrete. Steel in concrete initially, is in a passive state, safe from corrosion (Gonzalez et al., 1996) and corrosion occurs as a result of depassivation. The passivation layer is a thin ultra-film of iron oxide which forms around the steel due to the chemical reaction between the steel and the highly alkaline environment within the concrete. It is important to note that metals corrode in an acidic environment but are protected from corrosion within an alkaline environment (Broomfield, 2006). Concrete is a highly alkaline material, with a pH value ranging from 12.0 to 13.5 (Page

and Page, 2007). This environment promotes the formation of the protective covering called passivation layer, which decreases the rate of oxidation or dissolution of the steel to a negligible level (Poursaee, 2016). As a protective covering, the passivation layer also prevents moisture, oxygen and other aggressive substances from reaching the steel surface. If the protective layer is well preserved, corrosion is negligible. However, the passivation layer can be damaged directly by aggressive substances or by a change in the electrochemical environment of concrete, which may reduce its pH value.

Reinforced concrete corrosion is usually induced by two types of chemical attacks on concrete: chloride attack and carbonation. Depending on the level of concentration and the type of corrosion-inducing species present within the environment, both chloride and carbon dioxide may simultaneously induce corrosion in a given instance. Of these two, chloride ion is the most aggressive and destructive species, it damages the passivation layer directly without causing any change in the electrochemical environment of concrete. This type of corrosion is usually localised (pitting), causing significant damage to the steel and the initiation process is very fast. Carbonation-induced corrosion is the process that changes the electrochemical environment within concrete by the ingress of carbon dioxide and is usually considered uniform or generalised corrosion. The carbon dioxide gas reduces the high pH which promotes and sustains the passivation layer. Once the pH drops below the threshold value of 10.0 (Page and Page, 2007), depassivation occurs, and the steel is vulnerable to moisture and oxygen, which serve as electrolyte for the corrosion reaction. Carbonation-induced corrosion may not occur in water-saturated or very dry conditions. Be it chloride-induced, or carbonation-induced corrosion, the chemical reactions are the same (Bloomfield, 2006) but with different morphology, as described above. Details of carbonation- and chloride-induced corrosion, as well as their reaction mechanisms, are presented in Chapter 2. However, it is important to mention that chloride attack and carbonation are not the only causes of steel corrosion in concrete but the most frequent. Steel corrosion in concrete may also occur as stray current-induced corrosion or bacteria-induced corrosion (Bloomfield, 2006).

Corrosion of reinforcement in concrete often goes unnoticed from the initial stage until accompanied by cracks, followed by spalling of concrete cover or sometimes by rust stain appearing on the concrete surface. The development of cracks is due to the expansive nature of the corrosion products (oxides), which occupy more volume than the original steel. Figure 1.1 shows the relative volume of corrosion products of iron. As the corrosion product accretes, internal pressure develops on the surrounding concrete, and when this pressure exceeds the tensile strength of the concrete, crack initiates at the steel-concrete interface and then propagates toward the surface of the concrete cover. Apart from the other consequences of corrosion, the appearance of cracks increases the penetrability of concrete to deleterious substances, thus reducing the overall performance and durability of the structure (Nwaubani and Katsanos, 2014).

However, not all corrosions of reinforcement in concrete may develop internal pressure or expansive products; this happens in water-saturated condition when oxygen is deprived of the reaction and when the anode and cathode are well separated. The iron electron Fe^{2+}stays in

solution and no expansive products are generated (Bloomfield, 2006). Such conditions are difficult to detect visually in the absence of cracks or rust staining. Therefore, the subject of discussion of this research is on corrosion of reinforcement in concrete structures induced by chloride and carbonation, which are not permanently saturated in water but are subjected to wetting-drying cycle.

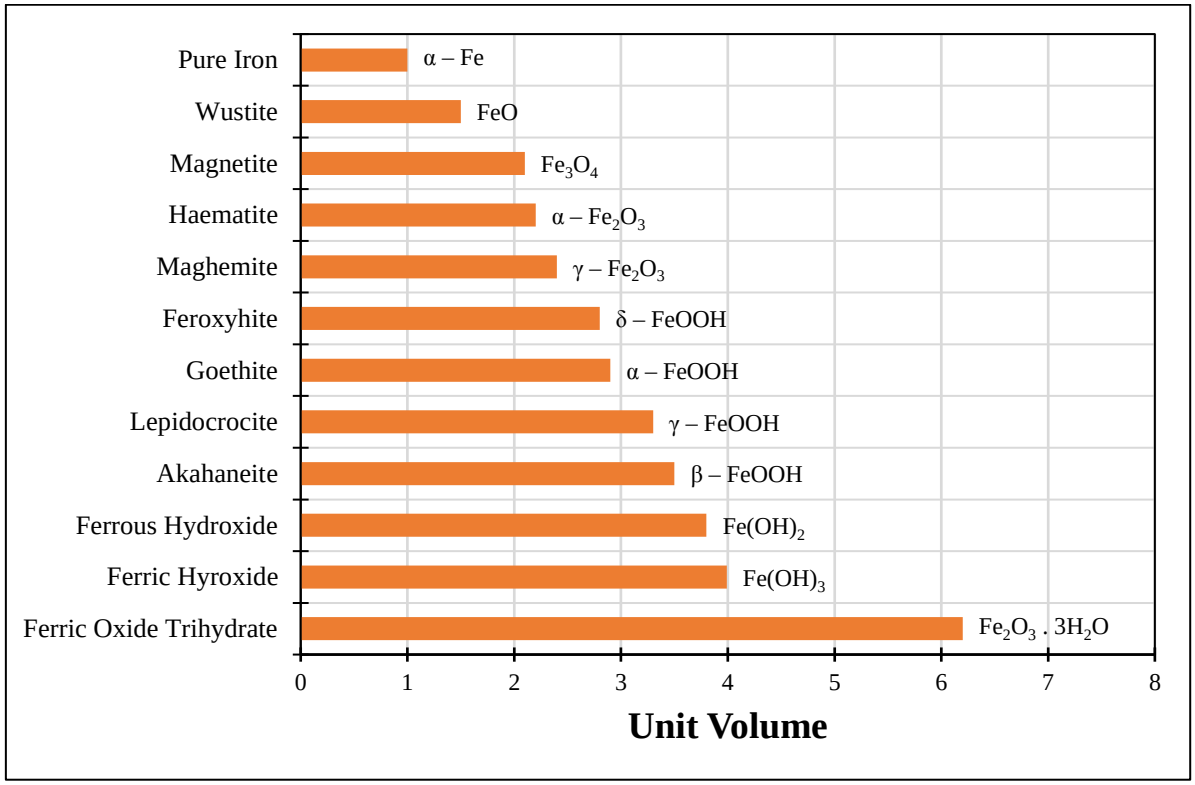

Figure 1.1 Relative volume of corrosion products of Iron (Jaffer and Hansson, 2009)

1.2 RESEARCH MOTIVATION

As mentioned above, maintenance of corroding concrete structures is a challenge to engineers, not only because of the complexity characterising corrosion process but also the uncertainty of corrosion damage quantification. Engineers are often required to assess corroding concrete structures for safety and appropriate maintenance intervention (Andrade et al., 2016). In most instances, these structures are in service thus requiring a non-destructive method of evaluation, which often leads to ambiguity. This situation often leads engineers and practitioners to recommend repair early than necessary or when the structure is beyond the limit state. According to Bloomfield (2006), if appropriate repairs are to be performed on corrosion-damaged concrete structures, then engineers must fully understand the cause and extent of the damage or risk wasting resources. Bloomfield's (2006) statement evinces that corrosion damage quantification is perhaps the most crucial tool in the assessment of corrosion-damaged structures. Appropriate repair is achievable if the extent of damage is fully known in terms of the remaining area or the cross-section loss of corroding bar.

It must be noted that it is the loss of material from the surface of the corroding bar that leads to loss in the cross-sectional area and consequently other structural effects (Dyer, 2014). Thus,

the reduction in rebar diameter or bar section is the primary effect of the corrosion process which leads to cracking and spalling of concrete cover, loss of the bonding between concrete and the embedded steel, and the loss of load-carrying capacity of both the rebar and the structure. Several studies, Zhang et al. (2010), Yu et al. (2015), Angst (2018) to name few, have revealed that the cross-section loss reduces both the load-carrying capacity and the bond between the concrete and the rebar. These studies confirmed that Andrade et al. (1988) got it right by considering the loss in rebar section due to corrosion as the fundamental parameter of failure. Therefore, to adequately predict the residual service life (load bearing capacity and serviceability) of corroding concrete structures, the remaining area of the corroding bar is required. The severity or degree of corrosion damage is an essential factor which should be quantified in terms of cross-section loss.

The need to accurately predict the degree of reinforcement corrosion in corroding concrete structures is so apparent and axiomatic. Corrosion damage quantification in reinforced concrete structures is one of the areas still underdeveloped and contentious. Other areas like the transport mechanism of both chloride and carbonation in concrete have received considerable research attention over the last decades, that there are acceptable standards now available (Angst, 2018). Although there are some suggested non-destructive models for corrosion damage prediction available in the literature, they do not adequately predict the degree of reinforcement corrosion. They are not as reliable as those of transport mechanism which has been adopted as international standards. There are more methods of corrosion detection than damage quantification. Detection methods, as the name suggests, only detect the presence of corrosion in reinforced concrete structures and tell how much steel is being converted to rust at the time of assessment but none can tell how much of the steel cross-section has been lost to corrosion. Listed below are summaries of major limitations associated with the current damaged prediction models:

1. Are laboratory-based, imprecise and cannot reproduce the same outcome as the experimental results from which they were fitted (Andrade et al., 2016).
2. The majority are empirically derived based on experimental data and subjected to the considerations and experience of their proponent (Andrade et al., 1993).
3. Empirical model cannot take into consideration all influencing parameters (Zhao et al., 2012).
4. Most corrosion damage prediction models do not permit the means of evaluating corrosion damage in terms of rebar cross-section loss (Khan et al., 2014).
5. Most models are concerned with the initiation stage of corrosion, i.e., predicting the time to cracking and the critical amount of corrosion needed to induce the first crack but very few are concerning with the prediction of corrosion damage during the propagation stage (Khan et al., 2014).
6. Most analytical and numerical models are too complicated and are not applicable in real or practical conditions (Malumbela et al., 2011).

Despite these ambiguities, inadequacies, and limitations of these damage prediction models, appreciation should be given to their proponents. Their work has set the path for further

development towards the quantification of residual life of corrosion-damaged concrete structures. Andrade et al. (1988) often considered pioneer of corrosion damage prediction, was the first to put forward a prediction model that permits the evaluation of the corrosion damage in terms of the rebar cross-section loss. Rodriguez et al. (1996) were also the first to establish a linear relationship between the corrosion-induced crack width and the rebar cross-section loss. Detailed discussions (critical reviews) on these models are presented in Chapter 2.

Corrosion-induced cracks in concrete structures are often visible, measurable and their widths commensurate with the severity of reinforcement corrosion (Andrade et al., 2016). Many researchers (Rodriguez et al. (1996), Alonso et al. (1998), Vidal et al. (2004), Andrade et al. (2016), etc.) acknowledge the existence of a relationship between the corrosion severity (cross-section loss) and the induced crack width, and believe it is the most appropriate means of evaluating the level of corrosion damage in concrete structures. However, limited consideration has been given to this relationship (Aligizaki, 2006) and detailed descriptions are yet to be fully developed. As a result, many questions concerning concrete cracking due to corrosion remain unanswered (Angst, 2018). Despite the limitation, corrosion-induced crack is still being used as damage assessment criteria. Many owners of concrete structures use the appearance of corrosion-induced cracks as an indication to execute appropriate interventions (Zhao and Jin, 2016). Therefore, quantitative descriptions of this relationship between the corrosion level and the induced crack width will assist engineers and practitioners in deciding as to when to recommend repairs.

Given the above, this research seeks to study the relationship between the crack width and the level of corrosion of the corroding bar and develop a precise non-destructive method of quantifying the level of corrosion damage in reinforced concrete structures. The model will permit the evaluation of corrosion damage in terms of the rebar cross-section loss using the corrosion-induced crack width. This proposed method will be developed based on both laboratory investigation (experiment) and mathematical modelling (analytical and numerical) which will consider key influencing parameters of corrosion mechanism as well as the theories of failure analysis and fracture mechanics of concrete. It must be noted that the proposed model may not address all the shortcoming of the existing models as listed above. However, it will present an accurate, reliable and less complicated method of quantifying corrosion damage in reinforced concrete structures in terms of the cross-section loss. It is worth emphasising that the intent of this study is not to predict the corrosion-induced crack width, which several studies have done but rather estimate the amount of rebar section loss as the result of corrosion using the corrosion-induced crack width.

1.3 AIM OF THIS RESEARCH

This research aimed to address the problem mentioned above by developing a less complicated and practicable method of quantifying the level of corrosion damage in reinforced concrete structures using the corrosion-induced crack width. This proposed non-destructive model will require input parameters that are easily obtainable both in the laboratory and the field and will be applicable to structures in service.

1.4 OBJECTIVES

The objectives of this research are divided into two parts, and outlined as follows:

1.4.1 LABORATORY EXPERIMENT

1. Conduct an accelerated corrosion test on reinforced concrete specimens to:
    - Investigate the influence of the specimens' properties (cover depth and binder type) on the corrosion process (time to corrosion initiation and cross-section loss).
    - Study the evolution of the corrosion-induced crack widths and its relationship with the rebar cross-section loss.
2. Conduct durability index tests of the mix designs to evaluate the specimens' resistance to oxygen permeation, water absorption and chloride conduction which will describe the specimen's pores structures (volume, size and interconnection), and study the influence on the corrosion process.

1.4.2 FINITE ELEMENT ANALYSIS

1. Construct prototypes of the laboratory specimens and other scenarios subjected to corrosion.
2. Logically develop the concept of stress-strain relationship in the context of corrosion in reinforced concrete for the derivation of the applied pressure.
3. Identify relevant parameters, their influence on the system being modelled (steel corrosion in concrete) as well as interdependencies.
4. Develop appropriate assumptions of the system based on relevant theories and research findings.
5. Develop a suitable or realistic numerical model of the system based on the developed concepts and assumptions.
6. Conduct simulation of the numerical model to obtain solutions.
7. Interpret the simulation results and compare it with the experimental results.
8. Derive a suitable mathematical relationship linking the corrosion-induced crack width and those relevant parameters from which the severity of corrosion damage can be estimated in terms of section loss.
9. Validate and verify this proposed relationship against the author's experimental data as well as against existing data from other researchers.

1.5 RESEARCH SIGNIFICANCE

The significances of this research are outlined as follows:

1. Provide further understanding of the relationship between corrosion-induced crack width and the level of corrosion damage (section loss) in reinforced concrete structures.
2. Provide information on parametric studies of reinforced concrete corrosion mechanism, which will:
    1. Improve service performance of existing concrete structures subjected to corrosion.

2. Contribute to the quantification of residual service life of reinforced concrete structures subjected to corrosion.
3. Contribute to the quantification of service life of reinforced concrete structures susceptible to corrosion from the design stage.

1.6 METHODOLOGY

Corrosion of steel in concrete structures is a sinuous phenomenon involving multiple causes and effects (Molina et al. 1993). Therefore, concluding corrosion damage evaluation from only experimental data or simulation results is not recommended. Thus, the methodology employed in this research are both experimental investigation and numerical analysis. The experimental investigation consisted of a laboratory accelerated corrosion test conducted on reinforced concrete specimens and durability index tests of the mix designs. The experimental investigation considered five specimens, each reinforced with nine (9) bars. The specimens were of the same dimension, have the same rebar size but with varying strengths and binder types. The numerical analysis considered three cases:

- Case I was based on sample descriptions (material properties and geometry) of the laboratory experiment.
- Case II served as the parametric studies and has material properties of the most used structural concrete.
- Case III was adopted from the literature to serve the purpose of validation and to study the influence of the properties of rust on the simulation results.

The simulation was developed based on an idealised steel corrosion mechanism in concrete and, on the theories of failure analysis and fracture mechanics of concrete. The simulation was conducted by finite element analysis software (ANSYS 19.2 student version). Detailed descriptions of the laboratory procedures and finite element analysis are presented in Chapter 3 and 5, respectively.

1.7 SCOPE AND LIMITATION

This research covers experimental and numerical investigations of the relationship between corrosion-induced crack width and the corresponding section loss of the corroding bar. The experimental investigation focused on chloride-induced corrosion while the numerical, considered uniform and non-uniform corrosion morphology. Several assumptions based on theories of failure analysis, fracture mechanics and linear elastic mechanics were employed in the numerical investigation for the purpose of simplification. This study is limited to the corrosion of steel reinforcement in concrete structures which are not permanently saturated in water but subjected to drying-wetting cycle. The influence of external load on the corrosion-induced crack width as well as that of the secondary reinforcement (stirrups) was not considered in this study. Also, this study did not include detailed analysis of factors that are highly variant within the corrosion process (e.g. corrosion rate), as the incorporation of these factors may increase the uncertainty of the proposed model.

1.8 RESEARCH OUTLINE

This thesis is divided into eight chapters and four appendixes, the brief of the remaining seven chapters are:

Chapter 2 presents the literature review and is divided into three parts: Part-I presents a review of the fundamental of steel corrosion mechanism and the principles of accelerated corrosion in concrete. Part II presents the critical review of corrosion damage prediction models that permit the evaluation of corrosion damage by means of the rebar cross-section loss. Part III gives a brief literature review of corrosion-induced cracks in relations to the rebar cross-section loss and its significance in visual assessment and damage evaluation.

Chapter 3 presents descriptions of the experimental procedures and characterisation of the materials used in this investigation. This chapter starts with an introduction, gives detailed descriptions of all materials used in this experiment and ends with a step-by-step description of the procedures of the accelerated corrosion test and the durability index tests.

Chapter 4 presents the results of the laboratory investigation and the analyses. These include strength tests, durability indexes and the accelerated corrosion results from the cyclic ponding period (resistivity and half-cell potential measurement) and the impressed current method.

Chapter 5 presents the pre-analysis of the finite element modelling. This chapter begins with an introduction, followed by the pre-analysis (geometry, materials properties, etc.) of the modelling. This chapter further outlines concepts of relevant theories and assumptions employed in the modelling and provides detailed discussions justifying the approach used in the simulation.

Chapter 6 presents discussions and analyses of the simulation results, as well as the comparison of simulation results with the laboratory investigation.

Chapter 7 presents the analytical derivation of the proposed model and its validations against the results of the laboratory investigation and some experimental data available in the literature.

Chapter 8 presents the concluding remarks, which include summary of the research (methodology and findings), conclusions and limitations as well as recommendations for future research.

1.9 PROJECT SCHEMATIC

The schematic of this project by which the objectives were achieved, is illustrated in Figure 1.2. Detailed descriptions of these events (experimental investigation, numerical investigation, derivation, etc.) are present in subsequence chapters.

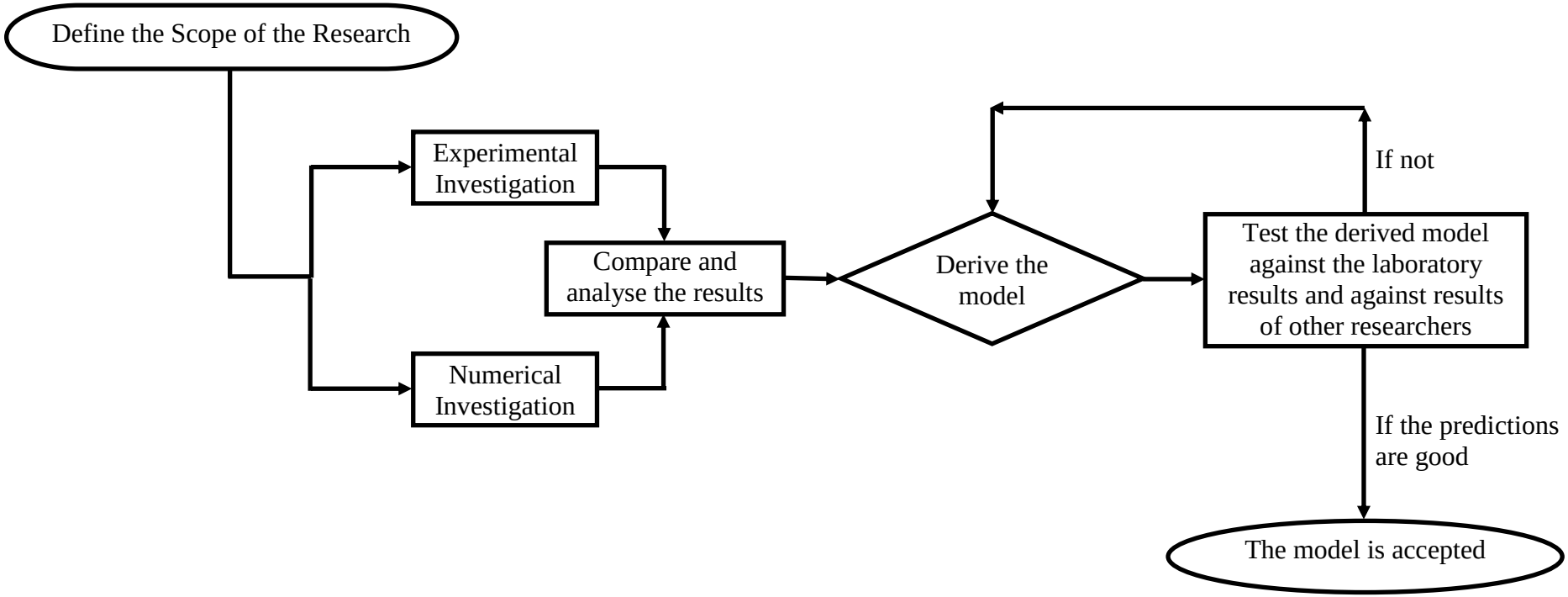

Figure 1. 2 Project Schematic

1.10 REFERENCES

1. Aligizaki, K., 2006, January. Concrete cover Cracking as a Function of Rebar Corrosion: Theoretical and Experimental Studies. In CORROSION 2006. NACE International.
2. Alonso, C., Andrade, C., Rodriguez, J. and Diez, J.M., 1998. Factors controlling cracking of concrete affected by reinforcement corrosion. Materials and structures, 31(7), pp.435-441.
3. Andrade, C., Cesetti, A., Mancini, G. and Tondolo, F., 2016. Estimating corrosion attack in reinforced concrete by means of crack opening. Structural Concrete, 17(4), pp.533-540.
4. Andrade, C., Alonso, C. and Molina, F.J., 1993. Cover cracking as a function of bar corrosion: Part I-Experimental test. Materials and structures, 26(8), pp.453-464.
5. Andrade, C, Alonso, M.C, Gonzalez J.A., 1988. An initial effort to use the corrosion rate measurements for estimating rebar durability. ASTM Symposium on "Corrosion Rate of Reinforcements in Concrete" - Baltimore (USA).
6. Angst, U.M., 2018. Challenges and opportunities in corrosion of steel in concrete. Materials and Structures, 51(1), p.4.
7. Broomfield, J.P., 2006. Corrosion of steel in concrete: understanding, investigation and repair. CRC Press.
8. Du, Y.G., Chan, A.H.C., Clark, L.A., Wang, X.T., Gurkalo, F. and Bartos, S., 2013. Finite element analysis of cracking and delamination of concrete beam due to steel corrosion. Engineering Structures, 56, pp.8-21.
9. Dyer, T., 2014. Concrete durability. CRC Press.
10. Ferreira, RM, 2004. Probability-based durability analysis of concrete structures in marine environment.
11. Gonzalez, J.A., Feliu, S., Rodriguez, P., Ramirez, E., Alonso, C. and Andrade, C., 1996. Some questions on the corrosion of steel in concrete—Part I: when, how and how much steel corrodes. Materials and structures, 29(1), p.40.
12. González, J.A., Feliu, S., Rodriquez, P., Lopez, W., Ramirez, E., Alonso, C. and Andrade, C., 1996. Some questions on the corrosion of steel in concrete. Part II: Corrosion mechanism and monitoring, service life prediction and protection methods. Materials and Structures, 29(2), pp.97-104.
13. Habibi, S., 2017. Finite Element Modelling of Corrosion Damaged Reinforced Concrete Structures, Master thesis, University of Toronto (Canada).
14. Jaffer, S.J. and Hansson, C.M., 2009. Chloride-induced corrosion products of steel in cracked-concrete subjected to different loading conditions. Cement and Concrete Research, 39(2), pp.116-125.
15. Jamali, A., Angst, U., Adey, B. and Elsener, B., 2013. Modelling of corrosion-induced concrete cover cracking: A critical analysis. Construction and Building Materials, 42, pp.225-237.
16. Kashani, M.M., Crewe, A.J. and Alexander, N.A., 2013. Nonlinear stress-strain behaviour of corrosion-damaged reinforcing bars including inelastic buckling. Engineering Structures, 48, pp.417-429.

17. Khan, I., François, R. and Castel, A., 2014. Prediction of reinforcement corrosion using corrosion-induced cracks width in corroded reinforced concrete beams. Cement and concrete research, 56, pp.84-96.
18. Malumbela, G., Alexander, M. and Moyo, P., 2011. Model for cover cracking of RC beams due to partial surface steel corrosion. Construction and Building Materials, 25(2), pp.987-991.
19. Mehta, P.K. and Monteiro, P.J., 2006. Concrete: microstructure, properties, and materials. 2006.
20. Molina, F.J., Alonso, C. and Andrade, C., 1993. Cover cracking as a function of rebar corrosion: part 2—numerical model. Materials and structures, 26(9), pp.532-548.
21. Nwaubani, S.O. and Katsanos, A., 2014. Effect of Alternative De-icers on the Corrosion Resistance of Reinforced Concrete Bridges and Highway Structures. In Developments in Corrosion Protection. In Tech.
22. Page, C.L. and Page, M.M. Eds., 2007. Durability of concrete and cement composites. Elsevier.
23. Raupach, M., Elsener, B., Polder, R. and Mietz, J. eds., 2014. Corrosion of Reinforcement in Concrete: Mechanisms, Monitoring, Prevention and Rehabilitation Techniques (Vol. 38). Woodhead Publishing.
24. Rodriguez, J., Ortega, L.M., Casal, J., Diez, J.M., 1996. Corrosion of reinforcement and service life of concrete structures. Durab. Build. Mater. Compon., 7 (1) pp 117–126.
25. Vidal, T., Castel, A., François, R. (2004) Analysing crack width to predict corrosion in reinforced concrete, Cement & Concrete Research, Vol. 34 pp 165–174.
26. Yu, L., François, R., Dang, V.H., L'Hostis, V. and Gagné, R., 2015. Distribution of corrosion and pitting factor of steel in corroded RC beams. Construction and Building Materials, 95, pp.384-392.
27. Zhang, R., Castel, A. and François, R., 2010. Concrete cover cracking with reinforcement corrosion of RC beam during chloride-induced corrosion process. Cement and Concrete Research, 40(3), pp.415-425.
28. Zhao, Y. and Jin, W., 2016. Steel Corrosion-Induced Concrete Cracking. Butterworth-Heinemann.
29. Zhao, Y., Yu, J., Hu, B. and Jin, W., 2012. Crack shape and rust distribution in corrosion-induced cracking concrete. Corrosion science, 55, pp.385-393.

2 LITERATURE REVIEW

2.1 INTRODUCTION

Being one of the major durability problems facing reinforced concrete infrastructures, corrosion of steel in concrete has received substantial attention over the past decades. Consequently, this chapter presents literature review relevant to the aim and objectives of this research. This chapter is divided into three parts: Part-I presents a review of the fundamentals of steel corrosion mechanism and the principles of accelerated corrosion in concrete. Part-II, which is the focus of this research, presents the critical review of corrosion damage prediction models that permit the evaluation of corrosion damage by means of the rebar cross-section loss, and Part-III gives a brief literature review of corrosion-induced cracks in relations to the rebar cross-section loss, and its significance in visual assessment and damage evaluation.

2.2 PART-I: FUNDAMENTALS OF STEEL CORROSION IN CONCRETE

2.2.1 THERMODYNAMICS OF STEEL

Like most metals, iron exists as minerals (iron ores) in the form of iron oxides and iron carbonate in the earth's crust. These compounds are thermodynamically stable and are in an equilibrium state with the environment. Unfortunately, the extraction of iron and other metals from their ores leave the metals in a thermodynamically metastable state (Hansson, 2016). Therefore, depending on the exposure environment, metallic iron will always seek to return to its equilibrium state. This reversion process or interaction of metals with the environment to return to a more stable state is termed corrosion. Corrosion is an electrochemical reaction which involves the oxidation of metal to its ion and consists of anodic and cathodic reactions, usually referred to as half-cell reactions. The oxidation of the metal occurs at the anode, while the reduction of oxygen which results in the generation of hydroxyl ions occurs at the cathode. As an electrochemical reaction, corrosion necessitates the exchange of electrons between the anode and the cathode which generates electric current. The measurement of the current flowing between anode and cathode is a direct measure of the rate of dissolution or oxidation of the metal and is known as the corrosion current (Hansson, 2016).

2.2.2 MECHANISM OF STEEL CORROSION IN CONCRETE

With regards to corrosion, the service life of reinforced concrete as described by Tuutti's model (1982) consists of two distinct stages: corrosion initiation and corrosion propagation and is illustrated in Figure 2.1. The initiation stage is the period taken by corrosion agents to cause depassivation and initiate corrosion. The propagation stage is period which begins after corrosion has initiated and last up to the point when the limit state is reached, or the point beyond which consequences of corrosion cannot be further tolerated (Bertolini, 2008). Therefore, from this simple perspective, yet one of the most significant contributions to service

life model of reinforced concrete structures susceptible to corrosion (Page and Page, 2007), the fundamental of steel corrosion in concrete will be discussed.

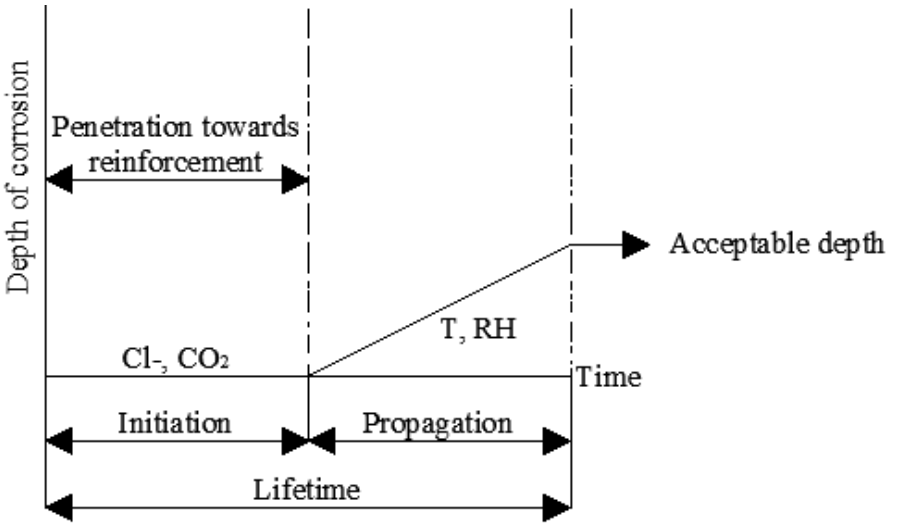

Figure 2. 1 Tuutti's model of service life (Tuutti, 1982)

2.2.3 CORROSION INITIATION

As previously mentioned in Section 1.1, steel in concrete is initially passivated (protected from corrosion) because of the high alkaline environment which promotes the formation of a thin layer of iron oxide on the steel surface. Iron oxides are thermodynamically stable in an alkaline environment. The high alkalinity in concrete is due to the presence of dissolved sodium and potassium hydroxides in the concrete pores, as well as the present of solid hydration products such as calcium hydroxide and calcium silicate hydrate (Bertolini et al., 2013). The formation of the passive layer reduces the dissolution rate of the metal to a negligible level, corresponding to an average of less than 1µm/year (Page and Page, 2007). The passive layer is about few nanometres thick and is immune to mechanical damage (Bertolini et al., 2013). However, the passive layer can break down as a result of reduction in alkalinity or damaged directly by chloride ion or stray current. Reduction in alkalinity is usually because of acid attack (mostly by carbonation, or biogenic sulfuric acid attack). However, biogenic sulfuric acid attack is usually the concrete problem before the reinforcement, and the effect of stray current mainly depends on the source.

Consequently, the focus of this discussion is on the two most common causes of steel depassivation in concrete as stated in Section 1.1. It is worth noting that the passive layer is also capable of recovering or repairing itself from damages if conditions permit. That is, the passivating environment is maintained (Broomfield, 2006) and the anodic or electrolytic (moisture and oxygen) process is stopped (Bertolini et al., 2013).

Once the passivity breaks down, corrosion initiates in the presence of moisture and oxygen. The steel begins to dissolve in the concrete's pose solution at the anode and giving up electrons (Broomfield, 2006). The electrons released by the anode are consumed at the cathode along with water and oxygen producing hydroxyl ions. In reinforced concrete, both the anode and the

cathode are located on the surface of the corroding bar. The depassive area is the anode while the remaining passive area serves as the cathode. The dissolution of the steel and the release of electrons as illustrated in Eq. – 2.1, is just the first step of the anodic reactions, several anodic reactions may occur. The Fe^{2+} may reacts with water (H_2O) as illustrated in Eq. – 2.2, forming ferrous hydroxide (rust) and hydrogen ions (Bertolini et al., 2013; Poursaee, 2016), which further react with oxygen and water to form ferric hydroxide and hydrated ferric oxide, respectively. The Fe^{2+} may also reacts with the hydroxyl ions that have migrated to the anode as illustrated in Eq. – 2.3, forming ferrous hydroxide (Ferreira, 2004; Broomfield, 2006; Dyer, 2014), which will also hydrate in the presence of oxygen to form ferric hydroxide and hydrated ferric oxide, respectively. These hydroxides may subsequently undergo several dehydration reactions (Dyer, 2014) to form other corrosion products of iron, from Akahaneite to Wustite, as illustrated in Figure 1.1.

Note the hydrolysis at illustrated in Eq. – 2.2 and the reaction of Fe^{2+} with hydroxyl ions at the anode increase the acidity at the anode. While the generation of hydroxyl ions at the cathode as illustrated in Eq. – 2.4, increases the alkalinity and strengthen the passive layer at the cathode, hence, providing resistance against depassivation (Broomfield, 2006). Thus, the metal loss and the generation of rust occur only at the anode. The chemical reactions described above are the same for both chloride-induced corrosion and carbonation-induced corrosion.

Anodic reactions

$$Fe \rightarrow Fe^{2+} + 2e^{-} \quad \text{---------- Eq. – 2.1}$$

$$Fe^{2+} + 2H_2O \rightarrow Fe(OH)_2 + 2H^{+} \quad \text{---------- Eq. – 2.2}$$

$$Fe^{2+} + 2OH^{-} \rightarrow Fe(OH)_2 \quad \text{---------- Eq. – 2.3}$$

Cathodic reaction

$$2e^{-} + H_2O + \frac{1}{2}O_2 \rightarrow 2OH^{-} \quad \text{---------- Eq. – 2.4}$$

2.2.3.1 Carbonation-Induced Corrosion

Carbonation in concrete refers to the process in which carbon dioxide (CO_2) gas from the atmosphere chemically reacts with some hydration products (calcium hydroxide and calcium silicate hydrate) of Portland cement in the presence of moisture to produce calcium carbonate. This process changes the electrochemical environment within concrete by neutralisation of the alkalis. Hence, it is also known as neutralisation. The process begins with the diffusion of carbon dioxide gas through the concrete pores. The diffused gas then dissolves in the water present in the concrete pores to form carbonic acid (H_2CO_3), which reacts with calcium hydroxide ($Ca(OH)_2$) and calcium silicate hydrate (C-S-H) to form calcium carbonate ($CaCO_3$) and water. Eq. – 2.5 and 2.6 below, describe the reactions of carbon dioxide gas and calcium hydroxide in Portland cement concrete. As illustrated in Eq. – 2.6, the water participating in the reaction is never consumed but instead released.

$$CO_2 + H_2O \rightarrow H_2CO_3$$ ----------Eq. – 2.5

$$H_2CO_3 + Ca(OH)_2 \rightarrow CaCO_3 + 2H_2O$$ ----------Eq. – 2.6

It is worth noting that in Portland cement concrete, calcium hydroxide ($Ca(OH)_2$) is the hydrate which reacts easily with carbon dioxide and when it has depleted, or as in the case of blended cement concrete, carbonation of calcium silicate hydrate (C-S-H) may occur (Bertolini et al., 2013). Also, studies have shown that even ettringites do carbonate as well as all calcium-bearing phases (Bertolini et al., 2013; Šavija and Luković, 2016). The reaction of carbonic acid with calcium hydroxide, calcium silicate hydrate and other products of hydration (ettringite and monosulfate hydrates) may release bound chloride if present and this increases the aggressiveness of the pore's solution. Bound chlorides are chloride physically or chemically bound to hydration products and may have been incorporated in concrete unintentionally (from aggregates or mixing water) or intentionally as an accelerator (calcium chloride, as in older structures).

The carbonated layer progressively extends into the concrete with time, and the innermost edge of the carbonated layer is referred to as the carbonation front. As the carbonation front progresses, it neutralises the environment, and once it reaches the steel reinforcement, depassivation occurs, and corrosion initiates in the presence of moisture and oxygen. As stated in Section 1.1, the corrosion morphology of carbonation-induced corrosion is usually generalised. The primary effect of carbonation in concrete is the reduction in alkalinity which leads to steel corrosion in reinforced concrete. Carbonation does not affect the concrete's integrity directly in ordinary Portland cement concrete. Carbonation in Portland cement concrete has some beneficial effects, the precipitation of calcium carbonate which lines the poses of the carbonated layer reduces porosity and increases strength. However, this is not the case for blended cement or binary binder concrete; carbonation is disruptive to the cement paste. Because of the low calcium hydroxide content, the calcium silicate hydrate gel tends to carbonate, and this leads to decomposition of calcium silicate hydrate gel. Being the primary strength-contributing gel, the decomposition of the calcium silicate hydrate gel weakens the mechanical integrity of the concrete and increases porosity.

The carbonation of concrete is mainly controlled by the diffusion rate of carbon dioxide (CO_2), which decreases with time. The rate of diffusion decreases with time because the carbon dioxide must penetrate further into the concrete through the carbonated layer, which has become more impermeable due to the precipitated calcium carbonated lining the pores and the continuation of hydration due to the presence of moisture (Bertolini et al., 2013; Poursaee, 2016). Several equations have been formulated to predict the depth of carbonation with time. The most general and simplified form is given in Eq. – 2.7, which assumes that the diffusion rate of carbon dioxide is constant (Ashraf, 2016; Broomfield, 2006; Bertolini et al., 2013).

$$d = k\sqrt{t}$$ ---------- Eq. – 2.7

Where $\boldsymbol{d}$ is the carbonation depth (mm), which is the average distance from the external surface to where the carbonation front has reached, $\boldsymbol{k}$ the carbonation coefficient (mm/year$^{1/2}$), and $\boldsymbol{t}$

the time (years). The carbonation depth can be measured directly by microscopic examinations to identify calcium carbonate on extracted samples or by a pH indicator (Phenolphthalein). Phenolphthalein is the most widely used test method to identify the carbonation front in cement-based systems, but it only provides an approximation of the carbonation depth (Ashraf, 2016).

2.2.3.1.1 Factors Affecting Carbonation in Concrete

Due to the presence of carbon dioxide in the earth's atmosphere, almost all cement-based material must undergo a certain extent of carbonation during its service life (Ashraf, 2016). However, the extent of carbonation depends on factors which are broadly categorised as extrinsic and intrinsic. Extrinsic factors refer to environmental factors which include the concentration of carbon dioxide, relative humidity and temperature. While the intrinsic factors relate to properties of the cement-based material, the most influential are the porosity, the binder type, and cover depth.

Concentration of CO_2: Being diffusion driven process, the concentration of carbon dioxide in the environment (atmosphere) plays an essential role in the carbonation of concrete. With other conditions constant, an increase in the carbon dioxide concentration in the atmosphere will lead to an increase in the rate of diffusion through the concrete, thus higher rate of carbonation.

Humidity: Humidity is generally the most crucial environmental factor influencing carbonation in concrete (Bertolini et al., 2013). The relative humidity of the environment affects the rate of carbonation in concrete because the humidity within the concrete is to some extent in equilibrium with its environment. As previously mentioned in Section 1.1, carbonation-induced corrosion may not occur in water-saturated or very dry conditions. At very high humidity, the concrete pores are filled with water, thus hindering the diffusion of carbon dioxide through the concrete. While, at very dry conditions, the concrete pores are filled with air, the diffusion of carbon dioxide is facilitated, but carbonation cannot occur in the absence of moisture. As described in Eq. – 2.6, moisture is required to react with carbon dioxide to form carbonic acid which then reacts with calcium hydroxide to form calcium carbonate and water. Therefore, the idea range of humidity of carbonation in concrete is between 50% – 70%.

Temperature: Like any chemical reaction, carbonation in concrete is temperature dependent. Not only the rate of the reaction is influenced by temperature but also the diffusion coefficient (Dyer, 2014). At high temperature the diffusion rate of carbon dioxide and the rate of reaction increase.

Concrete properties: Concrete properties have the utmost influence on the rate of carbonation. The diffusion rate of carbon dioxide through concrete or the progression of the carbonation front is controlled mainly by the porosity of the concrete, the type of binder used and the cover depth. The porosity of concrete is mainly controlled by the water-binder ratio and curing condition. The lower the water-binder ratio, the less porous the concrete becomes, thus slowing the progression of the carbonation front. The binder type influences the rate of carbonation with regards to the amount of calcium hydroxide present. Low calcium hydroxide content

results in a faster rate of progression of the carbonation front. This is usually the case with blended-cement concrete; these systems are less resistive to carbonation. However, by the using lower water-binder ratio coupled with longer curing time result in a denser microstructure, thus, leading to lower diffusion (Bertolini et al., 2013). The depth of the concrete cover mainly influences the time to corrosion initiation. The higher the cover depth, the longer the time to corrosion initiation. Carbonation is usually not a major problem in concrete having high cover depth.

2.2.3.2 Chloride-Induced Corrosion

The presence of chloride in concrete poses the greatest threat to steel reinforcement (Dyer, 2014) and is the frequent cause of steel corrosion in concrete (Bertolini et al., 2013). Chloride may enter concrete from various sources and are generally grouped into two categories: chloride-incorporated in the fresh concrete (as discussed in Section 2.2.3.1) and chloride-penetrating the hardened concrete form the environment (Poulsen and Mejlbro, 2014). From the environment, chlorides may penetrate the hardened concrete from sources such as seawater, soil containing chloride, de-icing salts containing chloride, and salt spray as in some industries (Poulsen and Mejlbro, 2014). Once in concrete, chlorides may be either free (dissolved in the pore's solution) or bound (chemically or physically) to the cement hydrates. It is the presence of free chloride in concrete that is detrimental to the steel reinforcement (Poulsen and Mejlbro, 2014; Poursaee, 2016). Chloride ion causes the local breakdown of the passivation layer, and this occurs when sufficient amount of chloride (chloride threshold) reaches the reinforcing bar. Once passivation is lost, corrosion initiates in the presence of moisture and oxygen, and localised pits are formed. However, if the concentration of the chloride is high at the steel-concrete interface and the concrete is very porous, corrosion may take the form of uniform or generalised corrosion.

The exact mechanism of depassivation of the reinforcing steel by chloride is not precisely known. However, it is generally expressed by the Eq. – 2.8 and 2.9. As illustrated in Eq. – 2.8, the chloride ion (Cl^-) reacts with the passivation layer competing for the ferrous ion (Fe^{2+}) to form ferrous chloride ($FeCl_2$), which reacts with water to form ferrous hydroxide and hydrogen chloride as shown in Eq. – 2.9. Due to the presence of moisture, the formation of hydrogen chloride leads to the formation of hydrochloric acid, a highly corrosive acid noted for reacting with ferrous oxide (FeO). Consequently, increasing the aggressiveness of chloride attack on the steel hence, an increase in the rate of dissolution of the steel. Since the chloride ion reacting with the Fe^{2+} is never consumed but recycled, the process becomes self-sustaining if moisture and oxygen are present.

$$Fe^{2+} + 2Cl^- \rightarrow FeCl_2$$ ---------- Eq. – 2.8

$$FeCl_2 + 2H_2O \rightarrow Fe(OH)_2 + 2HCl$$ ---------- Eq. – 2.9

2.2.3.3 Transport Mechanism of Chloride in Concrete

The transport mechanism of chloride into concrete is complex and may involve more than one mass transport process depending on the exposure and surface conditions of the concrete. Exposure conditions not necessarily refer to the intensity of chloride presence within the environment but the prevailing environmental conditions to which the concrete is subjected (dry, saturated, unsaturated, etc.), while the surface conditions refer to the presence of cracks or other surface defects.

Chloride may enter concrete from the environment by mean of sorption, diffusion, permeation, convection and migration. The mode of sorption occurs under the influence of capillary action, diffusion under the influence of concentration gradient, permeation under the influence of hydraulic pressure or externally applied pressure, while convection by the difference in moisture content and migration by the difference in electrical potential.

The exposure and surface conditions are what determine the mode of transport or perhaps modify the process. For example, when a dry concrete comes in contact with chloride solution (salt water), the solution itself moves into the concrete until saturation is reached. Under saturation, the ingress mechanism is predominantly driven by diffusion, that is the chloride ions move through the concrete under the influence of concentration gradient with no or minimal flow of the solution. However, before saturation, several mass transport processes may be involved depending on the surface condition. In the absence of hydraulic pressure gradient, surface defects and electrical potential, the initiate ingress mechanism will be sorption, and then convection as the chloride solution moves into the concrete further away from the exposed surface. The presence of surface cracks may switch the initial mode to convection and depending on the intensive of the cracks; permeation may occur. If there is an electrical potential, the mode of transport of the chloride ion will be governed by migration.

2.2.3.4 Factors Affecting the Initiation of Chloride-Induced Corrosion

At a given cover depth and environmental condition, the most influential factors affecting the time to initiation of chloride-induced corrosion in concrete depend on its properties; penetrability, chloride binding capacity and chloride threshold.

Penetrability: Concrete's penetrability generally determines the rate of chloride diffusion and is mostly influenced by the water-binder ratio, binder type and curing conditions. The rate of diffusion influences the time to initiation, generally a low rate of diffusion extends the time to corrosion initiation.

Chloride Binding: Chloride binding plays a significant role in reducing the rate of chloride ingress (Dyer, 2014). Chloride binding refers to the process in which chloride ions are physically or chemically bound to products of hydration. Physically bounding occurs by the absorption of chloride to the surface of calcium silicate hydrate (C-S-H) gel while chemical bounding by the reaction of chloride with the aluminate phases. The chemical bounding results in the formation of Friedel's salt ($3CaO.Al_2O_3.CaCl_2.10H_2O$). Chloride binging reduces the content of the free chloride which is responsible for corrosion, hence, extending the time to

corrosion initiation. The binding capacity of concrete is mostly influenced by the binder. Binders with higher aluminate content have greater binding capacity. The use of supplementary cementing materials (SCM) in Portland cement-based concrete increases the binding capacity because of the high aluminate content (except for silica fume) and by the consumption of calcium hydroxide which results in the production of additional calcium silicate hydrate gel.

Chloride threshold: Chloride threshold refers to the critical chloride content required to cause depassivation and initiate corrosion and, may be expressed as the total chloride content (free and bound) or only as the free chloride content, which is responsible for corrosion initiation. High threshold values extend the time to corrosion initiation. Chloride threshold value varies and depends on several factors such as binder type, porosity, the pH level within the concrete, the Cl^-/OH^- ratio within the concrete's pores solution, the porosity at the steel-concrete interface as well as the electrochemical potential of the steel.

2.2.4 CORROSION PROPAGATION

Corrosion propagation is the stage when corrosion is actively ongoing, and depending on exposure conditions, this stage is usually characterised by the appearance of cracks, spalling and delamination due to the expansive nature of the corrosion product.

2.2.4.1 Factors Affecting Propagation of Steel Corrosion in Concrete

The most critical factor affecting the propagation of steel corrosion in concrete is the resistivity of the concrete, which also depends on both the environment (relative humidity) and several properties of the concrete (binder type, water-binder ratio and cover depth). As discussed in Section 2.2.3, when corrosion initiates, the anode releases electrons and these electrons must be consumed as the cathode for corrosion to proceed. Therefore, the flow rate of the electrons between the anode and the cathode directly determines the rate of the corrosion process. This flow rate depends on the conductivity (inverse of resistivity) of the concrete. At high resistivity, the electron flow is restricted, limiting the rate of the corrosion reaction. At a given instance, the most influential factor affecting concrete resistivity is the relative humidity or the amount of moisture. An increase in humidity or moisture reduces the resistivity, thus, improving the flow rate of the electrons, and vice-versa. It is worth noting that the factors affecting the propagation of corrosion in concrete are synergistic at one instance and incompatible at the other. Moisture improves conductivity but because oxygen is also needed for corrosion to proceed, high moisture content (saturated condition) may deprive oxygen, thereby, limiting the rate of the corrosion reaction.

2.2.5 PRINCIPLES OF ACCELERATED CORROSION IN CONCRETE

Accelerated corrosion in concrete is a laboratory procedure for simulating corrosion in reinforced concrete for research (Ahmad, 2009). Many researchers adapt to accelerating corrosion to obtain results within a reasonable timeframe as steel corrosion in concrete under natural conditions is a slow process, even in the most severe environment (Ahmad, 2009; Torres-Acosta, 2010). The term accelerated corrosion refers to any corrosion test method from

which results are obtained in a shorter timeframe than from natural exposure (Meade, 1999), including corrosive-environment simulation or artificial climate environment technique. However, this term mostly refers to electrochemical methods of simulating steel corrosion in concrete. It is worth noting that there is no standard procedure for accelerating steel corrosion in concrete, researchers adopt various techniques to suit the context of their experiment (Malumbela et al., 2012).

The electrochemical method is the most popular corrosion accelerating technique among researchers, most especially the impressed current technique or galvanostatic method as it is also known. Therefore, the review here is focused on the principles of the impressed current technique as it was incorporated in the laboratory investigation. This technique consists of applying a direct current (DC) to the embedded steel to induce corrosion and operates on the same principles as an electrochemical cell, which comprises two conductive electrodes (anode and cathode) connected via an electrolyte containing ionic species such as Na^+ and Cl^-. In the impressed current setup, the rebar serves as the anode (working electrode) while the counter electrode serves as the cathode. The applied current causes the transfer of electrons from the anode (rebar) to the counter electrode. The release of electrons by rebar causes the loss of material from its surface, resulting in mass loss and cross-section loss. This setup allows the manifestation of the same half-cell reactions that occurs under natural corrosion as described Section 2.2.3, the rebar oxidised (giving up electrons) while the reduction occurs at the counter electrode. Although the impressed current technique does not mimic the scenario of nature corrosion (Yuan et al., 2007), it is necessary for use in cases where time is a major limiting factor of the experiment (Kashani et al., 2013). The major advantages of this technique are: it can achieve a high degree of corrosion (section loss) within the relatively short period and the ease with which the desired degree of corrosion can be controlled (Yuan et al., 2007; Poursaee and Hansson, 2009).

2.3 PART-II: CRITICAL REVIEW OF EXISTING MODELS

The prediction of corrosion damage in reinforced concrete structures has been the subject of discussion for decades (Khan et al., 2014). Due to the complications in quantifying such internal process and the significance attached, corrosion damage prediction has become an interesting topic to many researchers, most especially to those concerned with estimating the residual service life of corroding reinforced concrete structures (Du et al., 2013). Several theories and models have been developed in attempts to estimate the level of corrosion damage in reinforced concrete structures. However, the need to accurately quantify corrosion damage in reinforced concrete structures remains. This section presents a critical review of corrosion damage prediction models that permit the evaluation of the corrosion damage in terms of the rebar cross-section loss and evaluation reports on the prediction capabilities of these models.

2.3.1 Andrade et al.'s model (1988)

In the first attempt of subsequent studies, Andrade et al. presented the prediction of the residual service life of corroding concrete structures by introducing several corrosion intensity values into Tuutti's model of service life prediction. The authors considered only the propagation stage

of Tuutti's model in their analysis. This approach considered the reduction in the rebar diameter or bar section as the decisive parameter of failure due to corrosion, as well as in calculating the loss of load-carrying capacity of corroding concrete structures. The authors based their analysis on the definition of the unacceptable level of deterioration as suggested by the Comité Eurointernational du Béton (CEB) Bulletin No 162.

Several corrosion intensity values, which have been recorded over the period of twenty (20) years by polarisation resistance technique were tested against Tuutti's model of service life prediction, and the results are presented in Figure 2.2. According to the authors, assuming the corrosion intensity values to be constant, the prediction of the number of years to reach a deterioration level according to CEB Bulletin No. 164 is easily attained from Figure 2.2. This model represents a simple and graphical approach for predicting the residual service life of corroding concrete structures.

2.3.2 Andrade et al.'s model (1989)

As a continuation of previous studies of Andrade et al. (1988), an attempt is made here to establish an empirical relationship from which the loss in load-carrying capacity can be determined from corrosion intensity (i_{corr}) values assuming several simplifications as the previous studies. This model equates the loss in load-carrying capacity with the loss of rebar cross-section as a function of its corrosion rate. This loss in diameter decreases linearly with the corrosion rate. From Figure 2.2, the authors established the relationship linking the reduced diameter of the rebar due to corrosion and the corrosion rate.

$$\theta(t) = \theta_i - 0.023 \cdot i_{corr} \cdot t \qquad \text{---------- Eq. – 2.10}$$

Where: $\theta(t)$ = rebar diameter in millimetre at time (t)
θ_i = initial diameter (mm) of the rebar
i_{corr} = is the corrosion rate (µA/cm^2)
t = time after the beginning of the propagation period (years)
0.023 = conversion factor of µA/cm^2 into mm/year.

The major drawback of these approaches (1988 & 1989) is calculating the loss in cross-section of the rebar (corrosion damage) form the corrosion intensity with the assumption that it is constant. The recorded corrosion intensity values were instantaneous, varying with the temperature, relative humidity, availability of oxygen, etc. (Bouteiller et al., 2012). Such instantaneous or average assumed values often give inaccurate results (Broomfield et al., 1993). According to Broomfield (2006), the instantaneous corrosion intensity only tells how much steel is being converted into rust or how much metal is being lost at the time of measurement. Hence, such values should not be incorporated into prediction models. However, if these values are to be incorporated, they are to be recorded with a high degree of accuracy to avoid variation (Otieno et al., 2011).

Secondly, these models (1988 & 1989) do not consider the characteristics of concrete as influencing parameters in corrosion damage evaluation. If the 1989 model is to be applied to

concrete structures other than laboratory-based, the assumption of time (t) must be made, thus increasing the risk of inaccuracy. Steel corrosion in concrete is a complex process, therefore, such simple relationships like Eq. – 2.10 and the graphical approach presented in Figure 2.2 are often not recommended (Andrade et al., 2016).

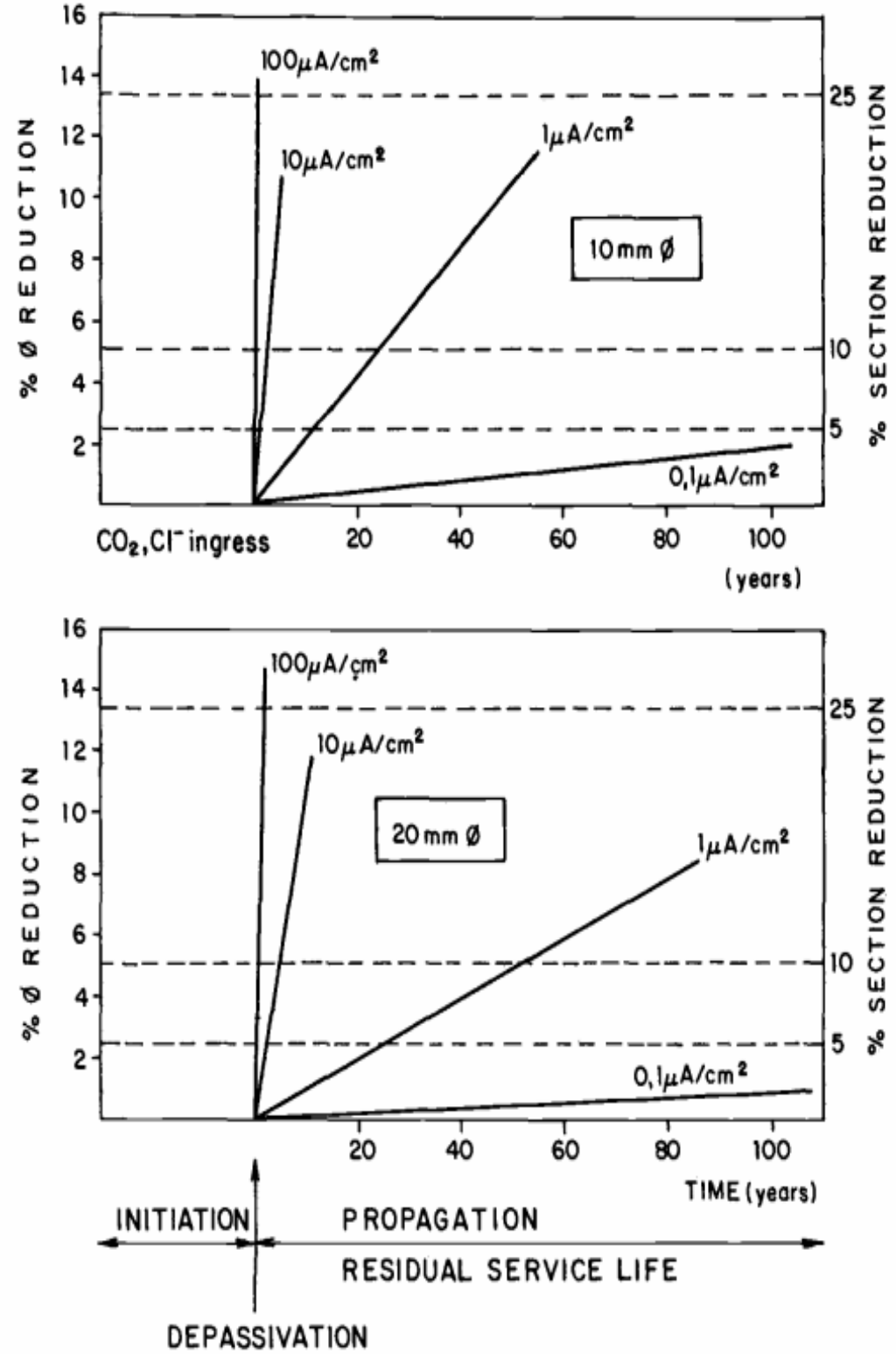

Figure 2. 2 Examples of residual service life for bar of 10- and 20-mm diameter implemented in Tuutti's model (Andrade et al., 1988)

2.3.3 Andrade et al.'s model (1993)

Still concerned with the prediction of service and residual life of corroding concrete structures, Andrade et al. conducted series of experiments and presented their findings in a two-part series titled "Cover cracking as a function of rebar corrosion". The goal of this study can be outlined as follows: (1) define the serviceability limit state (SLS) of corroding reinforced concrete structures, (2) identify the amount of corrosion needed to induce the first appearance of crack at the concrete surface (3) establish a relationship between the rebar cross-section loss and corrosion-induced crack width and (4) validate this relationship against a finite element modelling of the experiment.

Andrade et al. (1993) presented Part-I which outlined the experimental procedures and data collected from the accelerated corrosion test of four reinforced concrete beams (specimen I, II, III and IV), as well as their approach of defining serviceability limit state (SLS) for corroding concrete structures. The dimensions of these specimens were 38 x 15 x 15 cm. Each specimen contained single rebar of 16 mm diameter, whose position varies per specimen. The rebar of Specimen I was placed in the upper right corner while Specimens II, III and IV had their rebar placed in the centre of bottom side with a concrete cover depth 2 and 3 cm, respectively. The currents applied in this experiment were 100 and 10 $\mu A/cm^2$ for specimen I, II, III and IV, respectively, with the assumption that 100% of the applied current was consumed in the corrosion process. The applied currents (I_{corr}), which were considered as the corrosion rate were converted to the diameter loss by Eq. – 2.10 (Andrade et al., 1989). The following are the conclusions drawn from experimental results based on the condition tested, that is cover-rebar ratio is less than 2 and assuming a 100% current efficiency under which the specimens were tested:

- Only a few micrometres of loss in rebar cross-section (20 μm) are needed to induce visible cover cracks (0.1 mm width).
- The period between depassivation and the appearance of a crack of 0.05 – 0.1 mm width is relatively short, after which the crack width growth become slower.

2.3.4 Molina et al.'s model (1993)

Molina et al. presented Part-II of "Cover cracking as a function of rebar corrosion" with the goal of establishing a relationship between the rebar cross-section loss and corrosion-induced crack width from the experimental data and validate the relationship against a finite element modelling of the experiment. The proposed relationship is presented below (equation 2.11 and 2.12). The finite element modelling of all specimens was done based on smeared crack approach, and the corrosion effect was simulated by the application of radial displacement in three steps of cumulative loads, each representing an advance of 20 μm of attack penetration. The authors adopted properties of liquid water (bulk modulus and Poisson's ratio) as the rust properties, citing the lack of available information. The simulation aimed at corroborating the proposed relationships (equation 2.11 and 2.12) developed from the experimental data.

$$\Delta x = 0.032 \cdot I_{corr} \cdot \Delta t \quad \text{---------- Eq. – 2.11}$$

$$w = L\varepsilon \quad \text{---------- Eq. – 2.12}$$

Where: Δx = Attack penetration in µm
I_{corr} = Applied current (100 or 10 µA/cm^2 depending on the specimen)
Δt = Time increments in days
w = Crack width
L = Length of the crack
ε = Strain (recorded at the gauge)

However, the results of the simulation showed poor agreement to the analytic results thus the validation of the proposed relationships was not possible. The authors attributed the discrepancy to those influencing parameters (specific volume of the rust, initial penetration, etc.) which were arbitrarily chosen in the numerical model. The authors concluded that more studies need to be done to further understand those phenomena which have not yet been included in numerical modelling. The following limitations can be noted about this model are:

1. Firstly, it shows similar limitations as Andrade et al. (1988) & (1989) models, regarding corrosion intensity, the concrete characteristics and the simplicity of the relationship, moreover, it was not validated.
2. The attack penetration (Δx) is not evaluated in terms of rebar cross-section loss as was proposed in Part-I.
3. This model shows no connection or relationship between the attack penetration (Δx) and the corrosion-induced crack width (w) as was proposed in Part-I.

2.3.5 Rodriguez et al.'s model (1996)

Rodriguez et al. conducted series of experiments based on accelerated corrosion test and put forward two linear relationships. The first established relationship between the rebar diameter and level of corrosion damage.

$$\varphi = \varphi_0 - \alpha x \quad \text{---------- Eq. – 2.13}$$

Where **φ** is the residual bar diameter, $\boldsymbol{\varphi_0}$ the initial bar diameter, $\boldsymbol{x}$ the attack penetration and **α** the attack penetration parameter: **α = 2**, for homogenous corrosion and **4 < α < 8** for localised corrosion. The second linking the crack width with the attack penetration ($\boldsymbol{x}$) from the first equation:

$$w = 0.05 + \beta(x - x_0) \quad \text{---------- Eq. – 2.14}$$

Where $\boldsymbol{x}$ the attack penetration (µm), and **β** the coefficient depending on the position of the rebar: **β = 0.01** for top cast bars and **β = 0.0125** for bottom cast bars. The major drawbacks of this approach are: not considering concrete characteristics as influencing parameters and difficulty in deciding which value of attack penetration should be used as the accuracy of this model prediction depends on the value of attack penetration selected (Khan et al., 2014). The uncertainty of determining if it is generalised or localised corrosion within the concrete renders it unpractical to be used in real situations.

2.3.6 Alonso et al.'s model (1998)

Alonso et al. studied the relationship between the amount of corrosion and cover cracking. The mean variables studied were: cover-diameter ratio, proportions of cement, water-cement ratio, cast position of the rebar, and corrosion rate. The authors established two linear relationships based on results obtained from their studies. The first, deduced from Figure 2.3, expresses the relationship between the attack penetration, concrete cover and diameter.

$$X_0 = a + b\frac{c}{\emptyset} \qquad \text{---------- Eq. – 2.15}$$

Where $\mathbf{X_o}$ is the attack penetration for crack initiation (μm), **c** the concrete cover, and $\boldsymbol{\phi}$ the rebar diameter. "**a**" and "**b**" are constants obtained from regression whose values are **7.53** and **9.32,** respectively. While the second expresses the relationship between the corrosion-induced crack width and the amount of corrosion necessary to induce the first crack.

$$w = a + bx \qquad \text{---------- Eq. – 2.16}$$

Where **w** is the crack width, **x** the rebar radius loss also called attack penetration necessary to induce the first crack, and "**a**" and "**b**" are constants obtained from regression whose values are **7.53** and **9.32,** respectively. This work is a significant contribution to the field of reinforced concrete corrosion studies as it seeks to quantify the amount of corrosion necessary to generate the first crack and was the first to include concrete cover and the rebar diameter as influencing parameters. The following limitations can be noted about Alonso et al.'s model: statistically derived, applicable only for predicting the appearance of the crack under certain limit of attack during initiation stage, cannot be used for predicting level of attack during propagation stage and did not consider other characteristics of concrete such as the strength, elastic modulus, etc. as influencing parameters.

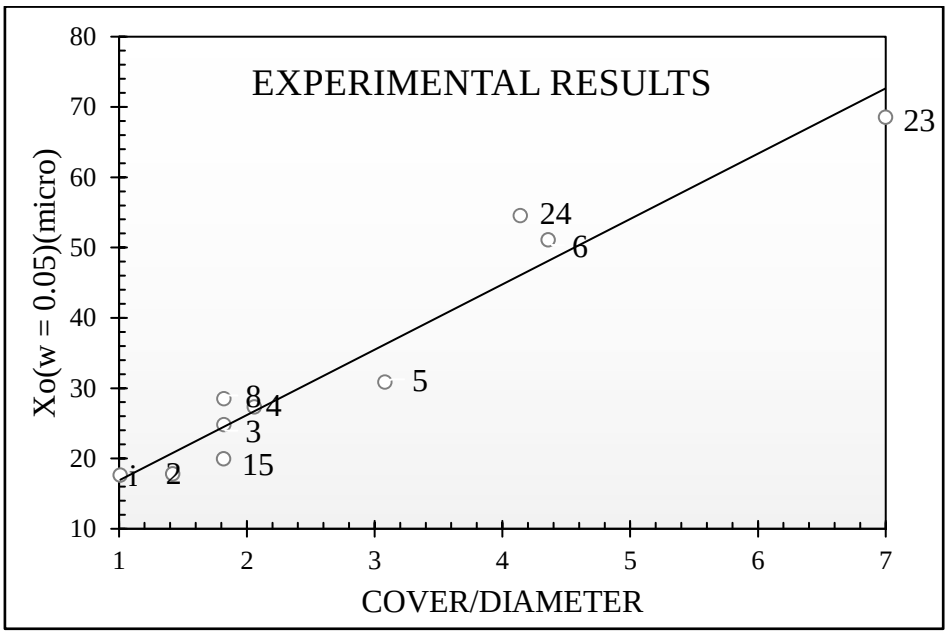

Figure 2. 3 Relationship between attack penetration which produced the first visible crack (w = 0.05 mm) and cover/diameter ratio (Alonso et al., 1998)

2.3.7 Vidal et al.'s model (2004)

Vidal et al. studied the relationships between crack widths and the mass of steel loss due to corrosion in two reinforced concrete beams. By visual inspection, the authors evaluated the level or degree of corrosion (cross-section loss) of the two beams under consideration and put forward two linear relationships linking the corrosion attack (cross-section loss) and crack width. The authors reveal that during the crack propagation phase, the crack width is directly linked to the volume of oxides produce, which is also proportional to the steel cross-section loss. Vidal et al.'s experiment was based on two reinforced concrete beams that have corroded naturally in a simulated chloride environment over the period of fourteen (14) and seventeen (17) years under loading. The chloride content of the simulated environment was 35 g/l of sodium chloride, which corresponding to the salt concentration of seawater. The beams have the dimensions of 3000 x 150 x 280 mm and were part of Laboratoire Matériaux et Durabilité des Constructions (LMDC) research project in Toulouse, France, which began since 1984 for the purpose of studying the relationship between mechanical loading and corrosion in reinforced concrete structures exposed to chloride environment.

Vidal et al. began the analysis by first testing their experimental results against Rodriguez et al.'s (1996) and Alonso et al.'s (1998) models and found discrepancies. The authors noted that these models partially predicted their experimental results based on the conditions tested. To minimise the discrepancies, they derived a modified version (formula) by introducing the change in steel cross-sectional area and the original steel cross-sectional area as shown below. Figure 2.4 illustrates the prediction capability of the new model.

$$\Delta A_{s0} = A_s \left[1 - \left[1 - \frac{\alpha}{\emptyset_0}\left(7.53 + 9.32\frac{c}{\emptyset_0}\right)10^{-3}\right]^2\right] \text{---------- Eq. – 2.17}$$

Where $\Delta \boldsymbol{A_{s0}}$ is the steel cross-section loss as the result of corrosion (mm^2), $\boldsymbol{A_s}$ the original steel cross-section (mm^2), $\boldsymbol{\phi_0}$ the original steel diameter (mm), **c** the thickness of concrete cover (mm) and **α** the attack penetration parameter whose value and condition remain the same as Rodriguez et al. (1996). The authors further established another linear relationship linking the reinforcement cross-section loss to the crack width.

$$w = K(\Delta A_s - \Delta A_{s0}) \qquad \text{---------- Eq. – 2.18}$$

Where **w** is the crack width (mm), **ΔAs** the steel cross-sectional area loss (mm^2) and **K** = **0.0575**. The limitations of this model are as follows:

1. Statistically derived as Alonso et al.'s model.
2. Did not include concrete characteristics (strengths, elastic modulus, etc.) as influencing parameters except for the cover depth.
3. This model also shows dependency on the corrosion attack penetration parameter. Khan et al.'s (2014) evaluation report reflects that the higher the value of the attack penetration selected, the closer Vidal et al.'s model predicts their experimental results. Thus, its accuracy depends on the value of attack penetration selected, as was the case with Rodriguez et al.'s (1996) model.

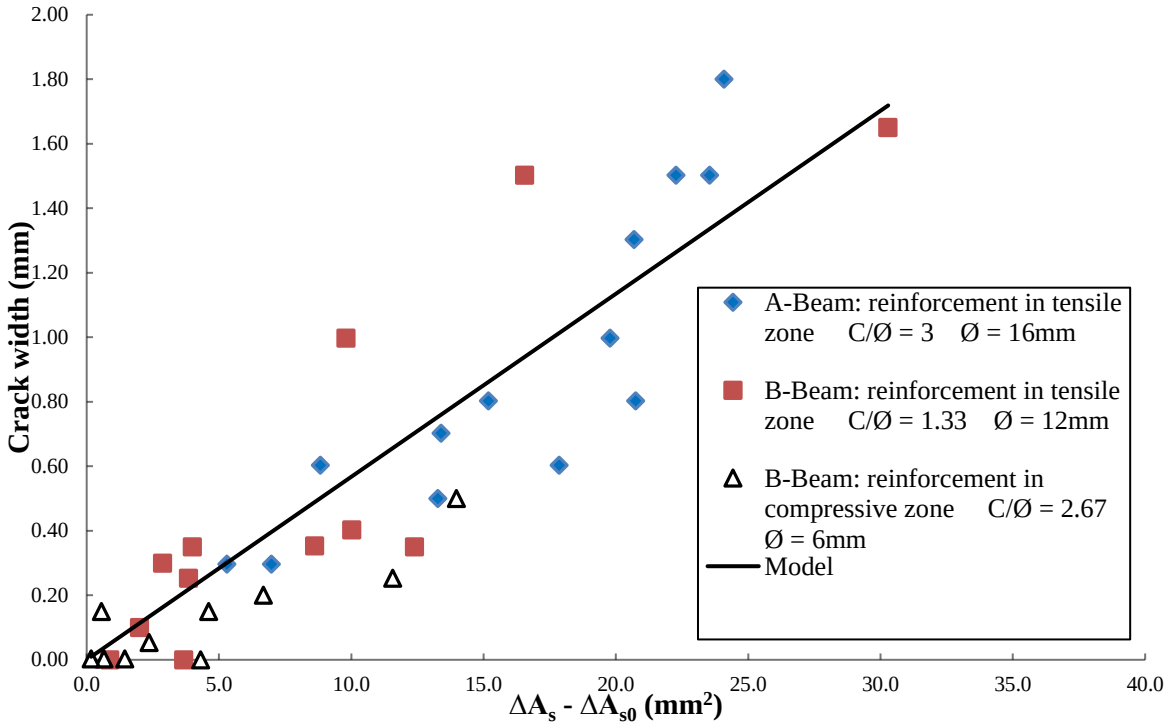

Figure 2. 4 Crack width versus cross-section loss of Beams A and B (Vidal et al., 2004)

2.3.8 Zhao and Jin's model (2006)

Zhao and Jin presented an analytical model to estimate the amount of steel corrosion at the cracking of concrete cover. Their work tends to contribute to a quantitative relationship between the amount of steel corrosion and concrete cover cracking. In this study, an elastic model was developed to estimate the total amount of steel corrosion existing at the onset of the cracking of concrete cover. The authors considered three stages in their analysis:

- Stage – I: free expansion of the corrosion products. As described by the authors, is the period that the corrosion product takes to fill the porous zone around the steel-concrete interface without initiate any stress in the surrounding concrete. The radius loss of the rebar required to fill the porous zone is term $\boldsymbol{\delta_1}$.
- Stage – II: stress initiation at the concrete cover. Is the period between stress initiation in the surrounding concrete and cracking of the concrete cover. After the porous zone is filled, any further radius loss will develop internal stresses. The authors termed this radius loss of the rebar that produces or initiate stresses on the surrounding concrete and cracked the concrete cover as $\boldsymbol{\delta_2}$.
- Stage – III: cracking of the concrete cover. Refers to the period that the corrosion product filled the space within the cracks. The authors term the radius loss of the rebar to fill the space within the cracks as $\boldsymbol{\delta_3}$.

Therefore, the total radius loss of the rebar ($\boldsymbol{\delta}$) due to corrosion is:

$$\delta = \delta_1 + \delta_2 + \delta_3 \qquad \text{---------- Eq. – 2.19}$$

Where $\boldsymbol{\delta_1}$ is the amount of corrosion (radius loss) required to fill the porous zone at the steel-concrete interface, $\boldsymbol{\delta_2}$ the amount of corrosion (radius loss) that will initial stress and cracks the concrete cover reaching the surface. $\boldsymbol{\delta_3}$ the amount of corrosion (radius loss) which will fill the space within the crack.

$$\delta_1 = r - \sqrt{r^2 - \frac{2r \cdot t_p + {t_p}^2}{n-1}} \qquad \text{---------- Eq. – 2.20}$$

Where $\boldsymbol{r}$ is the radius of the steel before corrosion, $\boldsymbol{n}$ the ratio between the volumes of corrosion product and its basic steel, and $\boldsymbol{t_p}$ the thickness of the steel-concrete interface.

$$t_p = \frac{V_p}{\pi \cdot d} = \frac{P_{vp} \cdot \pi \cdot d \cdot d_p}{\pi \cdot d} = P_{vp} \cdot d_p \qquad \text{---------- Eq. – 2.21}$$

Where $\boldsymbol{V_p}$ is the volume of porosity at the steel-concrete interface, $\boldsymbol{d}$ the diameter of steel before corrosion, $\boldsymbol{P_{vp}}$ the volume-percentage of capillary voids of the cement paste and $\boldsymbol{d_p}$ the average dimension of the capillary voids at the steel-concrete interface.

$$\delta_2 = \frac{d - {d^*}_\rho}{2} \qquad \text{---------- Eq. – 2.22}$$

Where ${\boldsymbol{d}^*}_{\boldsymbol{\rho}}$ is the residual diameter of steel bar after corrosion.

$${d^*}_\rho = d \cdot \sqrt{1 - \rho^*} \qquad \text{---------- Eq. – 2.23}$$

Where $\boldsymbol{\rho}^*$ is the corrosion rate when the concrete cover cracks.

$$\rho^* = \frac{x^2 - 1}{n-1} \qquad \text{---------- Eq. – 2.24}$$

Or $$\rho^* = \frac{\left[\sqrt[3]{-\frac{N_2}{2} + \sqrt{\left(\frac{N_2}{2}\right)^2 + \left(\frac{N_1}{3}\right)^3}} + \sqrt[3]{-\frac{N_2}{2} - \sqrt{\left(\frac{N_2}{2}\right)^2 + \left(\frac{N_1}{3}\right)^3}} - \frac{a_2}{3a_1}\right]^2 - 1}{n-1} \qquad \text{---------- Eq. – 2.25}$$

Where $N_1 = \frac{a_3}{a_1} - \frac{1}{3}\left(\frac{a_2}{a_1}\right)^2$ and $N_2 = \frac{2}{27}\left(\frac{a_2}{a_1}\right)^3 - \frac{1}{3}\left(\frac{a_2}{a_1}\right)\left(\frac{a_3}{a_1}\right) + \frac{a_4}{a_1}$

$$\delta_3 = r - \sqrt{r^2 - \frac{2R \cdot t_c + {t_c}^2}{n-1}} \qquad \text{---------- Eq. – 2.26}$$

Where $\boldsymbol{t_c}$ is the average thickness of the steel-concrete interface.

$$t_c = \frac{V_c}{\pi d} = \frac{(n-1)c}{d}\,\delta_2 \qquad \text{---------- Eq. – 2.27}$$

Where $\boldsymbol{V_c}$ is the total volume of cracks in the concrete cover and $\boldsymbol{c}$ the cover depth.

$$V_c = \frac{1}{2}\sum w_i \cdot c \qquad \text{---------- Eq. – 2.28}$$

Where $\boldsymbol{w_i}$ is the width of the **ith** crack at the surface of the steel bar.

$$\sum \frac{w_i}{\delta_2} = 2\pi(n-1) \qquad \text{---------- Eq. – 2.29}$$

The major drawbacks of Zhao and Jin's model are:

- Is very complicated, unpractical and cannot be used in field application.
- This model is more theoretical and applicable to analytical based experiment.
- Some of the variables incorporated in this model, particularly those relating to the porous zone (volume of porosity in the steel-concrete interface, volume-percentage of capillary voids of the cement paste, the average dimension of the capillary voids at the steel-concrete interface, etc.) are unmeasurable, unattainable and their properties varies with location around the rebar (Jamali et al. 2013). Incorporating these variables within prediction models increases the risk of uncertainty.
- Predication capability also shows dependency on corrosion rate.

2.3.9 Zhang et al.'s model (2010)

Zhang et al. studied the evolution of corrosion pattern in two reinforced concrete beams that have been exposed to chloride environment under sustained loading over the period of 14 and 23 years. These beams were also part of Laboratoire Matériaux et Durabilité des Constructions (LMDC) research project in Toulouse, France, which were previously studied by Vidal et al. (2004), particularly the 14-year exposure beam. The authors' objectives were to study the evolution of the corrosion-induced crack pattern and the corrosion distribution and, test the obtained data against existing models that predict corrosion damage (cross-section loss) from the corrosion-induced crack width.

Zhang et al. explicitly cited that both the loss of the rebar cross-section and the loss of bond between reinforcement and concrete are related to the corrosion-induced crack width. The authors further reveal that corrosion evolution pattern consists of three stages, and relationships linking the corrosion process with the crack width are not the same for all stages. The stages identified are the cracking initiation stage, the first stage of cracking propagation and the second stage of cracking propagation. At the cracking initiation stage and the first stage of cracking propagation, localised corrosion due to chloride ingress is the predominant corrosion pattern and pitting corrosion is the main factor that influences the cracking process. As the corrosion cracks increases, generalised corrosion develops rapidly and gradually becomes predominant in the second stage of cracking propagation.

The authors compared the data obtained from the beams under consideration against Vidal et al.'s (2004) and Rodriguez et al.'s (1998) models. The authors reported that Vidal et al.'s model

gives a better prediction of reinforcement corrosion under localised corrosion conditions (Stage I and II) and as the corrosion pattern changes to generalised condition (Stage III), the model prediction was over-conservative. According to the authors, Rodriguez's model did not predict the natural chloride corrosion irrespective of localised or generalised corrosion. Zhang et al. then developed a new model, based on the experimental results under generalised corrosion pattern, linking the crack width with average mass loss of steel reinforcement rather than cross-section loss at a particular point. The authors used the average steel cross-section loss of the main reinforcing bar. The section or length of the main reinforcing bar considered was the distance between two stirrups.

$$W = 0.1916\Delta A_{sm} + 0.164 \qquad \text{----------Eq. – 2.30}$$

Where **W** is the crack width (mm) and $\Delta \boldsymbol{A_{sm}}$ the average cross-section loss (mm^2) obtained from the mass loss (i.e. by equating the ratio of the change in mass to the initial mass multiply by the original area of the rebar). This model is believed to be useful in the crack propagation stage when corrosion is more generalized. However, the limitations of this model are: statistically derived, does not take into consideration influencing parameters like the concrete characteristics (cover depth, strengths, modulus of elasticity, etc.) and cannot predict the maximum cross-section loss at a given section. Moreover, this model is based on the average mass loss of rebar cross-section between two stirrups and did not subsume the distance between the two stirrups in the relationship.

2.3.10 Malumbela et al.'s model (2011)

Malumbela et al. presented a model that links the vertical and transverse strains on the surface of corroding reinforced concrete beams with the level of steel corrosion. The authors pointed out that steel corrosion is usually localised in the direction of the ingress of corrosion agents and the remaining section of the uncorroded bar is elliptical. The authors further stated that assuming uniform steel corrosion in concrete structures underestimate the applied pressure develop by corrosion product. With the assumption the of a uniform porous zone around the rebar, the authors modelled the cracking of the concrete cover due to corrosion into two stages:

The first stage is the period when the corrosion product fills the porous zone without exerting pressure on the surrounding concrete. The below relationship gives the area loss of the rebar required to fill the porous zone without exerting any pressure on the surrounding concrete:

$$\Delta A_{st-p} = \frac{1}{2}\pi r \Delta r_p \qquad \text{---------- Eq. 2.31}$$

Where $\boldsymbol{r}$ is the radius of the uncorroded steel and $\Delta \boldsymbol{r_p}$ the maximum radius of steel that must be lost to fill the porous zone. The corresponding volume of corrosion product to fill the porous zone is:

$$A_{cor-p} = \frac{n}{2}\pi r \Delta r_p \qquad \text{----------Eq. – 2.32}$$

Where $\boldsymbol{n}$ is the ratio of the volume of corrosion product to the volume of the original steel lost.

The maximum radius of steel lost Δr_p to fill the porous zone is:

$$\Delta r_p = \frac{2t_p(2r+t_p)}{r(n-1)} \qquad \text{----------Eq. – 2.33}$$

Where t_p is the thickness of the porous zone around the steel bar with uniform thickness ranging from 10 to 20 μm.

The second stage is the period when the porous zone has been fully-filled with the corrosion product, and stresses begin to initiate on the surrounding concrete. Consequently, the required area loss and volume of corrosion product require to initiate pressure on the surrounding concrete are given by the following equations:

$$\Delta A_{st\_cr} = \frac{1}{2}\pi r \Delta r_{cr} \qquad \text{----------Eq. – 2.34}$$

$$A_{cor\_cr} = \frac{n}{2}\pi r \Delta r_{cr} \qquad \text{----------Eq. – 2.35}$$

Where Δr_{cr} is the maximum radius that should be lost to initiate pressure on the surrounding concrete.

The initiation of pressure on the surrounding concrete will develop internal stresses which will result in external strains on the surface of the concrete cover. Thus, the maximum radial expansion at the time of cracking of the cover is:

$$\mu_{cr} = \frac{(n-1)r\Delta r_{cr} - 2t_p(2r+t_p)}{r+t_p} \qquad \text{----------Eq. – 2.36}$$

The authors noted that Eq. – 2.36 is valid only when the porous zone is fully-filled or if presented mathematically, when $(n-1)r\Delta r \geq 2t_p(2r+t_p)$. However, with the assumption that the concrete cover behaves like a thick-walled cylinder with varying internal pressure around the surface of the corroding bars which is dependent on the level of steel corrosion, Malumbela et al., expressed the theoretical maximum radial expansion of concrete in the corroding region or direction of the ingress of the corrosion agents as:

$$\mu_{cr} = \frac{P(r+t_p)}{E}\left[\frac{(r+t_p)^2+(r+c+t_p)^2}{(r+c+t_p)^2-(r+t_p)^2} + v\right] \qquad \text{----------Eq. – 2.37}$$

Where P is the internal pressure applied by the expansive corrosion product, c the cover depth and, E and v is the elastic modulus and Poisson's ratio, respectively of the concrete. The theoretical maximum transverse strain on the surface of the concrete, was expressed as:

$$\varepsilon_{ext} = \frac{2P(r+t_p)^2}{E\left[(r+c+t_p)^2-(r+t_p)^2\right]} \qquad \text{----------Eq. – 2.38}$$

Malumbela et al. presented a simple relationship that could have been very practical. However, due to the following limitations as listed below this model cannot serve that purpose.

- There is no direct relationship between the area loss and the maximum theoretical strain nor the area loss and the internal pressure. As the authors rightly said, the internal pressure depends on the level of steel corrosion. Therefore, relationship between the area loss and corresponding strain should have been established.
- This model did not make provision for the calculation the maximum radius (Δr_{cr}) that should be lost to initiate pressure on the surrounding concrete.
- The inclusion of the porous zone further complicates and increase the uncertainty of the model. The porous zone is never uniform, varies with location around the rebar (Jamali et al., 2013), and the thickness is practically unmeasurable.

2.3.11 Pengwei et al.'s model (2011)

Pengwei et al. investigated the expansive behaviour of concrete cover subjected to reinforcement corrosion through finite element analysis. The Authors evaluated the critical amount of steel corrosion needed for the cracking of concrete cover and proposed a mathematical relationship from which corrosion expansion rate required for the first crack to appear can be predicted. This critical amount of steel corrosion needed for cracking the concrete cover was evaluated in terms of the expansive rate of the corrosion product, which the authors defined as the ratio of expansive displacement to the rebar radius at the time when the crack entirely penetrates the concrete cover. As illustrated in Figure 2.5 to 2.7, Pengwei et al. found that the expansive rate required for cover cracking increases almost linearly with the cover depth, increases non-linearly as the tensile strength of concrete increases but decreases with rebar diameter. The authors also recognised that cover depth, rebar diameter, the elastic modulus of the concrete and tensile strength of concrete are critical parameters influencing the cracking behaviour of concrete cover.

$$\eta = 0.02989 d^{-1.05729} + 0.233194 {f_t}^{1.19997} {E_c}^{-2.2} d^{-1.05729} + 0.055281 {f_t}^{1.19997} {E_c}^{-2.2} c^{1.16947} d^{-1.05729}$$

----------Eq. – 2.39

Where η is the expansive rate in percentages, d rebar diameter (mm), f_t the tensile strength of concrete (MPa), E_c the elastic modulus of concrete, and c the cover depth (mm). The shortcomings of this model are:

- The approach of expressing corrosion damage in terms of expansive rate (ratio of expansive displacement to rebar radius) rather than the rebar cross-section loss. This expansive displacement is the result of the rebar being converted to rust (corrosion). Hence, the corrosion damage prediction should be expressed or evaluated using the rebar cross-section loss.
- This relationship shows no connection with the rebar cross-section loss which is the primary effect of corrosion.
- Limited to the corrosion initiation stage and cannot serve the purpose of predicting the expansive behaviour of the concrete cover during the corrosion propagation stage.

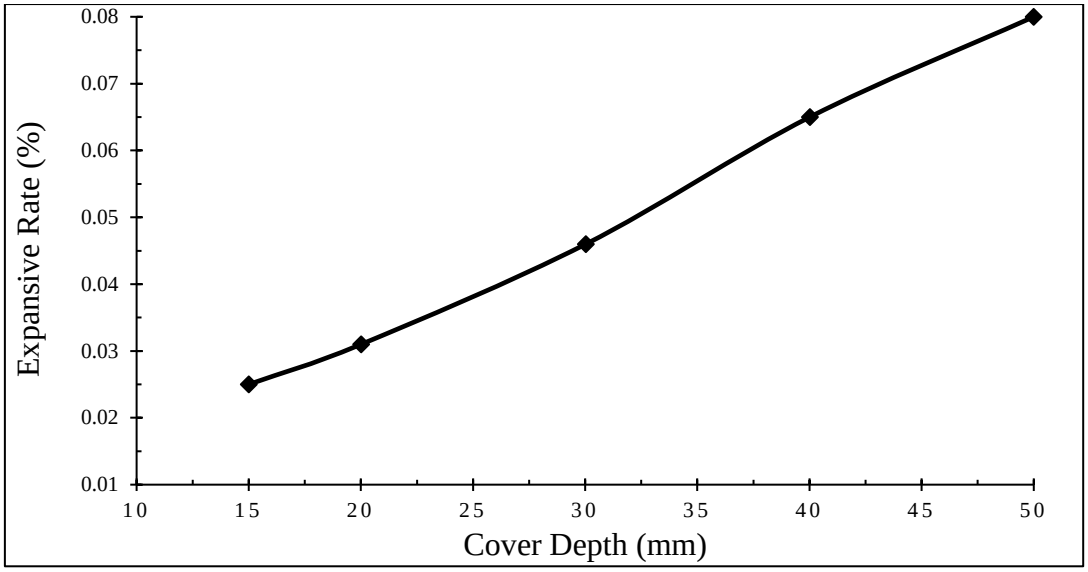

Figure 2. 5 Expansive Rate vs Cover Depth (Pengwei et al., 2011)

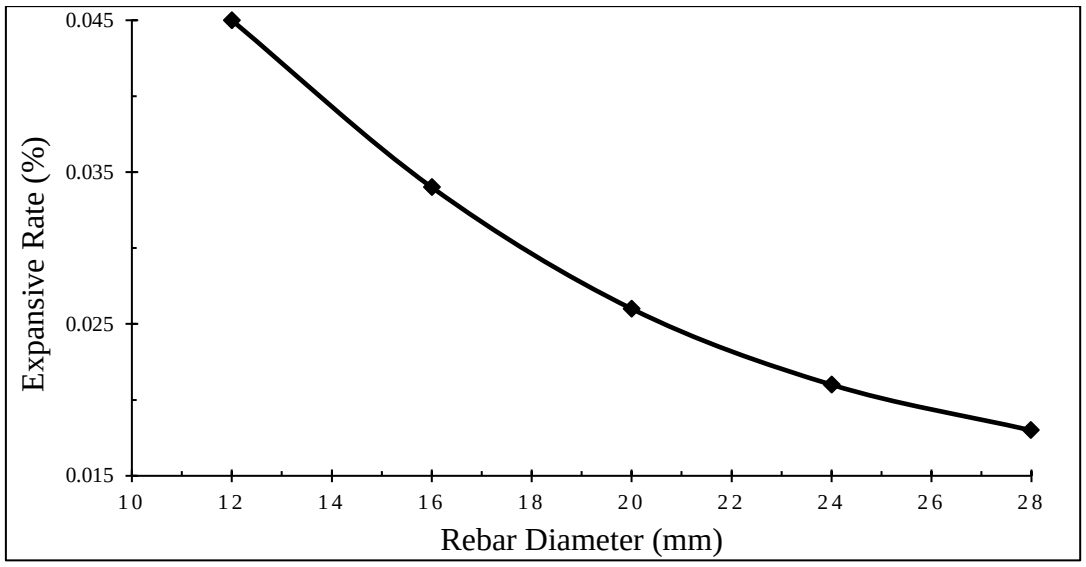

Figure 2. 6 Expansive Rate vs Rebar Diameter (Pengwei et al., 2011)

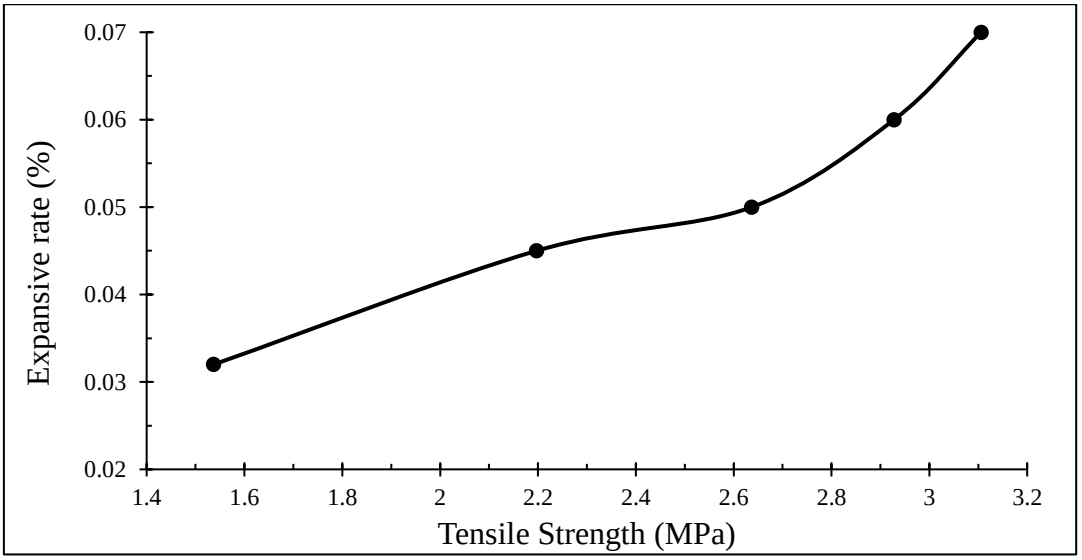

Figure 2. 7 Expansive Rate vs Tensile Strength (Pengwei et al., 2011)

2.3.12 Khan et al.'s review (2014)

Khan et al. studied the evolution of corrosion pattern in a 26-year-old reinforced concrete beam which has corroded naturally in a simulated chloride environment under sustained loading. This beam was subjected to wetting and drying cycles for 19 years in a saline environment, which contains sodium chloride concentration of 35 g/l. The beam under consideration was coded A2CL3, has the dimensions of 3000 x 280 x 1500 mm and was also part of Laboratoire Matériaux et Durabilité des Constructions (LMDC) research project in Toulouse, France. The beams previously studied by Vidal et al. (2004) and Zhang et al. (2010) were also part of this research project. The authors were interested in mapping the corrosion-induced cracks and its relations to the corresponding cross-section loss, as well as assessing the prediction capabilities of three models which link crack width and section loss. The authors' experimental results were tested against existing models linking crack width and corrosion attack (loss in cross-section or loss of mass) that have been proposed by Rodriguez et al. (1998), Vidal et al. (2004) and Zhang et al. (2010) The authors' findings can be summarised as follows:

- Rodriguez et al.'s (1998) model approximation of the experimental results varies depending on the value of the corrosion penetration factor **α** selected. For **α** = 2, which correspond to homogeneous corrosion, Rodriguez et al.'s (1998) model overestimates the cross-section loss of steel. When **α** is between **4** and **8**, which corresponds to localised (pitting) corrosion, the predicted cross-section loss shows good relations to the experimental results. At **α = 8** the percentage difference is 6%, which was the closest to the experimental results and at **α = 4** the percentage difference was 48%. The Authors reported that the Rodriguez et al.'s (1998) model shows dependency on the value of the attack penetration factor selected and deciding on which value to use in case of intermediate corrosion morphology is a major problem. Figure 2.8 shows the comparison of Rodriguez et al.'s (1998) model with the experimental results.
- Vidal et al.'s (2004) model predicted values show some approximation to the experimental values as illustrated in Figure 2.9. At **α = 8** the percentage difference of 19% was observed, which was the closest to the experimental results. This model also shows dependency on the corrosion penetration factor, the higher the value of the corrosion penetration factor selected, the closer the predicted value to the experimental results. The Authors attributed this deviation to the environmental conditions of the beams which Vidal et al. (2004) studied, or model was derived, citing at the time of their studies the beams were still subjected to wetting and drying cycles.
- Zhang et al.'s (2010) model predictions show the highest deviation from the experimental values with a percentage difference of 68%. Figure 2.10 shows the comparison of the Authors' experimental results with Zhang et al.'s (2010) model. It was observed that no relationship exists between the average steel cross-section loss over the length of the main reinforcing bar between two stirrups and the crack width of longitudinal corrosion. The authors attributed the deviation to the age of beams, rebar diameter, cover depth, and the corrosion morphology which was not the same as the beam studied by Zhang et al. (2010).

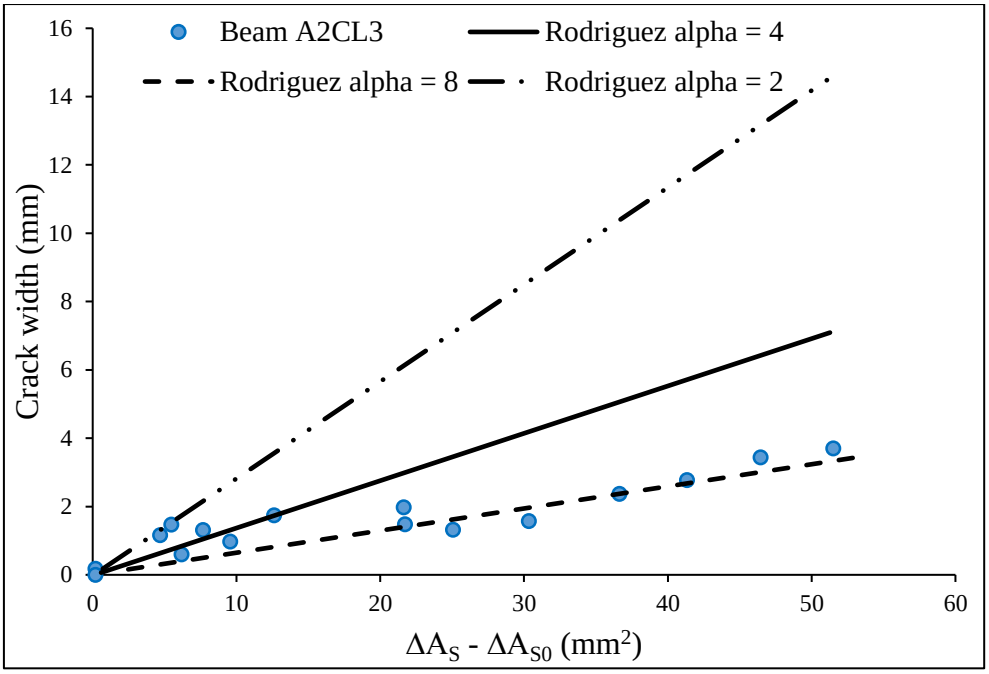

Figure 2. 8 Comparison of experimental results (Beam A2CL3) with Rodriguez et al.'s (1998) model (Khan et al., 2014)

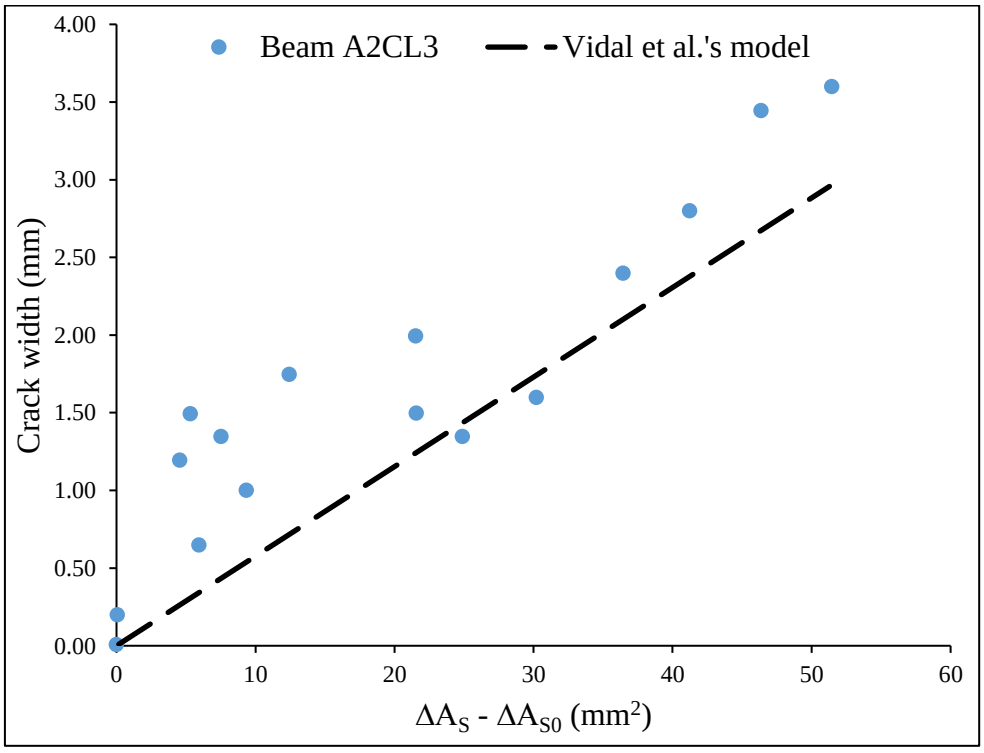

Figure 2. 9 Comparison of experimental results (Beam A2CL3) with Vidal et al.'s (2004) model (Khan et al., 2014)

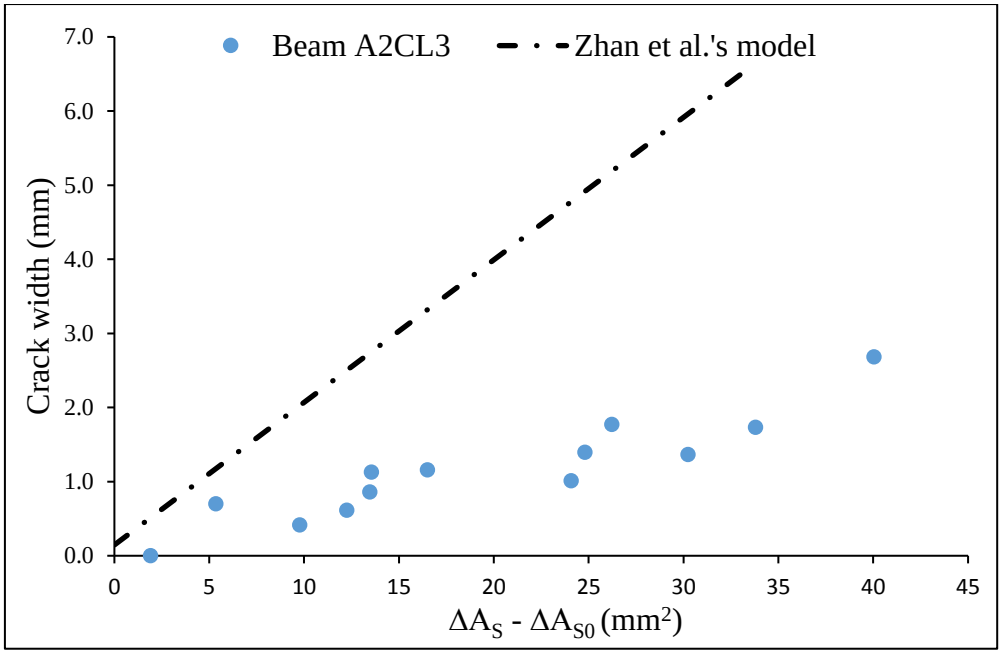

Figure 2. 10 Comparison of experimental results (Beam A2CL3) with Zhang et al.'s (2010) model (Khan et al., 2014)

2.3.13 Andrade et al.'s model (2016)

Andrade et al. presented an empirical formula linking corrosion-induced crack width with the level of corrosion. This formula was derived from statistical analysis of some experimental data available in the literature. These selected data were based on accelerated corrosion test whose corrosion current density did not exceed 200 µA/cm^2 and recorded crack width not greater than two (2) millimetre. The authors begin by plotting the selected data on a logarithmic scale as a function of the ratio of the average attack penetration to the radius of the reinforcement according to Torres-Acosta (2003) proposal, which shows scattering about the linear interpolation function as shown in Figure 2.11. To improve the correlation, a new interpolation function was established relating the average corrosion-induced crack width with the ratio of the average attack penetration to the radius of the reinforcement. Figure 2.12 shows the plotted data based on the new function.

$$W_{max=15.863\cdot\left(\frac{x_{ave}}{r_0}\cdot CT\right)^{0.928}} \qquad \text{----------Eq. – 2.40}$$

$$CT = \left(\alpha\frac{c}{\emptyset}\right)^{-\frac{\beta}{f_{ct}}} \qquad \text{----------Eq. – 2.41}$$

Where $\boldsymbol{W_{max}}$ = the average crack width
$\boldsymbol{x_{ave}}$ = the average attack penetration
$\boldsymbol{r_0}$ = the radius of the reinforcement
$\boldsymbol{c}$ = the depth of concrete cover
$\emptyset$ = the rebar diameter
$\boldsymbol{f_{ct}}$ = the average tensile strength of concrete
α & **β** = **0.63** and **1.141**, respectively obtained from the interpolation curve.

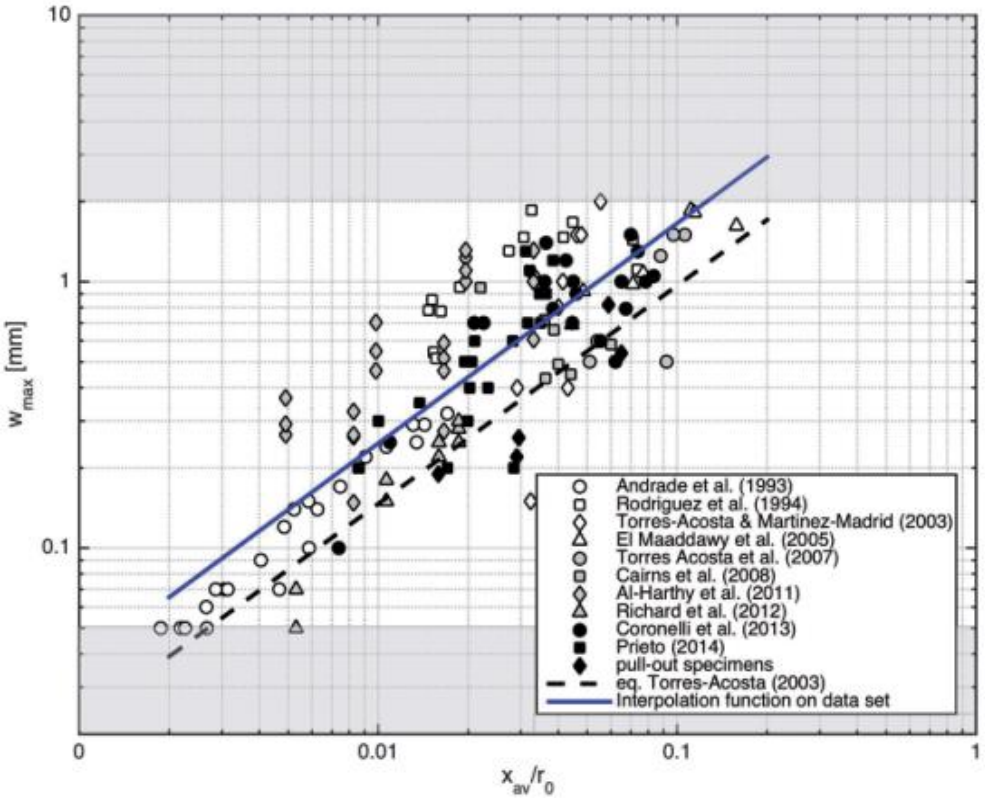

Figure 2. 11 Maximum crack opening vs the ratio of average attack penetration to the radius of the rebar based on Torres-Acosta 2003 (Andrade et al., 2016)

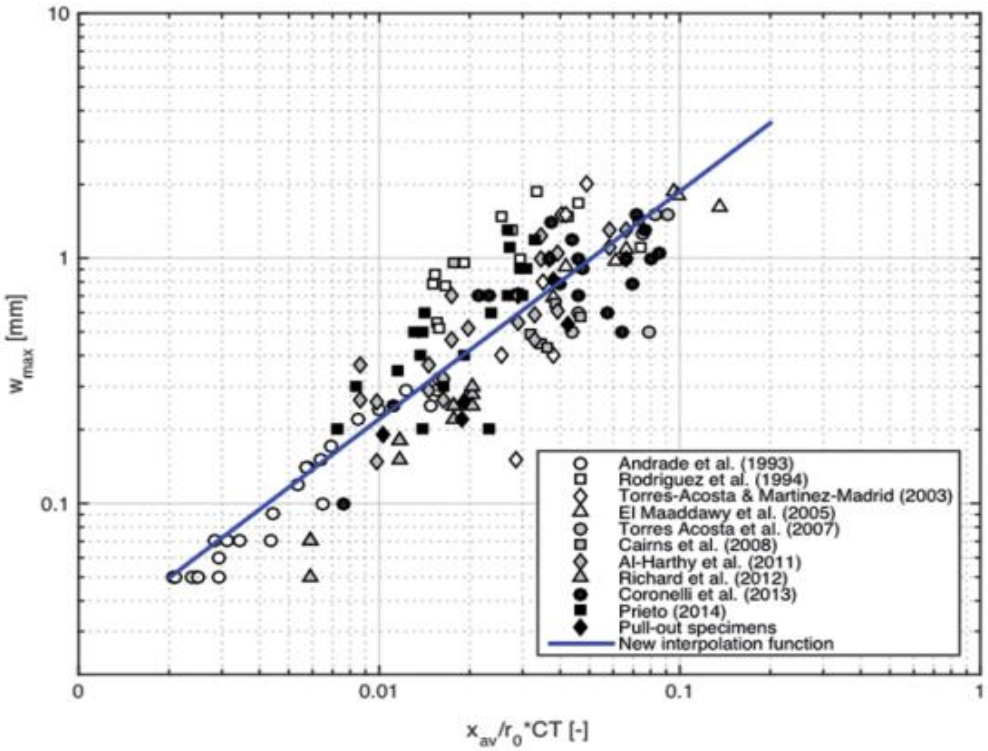

Figure 2. 12 Maximum crack opening vs the ratio of average attack penetration to the radius of the rebar based on the new function (Andrade et al., 2016)

The authors cited the limitation of this model and concluded with a call for further studies to clarify the difference between natural conditions and accelerated test setups regarding the structural consequences of corrosion. Listed below are shortcomings of this model:

1. Do not serve the purpose of predicting the severity of corrosion damage under natural corrosion.
2. Based on the functions obtained from a linear regression analysis of experimental data.
3. Laboratory-based and valid only for accelerated corrosion test.
4. Applicable only where homogeneous corrosion is expected.
5. Require an expert if it is to be applied to real structures.
6. Applicable to crack width not greater than 2 mm.
7. Cannot be applied to chloride-induced corrosion.

2.3.14 SUMMARY OF THE CRITICAL REVIEW

The premature deteriorations of reinforced concrete structures by corrosion have generated several theories and models to predict the service life (Andrade et al., 1988). Despite the development of several models, imprecision remains a major problem. From the above deliberations, the need for reliable corrosion damage prediction model is ostensible. It is apparent that these models, do not satisfactorily address the current problem. Given the above, this research seeks to address the problem by formulating a reliable model with which the level of corrosion in reinforced concrete structures can be quantified. As previously stated in Chapter 1, the proposed model will consider important parameters, most especially the concrete characteristics (cover depth, strengths, elastic modulus, etc.) from which the residual bar section in corroding concrete structures can be estimated based on the appearance of corrosion-induced cracks.

2.4 PART-III: REVIEW ON THE SIGNIFICANCE OF CORROSION-INDUCED CRACK WIDTH IN VISUAL ASSESSMENT

Corrosion of steel in concrete often produces cracks during the propagation stage. Corrosion-induced cracks are direct consequences of the loss in cross-section of the reinforcing steel. Corrosion being a chemical process, convert the chemical compositions of the steel into oxides (rust). These oxides occupy two to six time the original volume of the steel being oxidised (Bloomfield, 2006; Jaffer and Hansson, 2009). The types of oxides produce depend mostly on the availability of oxygen and moisture. Likewise, the appearance of cracks also depends on the amount of moisture present. With less moisture, the corrosion products (oxides) are more insoluble, producing greater pressure and consequently, early cracking and larger cracks width (Torres-Acosta, 2010). While under water-saturated conditions, oxygen is deprived of the reaction resulting in soluble corrosion products which migrate away from the steel-concrete interface, such condition does not lead to the generation of expansive products (Bloomfield, 2006; Charles et al., 2011). The corrosion-inducing species, as well as the morphology, also influence the amount of pressure exerted on the surrounding concrete by the corrosion product.

Generalised corrosion generally produces greater pressure and early cracking than localise or pitting corrosion. Under carbonation-induced corrosion, more insoluble corrosion products are generated, leading to greater pressure and early cracking as compared to chloride-induced corrosion (Val et al., 2009). The presence of chlorides increases the solubility of the corrosion products, thus permitting migration and diffusion of the corrosion products away from the steel-concrete interface (Angst, 2018). Therefore, at given conditions (humidity, cover depth, etc.), corrosion-induced cracks are most likely to appear earlier under carbonation-induced corrosion than chloride-induced corrosion.

In all corrosion-damaged assessment on reinforced concrete structures, visual inspection for stains of rust and corrosion-induced cracks are usually the first step. Rust staining of concrete surface and corrosion-induced cracks play an essential role; they provide some clues on the state of the reinforcement within the concrete. These signs provide a possible approach to non-destructive evaluation of the corrosion-damaged assessment of reinforced concrete structures (Zhang et al., 2010). Visual inspection provides an easy and cheap method compared to electrochemical techniques such as potential mapping and corrosion rate measurements (Charles et al., 2011). Not only that corrosion-induced cracks provide easier and cheap means of corrosions detections but can also serve as an essential factor in corrosion damage prediction (Torres-Acosta, 2010).

Corrosion-induced cracks develop as the result of the expansive pressure of the corrosion product exceeding the tensile strength of the concrete. The expansive pressure depends directly on the volume of steel begin oxidised, the corrosion-inducing species and the amount of moisture present. Therefore, it is logical to reason there exist a relationship between the corrosion-induced crack widths and the section loss or mass loss of the steel begin corroded. As mentioned in Chapter 1, many researchers (Andrade et al. (1993), Molina et al. (1993), Rodriguez et al. (1996), Alonso et al. (1998), Vidal et al. (2004), Zhao and Jin (2006), Zhang et al. (2010), Khan et al. (2014), Andrade et al., 2016, etc.) have acknowledge that the width of the corrosion-induced cracks somehow commensurate to the level of corrosion (section loss or mass loss).

However, these assertions are not without contentions, most especially with regards to chloride-induced corrosion. Charles et al. (2011) studied the relationship between visual signs of corrosion (crack width & rust stain) and corrosion state (cross-section loss) in a forty-year-old reinforced concrete beam stored in saturated marine environment and reported that visual signs along are insufficient for assessing the state of corrosion in concrete. Angst et al. (2012) also reviews some common misconceptions of chloride-induced corrosion as well as some practical case studies of steel corrosion in the marine environment and recommend that relying on externally visible signs must be done with utmost caution if the presence of chloride cannot be ruled out. Angst et al. (2012) cited several cases of structures failure due to corrosion in the marine environment without any visible signs of cracks.

2.4.1 SUMMARY OF THE SIGNIFICANCE OF CORROSION-INDUCED CRACKS IN VISUAL ASSESSMENT

The above discussions point out that the relationship between corrosion-induced crack with and the level of corrosion may be influenced by the solubility of the corrosion product, which depends on the presence of chloride and the amount of moisture. The migration of the corrosion product away from the steel-concrete interface reduces the pressure exerted on the surrounding concrete, thereby, affecting the relationship between the section loss to corrosion and the corrosion-induced crack width. However, in unsaturated conditions, the corrosion-induced crack width is still proportional to the volume of steel being oxidised. Hence, this study seeks to investigate this relationship under the worst scenario (chloride-induced corrosion).

2.5 GENERAL SUMMARY OF THE LITERATURE REVIEW

This chapter presented reviews of the fundamental of corrosion mechanism in concrete (both natural and accelerated), critical review of corrosion damage prediction models and review on the significance of corrosion-induced crack width in visual assessment and damage evaluation. The presented reviews disclose the need for a reliable corrosion damage prediction model and quantitative descriptions of the relationship between the level of corrosion (cross-section loss) and the corrosion-induced crack width. Also, presented are the major challenges facing the reliability of this relationship between the corrosion-induced crack width and the cross-section loss to corrosion, resulting from the migrating of the corrosion product away from the steel-concrete interface. Consequently, the approach of this study was to investigate this relationship under the worst scenario (chloride-induced corrosion) to minimise the migration effect on the derived model.

2.6 REFERENCES

1. Ahmad, S., 2009. Techniques for inducing accelerated corrosion of steel in concrete. Arabian Journal for Science and Engineering, 34(2), p.95.
2. Alonso, C., Andrade, C., Rodriguez, J., Diez, J.M. (1998) Factors controlling cracking of concrete affected by reinforcement corrosion, Materials & Structures, Vol. 31, pp 435–441.
3. Andrade, C., Cesetti, A., Mancini, G. and Tondolo, F., 2016. Estimating corrosion attack in reinforced concrete by means of crack opening. Structural Concrete, 17(4), pp.533-540.
4. Andrade, C., Muñoz, A. and Torres-Acosta, A., 2010. Correlation between crack width of concrete coating and reinforcement corrosion in elements exposed to a natural environment contaminated by chlorides. Concrete and cement. Research and Development, 1 (2), pp.30-41
5. Andrade, C., Alonso, C. and Molina, F.J., 1993. Cover cracking as a function of bar corrosion: Part I-Experimental test. Materials and structures, 26(8), pp.453-464.
6. Andrade, C., Alonso, C., González, J.A. and Rodriguez, J., 1989. Remaining service life of corroding structures. In Durability of Structures. Iabse Symposium, September 6-8, 1989, Lisbon (Iabse Report Volume 57/1).

7. Andrade, C., Alonso, M.C. and Gonzalez, J.A., 1988. An initial effort to use the corrosion rate measurements for estimating rebar durability. ASTM Symposium on "Corrosion Rate of Reinforcements in Concrete" - Baltimore (USA).
8. Angst, U.M., 2018. Challenges and opportunities in corrosion of steel in concrete. Materials and Structures, 51(1), p.4.
9. Angst, U., Elsener, B., Jamali, A. and Adey, B., 2012. Concrete cover cracking owing to reinforcement corrosion–theoretical considerations and practical experience. Materials and Corrosion, 63(12), pp.1069-1077.
10. Ashraf, W., 2016. Carbonation of cement-based materials: challenges and opportunities. Construction and Building Materials, 120, pp.558-570.
11. Austin, S.A., Lyons, R. and Ing, M.J., 2004. Electrochemical behaviour of steel-reinforced concrete during accelerated corrosion testing. Corrosion, 60(2), pp.203-212.
12. Bard, A.J. and Faulkner, L.R., 2001. Fundamentals and applications. Electrochemical Methods, 2, p.482.
13. Bertolini, L., Elsener, B., Pedeferri, P., Redaelli, E. and Polder, R.B., 2013. Corrosion of steel in concrete: prevention, diagnosis, repair. John Wiley & Sons.
14. Bouteiller, V., Cherrier, J.F., L'Hostis, V., Rebolledo, N., Andrade, C. and Marie-Victoire, E., 2012. Influence of humidity and temperature on the corrosion of reinforced concrete prisms. European journal of environmental and civil engineering, 16(3-4), pp.471-480.
15. Broomfield, J.P., 2006. Corrosion of steel in concrete: understanding, investigation and repair. CRC Press.
16. Broomfield, J.P., Rodriguez, J., Ortega, L.M. and Garcia, A.M., 1993. Corrosion rate measurement and life prediction for reinforced concrete structures. Proceedings of Structural Faults and Repair, 93(2), pp.155-164.
17. Charles, S., L'Hostis, V. and Poyet, S., 2011. Visual parameters of chloride-induced corrosion of reinforced concrete structures. European Journal of Environmental and Civil Engineering, 15(1), pp.9-24.
18. Claisse, P.A., 2014. Transport properties of concrete: Measurements and applications. Elsevier.
19. Du, Y.G., Chan, A.H.C., Clark, L.A., Wang, X.T., Gurkalo, F. and Bartos, S., 2013. Finite element analysis of cracking and delamination of concrete beam due to steel corrosion. Engineering Structures, 56, pp.8-21.
20. Dyer, T., 2014. Concrete durability. CRC Press.
21. Jaffer, S.J. and Hansson, C.M., 2009. Chloride-induced corrosion products of steel in cracked-concrete subjected to different loading conditions. Cement and Concrete Research, 39(2), pp.116-125.
22. Jamali, A., Angst, U., Adey, B. and Elsener, B., 2013. Modelling of corrosion-induced concrete cover cracking: A critical analysis. Construction and Building Materials, 42, pp.225-237.
23. Jang, B.S. and Oh, B.H., 2010. Effects of non-uniform corrosion on the cracking and service life of reinforced concrete structures. Cement and Concrete Research, 40(9), pp.1441-1450.

24. Kashani, M.M., Crewe, A.J. and Alexander, N.A., 2013. Use of a 3D optical measurement technique for stochastic corrosion pattern analysis of reinforcing bars subjected to accelerated corrosion. Corrosion Science, 73, pp.208-221.
25. Khan, I., François, R. and Castel, A., 2014. Prediction of reinforcement corrosion using corrosion-induced cracks width in corroded reinforced concrete beams. Cement and concrete research, 56, pp.84-96.
26. Malumbela, G., Moyo, P. and Alexander, M., 2012. A step towards standardising accelerated corrosion tests on laboratory reinforced concrete specimens. Journal of the South African Institution of Civil Engineering, 54(2), pp.78-85.
27. Malumbela, G., Alexander, M. and Moyo, P., 2011. Model for cover cracking of RC beams due to partial surface steel corrosion. Construction and Building Materials, 25(2), pp.987-991.
28. Meade, C.L., 1999. Accelerated corrosion testing. Metal Finishing, 5(97), pp.526-528.
29. Mehta, P.K. and Monteiro, P.J., 2006. Concrete: microstructure, properties, and materials. 2006.
30. Molina, F.J., Alonso, C. and Andrade, C., 1993. Cover cracking as a function of rebar corrosion: part 2—numerical model. Materials and structures, 26(9), pp.532-548.
31. Otieno, M., Beushausen, H. and Alexander, M., 2011. Prediction of corrosion rate in RC structures-a critical review. In Modelling of Corroding Concrete Structures (pp. 15-37). Springer, Dordrecht.
32. Page, C.L. and Page, M.M. Eds., 2007. Durability of concrete and cement composites. Elsevier.
33. Pengwei, X., Ning, Y., Linwang, S., Guobao, L. and Lebin, W., 2011. Finite element analysis of expansive behaviour due to reinforcement corrosion in RC structure. Procedia Engineering, 12, pp.117-126.
34. Poulsen, E. and Mejlbro, L., 2014. Diffusion of chloride in concrete: theory and application. CRC Press.
35. Poursaee, A., 2016. Corrosion of steel in concrete structures. In Corrosion of Steel in Concrete Structures (pp. 19-33).
36. Poursaee, A. and Hansson, C.M., 2009. Potential pitfalls in assessing chloride-induced corrosion of steel in concrete. Cement and Concrete Research, 39(5), pp.391-400.
37. Rodriguez, J., Ortega, L.M., Casal, J., Diez, J.M. (1996). Corrosion of reinforcement and service life of concrete structures, Durab. Build. Mater. Compon. 7 (1) pp 117–126.
38. Šavija, B. and Luković, M., 2016. Carbonation of cement paste: understanding, challenges, and opportunities. Construction and Building Materials, 117, pp.285-301.
39. Thiery, M., Villain, G., Dangla, P. and Platret, G., 2007. Investigation of the carbonation front shape on cementitious materials: effects of the chemical kinetics. Cement and Concrete Research, 37(7), pp.1047-1058.
40. Torres-Acosta, A.A., 2010, July. Accelerated vs Natural Corrosion Experimental Results for Remaining Life Stage Forecasting. In Sixth International Conference on Concrete under Severe Conditions.
41. Val, D.V., Chernin, L. and Stewart, M.G., 2009. Experimental and numerical investigation of corrosion-induced cover cracking in reinforced concrete structures. Journal of Structural Engineering, 135(4), pp.376-385.

42. Vidal, T., Castel, A., François, R. (2004) Analysing crack width to predict corrosion in reinforced concrete, Cement & Concrete Research, Vol. 34 pp 165–174.
43. Yuan, Y., Ji, Y. and Shah, S.P., 2007. Comparison of two accelerated corrosion techniques for concrete structures. ACI Structural Journal, 104(3), p.344.
44. Zhang, R., Castel, A., François, R. (2010). Concrete cover cracking with reinforcement corrosion of RC beam during chloride-induced corrosion process, Cement & Concrete Research, Vol. 40, pp 415–425.
45. Zhao, Y.X. and Jin, W.L., 2006. Modelling the amount of steel corrosion at the cracking of concrete cover. Advances in structural engineering, 9(5), pp.687-696

3 LABORATORY INVESTIGATION

3.1 INTRODUCTION

This chapter presents discussions of the experimental procedures and detailed descriptions of the materials used in this investigation. This laboratory investigation consisted of accelerated corrosion test conducted on reinforced concrete specimens and durability index tests of the mix designs. The specimens were reinforced with nine (9) bars and had three levels of cover depths; three (3) bars at each cover depth. All specimens were of the same dimensions, had the same rebar size but with varying compressive and tensile strengths, as well as the binder types. The binder used were Rapid Hardening Portland Cement (RHPC), Fly Ash (FA), Ground Granular Blast-Furnace Slag (GGBS), Silica Fume (SF) and Metakaolin (MK). This laboratory investigation has been conducted with the aim of this research in mind; to develop a less complicated and practicable method of quantifying the level of corrosion damage in reinforced concrete structures in terms of cross-section loss, using the corrosion-induced crack width. Hence, the purpose of the laboratory experiment was to investigate the relationship between the corrosion-induced crack width and the corrosion level (section loss/mass loss) with respect to binder type and cover depth. This was achieved by following the objectives:

1. To study the evolution of the corrosion-induced crack widths and its relationship with the cross-section loss.
2. To investigate the influence of the specimen properties (cover depth and binder type) on the corrosion process (time to corrosion initiation and cross-section loss) as well as the time to cracking.
3. To evaluate the specimens' resistance to oxygen permeation, water absorption and chloride conductivity by conducting durability index tests of the mix designs and study the influence on the corrosion process.

This experiment comprised five (5) concrete specimens, each corresponding to mix design. The accelerated corrosion process was divided into two stages: cyclic ponding period (corrosion initiation), during which the specimens were ponded with sodium chloride solution without the application of direct current and corrosion potential measured, and the impressed current period (corrosion propagation), where direct current was applied to the rebars to accelerate the corrosion damage after 90% probability of active corrosion was detected. The method of ponding chloride solution on selected face of each specimen was adopted to simulate the following exposure conditions: wetting-drying cycle during the cyclic ponding period, the ingress of chloride ions from the directions of lesser cover, and the effect of pitting or non-uniform corrosion. Corrosion in the natural exposure condition is never uniform as the rebar begins to corrode from areas closer to the exposed surface or area of lesser concrete cover (Chen and Leung, 2013). Several researchers have reported these conditions. Malumbela et al. (2011), Yuan & Ji (2009) and Yuan et al. (2007) reported on the latter condition that steel corrosion is usually localised within the direction of ingress of corrosion agents (Malumbela et al. 2012).

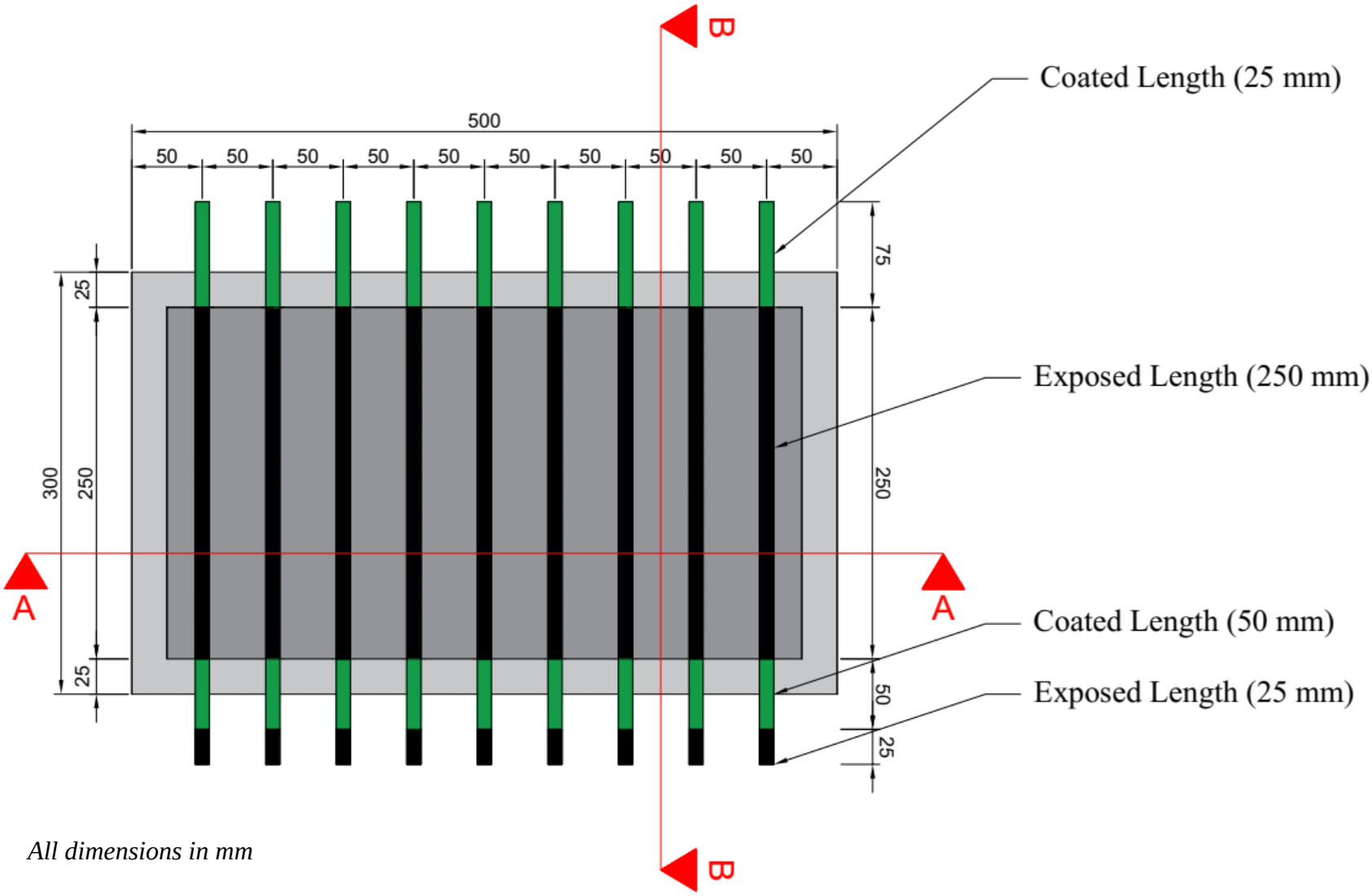

All dimensions in mm

Figure 3. 1 Plan View of the Specimen

3.2 GEOMETRY DESCRIPTION OF THE SPECIMENS

The specimens considered in this experiment had the dimensions of 500 x 300 x 120 mm. The geometry configuration of these specimens, as illustrated in Figure 3.1, was adopted from Nwaubani and Katsanos (2014). This configuration offers numerous advantages, thus eliminating the need for more specimens. The most prominent which is of interest to this study is, it enables studying the influence of various cover depths within a given specimen. Which include the time to cover cracking, cover depth to diameter relationship, cover depth to rebar's section loss relationship, as well as the relationship of the crack width to the corresponding section loss of the rebar. This geometry configuration also allows for a ponding basin at the top the specimen with dimensions of 450 x 250 x 25 mm. Figure 3.2 and 3.3 show the cross-section of the specimens at Section A-A and Section B-B, respectively.

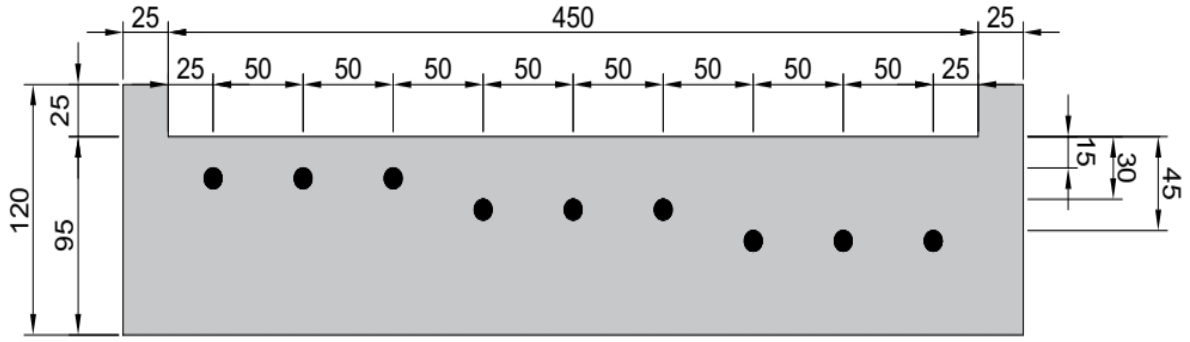

All dimensions in mm

Figure 3. 2 Section A-A

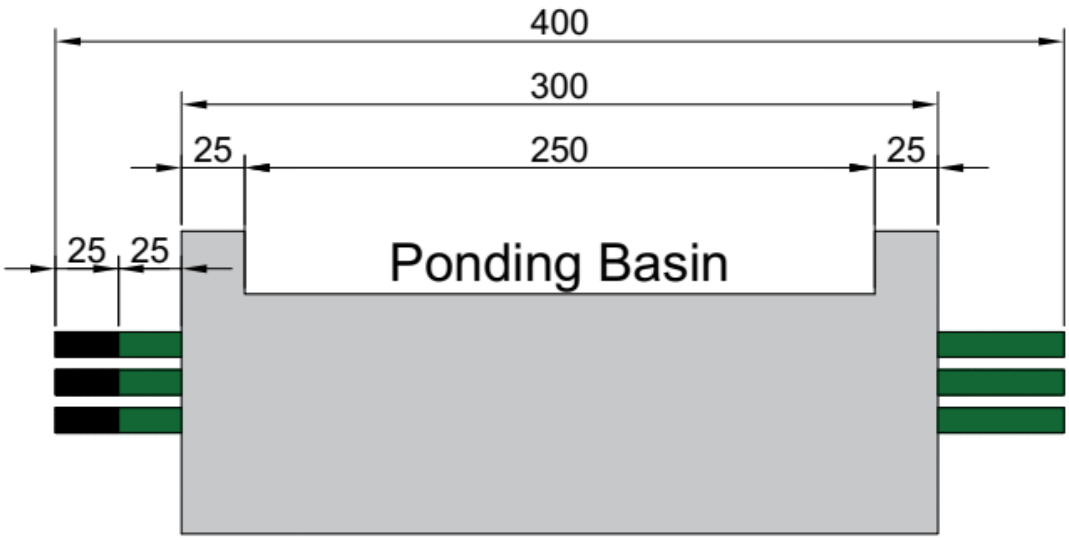

All dimensions in mm

Figure 3. 3 Section B-B

3.2.1 SPECIMEN NOMENCLATURE

The following nomenclatures were adopted for the specimens: SP-PC100, SP-FA30, SP-BS50, SP-SF10 and SP-MK30, which correspond to Mix 100% RHPC, Mix FA-30, Mix GGBS-50, Mix SF-10, and Mix MK-30, respectively. The specimens' nomenclatures reflect the binder type of which the specimens were made. Note: the "SP" in the nomenclature stands for specimen. Also, within a given specimen, the rebars were labelled as illustrated in Figure 3.4.

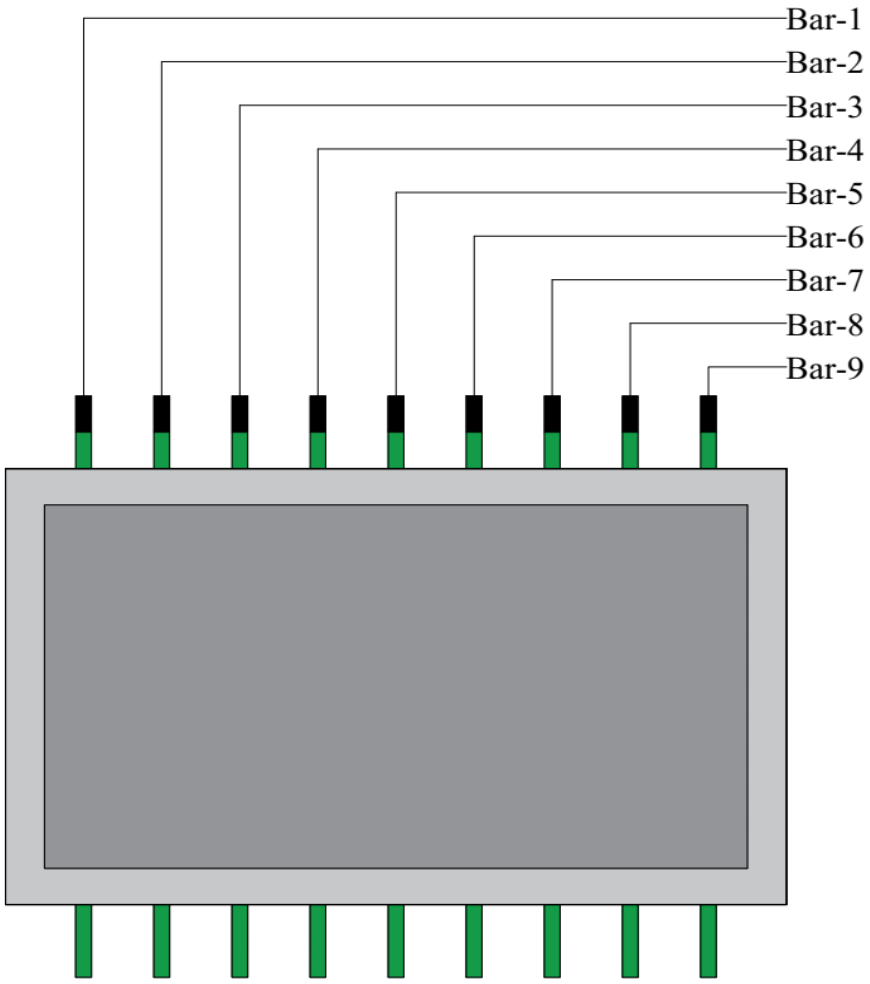

Figure 3. 4 Schematic of Rebars Nomenclature Per Specimen.

3.3 MATERIAL DESCRIPTION

The specimens were made of various binders, natural river sand and crushed granite stone. The binder types used were: 100% Rapid Hardening Portland cement, and binary binders consisting of Rapid Hardening Portland cement with each of the supplementary cementing materials (SCM) listed in Section 3.1. Supplementary cementing materials (SCM) have become a common ingredient of concrete mix designs nowadays (De Belie et al., 2018) and have been subsumed in this investigation to evaluate their performance resistance against chloride-induced corrosion as well as studying the relationship between the corrosion level and the corrosion-induced crack width with concrete containing different types of binders.

These materials were used as partial replacement of the Rapid Hardening Portland cement (RHPC) by mass based on the optimum replacement level available in the literature. The descriptions of these materials are as follows:

3.3.1 BINDER TYPE

3.3.1.1 Rapid Hardening Portland Cement (RHPC)

The cement used was rapid hardening cement (CEM-I, 52.5R) manufactured by AfriSam, South Africa. Due to the complication of the moulds, this cement was selected to meet the early strength required for demoulding the specimens twenty-four (24) hours after casting. As indicated by the manufacturer, the early-strength development is attributed to the large surface area of the cement particle (high fineness) and the incorporation of chloride-based strength modifier with content of less than 0.1%. This CEM-I, 52.5R has the specific gravity of 3.12, and the oxide composition as indicated by the manufacturer are presented in Table 3.1.

3.3.1.2 Fly Ash (FA)

Fly ash, also known as pulverised fuel ash, are ashes resulting from the burning of pulverised coal in a coal-fired electricity power station. Fly ash has a fine dust texture, sphere-shaped and glassy in nature with particle size finer than ordinary Portland cement. As a pozzolanic material, these ashes are known to improve the fresh and hardened properties of concrete. The optimum replacement level of fly ash reported in the literature varies greatly. However, Siddique and Khan (2011) reported that at 28 days and beyond, most fly ashes at the replacement levels of up to 30% by cement weight may exhibit strength generally close to that of the control concrete. Based on Siddique and Khan's (2011) report and the consideration that 30% is the most common replacement level used in South Africa (Otieno, 2014), the replacement level of thirty per cent (30%) was adopted in this investigation. The fly ash used was class F, and the brand is Durapozz, manufactured by Ash Resources, South Africa. Its oxide composition was determined by XRF and are presented in Table 3.1. The particle size analysis was determined by laser diffraction, and the distribution curves are present in Figure 3.5.

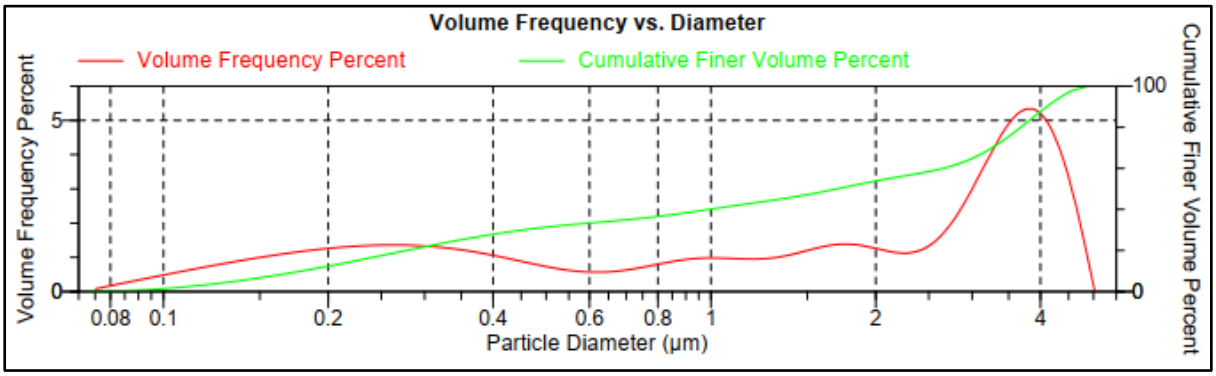

Figure 3. 5 Fly Ash Particle Size Distribution

3.3.1.3 Ground Granulated Blast-Furnace Slag (GGBS)

Ground granulated blast-furnace slag is a by-product of iron manufacturing industries obtained by quenching molten iron slag from a blast furnace either in water or steam. It is a fine glassy granular material, consisting primarily of silicates, aluminosilicates, and calcium-alumina-silicates. Ground granulated blast furnace slag exhibit both latent hydraulic and pozzolanic properties. It has the same primary chemical components as ordinary Portland cement but in different proportions. Hence, it can be used as a direct replacement for ordinary Portland cement on a one-to-one basis by weight (Siddique and Khan, 2011). Replacement level for GGBS varies from 30% up to 85%. Generally, 50% is used in most applications (Siddique and Khan, 2011) and is considered the optimal replacement level in terms of the fresh properties of concrete and late-strength development (Matthes et al., 2018). In this regard, 50% replacement level was considered in this investigation. The slag used was supplied by AfriSam, South Africa and its oxide composition determined by XRF are presented in Table 3.1. The particle size analysis was determined by laser diffraction, and the particle size distribution curves are presented in Figure 3.6.

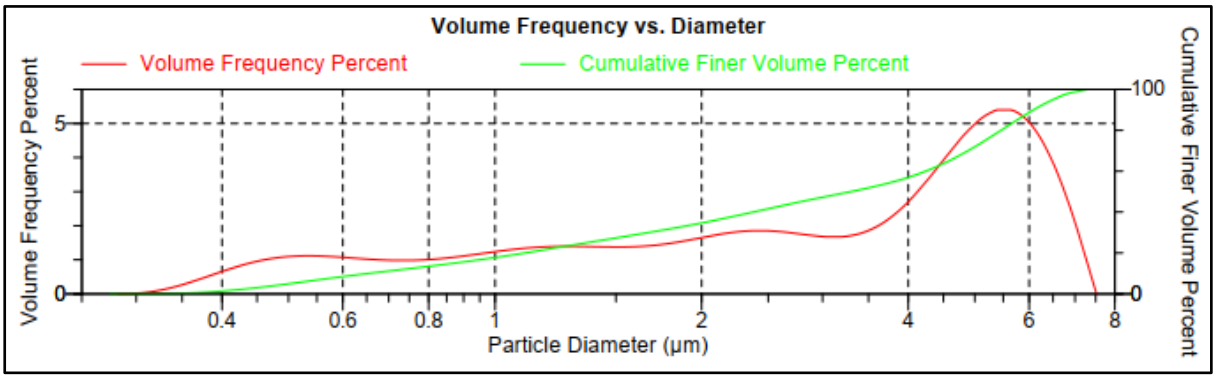

Figure 3. 6 Slag Particle Size Distribution

3.3.1.4 Silica Fume (SF)

Silica fume, also branded as condensed silica fume and micro silica, is a non-crystalline amorphous consisting entirely of silica (more than 80%) and is a by-product of the production silicon and ferrosilicon alloy. Silica fume is an ultrafine powder with the average particle size approximately 100 times smaller than the average cement particle. As a pozzolanic material, silica fume is very useful in enhancing the mechanical properties of concrete (Siddique and Khan, 2011). Silica fume improves the durability of concrete through pore structures refinement, which leads to the reduction in permeability and diffusion of harmful ions. The replacement level of 10% has been reported to be the optimum for normal concrete (Lewis, 2018) and, consequently adopted in this investigation. The brand used was Microfume manufactured by FerroAtlantica, South Africa. The oxide composition was determined by XRF and are presented in Table 3.1. The particle size analysis was determined by laser diffraction, and the particle distribution curves are presented in Figure 3.7.

Table 3. 1 Oxide Composition of the Binders

Oxide Composition	**Percentage (%)**				
	Rapid Hardening Portland Cement	**Fly Ash**	**Blast-Furnace Slag**	**Silica Fume**	**Metakaolin**
Silica (SiO_2)	20.79	56.01	37.11	87.8	54.02
Titanium (TiO_2)	0.39	1.59	0.63	<0.01	1.39
Aluminium (Al_2O_3)	4.64	31.74	14.34	1.45	42.65
Iron (Fe_2O_3)	2.69	3.31	0.52	2.46	0.41
Manganese (Mn_2O_3)	0.12	0.01	0.99	0.21	<0.01
Magnesium (MgO)	1.73	1.22	9.33	1.14	0.29
Calcium (CaO)	65.05	5	34.61	0.77	0.09
Sodium (Na_2O)	0.15	<0.01	<0.01	0.55	<0.01
Potassium (K_2O)	0.47	0.77	1.04	2.14	0.17
Phosphorous (P_2O_5)	0.07	0.56	<0.01	0.13	0.07
Sulphur (SO_3)	2.99	0.13	1.27	<0.01	<0.01
Loss on Ignition (1000 °C)	-	100.36	99.63	99.66	100.10
Loss of Moisture (105°C)	-	0.04	-0.01	0.40	0.07

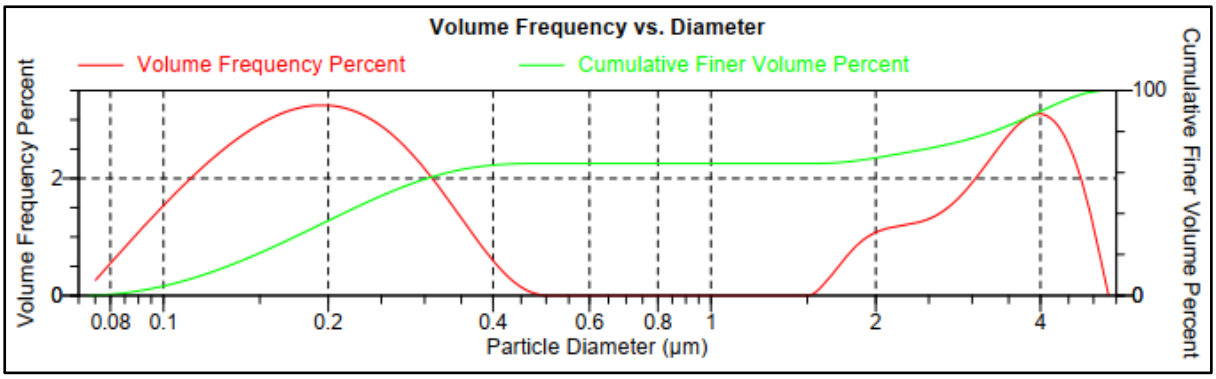

Figure 3. 7 Silica Fume Particle Size Distribution

3.3.1.5 Metakaolin (MK)

Metakaolin is a dehydroxylated form of the clay mineral kaolinite which has pozzolanic properties. Metakaolin is a refined kaolin clay that is heated to a temperature between 500 °C and 800ºC under carefully controlled conditions to create amorphous aluminosilicates that are reactive in concrete. Metakaolin is not a by-product like other pozzolans (fly ash, slag and silica fume), instead it is manufactured for use. The optimum replacement of metakaolin varies in the literature depend on what is required. However, regarding late age strength and better durability properties, 30% has been reported (Sabir et al., 2001). Consequently, 30% replacement level was adopted in this experiment. The brand used was Metakaolin K40 produced by Kaolin-group, South Africa. The oxide composition was determined by XRF and are presented in Table 3.1. The particle size analysis was determined by laser diffraction, and the particle size distribution curves are presented in Figure 3.8.

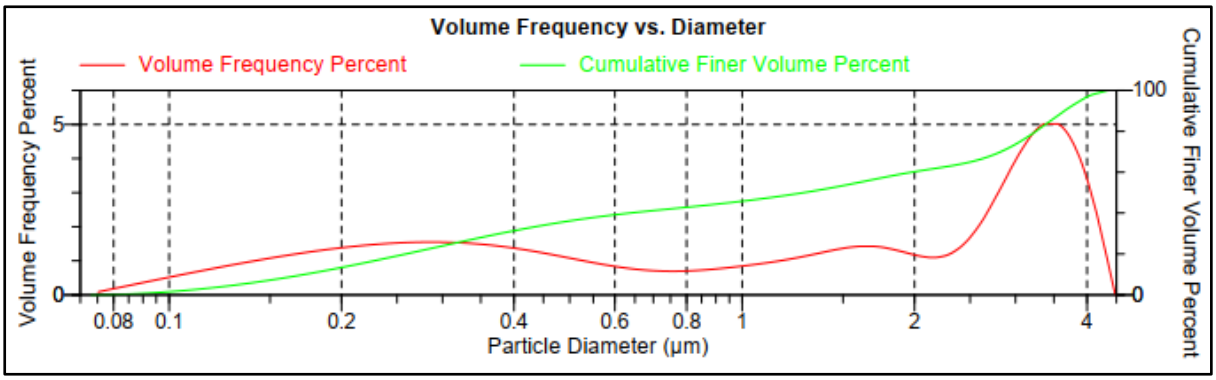

Figure 3. 8 Metakaolin Particle Size Distribution

3.3.2 AGGREGATES

3.3.2.1 Fine Aggregates

The fine aggregates were natural river sand obtained from Builders, South Africa. The fine aggregates were categorised as coarse river sand with a fineness modulus of 3.20 and have the maximum particles size passing sieve size of 9.5 mm but retained on 4.75 mm. Over 90% of the mass of the sample was retained between sieve size of 2.36 mm and 150 µm, which confirmed the category as coarser river sand (Owens and Fulton, 2009). The specific gravity determined by the pycnometer method was 2.61. The sieve analysis and aggregates grading curve are presented in Appendix A.

3.3.2.2 Coarse Aggregates

The coarse aggregates were crushed granite stones, angular in shape and were supplied by AfriSam, South Africa. The maximum particle size, the compacted bulk density, and specific gravity were determined as 13.2 mm, 1726 kg/m^3, and 2.65, respectively. The sieve analysis and aggregates grading curve are presented in Appendix A.

3.3.3 REINFORCEMENT

The reinforcing bars were high tensile strength bars (Y10) which conform to SANS 902:2011, 450 MPa and were obtained from Builders, South Africa. These bars have surface deformation and a diameter of 10 mm as indicated by the nomenclature. The bars for each specimen were cut to the required length of 400 mm and a hole of 4-mm in diameter drilled approximately 20 mm from one end to permit wire connectivity. The bars were cleaned with acetone, portion of the length coated with polyurethane paint and then with insulator tape and, weighed before being placed in position. The coating was meant to protect some area of the bar from corrosion and ensured an exposed length of 250 mm. A 25-mm length from the side of the rebars with the 4-mm hole was left uninsulated to allow for connectivity as shown in Figure 3.1 to 3.3.

3.4 MIX DESIGNS

This experiment consisted of five mixes, the control (labelled as 100% RHPC) and four binary binders. The control was made of 100% Rapid Hardening Portland Cement (100% RHPC) and designed based on the standard procedure of volumetric mix design as described by Owens and Fulton (2009), while the binary binders were obtained by replacing various portion (by mass) of the cement content of the control with each of the supplementary cementing material described in Section 3.3. These binary binders were labelled as FA-30, GGBS-50, SF-10 and MK-30. The label indicates the replacing material and the replacement level, respectively, of the rapid hardening Portland cement. The water-binder ratio was held constant for all mix designs and superplasticizer added by mass of the total binder in varying quantity to have the same consistency. Superplasticizer was added to all mix designs to give self-consolidating behaviour as moderate vibration was required to keep the rebars in positions. Details of the mix designs are presented in Table 3.2, and the description of the superplasticiser are presented in Appendix A.

3.5 CASTING AND CURING PROCEDURE

The casting was done in the Concrete Laboratory at the School of Civil and Environmental Engineering, University of the Witwatersrand. The moulds were prepared, oiled and the rebars fixed in position with silicon sealant as shown in Figure 3.9, before casting. The rebars projected 32 mm on both sides of the mould to ensure the variation of the concrete cover depth and to have 50 mm projection out of the specimens after demoulding. These specimens were cast in the inverted position due to the configuration of the moulds. The concrete was poured into the moulds and moderately vibrated in three layers along with a total of 250 cubes (100mm).

Table 3. 2 Mix Designs

MATERIALS (kg/m^3)	MIX DESIGNS				
	100% RHPC	**FA-30**	**GGBS-50**	**SF-10**	**MK-30**
	CONTROL	**70/30 RHPC/FA**	**50/50 RHPC/GGBS**	**90/10 RHPC/SF**	**70/30 RHPC/MK**
Rapid Hardening Portland Cement	320.3	224.2	160.15	288.3	224.2
Fly Ash	-	96.1	-	-	-
Ground Granulated Blast-Furnace Slag	-	-	160.15	-	-
Silica Fume	-	-	-	32.0	-
Metakaolin	-	-	-	-	96.1
Coarse Aggregates	1001	1001	1001	1001	1001
Fine Aggregate	821.1	821.1	821.1	821	821
Water Content	205	205	205	205	205
w/b ratio	0.64	0.64	0.64	0.64	0.64
Superplasticiser [a]	0.6	0.3	0.5	0.9	1.3
Slump (mm)	170	160	160	170	160
28-day Compressive strength (MPa)	39.8	31.6	28.6	40.5	46.4

[a] by mass of the binder

After casting, the specimens along with the cubes were covered with polyethene sheet to prevent the rapid loss of moisture. They were immediately demoulded after 24 hours and cured in water at room temperature. During the curing period, compressive and tensile strength tests were performed to track the trend of strength development for each mix. The compressive and tensile strength tests were performed up to the 56th day after casting. After 28 days of water curing, the specimens along with some cubes were removed from the curing pool and prepared for the cyclic ponding stage and the durability index tests, respectively. The preparations of the specimens and the required numbers of cubes are described under the accelerated corrosion and durability index sections, respectively. Since the specimens were subjected to ponding or exposed to moisture, the remaining cubes were kept in the curing pool until the 56th day.

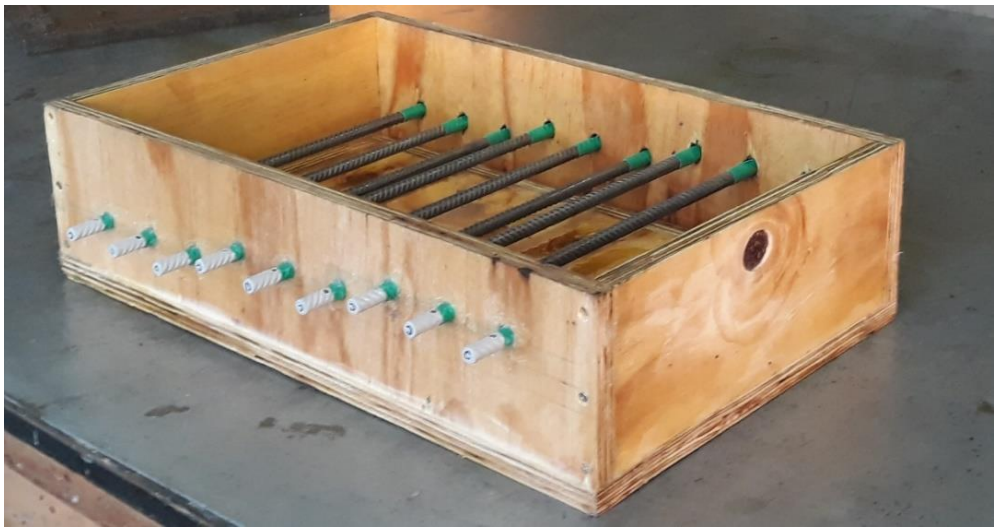

Figure 3. 9 Configuration of the mould

3.6 ACCELERATED CORROSION TEST PROCEDURE

There are several methods of accelerating corrosion in concrete, but for this study, the approach mentioned in Section 3.1 was adopted. The accelerated corrosion test was divided into two stages; the initiation period which consisted of cyclic ponding the specimens with sodium chloride solution and the propagation period during which direct current was applied after 90% probability of active corrosion was detected. After 28 days of water curing, the specimens were removed from the curing pool and allowed to dry for three (3) day in the laboratory at ambient condition. The specimens were then coated with three layers of polyurethane paint and allowed to dry for one day, after which the cyclic ponding period began.

3.6.1 CORROSION INITIATION

The initiation period consisted of ponding the specimens with sodium chloride (NaCl) solution containing 5% concentration and allowing the chloride ions to travel predominantly under concentration gradient. The initiation period comprised wetting-drying cycles, with each cycle consisting of four (4) days wetting and three (3) days drying. During these cycles, the surface resistivity of the specimens and half-cell potential of each bar per specimen were measured. The setup of the initiation period is shown in Figure 3.10.

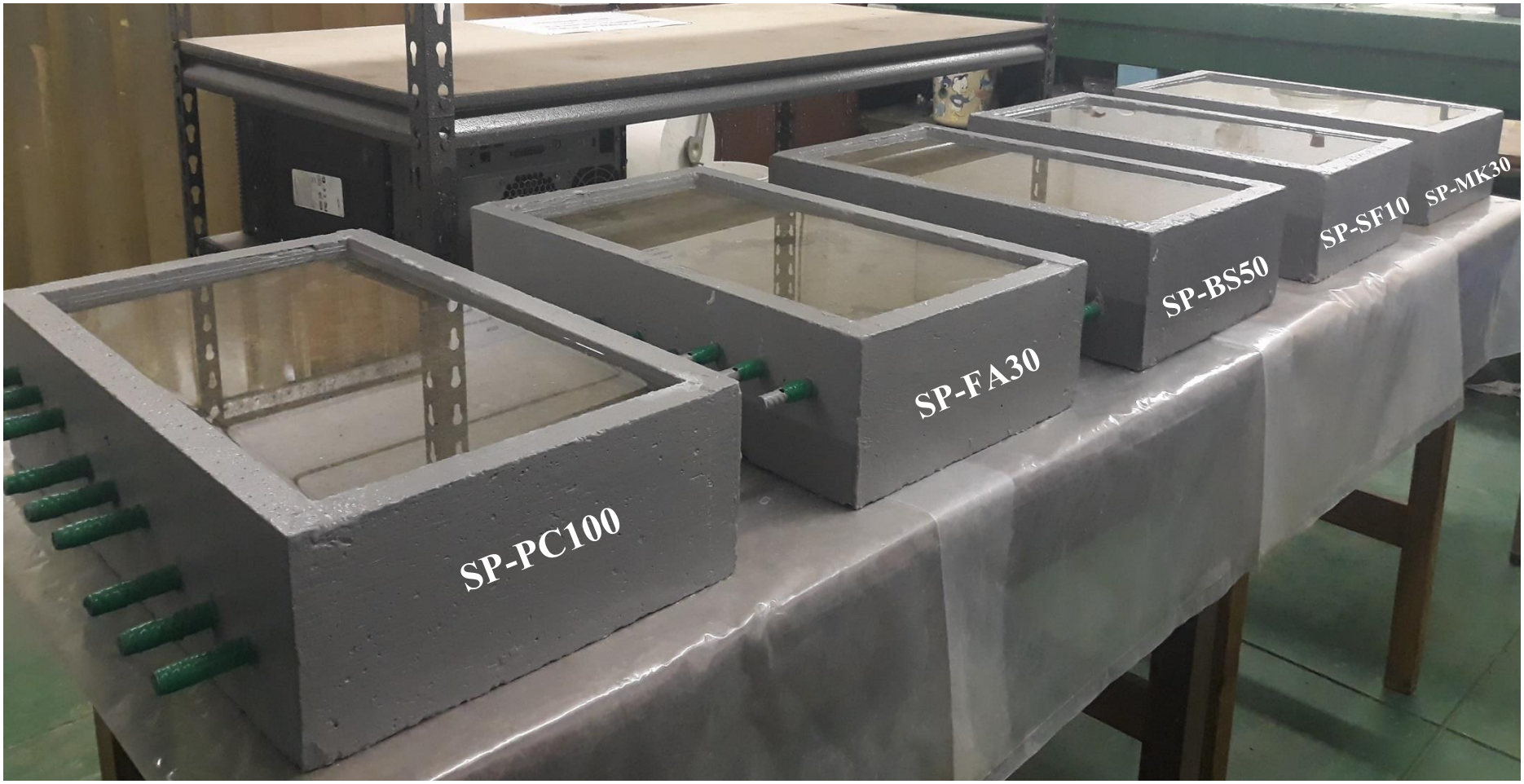

Figure 3. 10 Setup of the Initiation Period

3.6.1.1 Surface Resistivity Measurement

The specimen's surface resistivity was measured with Resipod resistivity meter, shown in Figure 3.11. Resipod is a surface resistivity meter that operates on the four-point principles of Wenner Probe. The schematic of the operating principles is illustrated in Figure 3.12, a current is applied between the two outer probes via the concrete, and the potential difference is measured between the two inner probes. The measured resistivity depends on the spacing of the probes, the dimensions of the concrete and the amount of moisture. The measurement was done on the surface of the ponding basin, and electrical contact was made by slightly wetting the surface and placing a damp towel between the resistivity meter and the surface.

Figure 3. 11 Image of Resipod Resistivity Meter (www.proceq.com)

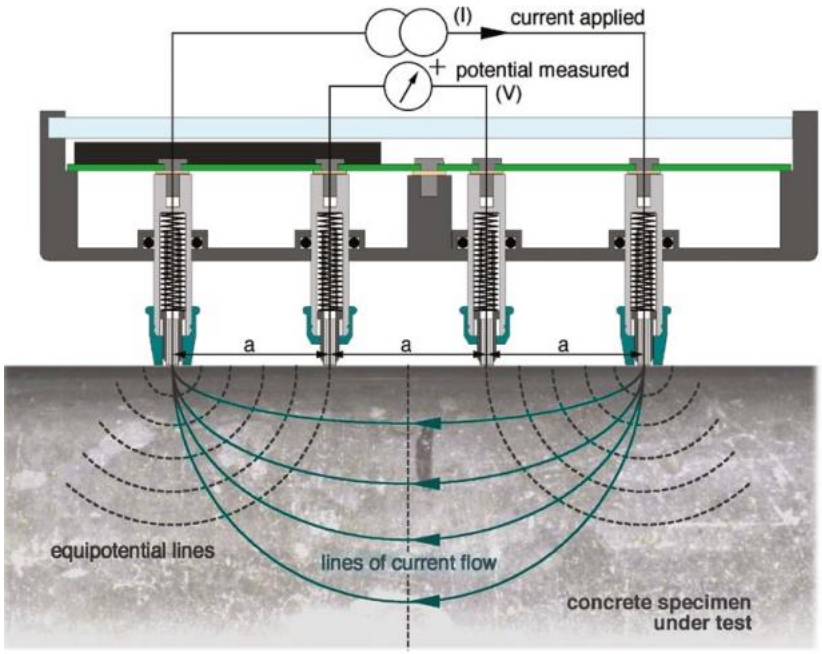

Figure 3. 12 Schematic of Operating Principle (www.proceq.com)

3.6.1.2 Half-cell Potential Measurement

The half-cell potential measurement is the most widely used and standardised non-destructive method of assessing corrosion potential or the corrosion state of rebars in concrete (Bertolini et al., 2013). This method does not provide quantitative information on the actual corrosion rate of the rebars (Elsener et al., 2003) nor the level of corrosion but only evaluates the probability of corrosion or risk of corrosion at a given time. This method consists of measuring the potential difference between the rebar and a given reference electrode. The potential difference (corrosion potential) can be measured using a high impedance voltmeter or a half-cell meter, connected to the rebar and a reference electrode. As illustrated in Figure 3.13, the reference electrode is placed directly above the rebar on the concrete surface, and the readings are taking. The negative terminal of the voltmeter is connected to the reference electrode and the rebar connected to the positive terminal, to have negative readings. The measured corrosion potential depends on the type of the reference electrode used and is influenced mainly by the availability of oxygen, chloride concentration, concrete cover depth, and the concrete resistivity, which is also influenced by the amount of moisture. In this experiment, a copper-copper sulphate (CSE) reference electrode was used, and the interpretation of the reading is presented in Table 3.3. During measurement, electrical connection was established by slightly wetting the concrete surface and placing a damp towel between the concrete surface and the reference electrode. Two sets of five readings were taken per bar, equally space alone the exposed length of the bars, at an interval of two minutes. Figure 3.14 shows the half-cell meter used in this experiment.

Table 3.3 Interpretation on Half-cell Potential Based on CSE reference Electrode

Half-cell Potential Reading	**Corrosion Activity/Probability**
Positive or less negative than -200 mV	90% probability of no corrosion
Between -200 mV and -350 mV	corrosion activity is uncertain
More negative than -350 mV	90% probability of corrosion

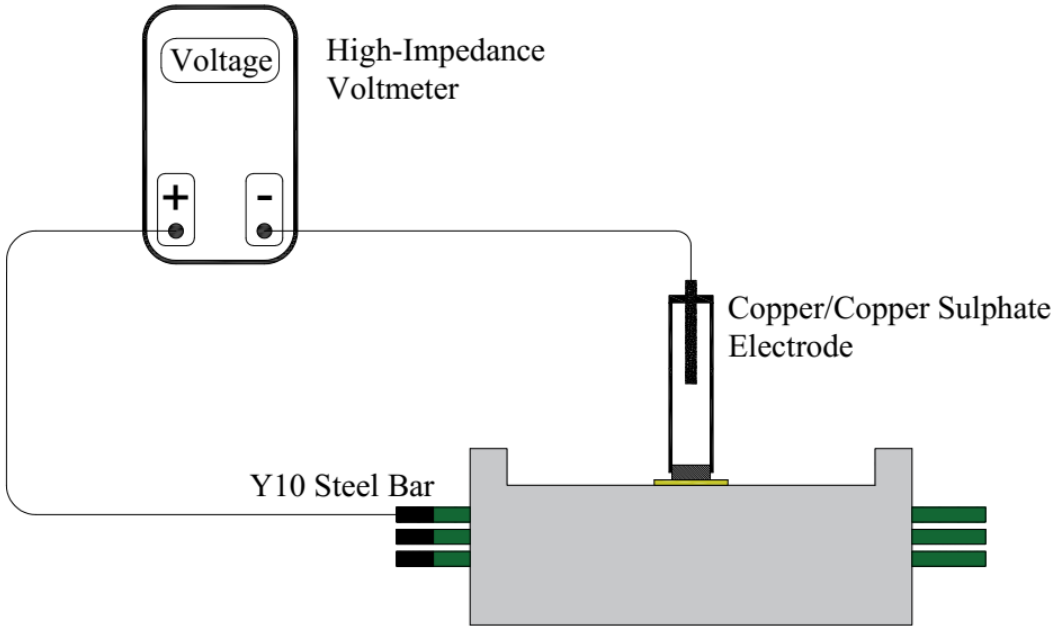

Figure 3. 13 Schematic of the Half-Cell Potential Measurement

Figure 3. 14 Image of the Half-Cell meter (www.elcometer.com)

3.6.2 IMPRESSED CURRENT

After the cyclic ponding period, the impressed current technique was used to propagate the corrosion after 90% probability of active corrosion was detected in some bars. This technique consists of applying a direct current (DC) to the embedded steel to induce corrosion and has been selected based on the following reasons: easy to set up, required less sophisticated equipment and saved time. The setup of this technique was based on ASTM standard procedure of conducting accelerated corrosion in concrete specimens and on findings of other researchers, most especially Malumbela et al. (2012).

Figure 3.15 and 3.16, show the setup schematic per specimen and the setup of the impressed current, respectively. The current was impressed through the rebars, thus serving as the anode and 304 stainless-steel plate serving as the cathode. The stainless-steel plate had dimensions of 350 x 150 x 4.75 mm and these dimensions were selected to have the anodic-to-cathodic area ratio of 1:1.5, to avoid cathodic current limitation. The anodic area used in the ratio comprised the total exposed areas of the nine (9) bars within the specimen. The DC power suppliers were set to the maximum of 1 Ampere, and the voltage reaching each was logged across a 12-Ohm resistor at an interval of ten (10) minutes. Although not explicitly shown in Figure 3.15, the voltage across each resistor was logged individually.

The application of the impressed current lasted for fourteen (14) days, and during this period, the variables recorded were the inducing current and the time to cracking per specimens. Upon termination of the impressed current, the specimens were examined, and all connections to the bars checked as there was seepage of the salt solution from cracked specimens. After that, the corrosion-induced crack widths were measured by Elcometer 900 concrete crack microscope, and the crack's pattern mapped out. The specimens' resistivity and half-cell potential were also measured. The rebars were then extracted, cleaned in accordance with ASTM G1 90 and the gravimetric analysis conducted. The average diameter loss was then measured with Vernier calliper which has the accuracy of ± 0.01 mm. The cleaning solution consisted of 1000 millilitre of hydrochloric acid (HCl), 20 grams of antimony trioxide (Sb_2O_3) and 50 grams of stannous chloride ($SnCl_2$).

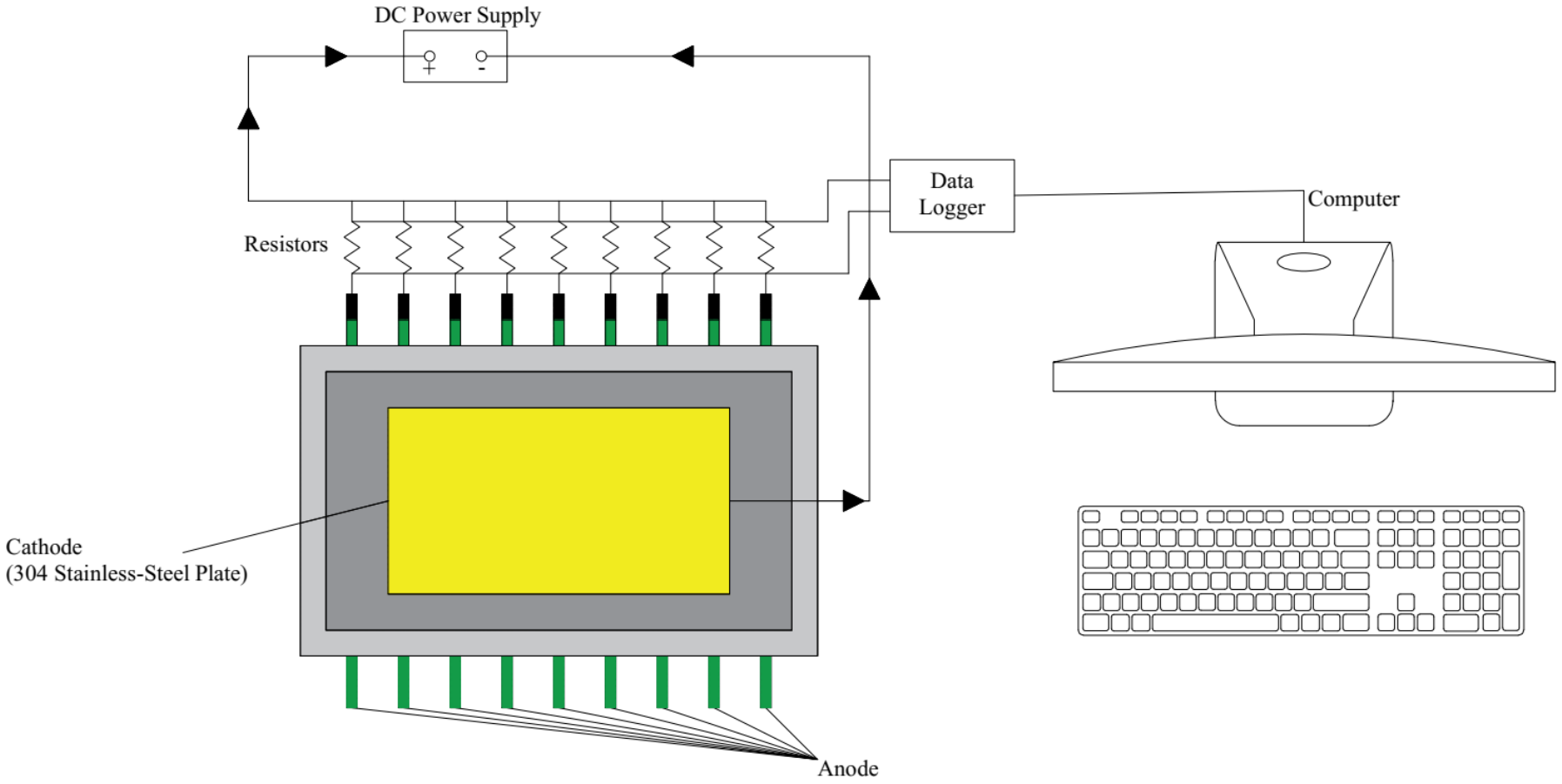

Figure 3. 15 Schematic of the Impressed Current Setup Per Specimen

Figure 3. 16 Setup of the Impressed Current

3.7 DURABILITY INDEX TESTING PROCEDURE

The durability of concrete directly links to its penetrability, and the ease with which substances (ions or fluid) move through the concrete pores structure determine its penetrability (Owens and Fulton, 2009). Given that the specimens were made of various binders and that the accelerated corrosion test set up to mimic some natural conditions (the movement of chloride ions, water and oxygen, from the direction of lesser concrete cover), it was imperative to evaluate the specimens' resistances to penetration and conductivity as an aid in interpreting the results of accelerated corrosion test. Therefore, durability indexes of the mix designs were conducted to evaluate the specimens' resistance to oxygen permeation, water absorption and chloride conductivity. Developed in South Africa to promote performance-based thinking, durability index tests evaluate the overall concrete quality and are sensitive to materials, mix proportions and curing conditions (Alexander et al., 2008). The durability indexes consist of Oxygen Permeability Index (OPI), Water Sorptivity Index (WSI) and Porosity, and Chloride Conductivity Index (CCI). These indexes describe the leading transport mechanisms associated with concrete deterioration (Owens and Fulton, 2009). The durability index tests require samples of circular concrete discs with diameter and thickness of 70 ± 2 mm and 30 ± 2 mm, respectively, and require four samples (circular concrete discs) per test. The samples were prepared, and the tests conducted accordingly, as described by the Durability Index Testing Procedure Manual. A set of three tests per index was performed to improve the credibility of results and for statistical analysis. Detailed of samples preparation, the overview of each test and the testing procedures are presented in the sections below.

3.7.1 SAMPLES PREPARATION

The samples required for conducting Durability Index Test are circular concrete discs with diameter and thickness of 70 ± 2 mm and 30 ± 2 mm, respectively. The samples (circular discs) were obtained by coring concrete cubes of 100 mm after 28 days of wet curing. The total of 75 cubes was cored, 15 cubes per mix. This number of cored cubes was in excess to compensate for any damage that may occur to the sample's surface during cutting, as the manual prescribes that damage samples should not be used for testing.

Again, it is worth mentioning that the preparations of the samples were done in the Concrete Laboratory at the School of Civil and Environmental Engineering, University of the Witwatersrand. The direction of coring was perpendicular to the direction of casting as prescribed by the Durability Index Testing Manual. After coring, the samples were left under ambient conditions in the Concrete Laboratory for three (3) days before cutting. The cutting was performed as illustrated in Figure 3.17; two samples were obtained from a cube. The first 5 mm at the two extreme ends of the core were cut off, and the samples labelled on the interior faces. Immediately after cutting, the samples were moved from the Concrete Laboratory to the Concrete Durability Laboratory and placed in a ventilated oven for seven (7) days at a constant temperature of 50 ± 2 °C. The Concrete Durability Laboratory at the School of Civil and Environmental Engineering, University of the Witwatersrand, is a controlled environment with constant temperature of about 23 ± 2 °C. After seven (7) days of oven drying, the OPI and the

CCI tests began, followed by the WSI for each mix. It is worth noting that the samples used for the OPI test were the same ones used in the WSI and Porosity test.

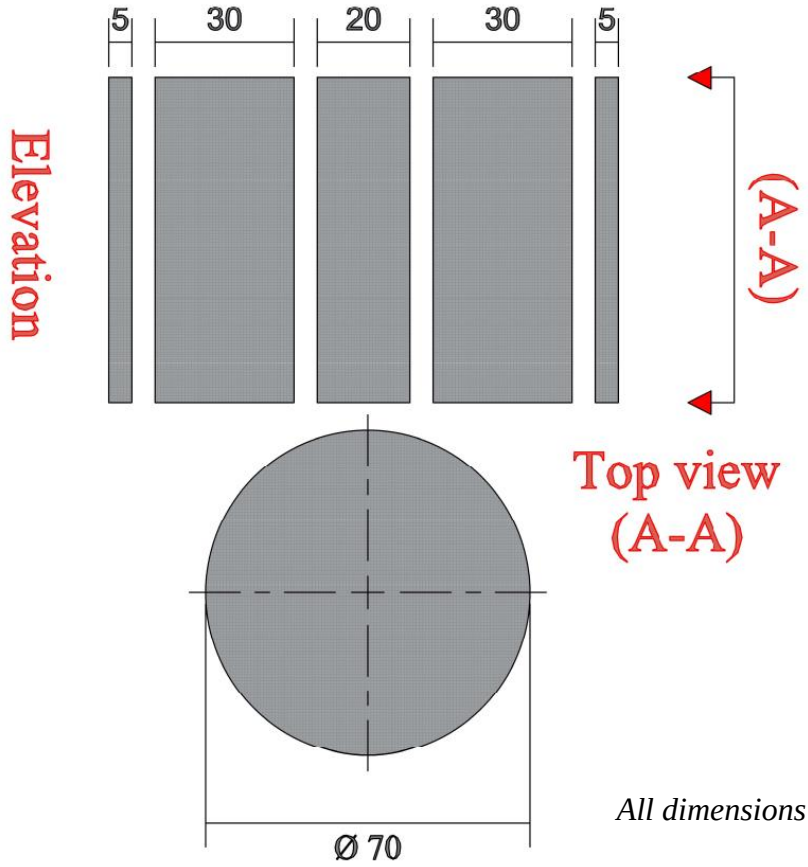

Figure 3. 17 Disc Cutting Schematic

3.7.2 OXYGEN PERMEABILITY INDEX (OPI)

The oxygen permeability test assesses the overall pore structures of concrete and its interconnectedness. This test evaluates the resistance of concrete to the ingress of gases in general and is sensitive to water-binder ratio, binder type, curing condition, as well as compaction (Owens and Fulton, 2009). Oxygen permeability test consists of measuring the pressure decay of oxygen passed through the test sample in a falling head permeameter (permeability cell) and the oxygen permeability index is expressed as the negative log of the coefficient of permeability (Owens and Fulton, 2009). The higher the oxygen permeability index (OPI) value, the higher the impermeability of the sample tested. Figure 3.18 illustrates the schematic of the permeability cell used for OPI testing.

3.7.2.1 Procedure of the Oxygen Permeability Index Test

After seven days of drying, the samples were removed from the oven and placed in a desiccator. The samples were left in the desiccator to cool for two to four hours, after which the samples were removed, and the diameter and thickness measured to the nearest 0.02 mm with a Vernier calliper. The measurements were taken at four points equally spaced across the perimeter of the samples and averaged recorded.

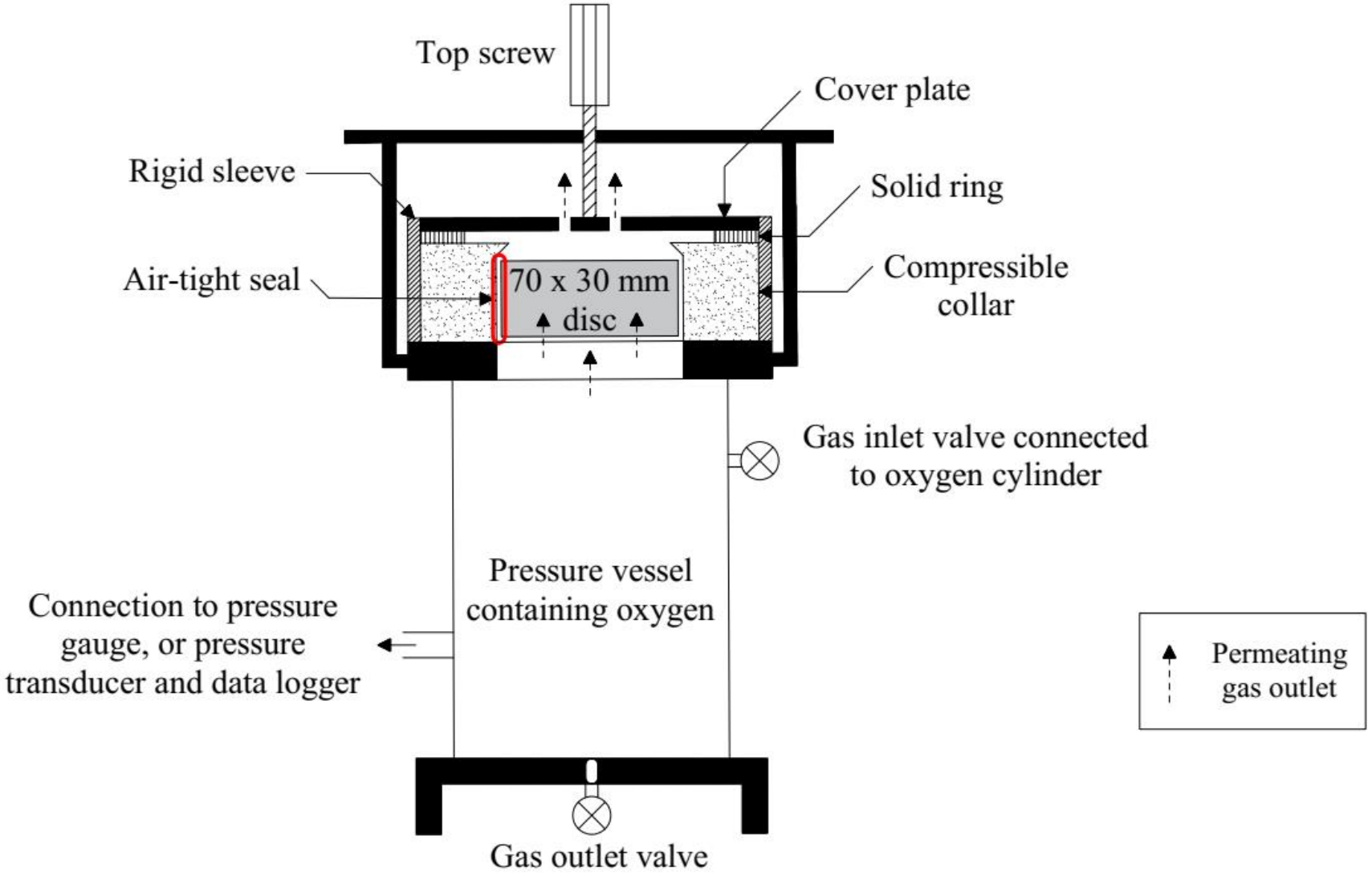

Figure 3. 18 Schematic of the permeability cell

Immediately after recording the dimension and within less than thirty minutes after the removal of the samples from the desiccator, the samples were placed in the oxygen permeability cells with the internal face (the marked surface) facing the direction of the oxygen. Figure 3.19 shows the setup or arrangement of the permeability cell used. The cells were checked for leakages or a sudden drop in pressure of 5 kPa/min. When no leakage was detected, the data logger was activated, and the test began. The data was automatically logged at an interval of five (5) minutes by a data logger. As prescribed by the manual, the test should be terminated when the pressure dropped to 50 ± 2.5 kPa or after 6 hours ± 15 min, whichever comes first. Six (6) hours was the condition that first occurred, and upon which the test was terminated. Upon termination, the data was retrieved and imported to the calculation sheet recommended by the manual, and the OPI values obtained.

Figure 3. 19 Arrangement of the permeability cells used

3.7.3 WATER SORPTIVITY INDEX AND POROSITY TEST

Water sorptivity index and porosity test also describe the pores structures of concrete and its ability to absorb moisture. This test measures the resistance of unsaturated concrete to water absorption under capillary suction as well as its porosity. Water sorptivity index is the rate of water uptake by a dry sample (Alexander et al., 2008) and the lower the sorptivity index, the better the concrete quality.

3.7.3.1 Procedure of the Water Sorptivity and Porosity Test

The same samples used for the oxygen permeability test were used for the water sorptivity and porosity test. After the OPI test, the samples were prepared for the water sorptivity and porosity test. The preparations include taping the curve edges with Sellotape and weighing. The samples were weighed and recorded to an accuracy of 0.01 gram. The initiate mass determined was recorded as the dry mass.

The samples were then placed in a plastic tray containing ten (10) layers of absorbent paper towel saturated with calcium hydroxide solution, which contained 5 gram of $Ca(OH)_2$ per litre of water. The schematic of water sorptivity and porosity test is shown in Figure 3.20. The external surface served as the test surface and was placed in the calcium hydroxide solution. The solution was visible above the absorbent paper towel and was at the maximum of 2 mm above the test surface (surface in contact with the solution). The samples were weighed to the nearest 0.01 gram at various intervals: 3, 5, 7, 9, 12, 16, 20 and 25 minutes. During weighing, the samples were wiped to a saturated surface dry condition, weighed and placed back (the test surface) in the solution within ten (10) seconds.

After weighing at the various intervals, the samples were placed within a vacuum saturation tank with the Sellotape in placed and evacuated to the pressure between -75 and -80 kPa. As prescribed by the manual, the samples were placed standing on the curved edges to maximise their exposed surface area. The pressure was maintained for three (3) hours ± 15 min. After this period, calcium hydroxide solution was allowed into the tank to about 40 mm above the samples without air entering. The vacuum was re-established to between -75 and -80 kPa and maintained for one (1) hour ± 15 minutes. After this period, the pressure was released, and air was allowed in the vacuum saturation tank. The samples were then allowed to soak in the calcium hydroxide solution for 18 hours ± 1 hour. After the 18 hours period of soaking, the samples were removed, wiped to saturated surface dry condition, immediately weighed and recorded as the vacuum saturated mass of the samples. The data was imported to the calculation sheet (spreadsheet developed to perform the calculation) and the WSI and porosity obtained.

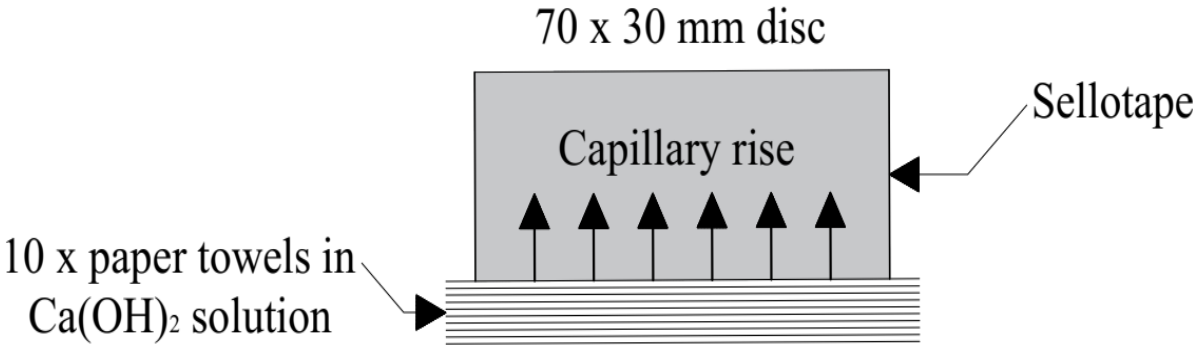

Figure 3. 20 Schematic of water sorptivity and porosity test

3.7.4 CHLORIDE CONDUCTIVITY INDEX TEST (CCI)

Chloride conductivity index test is a rapid chloride conduction test that measures the resistance of concrete to the diffusion of chloride ions (Otieno, 2018). The resistance is given in terms of chloride conductivity index (CCI), and higher values indicate lower resistance. The chloride conductivity test is more sensitive to binder type (Alexander et al., 2008). This test consists of measuring current and voltage across the sample in a conduction cell. The conduction cell used in the experiment was of telescopic tube arrangement or configuration, and the schematic is illustrated in Figure 3.21.

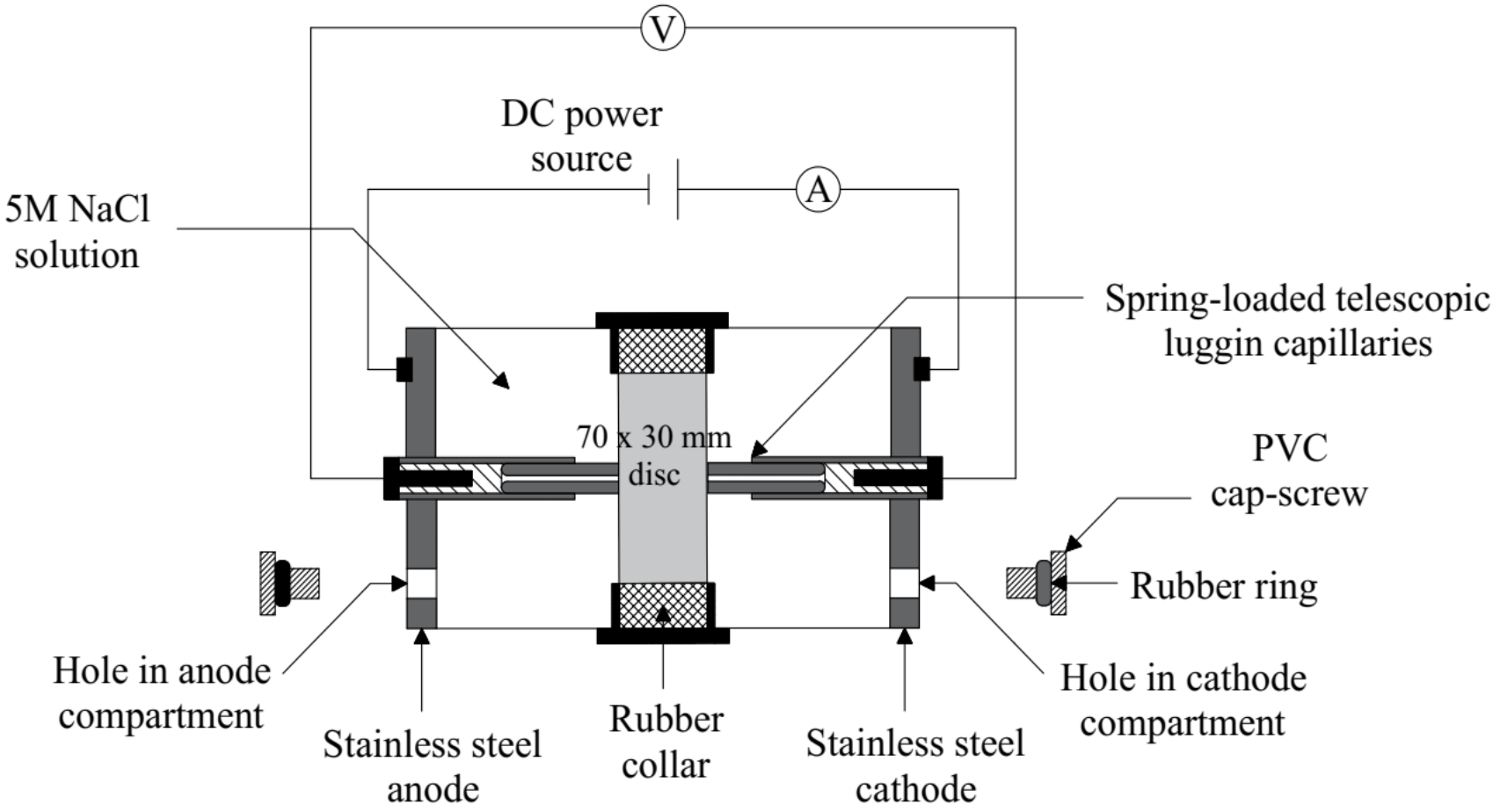

Figure 3. 21 Schematic of the conduction cell

3.7.4.1 Procedure of the chloride conductivity Test

The test samples were removed from the oven after seven days of dying and placed in a desiccator. The samples were allowed to cool in the desiccator for the minimum period of 2 hours but not more than 4 hours. Within 30 minutes after removing the samples from the desiccator, the diameter and thickness were measured at four points equally spaced across the perimeter of the samples with a Vernier calliper to the nearest 0.02 mm and the average recorded. The samples masses were also recorded as the dry mass of the specimen to the nearest 0.01 gram.

The samples were then placed into a vacuum saturation tank, and as in similar manner, as described in the water sorptivity test, the samples were placed standing on the curved edges to maximise the exposed surface area. The vacuum saturation tank was then evacuated to pressure between -75 and -80 kPa and maintained for 3 hours ± 15 minutes. After this period, sodium chloride (NaCl) solution was allowed in and submerged the samples at approximately 40 mm above the top without air entering the vacuum saturation tank. The solution contained 5M of NaCl with tap water as the solvent and was prepared at least 24 hours before being used and stored under the ambient condition of the durability laboratory. The pressure was then re-established to between -75 and -80 kPa and maintained for one (1) hour ± 15 minutes.

After the one (1) hour ± 15 minutes, the pressure was released, and air allowed to enter the vacuum saturation tank. The samples were allowed to soak in the sodium chloride solution for additional 18 hours ± 1 hour. After this 18 ± 1-hour period of soaking, the samples were removed, wiped to a saturated surface dry condition, weighed to the nearest 0.01 gram and recorded as the vacuum saturated mass of the samples. The samples were then placed into a vessel containing the same 5M NaCl solution as the voltage and current were being measured.

The samples were placed in the conduction cell one at a time, and both chambers of the cell filled with the 5M NaCl solution and tighten to ensure there is no leakage. The conduction cell was then connected to the circuit consisting of a DC power supply, an ammeter, and a voltmeter. The DC power supply was switch on, and the reading of the voltage and the current was simultaneously done within 10 seconds after the readings have stabilised. As recommended by the manual, the voltage been read from the voltmeter was always in the range of 10 V. Thus, adjustment was made from the power supply when the voltage was outside the range of 10 V. Upon completion of the readings, the data was imported to the spreadsheet, and the CCI calculated.

3.8 REFERENCES

1. Alexander, M.G., 2017. Durability Index Testing Procedure Manual.
2. Alexander, M.G., Ballim, Y. and Stanish, K., 2008. A framework for the use of durability indexes in performance-based design and specifications for reinforced concrete structures. Materials and structures, 41(5), pp.921-936.
3. Bertolini, L., Elsener, B., Pedeferri, P., Redaelli, E. and Polder, R.B., 2013. Corrosion of steel in concrete: prevention, diagnosis, repair. John Wiley & Sons.

4. Chen, E. and Leung, C.K.Y., 2013. Numerical modelling of non-uniform steel corrosion development and its mechanical influences on reinforced concrete structures. In 8th International Conference on Fracture Mechanics of Concrete and Concrete Structures-FraMCoS-8, Toledo, Spanin.
5. De Belie, N., Soutsos, M. and Gruyaert, E. eds., 2018. Properties of Fresh and Hardened Concrete Containing Supplementary Cementitious Materials: State-of-the-Art Report of the RILEM Technical Committee 238-SCM, Working Group 4 (Vol. 25). Springer.
6. Elsener, B., Andrade, C., Gulikers, J., Polder, R. and Raupach, M., 2003. Hall-cell potential measurements—Potential mapping on reinforced concrete structures. Materials and Structures, 36(7), pp.461-471.
7. Jaffer, S.J. and Hansson, C.M., 2009. Chloride-induced corrosion products of steel in cracked-concrete subjected to different loading conditions. Cement and Concrete Research, 39(2), pp.116-125.
8. Lewis R.C., 2018. Silica Fume. In: De Belie N., Soutsos M., Gruyaert E. (eds) Properties of Fresh and Hardened Concrete Containing Supplementary Cementitious Materials. RILEM State-of-the-Art Reports, vol 25. Springer, Cham.
9. Malumbela, G., Moyo, P. and Alexander, M., 2012. A step towards standardising accelerated corrosion tests on laboratory reinforced concrete specimens. Journal of the South African Institution of Civil Engineering, 54(2), pp.78-85.
10. Malumbela, G., Alexander, M. and Moyo, P., 2011. Model for cover cracking of RC beams due to partial surface steel corrosion. Construction and Building Materials, 25(2), pp.987-991.
11. Matthes W. et al., 2018. Ground Granulated Blast-Furnace Slag. In: De Belie N., Soutsos M., Gruyaert E. (eds) Properties of Fresh and Hardened Concrete Containing Supplementary Cementitious Materials. RILEM State-of-the-Art Reports, vol 25. Springer, Cham.
12. Nwaubani, S.O. and Katsanos, A., 2014. Effect of alternative De-icers on the corrosion resistance of reinforced concrete bridges and highway structures. In Developments in Corrosion Protection. InTech.
13. Otieno, M., 2018. Sensitivity of the rapid chloride conductivity index test to concrete quality and changes in various test parameters. Cement and Concrete Composites, 86, pp.110-116.
14. Otieno, M. and Alexander, M., 2015. Chloride conductivity testing of concrete-past and recent developments. Journal of the South African Institution of Civil Engineering, 57(4), pp.55-64.
15. Otieno, M.B., 2014. The development of empirical chloride-induced corrosion rate prediction models for cracked and uncracked steel reinforced concrete structures in the marine tidal zone (Doctoral dissertation, University of Cape Town).
16. Owens, G. and Fulton, F., 2009. Fulton's concrete technology. Midrand: Cement & Concrete Institute.
17. Sabir, B.B., Wild, S. and Bai, J., 2001. Metakaolin and calcined clays as pozzolans for concrete: a review. Cement and concrete composites, 23(6), pp.441-454.
18. Siddique, R. and Khan, M.I., 2011. Supplementary cementing materials. Springer Science & Business Media.

19. Yuan, Y. and Ji, Y., 2009. Modeling corroded section configuration of steel bar in concrete structure. Construction and Building Materials, 23(6), pp.2461-2466.
20. Yuan, Y., Ji, Y. and Shah, S.P., 2007. Comparison of two accelerated corrosion techniques for concrete structures. ACI Structural Journal, 104(3), p.344.
21. Zhang, S.P. and Zong, L., 2014. Evaluation of relationship between water absorption and durability of concrete materials. Advances in Materials Science and Engineering, 2014.
22. Zou, Z.H., Wu, J., Wang, Z. and Wang, Z., 2016. Relationship between half-cell potential and corrosion level of rebar in concrete. Corrosion Engineering, Science and Technology, 51(8), pp.588-595.

4 EXPERIMENTAL RESULTS AND DISCUSSIONS

4.1 INTRODUCTION

This chapter presents analyses and discussions on the results of the laboratory investigation. As described in Chapter 3, the laboratory investigation consisted of accelerated corrosion test conducted on reinforced concrete specimens and durability index tests of the mix designs. The accelerated corrosion test consisted of cyclic ponding the specimens with sodium chloride solution (initiation period) and then applying direct current after 90% probability of active corrosion was detected (propagation period). During the cyclic ponding period, the specimens' resistivity and half-cell potential of each bar per specimen were measured. While during the impressed current application, the voltages reaching each bar per specimen were logged across 12-ohm resistors. After the termination of the impressed current, the specimens' resistivity and half-cell potential of each bar were measured, and gravimetric analysis of the rebars conducted. The accelerated corrosion test lasted over two and a half months; nine weeks for the initiation period and two weeks for the propagation period.

4.2 RESULTS AND DISCUSSIONS OF STRENGTH DEVELOPMENT

Compressive and tensile strength tests were conducted for all mix designs. These tests were conducted on cubes of 100 mm, according to SANS 5860, as described by Owens and Fulton (2009) in chapter seven of Fulton's Concrete Technology. The strength tests served the purpose of tracking the trend of strength development, and these results were required as input parameters in the finite element analysis of Case I.

4.2.1 COMPRESSIVE STRENGTH

The compressive strength test was conducted with an automatic compression machine at the loading rate of 150 kN/min. The cubes were tested at the following ages: 1, 3, 5, 7, 14, 21, 28 and 56th day respectively, after casting. As per the SANS standard, the cubes were tested in saturated surface dry condition and the values presented are based on the average of three (3). The results of the compressive strength test are presented in Table 4.1. Figure 4.1 and 4.2, also present the compressive strength test results as a bar chart and strength development curves, respectively. The error bars in Figure 4.1 indicate the confidence interval (95.5%) and are based on the average values ± two (2) times the standard deviation, assuming normal distribution. Mix MK-30 obtained the highest compressive strength of all mix designs from the 14th day onward. In descending order, the results of the 56-day strength are Mix MK-30, Mix SF-10, Mix 100% RHPC, Mix GGBS-50 and Mix FA-30. The 56-day compressive strengths of Mix MK-30 and Mix SF-10 were 22.3 and 9.1%, respectively, more than the control (Mix 100% RHPC). While Mix FA-30 and Mix GGBS-50 were 13.3 and 9.8%, respectively, less than the control.

Mix 100% RHPC (control) exhibited the highest early strength up to the seventh (7th) day, after which the rate of strength development began to decline. Silica fume and metakaolin are highly

reactive pozzolans and usually exhibit rapid early strength development because of their extreme fineness. However, the rate of early strength development of Mix SF-10 and Mix MK-30 was slower than the control, particularly Mix SF-10, which exhibited lower strength than the control up to the 21st day. The slow strength development was undoubtedly due to the particles size of the silica fume and the replacement level of the metakaolin. The particle size gradation of silica fume is an important factor controlling its contribution to the mechanical and durability properties of concrete. Silica fume usually has 95% of its particles finer than 1µm (Siddique and Khan, 2011; Siddique, 2011). However, from the particles size analysis presented in Section 3.3.1.4, the silica fume used had only 64.4% of its particles finer than 1µm. It is worth noting that fineness is one of the major properties contributing to the reactivity of pozzolanic material. The finer the material, the more reactive it is, thus the contribution to higher early strength. For Mix MK-30, the slow strength development is attributed to the replacement level. At 30% replacement level, metakaolin-based concrete will usually produce lower strength than Portland cement concrete up to the 7-day (Vu et at., 2001; Sabir et al., 2001). Although superplasticiser may have some retarding effects, this effect was ruled out as the brand used has accelerating effect.

Mix FA-30 and Mix GGBS-50 were the least in terms of strength development, with Mix GGBS-50 being the slowest regarding early strength development. The slow rate of strength development observed in Mix FA-30 and Mix GGBS-50 is typical of these materials. These materials are far less reactive than silica fume or metakaolin because of the small surface area they possess. Consequently, the replacement of the Portland cement with less reactive pozzolanic material generally results in slower strength development. Although fly ash is finer than blast-furnace slag, the slowest rate of strength development shown by Mix GGBS-50 is mainly due to the replacement level. At the same level of replacement, ground granulated blast-furnace slag blended concrete usually exhibit higher strength than fly ash concrete at all ages because of its dual properties (latent hydraulic and pozzolanic). Despite having the slowest early strength development, Mix GGBS-50 exhibited higher 56-day strength than Mix FA-30.

Table 4. 1 Results of Compressive Strength Test

AGE TESTED	STRENGTH (MPa)				
	100% RHPC	FA-30	GGBS-50	SF-10	MK-30
Day-1	8.8 (0.25)	3.6 (0.05)	3.6 (0.06)	6.0 (0.15)	6.9 (0.24)
Day-3	22.8 (0.18)	13.7 (0.21)	9.3 (0.08)	19.9 (0.14)	20.4 (0.25)
Day-7	32.5 (0.18)	20.1 (0.27)	14.7 (0.19)	27.7 (0.07)	31.9 (0.11)
Day-14	36.8 (0.21)	26.0 (0.07)	20.8 (0.25)	33.9 (0.12)	39.6 (0.03)
Day-21	38.9 (0.14)	29.5 (0.21)	25.3 (0.33)	37.9 (0.14)	44.9 (0.04)
Day-28	39.8 (0.21)	31.6 (0.34)	28.6 (0.07)	40.5 (0.24)	47.6 (0.03)
Day-56	43.0 (0.17)	37.3 (0.38)	38.8 (0.14)	46.9 (0.09)	52.6 (0.08)

( ) Standard Deviation

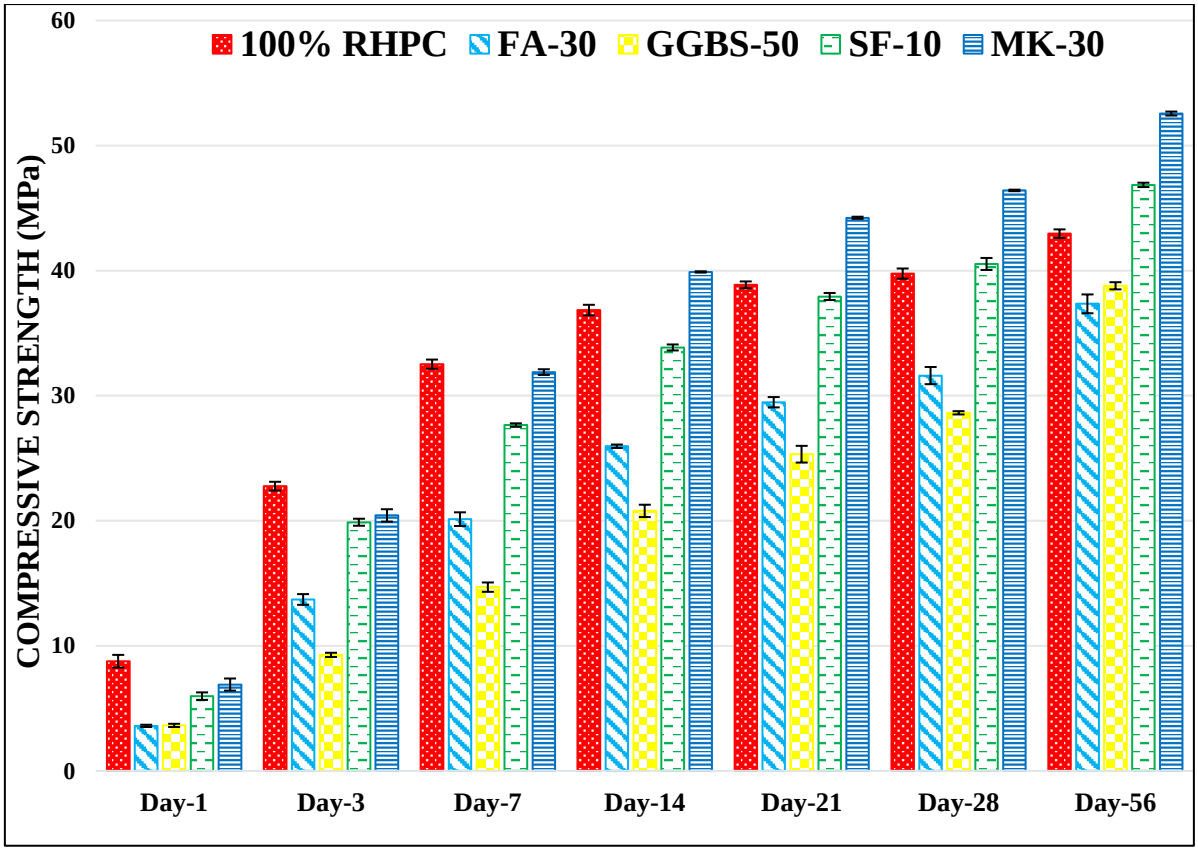

Figure 4. 1 Results of Compressive Strength Test

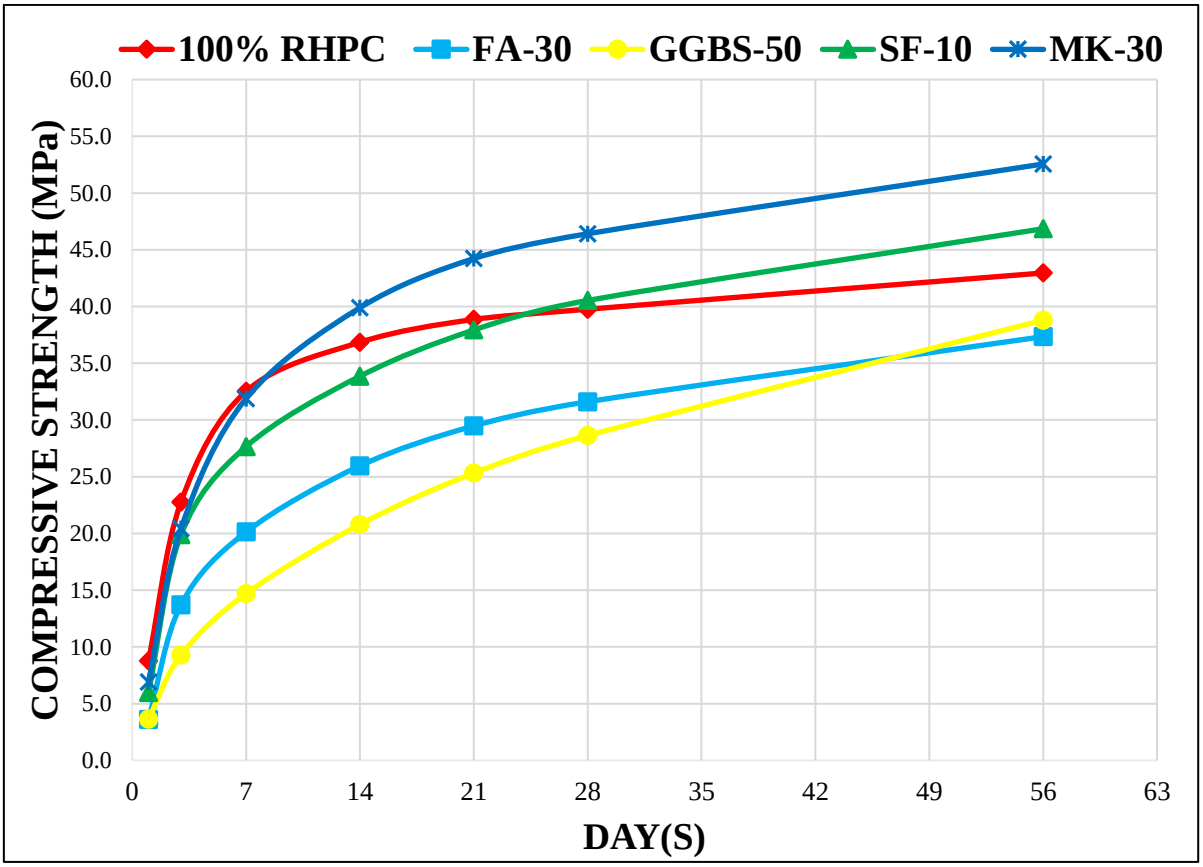

Figure 4. 2 Compressive Strength Development Curves

4.2.2 TENSILE STRENGTH

The tensile strength was determined indirectly by splitting cubes in the diagonal position with a compression machine. As shown in Figure 4.3, the compressive force was applied diagonally thus causing splitting along the plane of the applied load. Although this method is unpopular, it offers numerous advantages especially the almost constant maximum stress in the plane of loading (Ince, 2012; Ince et al., 2015). The cubes were of the same dimension as those used in the compression test. Unlike the compressive strength test, the splitting tensile test was conducted only on the 28th and 56th day after casting. The results of the tensile strength follow the same sequence of the compressive strength and are presented in Table 4.2 and Figure 4.4. The error bars in Figure 4.4 indicate the confidence interval (95.5%) and are based on the average values ± two (2) times the standard deviation, assuming normal distribution.

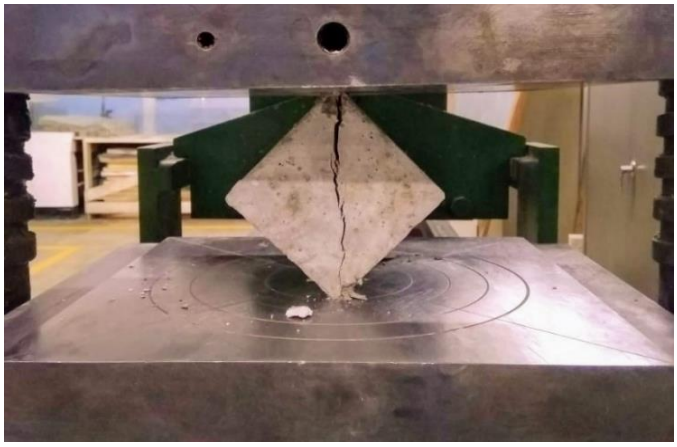

Figure 4. 3 Schematic of Splitting Cube Tensile Test

Table 4. 2 Results of Tensile Strength Test

AGE TESTED	STRENGTH (MPa)				
	100% RHPC	FA-30	GGBS-50	SF-10	MK-30
Day-28	3.9 (0.21)	3.4 (0.30)	3.0 (0.20)	3.6 (0.29)	4.1 (0.17)
Day-56	4.4 (0.16)	3.9 (0.19)	4.1 (0.22)	4.6 (0.16)	4.9 (0.10)

( ) Standard Deviation

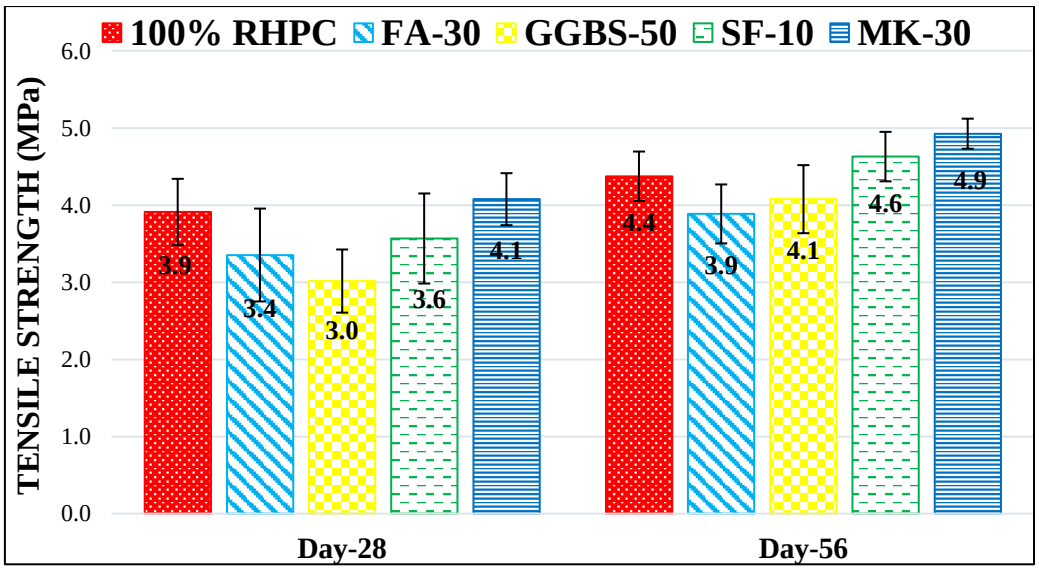

Figure 4. 4 Results of Tensile Strength Test

4.3 RESULTS AND DISCUSSIONS OF DURABILITY INDEX TESTS

Most attacks on concrete are due to the ingress of deleterious substances. The durability of concrete directly depends on the ease with which fluids or ions enter and move through its pore's structures (Sabir et al., 1998). Thus, the less porous or impermeable a concrete, the more durable it is.

Given the above, durability index tests were conducted to evaluate the specimens' resistance to penetration and conductivity. As stated in Section 3.7, three tests per index were conducted, and each test consisted of four (4) samples. As recommended by the Durability Index Testing Procedure Manual, the data analysis was done with the aided of the durability indexes spreadsheet jointly developed by the University of Cape Town and the University of the Witwatersrand to perform the required calculations. The summary of these durability indexes are presented below, and details about the input data and calculations (spreadsheets) are presented in Appendix B. The standard deviation presented here are based on the three tests per index, and the error bars indicate the confidence interval (95.5%) and are based on the average of the three tests ± two (2) times the standard deviation, assuming normal distribution. The statistical analysis of each test is found in Appendix B. Since the durability index tests began immediately after 28 days of water curing, the results presented are considered for the age of 28-day.

4.3.1 OXYGEN PERMEABILITY INDEX (OPI)

The summary of the OPI results is presented in Table 4.3 and Figure 4.5. Mix MK-30 showed the highest resistance to oxygen permeation followed by Mix GGBS-50, Mix FA-30, Mix 100% RHPC and Mix SF-10. The performance Mix MK-30 is attributed to the rapid rate of maturity (rate of consumption of calcium hydroxide) and the high aluminate content that results in the formation of C-S-H and C-A-S-H gels, respectively, leading to finer poses and denser microstructures. While Mix GGBS-50 performance is attributed to the dual nature of blast-furnace slag, which usually outperformed fly ash even at the same replacement level.

Pozzolans are known for improving the microstructural properties of concrete including the resistance to gas permeation. However, the Mix SF-10 underperformed than the control (Mix 100% RHPC). The poor performance of Mix SF-10 can mostly be ascribed to the particles size distribution of the silica fume, as mentioned in Section 4.2.1. The effectiveness of silica fume in concrete is controlled by its fineness.

Table 4. 3 Oxygen Permeability Index (OPI) of the Mixes

OXYGEN PERMEABILITY INDEX (OPI)					
MIX	**Test-1**	**Test-2**	**Test-3**	**Average**	**SD**
100% RHPC	10.09	10.12	10.18	10.13	0.046
FA-30	10.19	10.12	10.15	10.15	0.035
GGBS-50	10.27	10.25	10.19	10.24	0.042
SF-10	10.09	9.99	9.95	10.01	0.072
MK-30	10.42	10.36	10.35	10.38	0.038

SD (Standard Deviation)

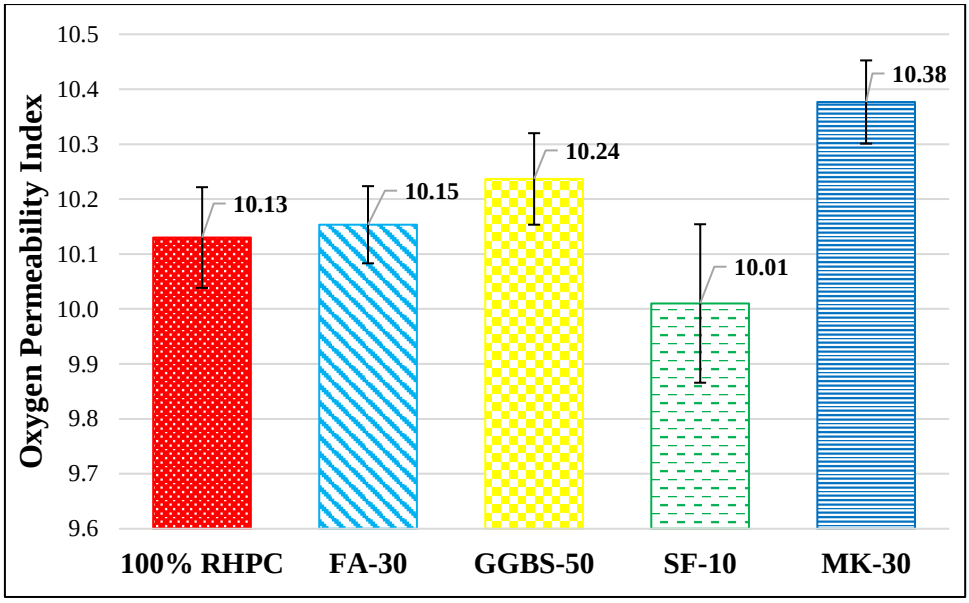

Figure 4. 5 Oxygen Permeability Index (OPI) of the Mixes

4.3.2 WATER SORPTIVITY INDEX AND POROSITY

Results of the water sorptivity index followed a different trend than those of the oxygen permeability. Samples of Mix SF-10 exhibited the highest resistance to water absorption, followed by Mix MK-30, Mix GGBS-50, Mix 100% RHPC and Mix FA-30. The lowest water absorption shown by Mix SF-10 is typical of silica fume and is one of the most reputable properties of silica fume-based concrete in terms of durability. Apart from enhancing mechanical properties, the presence of silica fume in concrete significantly reduces the concrete's ability to absorb water resulting from the pores-size refinement and mainly the filler effects that block the pores, thereby, increasing the concrete's resistance to absorb water (Siddique and Khan, 2011). Mix MK-30 and Mix GGBS-50 performed as expected, and the difference between the two may seem negligible but its substantial. Samples of Mix FA-30 showed the lowest resistance to water absorption. The poor performance of Mix FA-30 is probably due to the replacement level and the slow reactivity of fly ash. Blast-furnace slag is also a slow reacting pozzolan and replaced a higher percentage of the Portland cement than fly ash, but Mix GGBS-50 exhibited better resistance than Mix FA-30. The performance of Mix GGBS-50 is ascribed to its dual nature: latent hydraulic and pozzolanic. The summary of the water sorptivity results is presented in Table 4.4 and Figure 4.6.

Table 4. 4 Water Sorptivity Index (WSI) of the Mixes

WATER SORPTIVITY INDEX ($mm/hr^{0.5}$)					
MIX	**Test-1**	**Test-2**	**Test-3**	**Average**	**SD**
100% RHPC	5.53	5.80	6.18	5.84	0.33
FA-30	7.93	7.56	6.88	7.46	0.53
GGBS-50	5.26	4.81	4.93	5.00	0.23
SF-10	4.39	3.90	3.82	4.04	0.31
MK-30	5.54	4.64	4.75	4.98	0.49

SD (Standard Deviation)

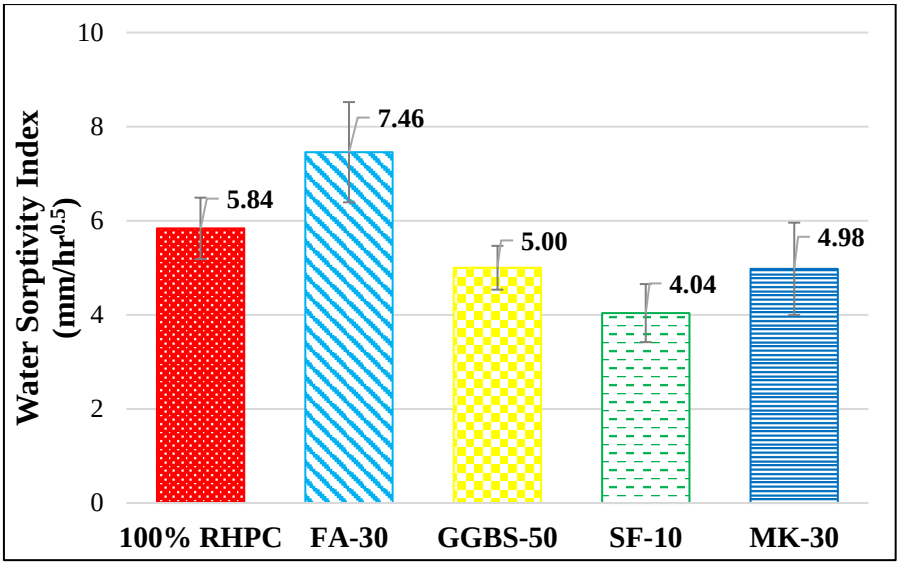

Figure 4. 6 Water Sorptivity Index (WSI) for the Mixes

The porosity results showed an unexpected trend. Samples of Mix SF-10 exhibited the highest porosity, performing less than expected while samples of Mix MK-30 exhibited the lowest porosity. In ascending order, the porosity results are Mix MK-30, Mix GGBS-50, Mix 100% RHPC, Mix FA-30 and Mix SF-10. The high porosity of Mix SF-10 could be the reason for its poor performance exhibited in the oxygen permeability index test. The trend of this porosity results was verified by those obtained from the chloride conductivity index test. The summary of the porosity results is presented in Table 4.5 and Figure 4.7.

Table 4. 5 Porosity of the Mixes

POROSITY (%)					
MIX	**Test-1**	**Test-2**	**Test-3**	**Average**	**SD**
100% RHPC	12.00	12.80	11.66	12.15	0.59
FA-30	13.38	13.80	14.03	13.74	0.33
GGBS-50	11.84	12.04	12.13	12.00	0.15
SF-10	14.05	14.07	13.64	13.92	0.24
MK-30	10.60	9.88	9.66	10.05	0.49

SD (Standard Deviation)

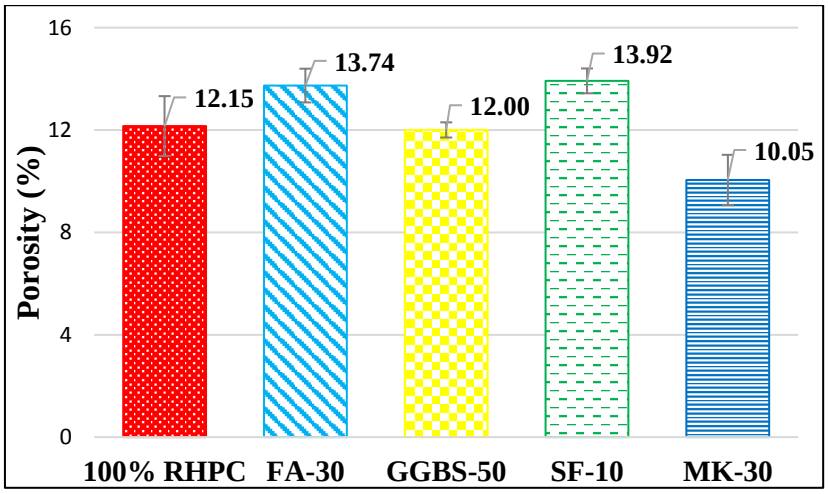

Figure 4. 7 Porosity of the Mixes

4.3.3 CHLORIDE CONDUCTIVITY INDEX (CCI)

Samples of Mix MK-30 showed the highest resistance to chloride conduction (lowest CCI value), followed by Mix GGBS-50, Mix SF-10, Mix 100% RHPC and Mix FA-30. Mix FA-30 showed the lowest resistance to chloride conduction. This behaviour is distinctive of slow reacting supplementary cementing material like class F fly ash. Research has shown that the diffusivity of chloride in fly ash-based concrete less than 90 day-old is usually higher than those of plain Portland cement concrete.

The results presented here agree with the well-known fact that depending on the age tested, the partial replacement of Portland cement with supplementary cementing materials improved concrete resistance to chloride penetration. The summary of the chloride conductivity test results is presented in Table 4.6 and Figure 4.8. While Table 4.7 and Figure 4.9, present the porosity results obtained from the chloride conductivity test. The porosity results of the CCI test followed the same order as the porosity obtained from the water sorptivity and porosity test, thus, validating the trend. However, it is worth noting that the porosity values presented here are lower than those of the water sorptivity and porosity test. The difference is mainly due to the density of the solutions used in each calculation.

Table 4. 6 Chloride Conductivity Index (CCI) of the Mixes

CHLORIDE CONDUCTIVITY INDEX (mS/cm)					
MIX	**Test-1**	**Test-2**	**Test-3**	**Average**	**SD**
100% RHPC	1.32	1.46	1.38	1.39	0.070
FA-30	1.53	1.46	1.66	1.55	0.101
GGBS-50	0.61	0.57	0.60	0.59	0.021
SF-10	0.93	0.92	0.93	0.93	0.006
MK-30	0.41	0.39	0.41	0.40	0.012

SD (Standard Deviation)

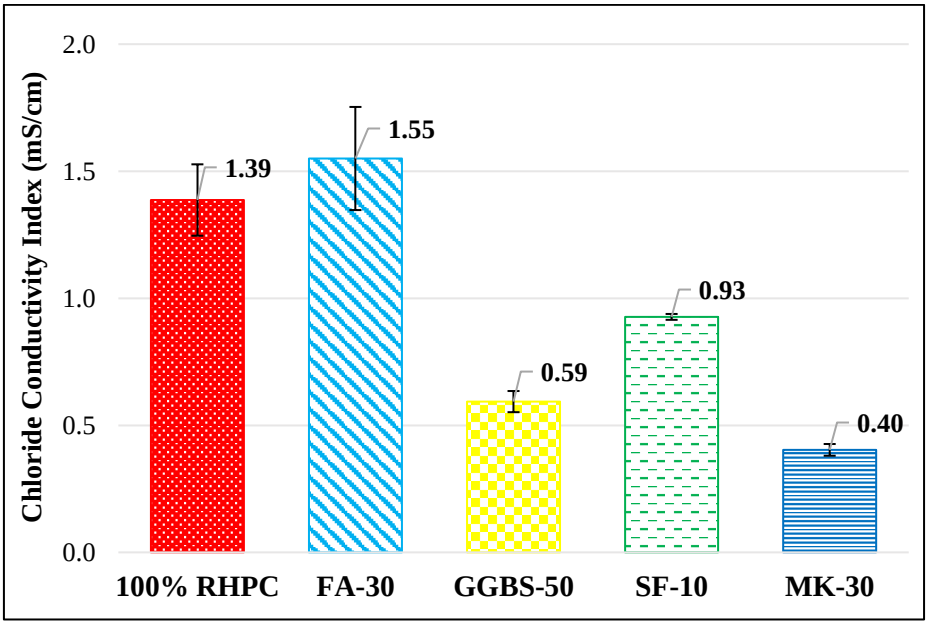

Figure 4. 8 Chloride Conductivity Index (CCI) of the Mixes

Table 4. 7 Porosity for the Mixes Based on CCI Test

POROSITY (%) BASED ON CCI TEST					
MIX	**Test-1**	**Test-2**	**Test-3**	**Average**	**SD**
100% RHPC	4.70	5.07	4.76	4.84	0.20
FA-30	5.30	5.10	5.33	5.24	0.13
GGBS-50	4.60	4.64	4.66	4.63	0.03
SF-10	5.64	5.26	5.76	5.55	0.26
MK-30	4.09	4.08	4.10	4.09	0.01

SD (Standard Deviation)

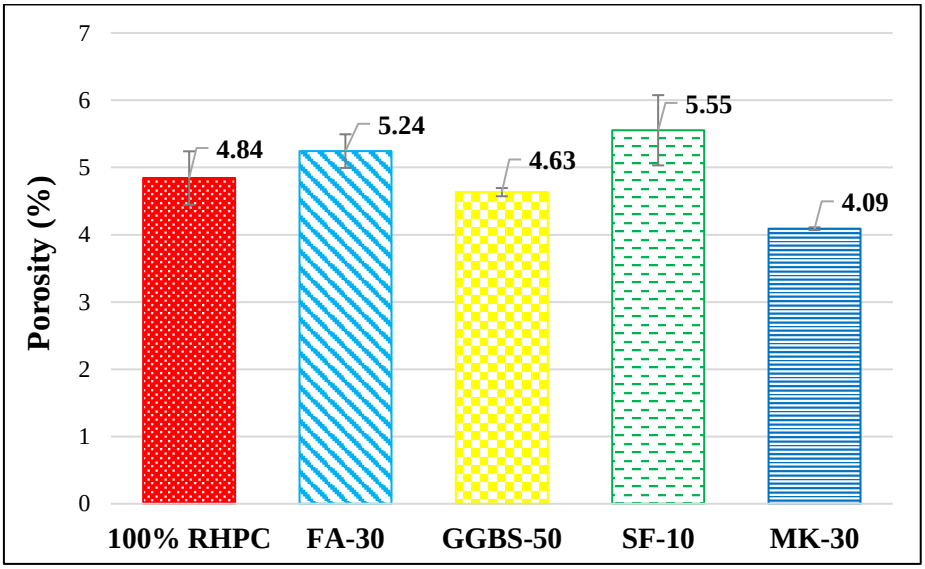

Figure 4. 9 Porosity of the Mixes based on CCI Test

4.4 RESULTS AND DISCUSSIONS OF THE ACCELERATED CORROSION TEST

4.4.1 CYCLIC PONDING PERIOD

The cyclic ponding period lasted for nine (9) cycles, with each cycle consisting of four (4) days of ponding the specimens with solution containing 5% concentration of sodium chloride and three (3) days of drying. The duration of the cyclic ponding period was governed by the bars at 15 mm cover depth in the control specimen (SP-PC100). During this period, the specimens' resistivity and half-cell potential of all bars per specimen were measured.

4.4.1.1 Resistivity Measurement

The electrical resistivity of concrete is an essential factor which can also be used as an indicator of its durability. Given that ions transport electrical charges through the pores in concrete, the measurement of the concrete resistivity directly describes the ease with which the ions move as well as the rate of corrosion reaction or how fast corrosion will propagate. In this regard, the specimens' resistivity was measured and results from the cyclic ponding period are presented in Figure 4.10. The resistivity measurements at Cycle-0, were termed the initial resistivity (IR) while those at Cycle-9 the intermediate resistivity (IMR). As shown in Figure 4.10, the

resistivity of all specimens increased initially with time before decreasing. However, the intermediate resistivities were still higher than the initial resistivity for all specimens. The comparison of the initial resistivity with the intermediate is presented in Figure 4.11. The increase in the resistivity is attributed to the continuation of hydration and pozzolanic reaction of the Portland cement and supplementary cementing materials, respectively. The decrease observed at the end of the initiation period can be attributed to the increase in chloride content within the specimen, thus, increasing the conductivity. Chloride in concrete is hygroscopic, and its presence increases conductivity, thus, reducing the concrete's resistivity. The fluctuations observed in the curves is due to the variation of the moisture content at the time of measurement.

These results agree with the well-known fact that binder type also influences concrete resistivity. The intermediate resistivity of all specimens containing binary binder was higher than the control (SP-PC100). Results of the intermediate resistivity in descending order are SP-MK30, SP-BS50, SP-SF10, SP-FA30 and SP-PC100. SP-MK30 exhibited the highest initial resistivity while SP-BS50 the lowest. Despite having the lowest initial resistivity, the resistivity of SP-BS50 increased sharply and obtained the second highest resistivity from the second cycle onward. It is worth noting that the performance of SP-MK30 and SP-BS50 is strongly linked to the performance of their mixes in the durability index tests. Mix MK-30 and Mix GGBS-50 exhibited the two highest resistance, respectively, against oxygen permeation and chloride conductivity as well as the lowest porosity. Also, the second and third lowest water absorption, respectively, behind Mix SF-10. Likewise, the performance of SP-SF10 having the third highest resistivity is linked to its high resistance against water absorption. As illustrated in Figure 4.12, the results of the resistivity showed a relationship with results of chloride conductivity test of the mix designs. When the intermediate resistivities of the specimens are plotted against the chloride conductivity index of their respective mixes, a linear trend is observed. Details of the measured resistivity are found in Appendix C.

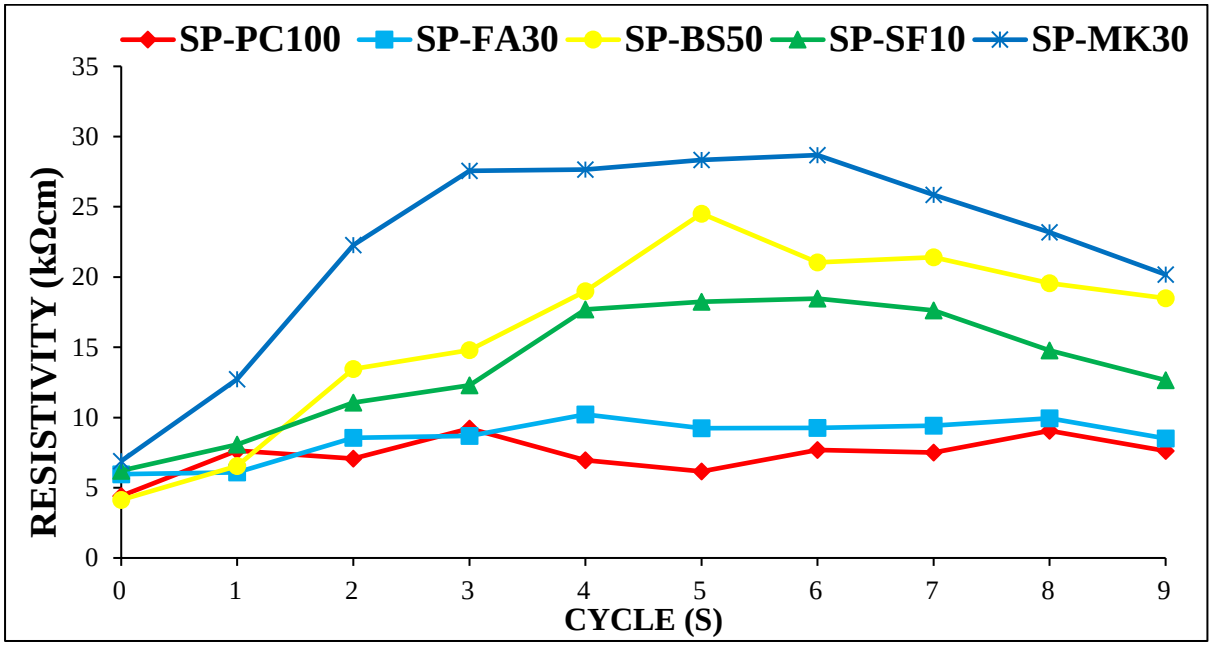

Figure 4. 10 Specimens' Resistivity During the Cyclic Ponding Period

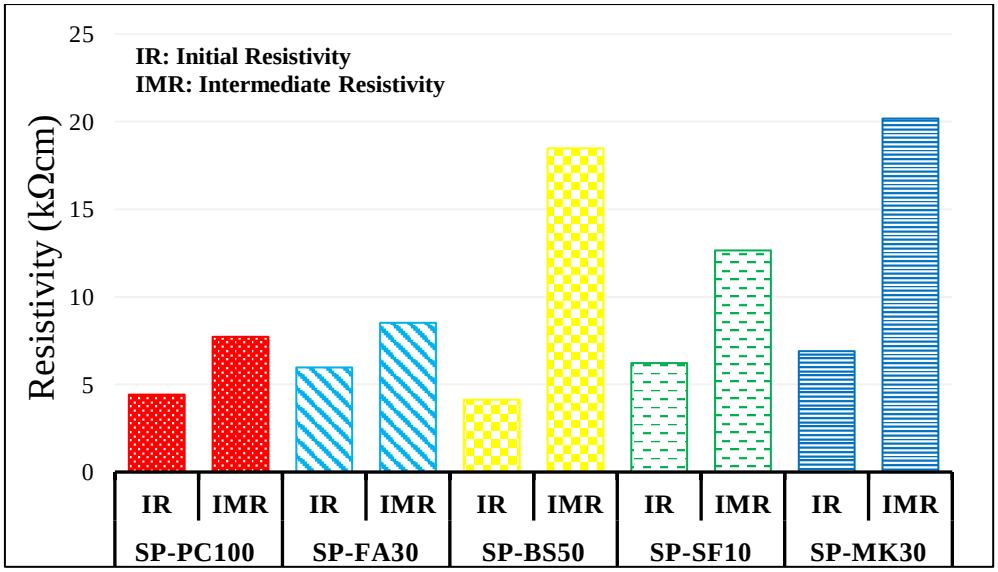

Figure 4. 11 Comparison of the Initial and Intermediate Resistivities

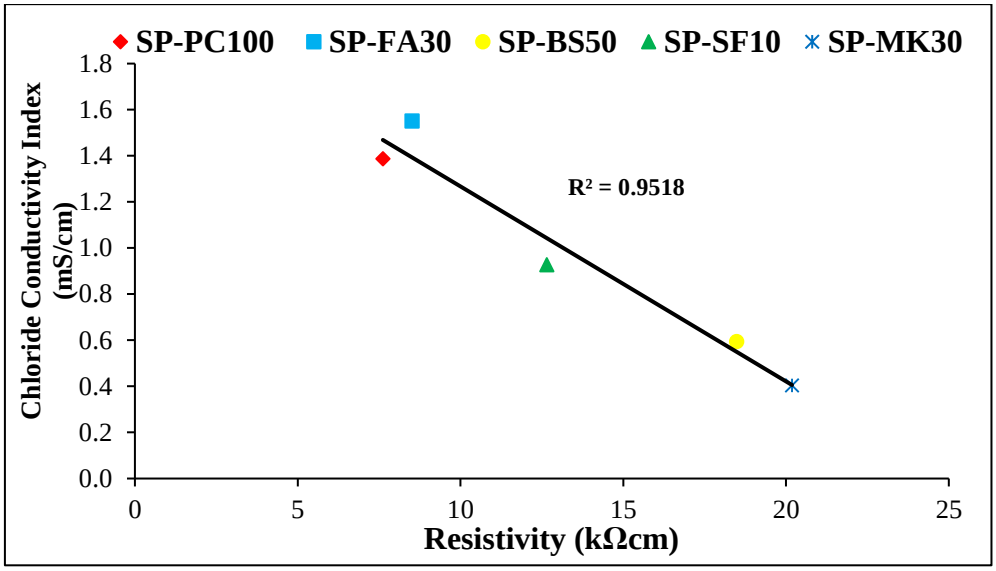

Figure 4. 12 Intermediate Resistivity vs Chloride Conductivity Index

4.4.1.2 Half-cell Potential Measurement

The half-cell potential measurements were taken once per cycle at the same time as the resistivity. The initial readings of the half-cell potential measurements for all bars in all specimens were in the range of -60 to -120 mV CSE, with bars of SP-MK30 having the lowest negative potential and bars of SP-BS50 the highest. These initial values indicate that these bars were in the passive state. As reported in the literature, the passive state of steel in concrete exposed to the atmosphere (unsaturated) is in the range of 50 to -200 mV CSE (Bertolini et al., 2013). Before presenting the results, it is worth noting that the interpretation of half-cell potential readings is not unambiguous since several variables are influencing the readings. Therefore, concluding exclusively from these readings might be misleading. However, effort is made to interpret these readings in conjunction with the durability indexes and the resistivity results.

Results of the half-cell potential measurement are presented per bar in Figure 4.13 to 4.21 and details are presented in Appendix C. The bold horizontal line at -350 mV in these figures is the baseline, at or above, which indicates that 90% probability of active corrosion is ongoing. The last readings recorded showed that all bars at 15 mm cover depth in SP-PC100, SP-FA30, SP-MK30 were above the baseline of 90% probability of active corrosion. Considering the durability indexes of Mix 100% RHPC and the resistivity of SP-PC100 conclusion can be drawn that the half-cell potential reflected the actual state of bars in SP-PC100.

The initial high negative potential displayed by bars in SP-BS50 are typical of Portland cement-slag concrete and have been reported in the literature (Bertolini et al., 2013). Despite the initial high readings, the corrosion potential of all bars in SP-BS50 did not exceed the 90% probability of active corrosion baseline through the entire cyclic ponding period. SP-BS50 and SP-SF10 were the two specimens that had the lowest negative potential at the end of the cyclic ponding period. The measured potential of bars in SP-BS50 are substantiated by the measured resistivity of the specimen and durability indexes of Mix GGBS-50. SP-BS50 exhibited the second higher intermediate resistivity which relates to the performances of Mix GGBS50 in the durability index tests.

At the end of the cyclic ponding period, SP-FA30 had more bars (all bars at 15- and 30-mm cover depth) with potential readings at or above the 90% probability of active corrosion baseline as well as the highest negative potential. The results indicate that SP-FA30 underperformed during the cyclic ponding period. Relating the half-cell potential readings of SP-FA30 to the durability indexes of Mix FA-30, conclusion can be drawn that these readings reflected the actual states of the bars in SP-FA30 as Mix FA-30 exhibited the lowest resistance to water absorption and chloride conductivity. The underperformance of SP-FA30 is attributed to the early age of exposure, the slow reactivity of fly ash and the replacement level. As was discussed in Section 4.3.3, class F fly ash, like the one used in this experiment, is a slow reacting pozzolan and usually, exhibit low resistance to chloride diffusion at age less than 90 days. It is worth noting that these results correlate with those of Ha et al. (2007) who studied the performance resistance of concrete containing fly ash against chloride-induced corrosion and reported that increase in the replacement level results in higher negative potential reading at early age of exposure.

Bars of SP-SF10 had the lowest negative readings at the end of the cyclic ponding period. The low readings are probably due to the outstanding performance of Mix SF-10 in the water sorptivity test. Apart from obtaining the lowest sorptivity index, Mix SF-10 also exhibited good resistance to chloride conduction. These are the most important durability attributes of silica fume-based concrete; higher resistance against water absorption and chloride permeation as the result of pore-size refinement and filler effects.

Bars at 15 mm cover depth in SP-MK30 had readings above the 90% probability of active corrosion baseline as well as higher readings of other bars as compare to SP-SF10 and SP-BS50. Conclusion about the states of these bars cannot be reached giving the excellent performance of Mix MK-30 in the durability index tests as well the highest resistivity exhibited

by SP-MK30. However, one can speculate that the high negative values could be attributed to the limited supply oxygen. Baseline of 90% probability of active corrosion

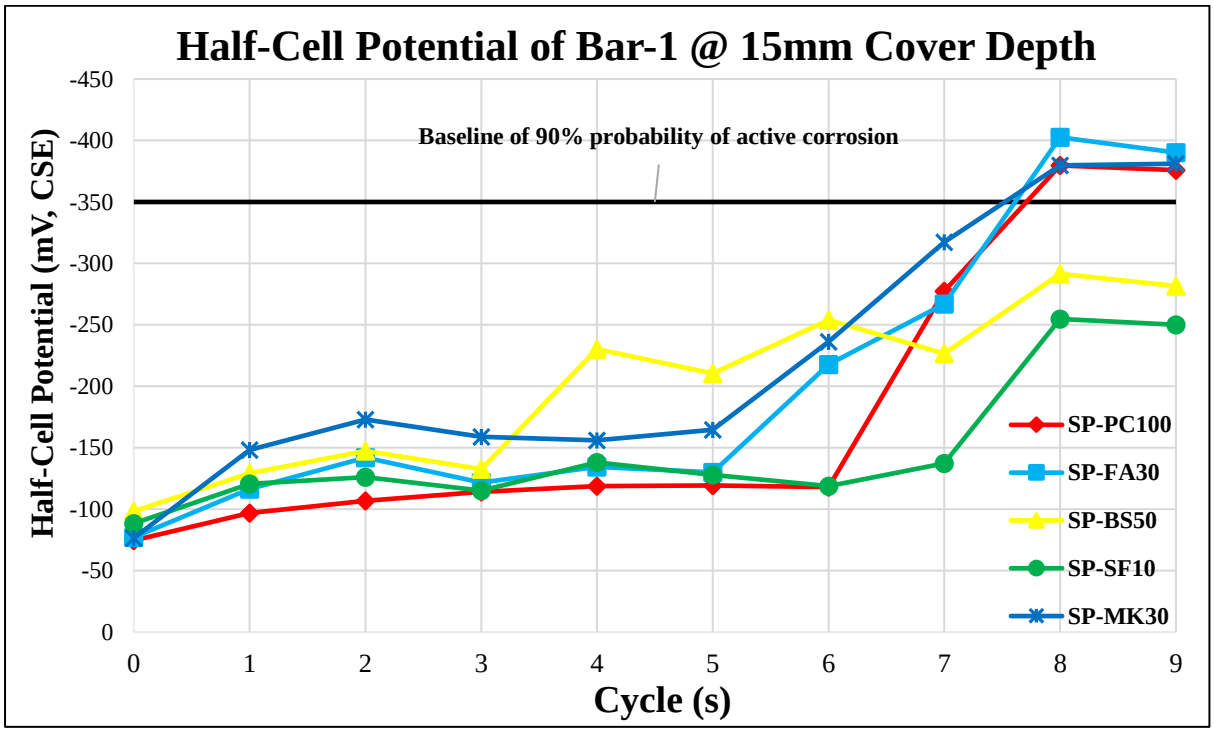

Figure 4. 13 Half-Cell Potential of Bar-1

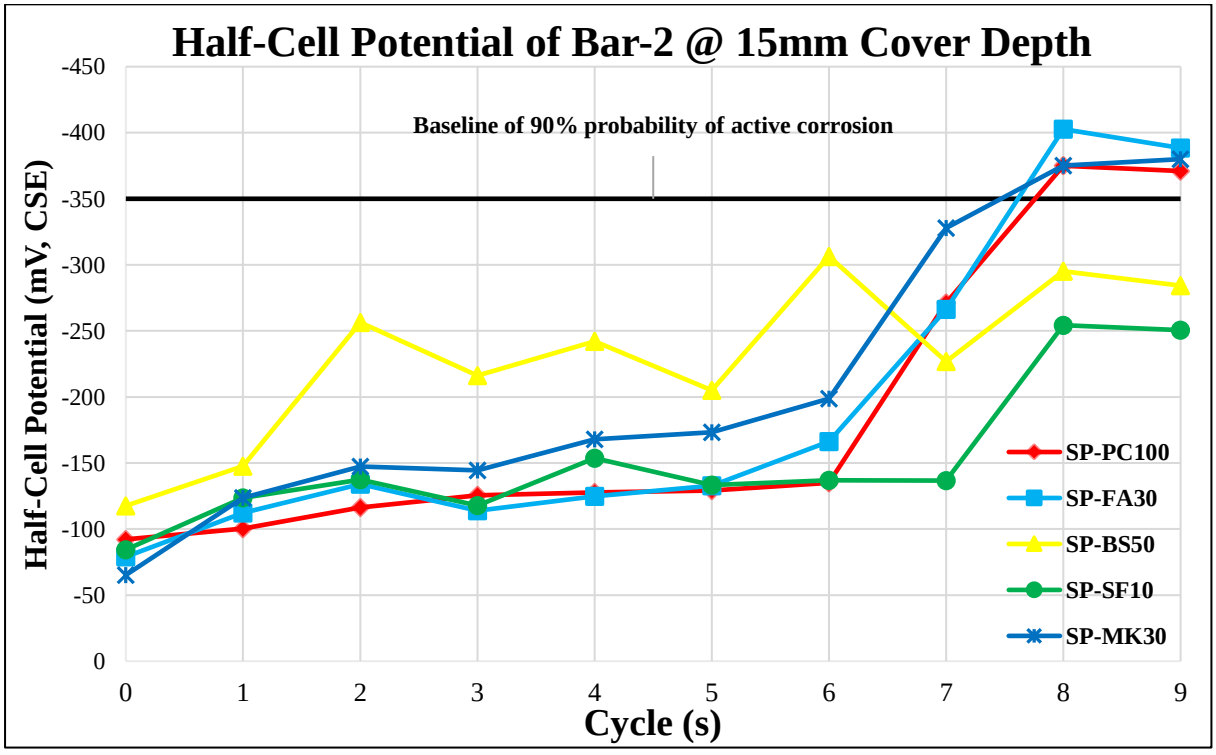

Figure 4. 14 Half-Cell Potential of Bar-2

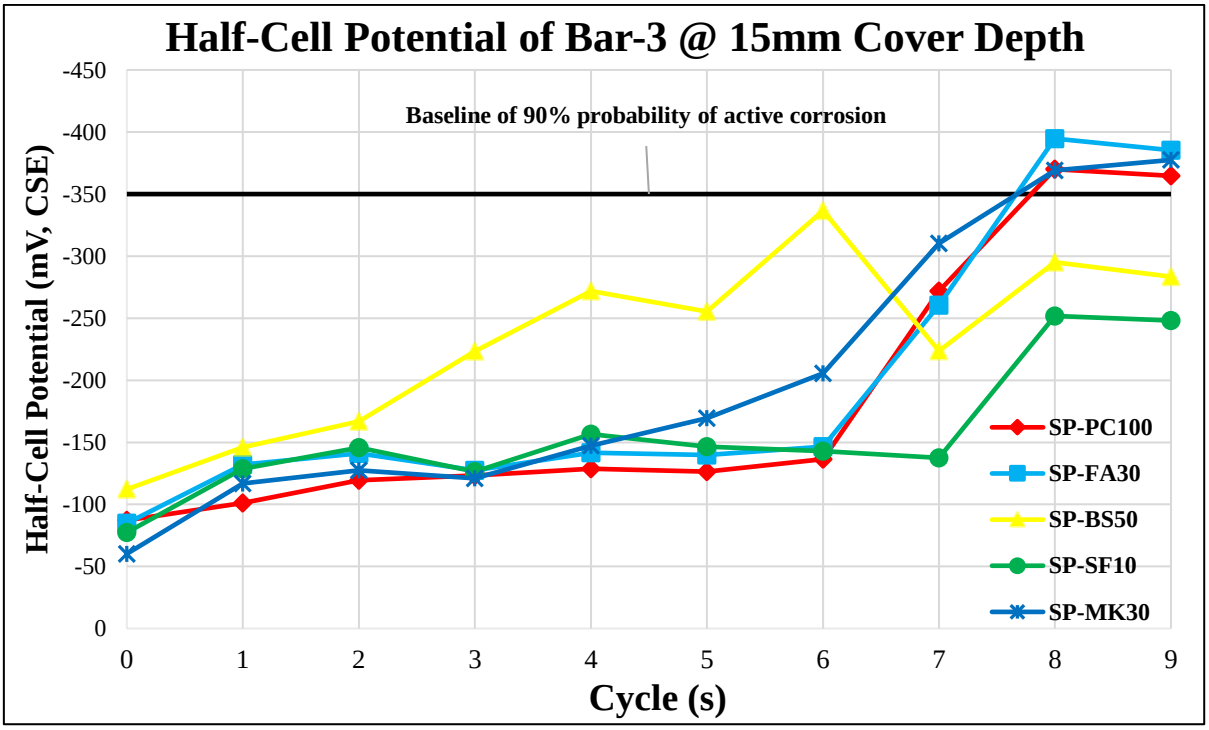

Figure 4. 15 Half-Cell Potential of Bar-3

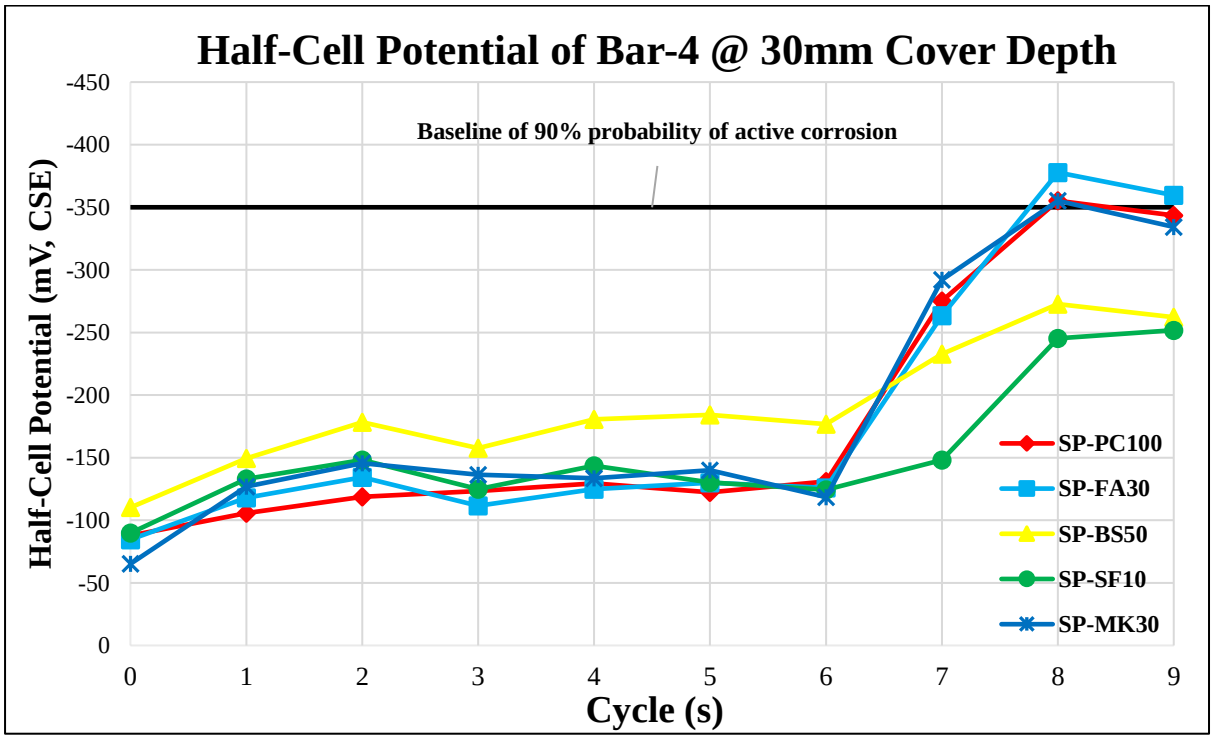

Figure 4. 16 Half-Cell Potential of Bar-4

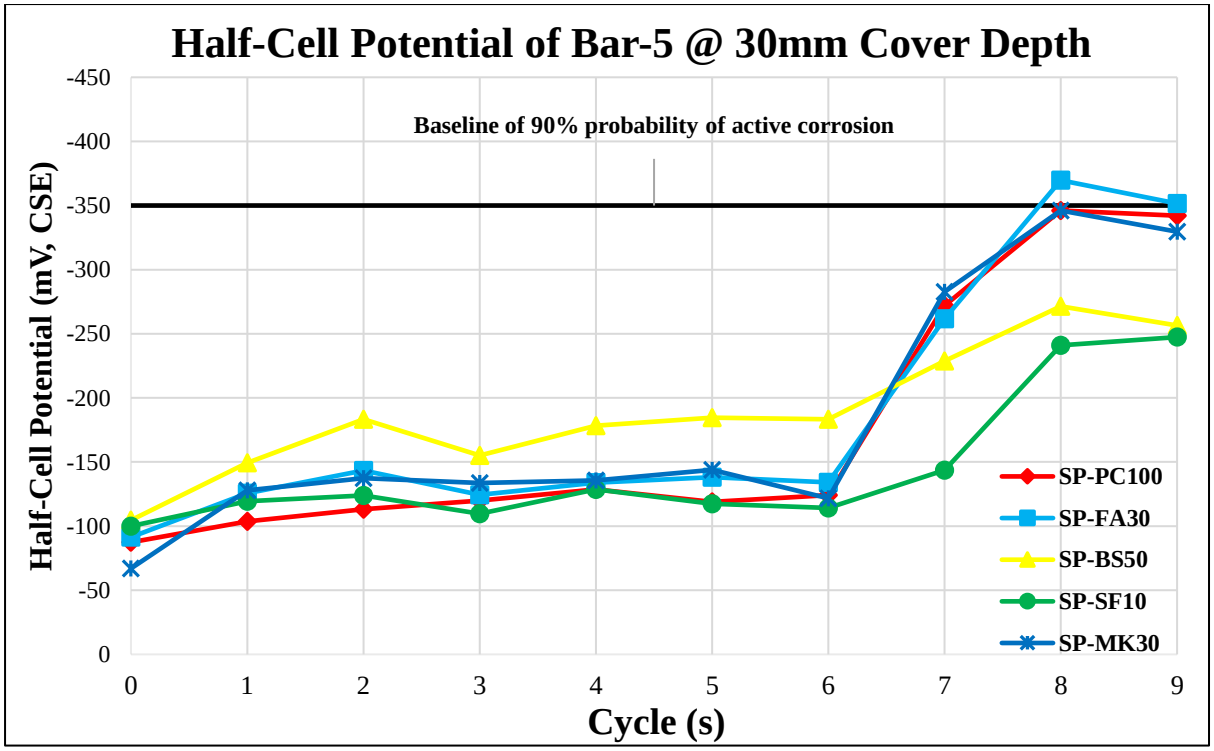

Figure 4. 17 Half-Cell Potential of Bar-5

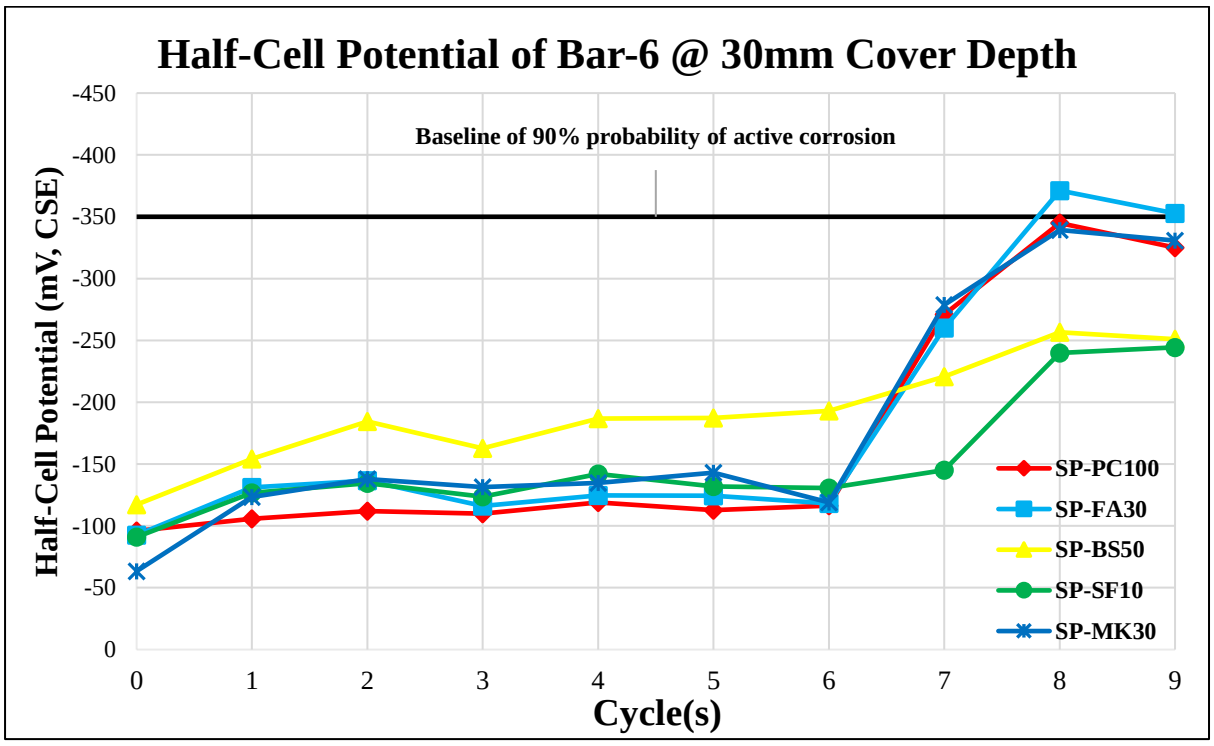

Figure 4. 18 Half-Cell Potential of Bar-6

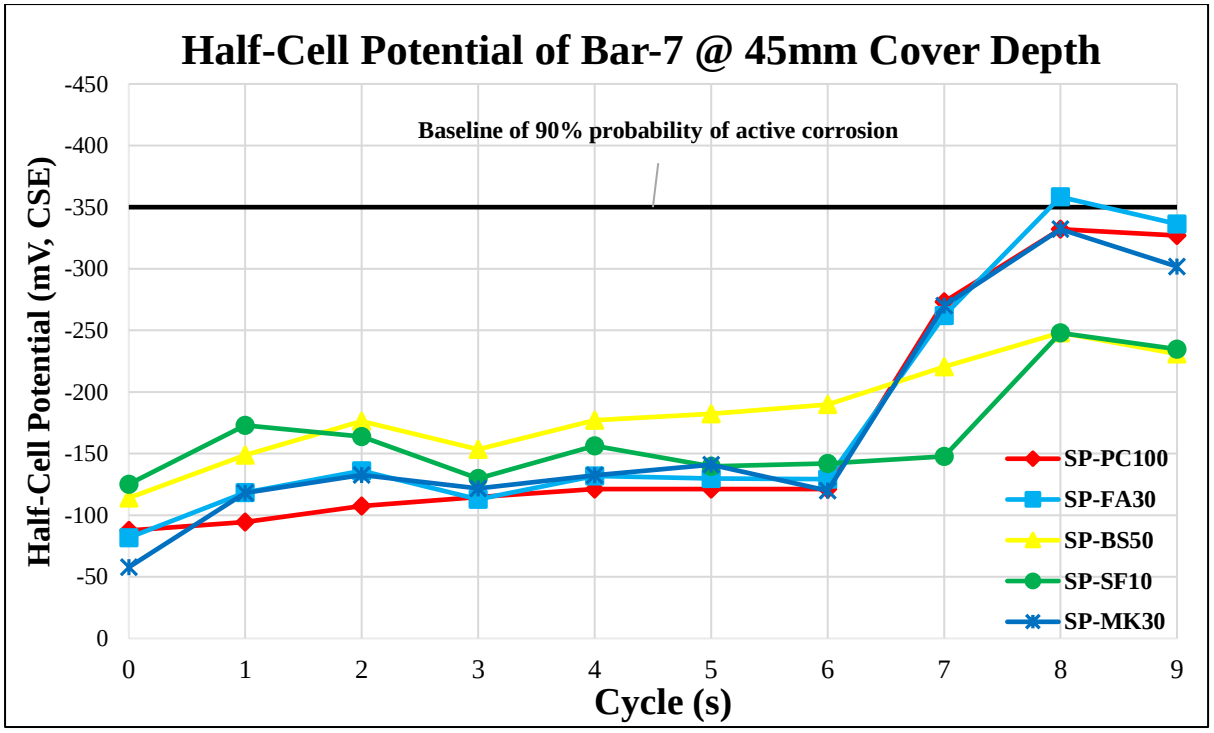

Figure 4. 19 Half-Cell Potential of Bar-7

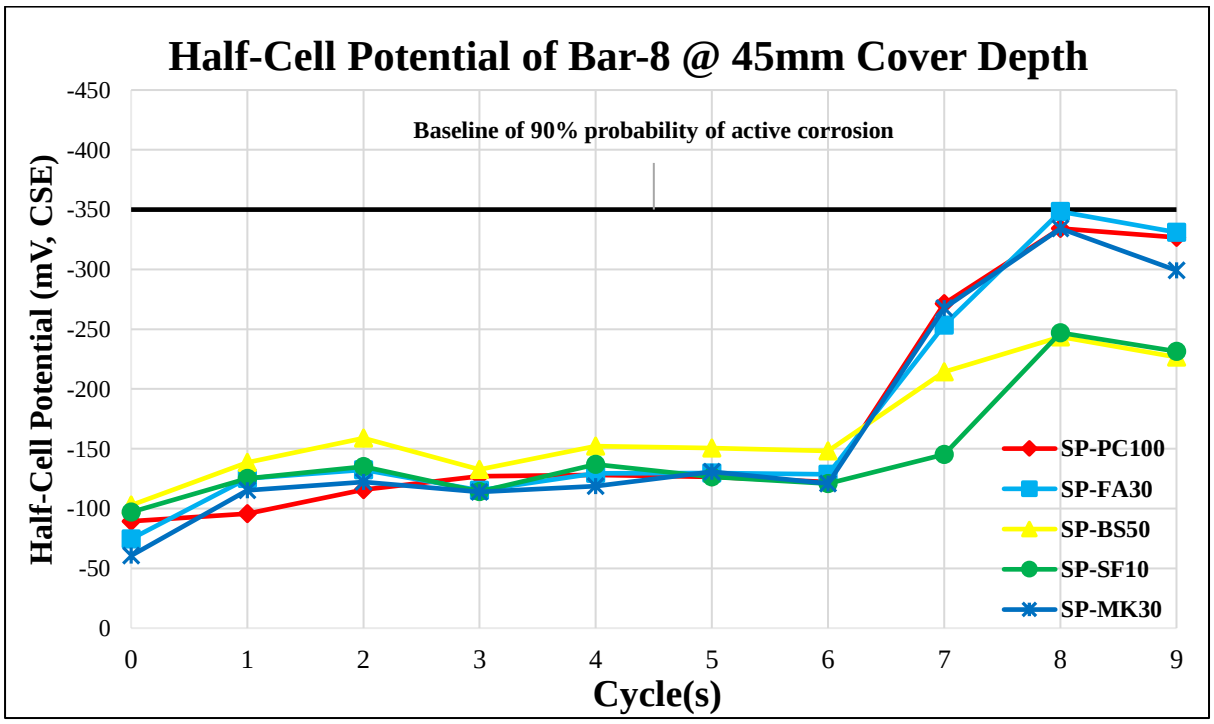

Figure 4. 20 Half-Cell Potential of Bar-8

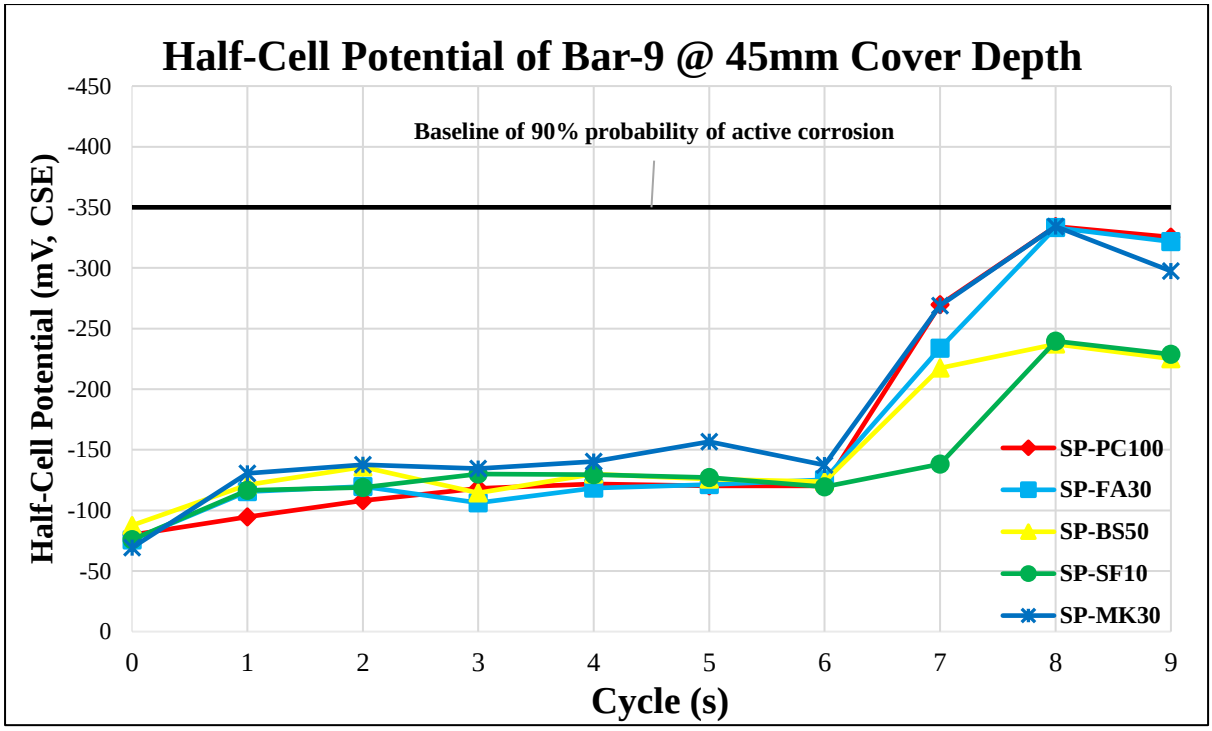

Figure 4. 21 Half-Cell Potential of Bar-9

4.4.2 IMPRESSED CURRENT APPLICATION

After 90% probability of active corrosion was detected in bars at 15 mm cover depth of the control specimen (SP-PC100), direct current was applied to propagate the corrosion. During this period, the applied voltage reaching each bar per specimen was logged across 12-Ohm resistors at an interval of ten (10) minutes. The duration of the impressed current was governed by the control specimen (SP-PC100). After severe structural damage (corrosion-induced cracks) was seen of the control specimen (SP-PC100), the impressed current was terminated. Upon termination, the connections of each bar were checked to identify any disconnection that may have been caused by the salt solution that seeped out of cracked specimen. The ponding surface of the specimens was cleaned, the cracks width measured as well as the specimens' resistivity and half-cell potential of each bar. The rebars were then extracted, cleaned with Clark's solution and gravimetric analysis conducted.

The resistivity and half-cell potential measurement were taken 24 hours after the impressed current was terminated. From the inspection, it was found that the wires connecting Bar-1 to Bar-4 in SP-FA30 and SP-SF10, were disconnected and corroded. The time at which the disconnections occurs is uncertain but could be estimated from the logged voltages. Due to the disconnection, the logged inducing current and mass loss could not be presented per bar as was done with the half-cell potential measurement in Section 4.4.1.2. Presenting the results in that manner would be misleading. Consequently, the results of the logged current and mass loss were presented as the average (mean of the nine bars) per specimen. This approach provides the most efficient means in this case for comparing and evaluating the specimens' resistance. Results from the impressed current application are as follows:

4.4.2.1 Evolution of the Corrosion-Induced Crack and the Crack Pattern

The appearances of visible corrosion-induced cracks were influenced by the specimen's resistivity and within a given specimen, the cover depth. The first visible crack appeared on the specimens in ascending order of the measured intermediate resistivity. The first visible crack was seen on SP-PC100, Bar-1 about 12 hours after the impressed current was applied. Followed by SP-FA30, SP-SF10 and SP-BS50 at 20, 72 and 120 hours, respectively. The first visible crack on SP-FA30, SP-BS50 and SP-SF10 was seen on Bar-3. No visible crack was seen on SP-MK30 up to the time the impressed current was terminated. For those specimens that cracked, the crack first appeared on bars at 15 mm cover depth, and no crack was seen on bars at 45 mm cover depth up to the time the test was terminated. The first crack seen on bars at 30 mm cover depth was on SP-PC100, Bar-5, about 86 hours during the application of the impressed current, then Bar-4 and Bar-6 at 88 and 89 hours, respectively. More cracks and larger crack width were seen on SP-PC100. Cracks appeared not only on the ponding surface but also along the vertical sides (length and width) of the specimens. These cracks tend to propagate parallel to the horizontal plane of the bars, thus, attempting to cause spalling or delamination. These effects were seen at all level of cover depth mostly on SP-PC100 and SP-FA30 and, are shown in Figure 4.22 and 4.23, respectively. The map-out patterns of the corrosion-induced crack on the ponding surface are presented in Figure 4.24 to 4.27. The crack widths were measured at four locations along the exposed length at an interval of 50 mm with the aided of Elcometer crack microscope for those crack widths less than 1.8 mm and with a crack ruler for those greater than 1.8 mm. It must be noted that the map-out patterns of the corrosion-induced cracks are just approximation of the actual crack pattern.

Figure 4. 22 Vertical Sides of SP-PC100

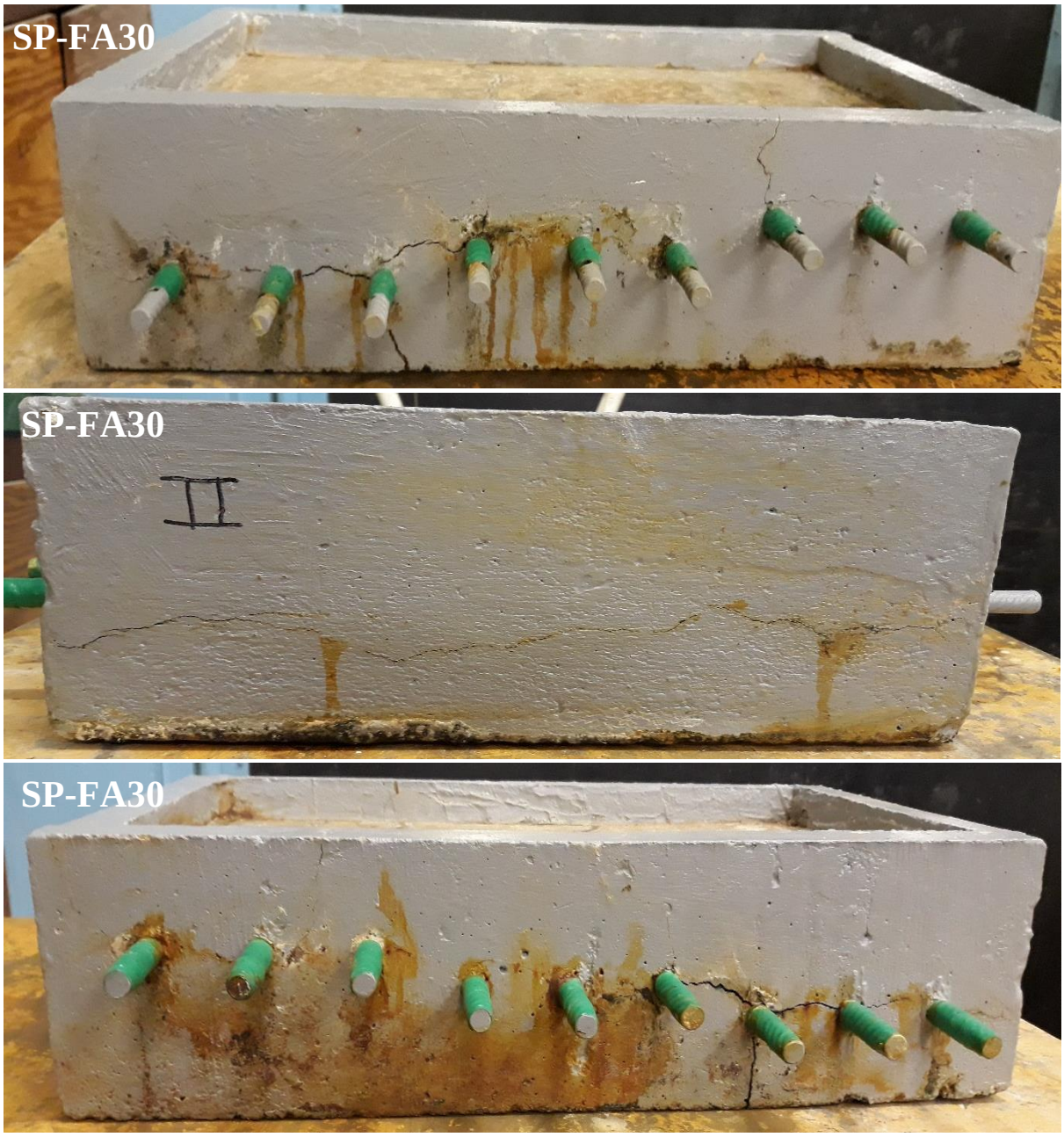

Figure 4. 23 Vertical Sides of SP-FA30

4.4.2.2 Inducing Current

The inducing voltages were logged across 12-Ohm resistors and the current obtained by Ohm's law. The results presented are based on the area under the curve (shaded area as in Figure 4.28 and 4.29) obtained by plotting the current against the time at which the voltages were logged. The average current per specimen and the current per bar within each specimen are presented in Figure 4.30, and Figure 4.31 to 4.35, respectively. The inducing current per bar is also presented along with the mass loss in the gravimetric analysis section. The average current per specimen followed the opposite trend of the specimens' intermediate resistivity; specimens with higher resistivity experienced lower current reaching their bars. SP-PC100 had the highest amount of current reaching its bars followed by SP-FA30, SP-SF10, SP-BS50 and SP-MK30.

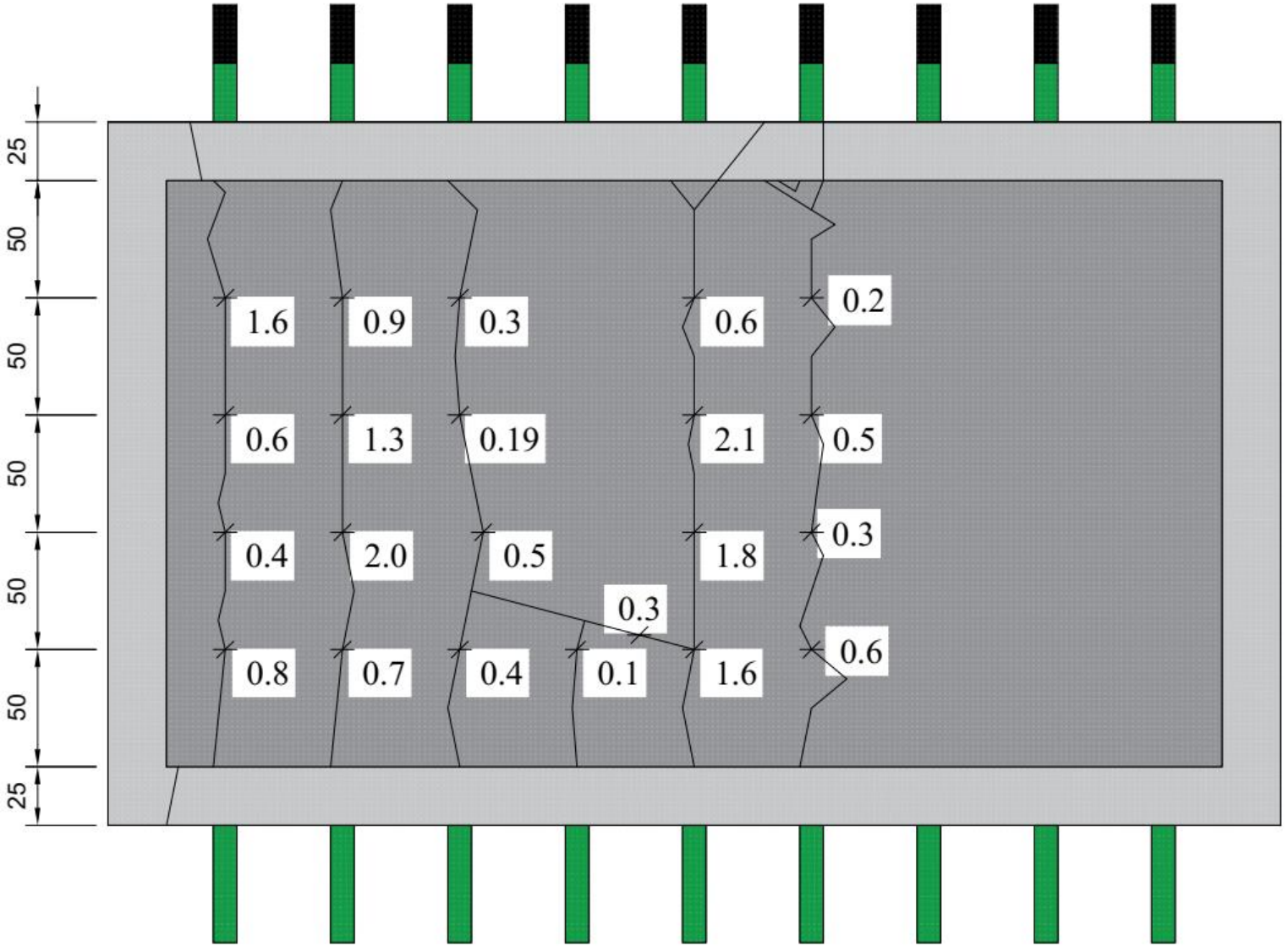

Figure 4. 24 Crack Pattern of SP-PC100

All dimensions in mm

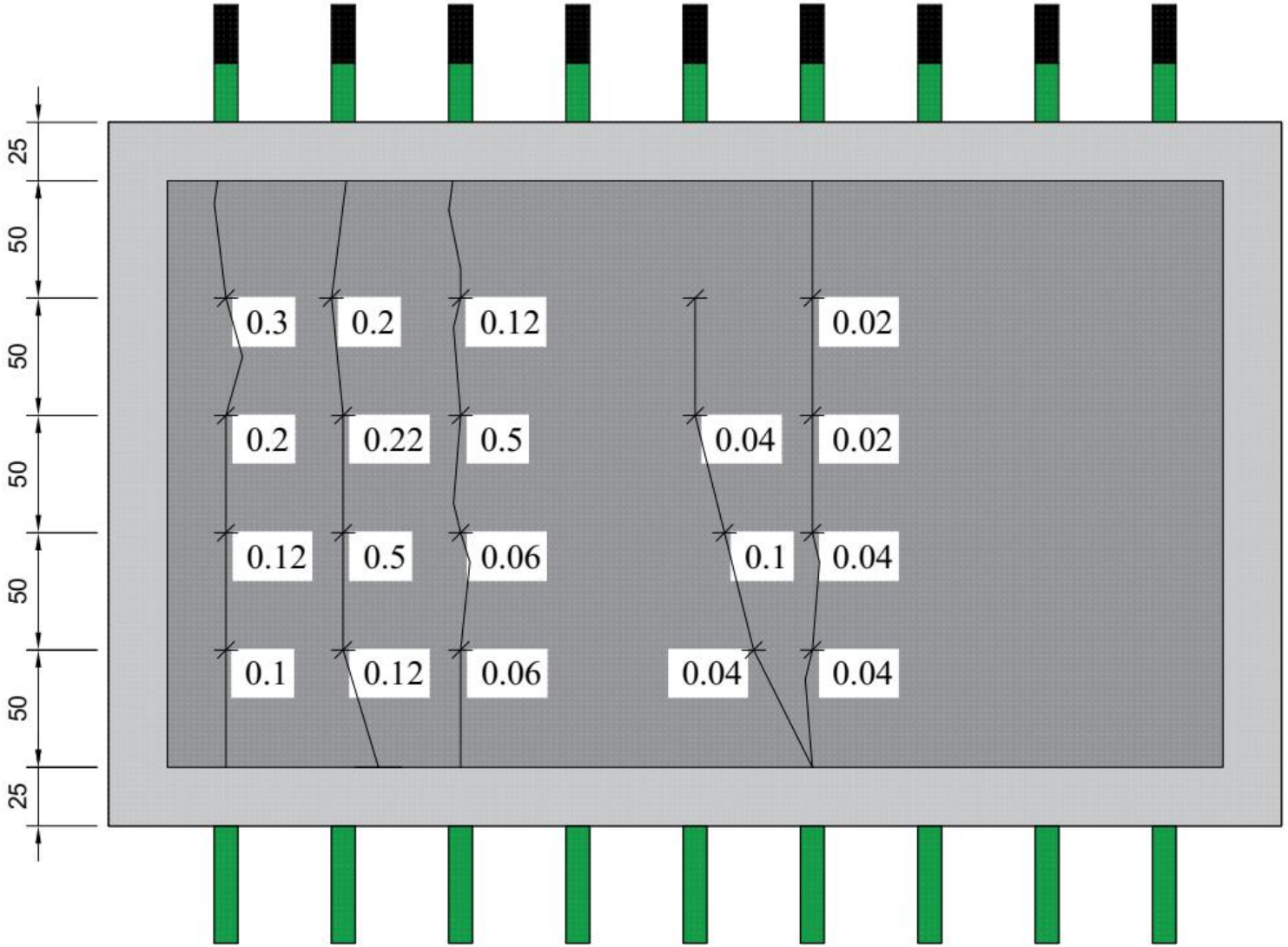

Figure 4. 25 Crack Pattern of SP-FA30

All dimensions in mm

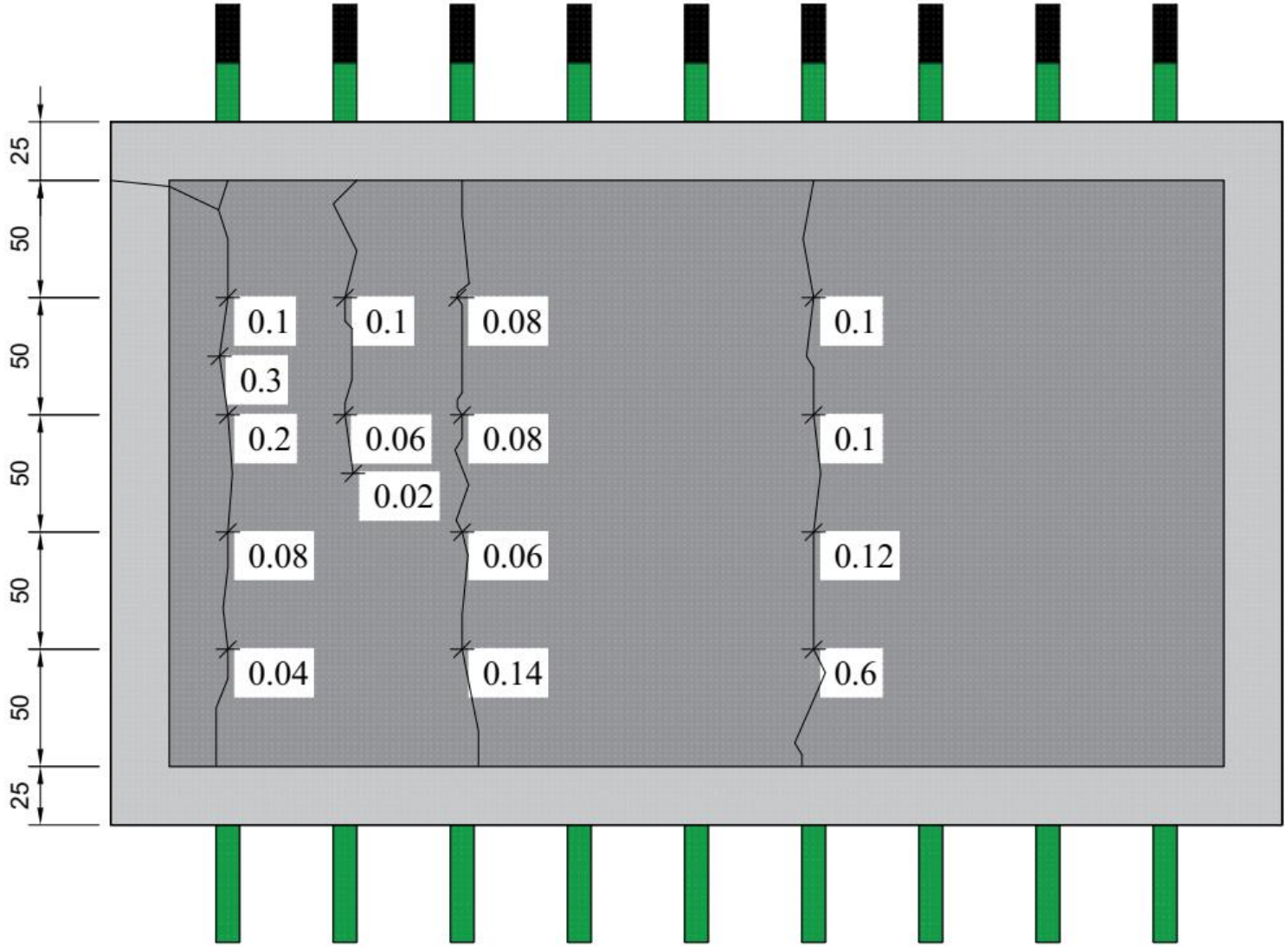

Figure 4. 26 Crack Pattern of SP-BS50 *All dimensions in mm*

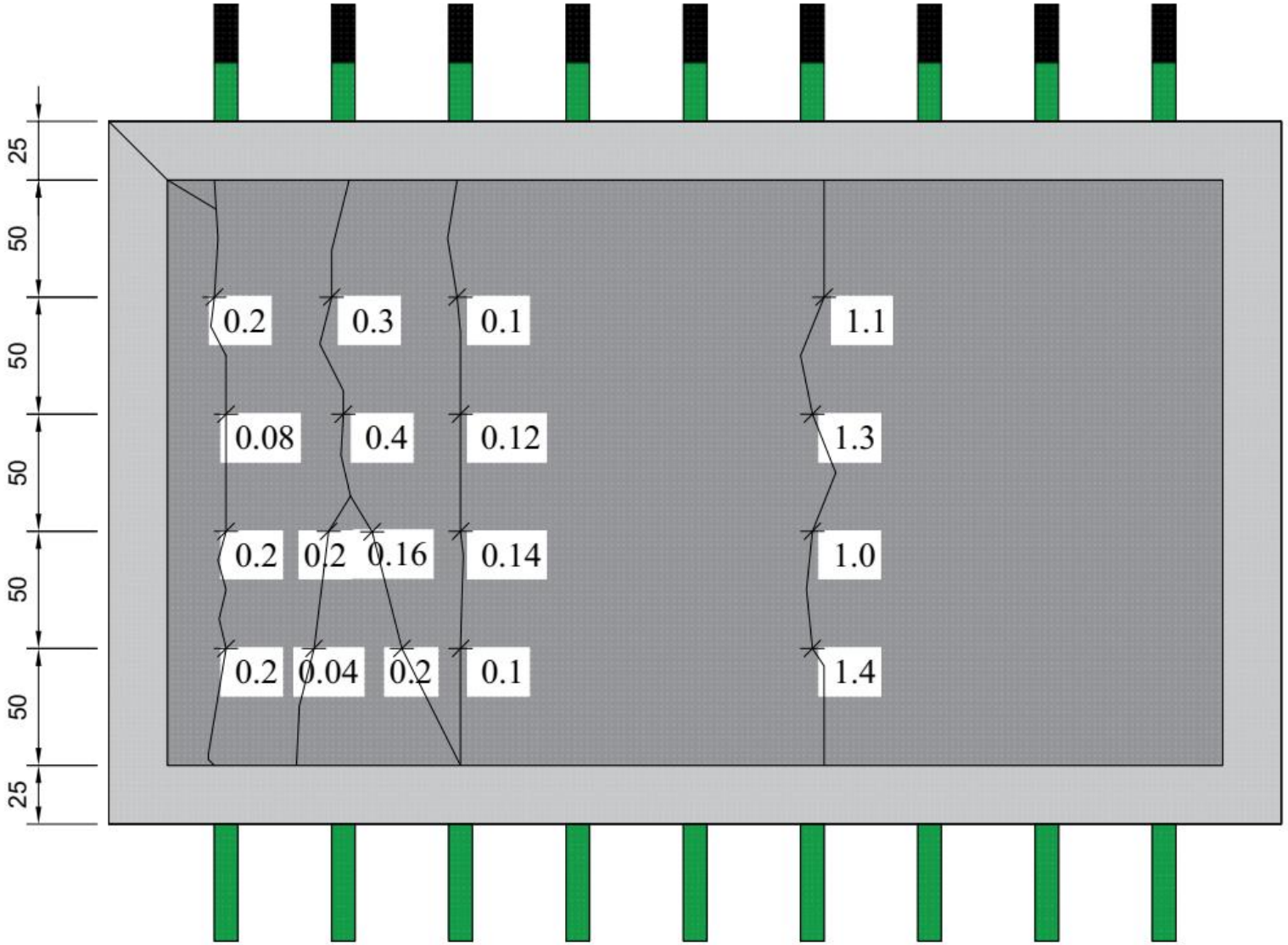

Figure 4. 27 Crack Pattern of SP-SF10

All dimensions in mm

Although SP-FA30 had some bars (Bar-1 to Bar-4) disconnected, the average current was still higher than those of SP-SF10, SP-BS50 and SP-MK30. A similar effect was observed with SP-SF10, the average current was higher than SP-BS50 and SP-MK30.

Except for SP-FA30, the data presented in Figure 4.31 to 4.35 showed that current reaching each bar within a given specimen was influenced by the cover depth which also influenced the resistivity of the specimen. The difference observed in SP-FA30 is due to the disconnection of Bar-1 to Bar-4 which may have happened early. As illustrated in Figure 4.36 (the graph of the inducing current vs the time) the loss in connectivity began as early as the 4th day during the application of the impressed current.

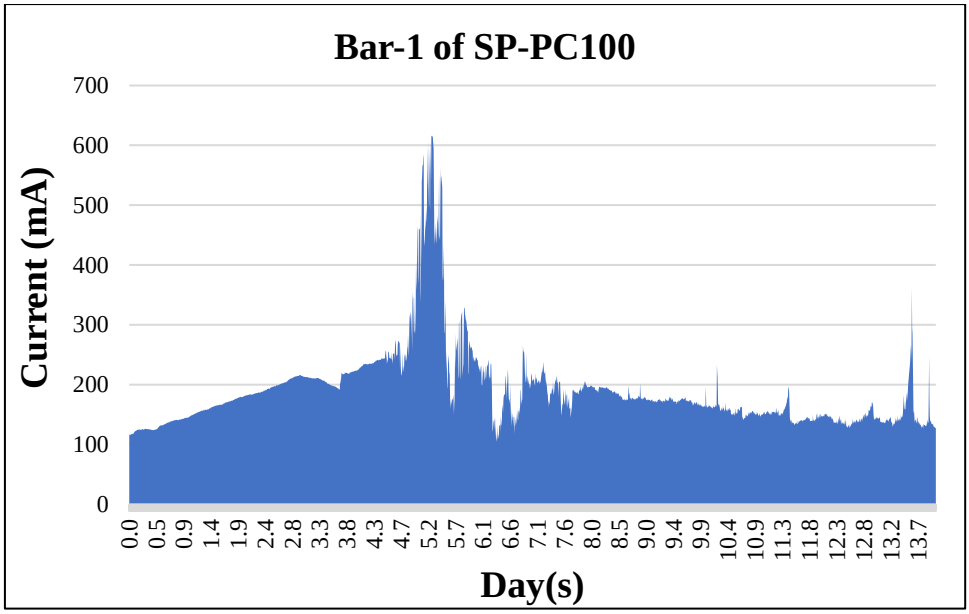

Figure 4. 28 Logged Current of Bar-1 of SP-PC100

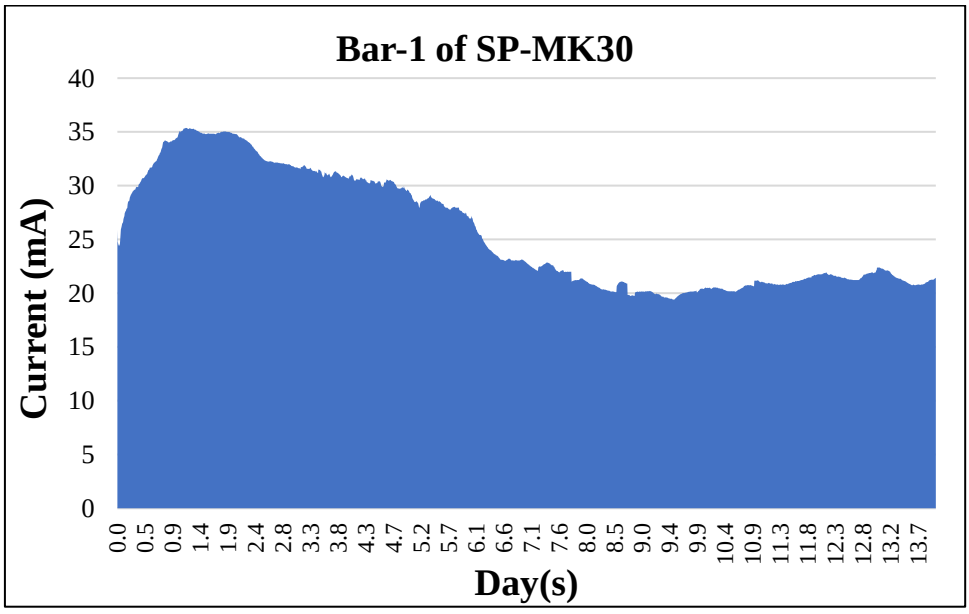

Figure 4. 29 Logged Current of Bar-1 of SP-MK30

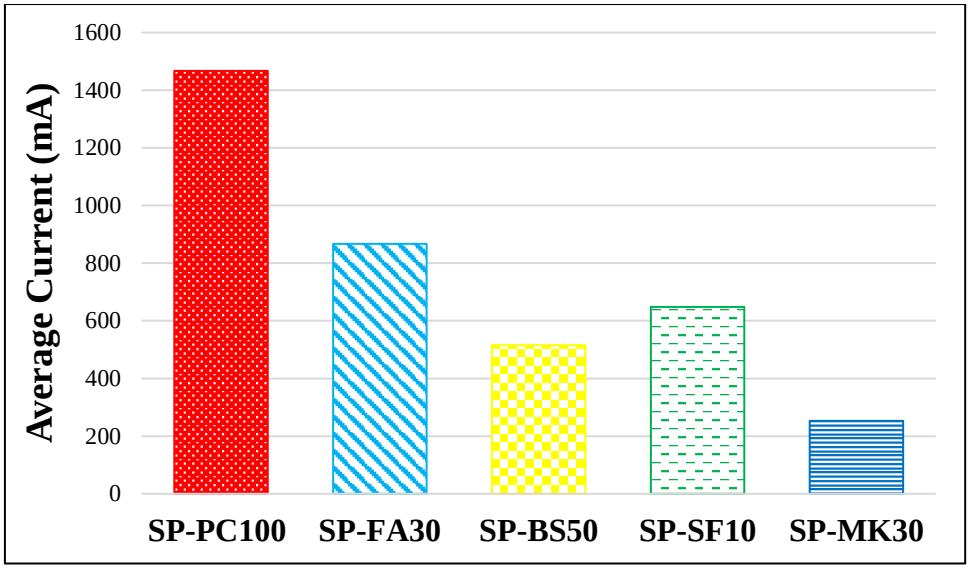

Figure 4. 30 Average Logged Current per Specimen

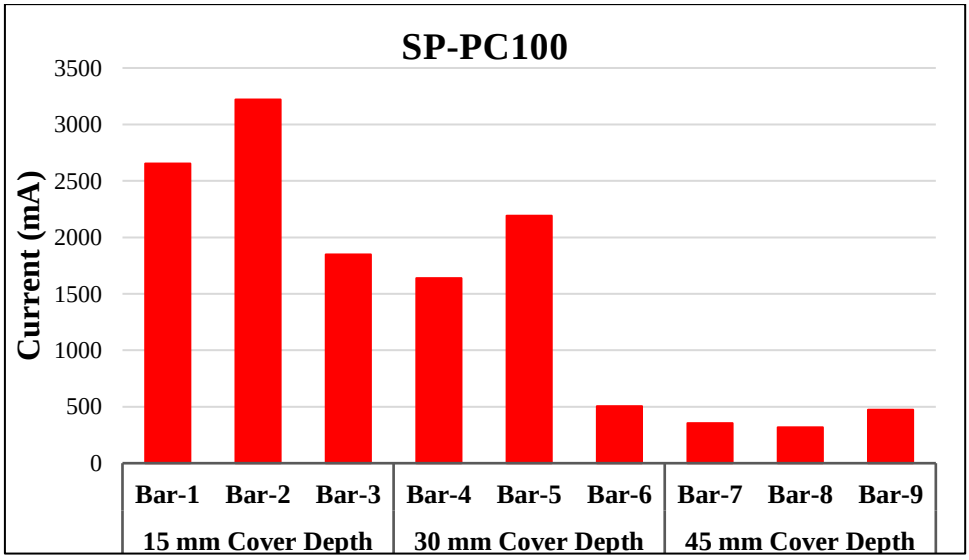

Figure 4. 31 Logged Current across Bars in SP-PC100

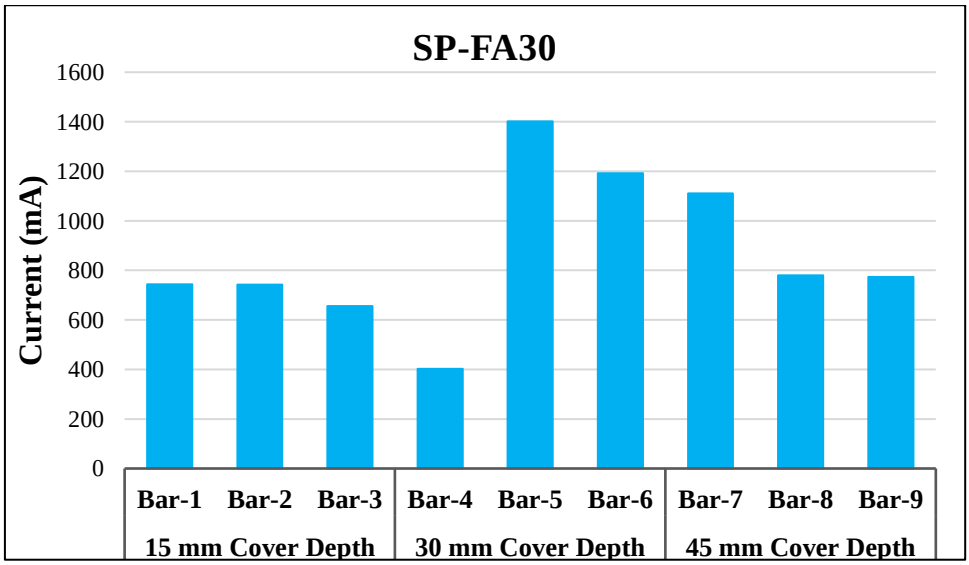

Figure 4. 32 Logged Current across Bars in SP-FA30

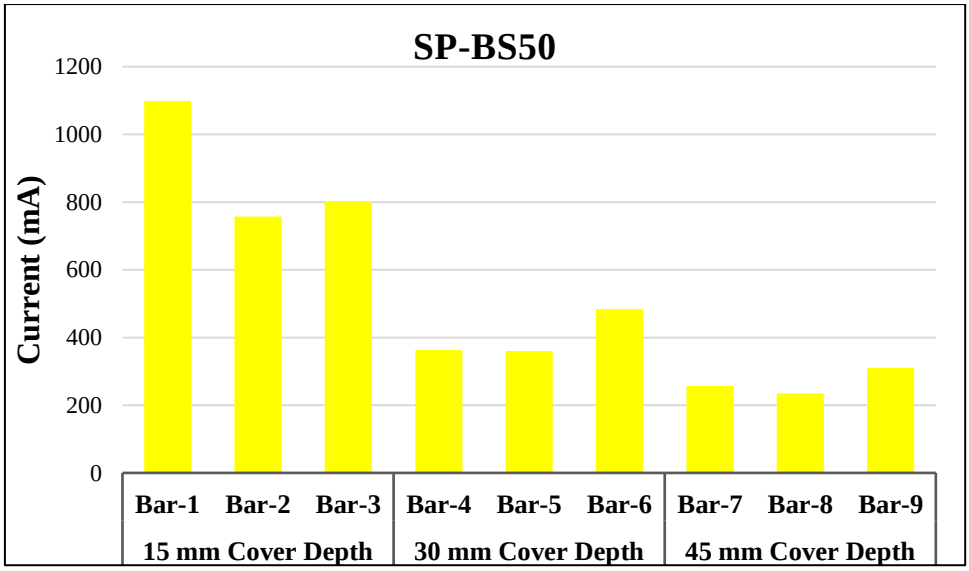

Figure 4. 33 Logged Current across Bars in SP-BS50

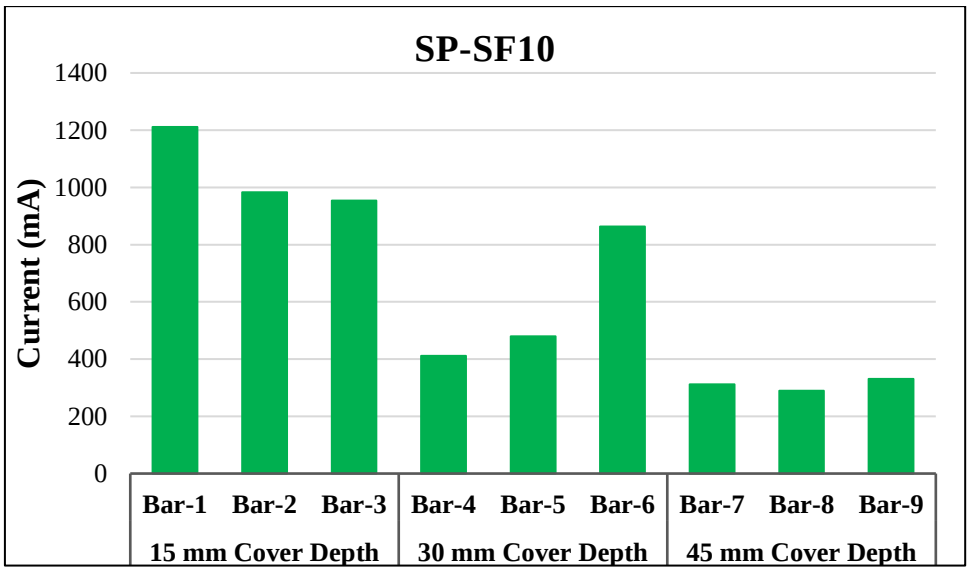

Figure 4. 34 Logged Current across Bars in SP-SF10

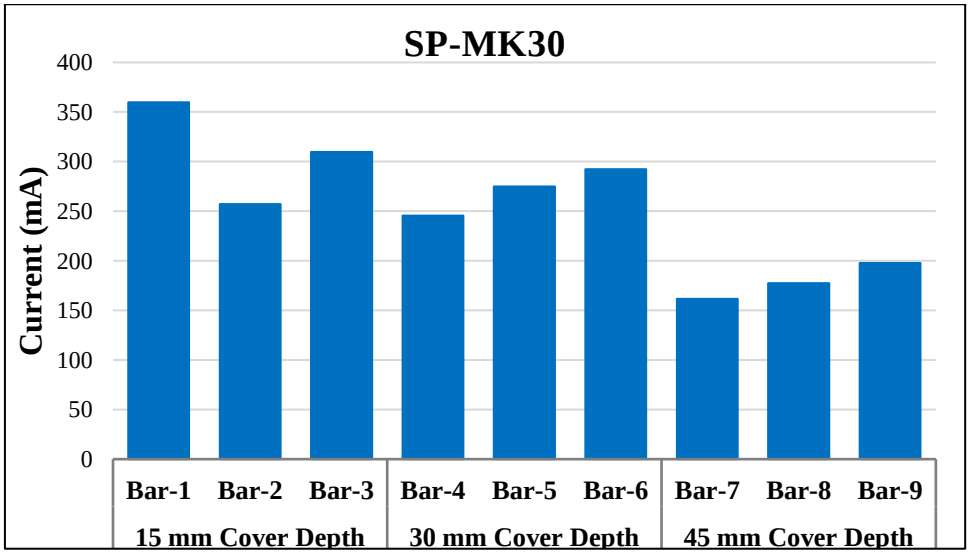

Figure 4. 35 Logged Current across Bars in SP-MK30

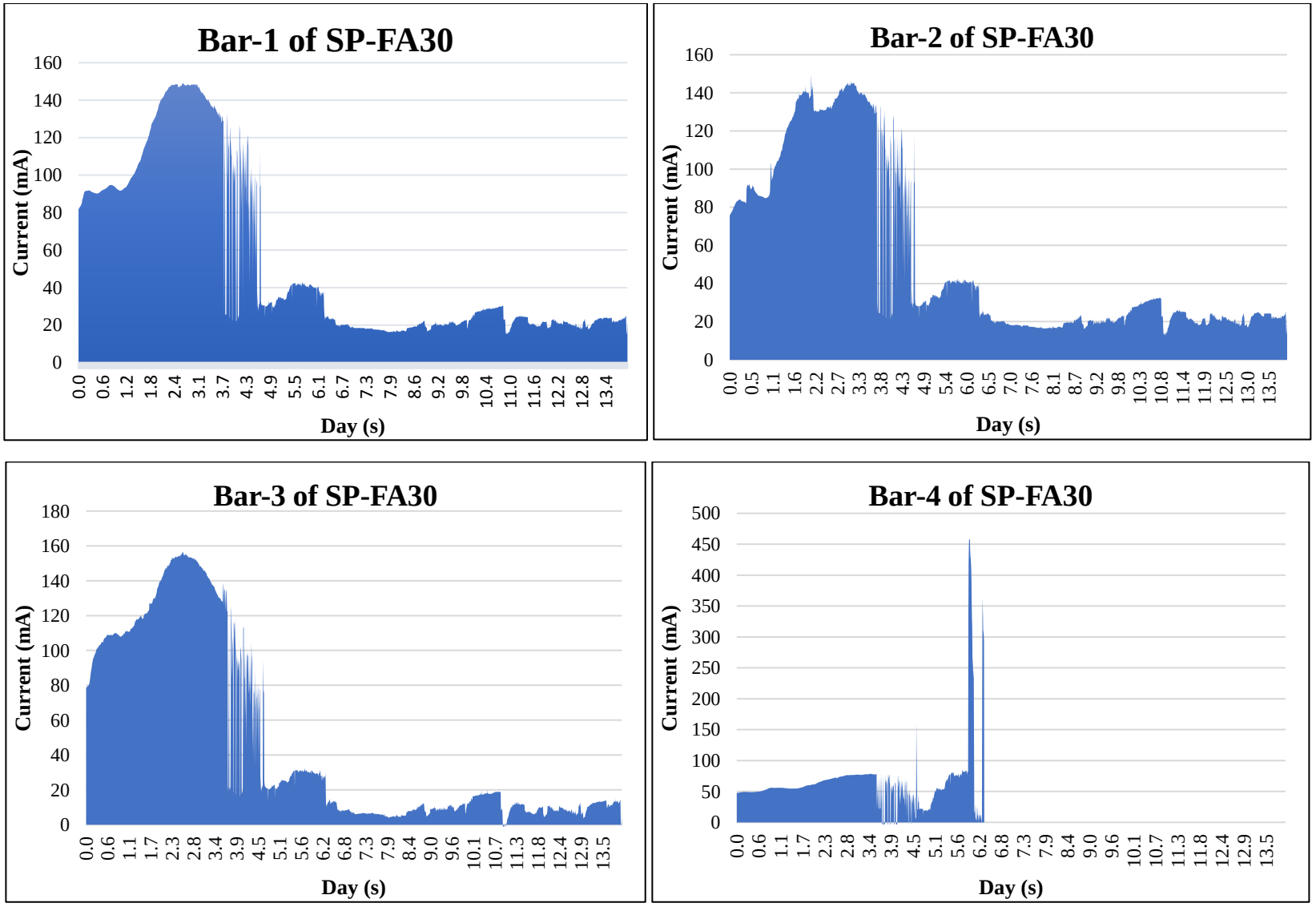

Figure 4. 36 Logged Current of Bar-1 to Bar-4 of SP-FA30

4.4.2.3 Resistivity

The resistivity measured at the end of the impressed current was termed the final resistivity. The results are in similar order as the intermediate resistivity but showed that there was a decline in the final resistivity for all specimens, except for SP-MK30. SP-MK30 showed a slight increase in resistivity. These results further validate the trend of the inducing current presented above. The increase in the resistivity of SP-MK30 is due to the continuation of hydration, mostly the formation of additional strength contributing gel other than C-S-H, such as calcium aluminium silicate hydrate (C-A-S-H) due to the high aluminate content of metakaolin. The formation of these gels also increases the chloride binding capacity and produces denser microstructures in metakaolin-based concrete. The results of the final resistivity in comparison with the intermediate resistivity are presented in Figure 4.37. It is worth noting that the resistivity results, as well as the entire results from the impressed current, correspond with the discussions presented in Section 2.2.4, that the resistivity of concrete is the most critical factor affecting the rate of corrosion propagation.

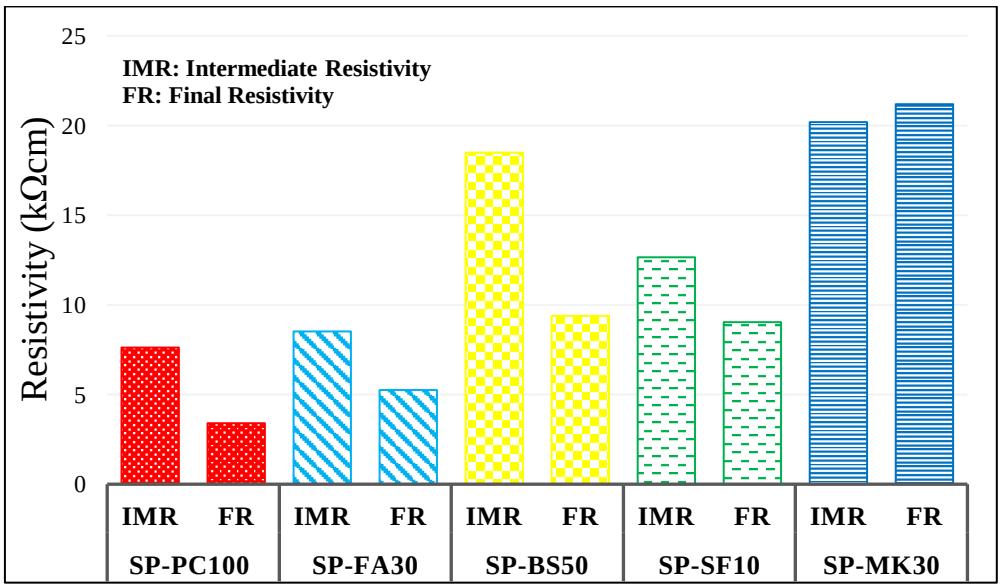

Figure 4. 37 Final Resistivity in Comparison with the Intermediate Resistivity

4.4.2.4 Half-Cell Potential Measurement

The half-cell potential measured at the end of the impressed current indicates all bars of all specimens were actively corroding. Similarly, the half-cell potential readings measured at the end of the cyclic ponding period (Cycle-9) were termed intermediate while those measured at the end of the impressed current were termed final. Results of the final half-cell potential measurements are presented per bar in Figure 4.38 to 4.46, in comparison with the intermediate readings. The highest negative values were seen in SP-PC100, Bar-7 and the lowest also in SP-PC100, Bar-1. It is important to note that Bar-1 of SP-PC100 was one of the most affected bars regarding mass loss. Therefore, the low negative reading could probably be due to the availability of enough oxygen at bar surface as the result of cracks or due to the corrosion product clogging the pores, thus restricting the flow of the voltage between the reference electrode and the bar.

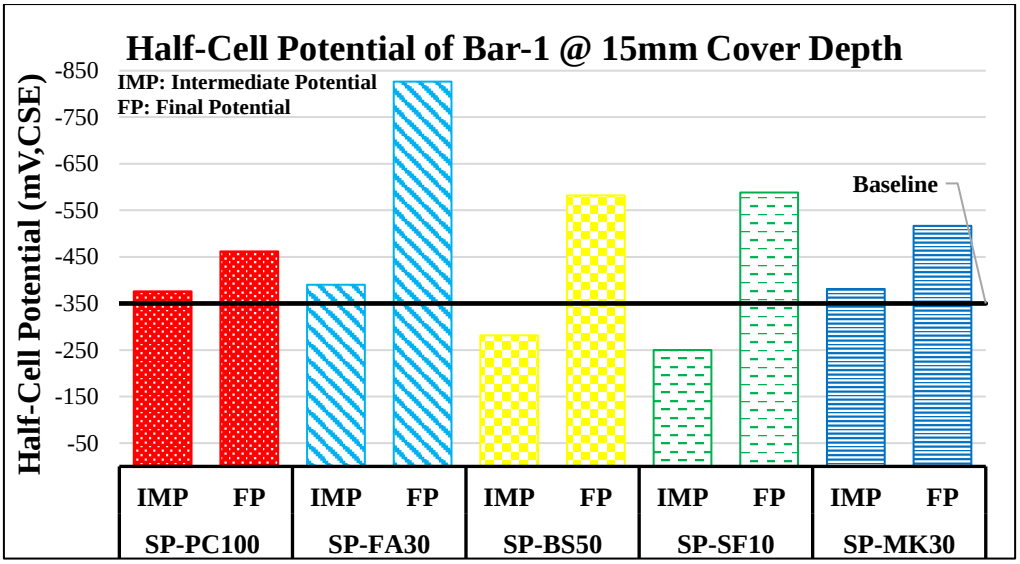

Figure 4. 38 Half-Cell Potential of Bar-1

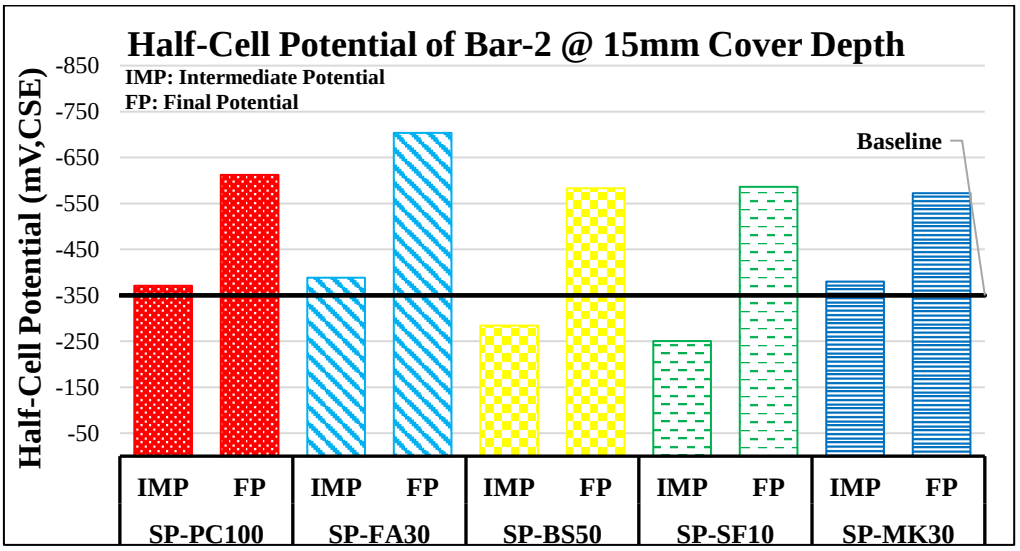

Figure 4. 39 Half-Cell Potential of Bar-2

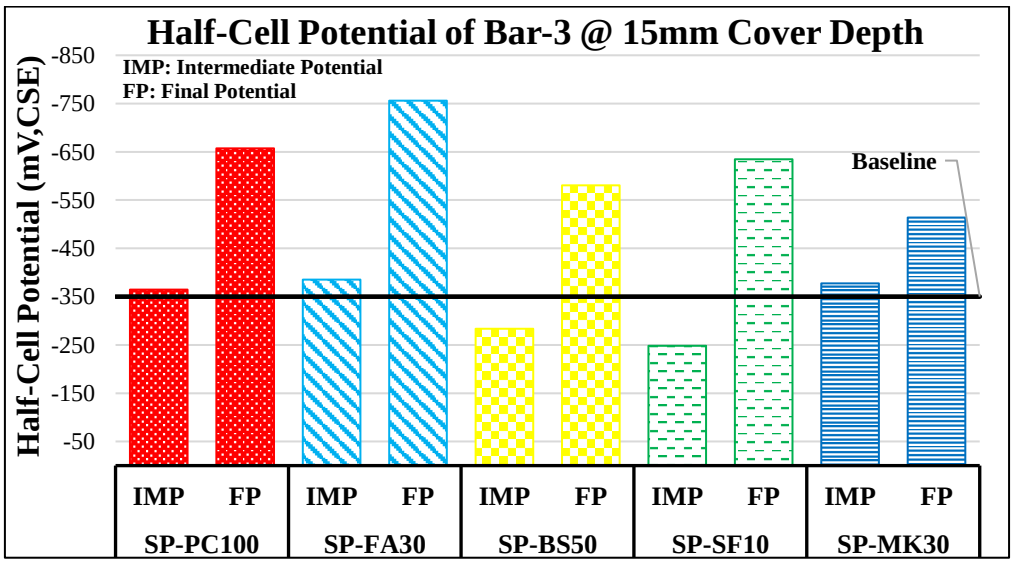

Figure 4. 40 Half-Cell Potential of Bar-3

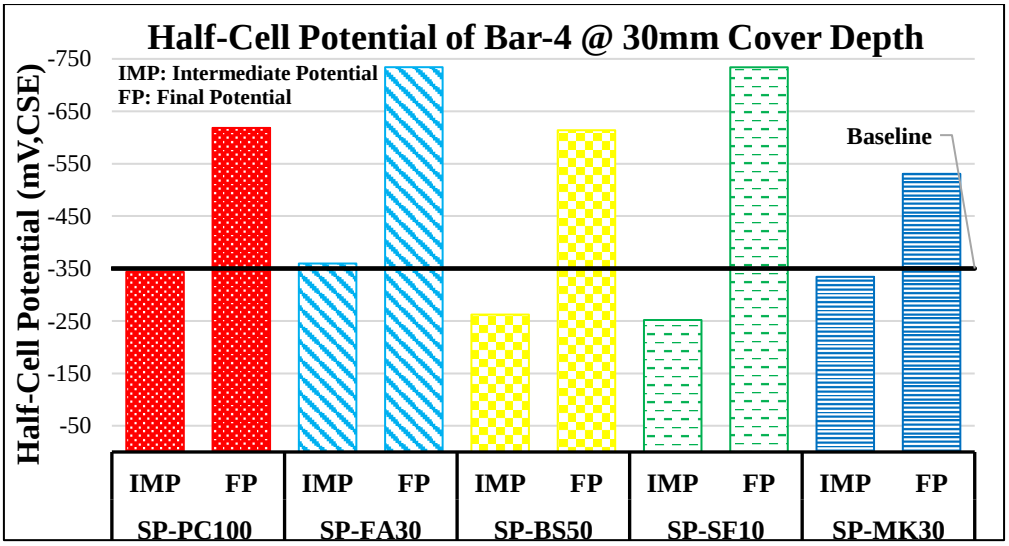

Figure 4. 41 Half-Cell Potential of Bar-4

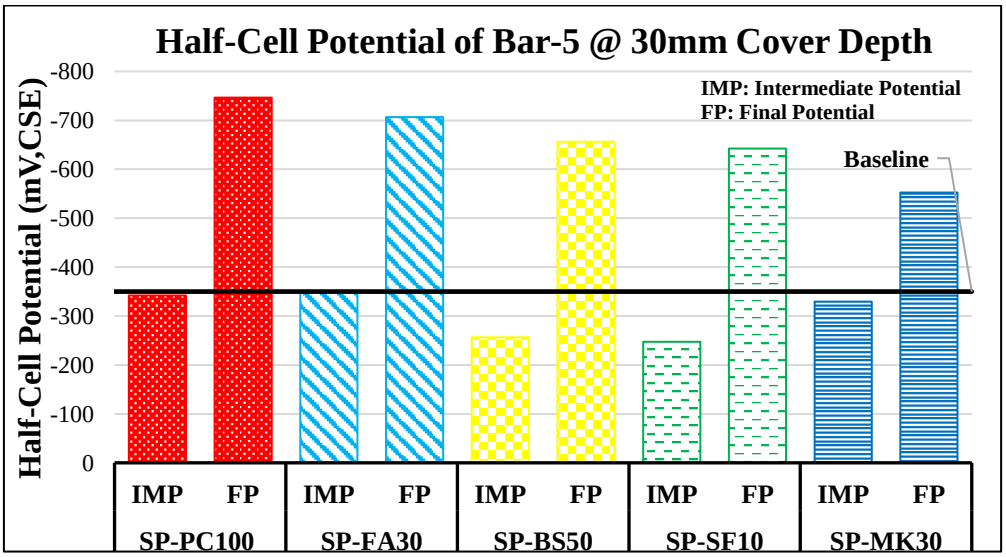

Figure 4. 42 Half-Cell Potential of Bar-5

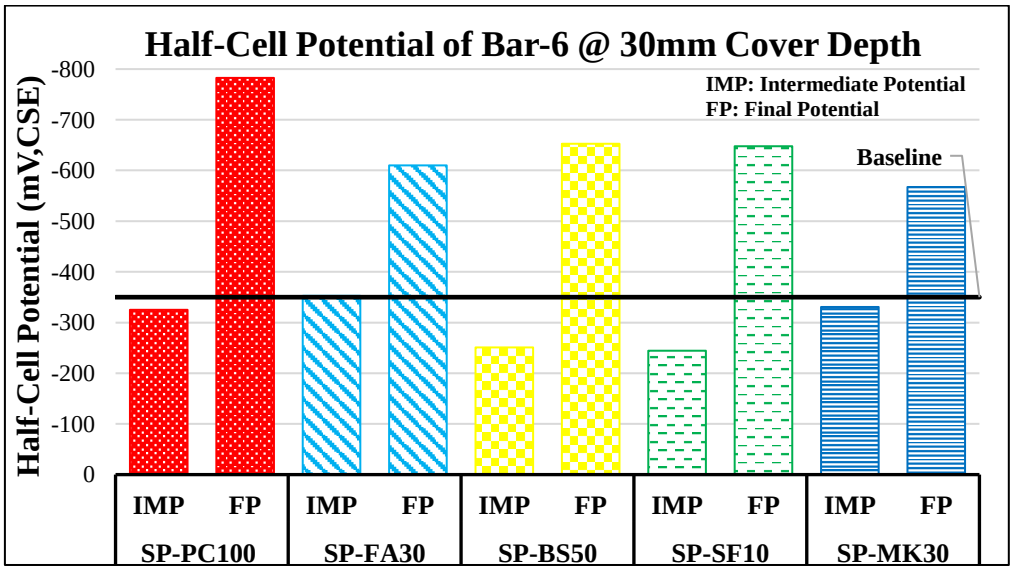

Figure 4. 43 Half-Cell Potential of Bar-6

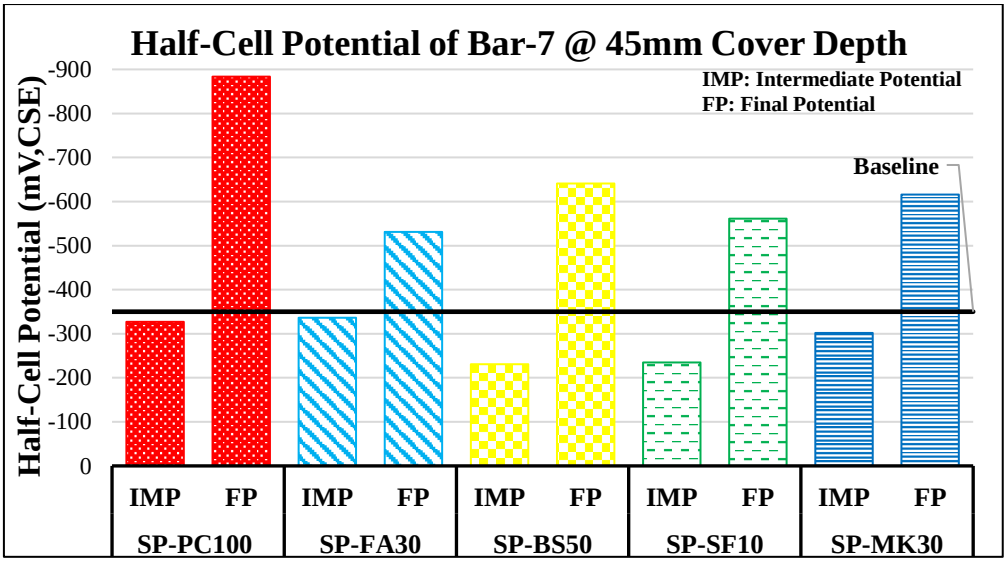

Figure 4. 44 Half-Cell Potential of Bar-7

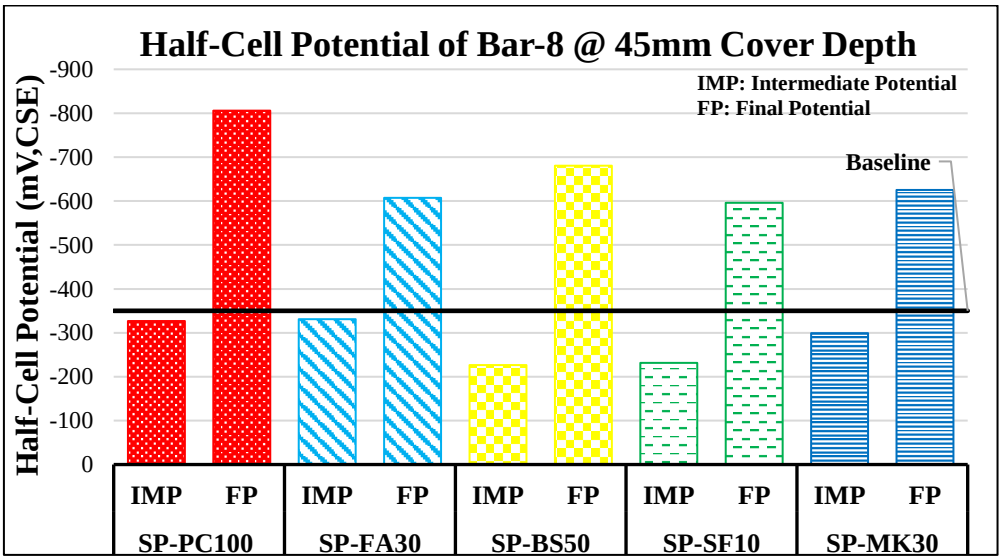

Figure 4. 45 Half-Cell Potential of Bar-8

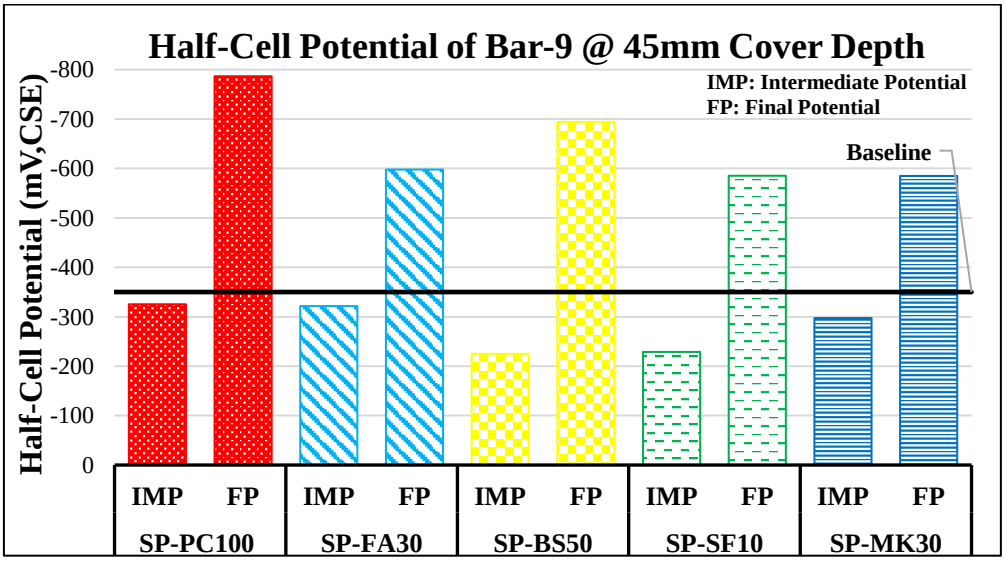

Figure 4. 46 Half-Cell Potential of Bar-9

4.4.2.5 Cross-Section Loss

The corrosion morphology took the expected form of localised corrosion in the direction of ingress of the chloride solution. The cross-section loss was influenced by the amount of current reaching the bars, which was also influenced by the specimens' resistivity. The average cross-section loss varies across specimens as was the inducing current. Specimens with higher resistivity experienced the minimal effect of cross-section loss. Within a given specimen, bars at 15 mm cover depth were the most affected, except for SP-FA30. An increase in cover depth generally reduces the section loss but mainly depends on the amount of current reaching the bar. The depth of the various pits was difficult to measure due to the narrowness of the pits' openings. However, the diameter across the most affected sections and those corresponding to the position of the map-out crack pattern were measured and used in the validation of the derived model.

4.4.2.6 Mass Loss

As with the cross-section loss, the mass loss was influenced by the amount of current reaching the bars, which was also influenced by the specimens' resistivity. Bars of SP-PC100 exhibited the greatest mass loss followed by SP-FA30, SP-SF10, SP-BS50 and SP-MK30. Bars of SP-MK30 experienced the lowest mass loss because of its high resistivity. The mass loss per bar is directly proportional to the amount of current reaching the bar and inversely proportional to the specimens' resistivity. Figure 4.47 presents the average mass loss per specimen while Figure 4.48 illustrates the relationship between the average logged inducing current per specimen and the average mass loss per specimen. It must be noted that the neat fitting of the data to the regression line observed in Figure 4.48 is attributed to the average (mean of the nine bars) approach adopted as discussed in Section 4.4.2. Details of the gravimetric analysis along with the logged inducing current per bar are presented in Table 4.8 to 4.12.

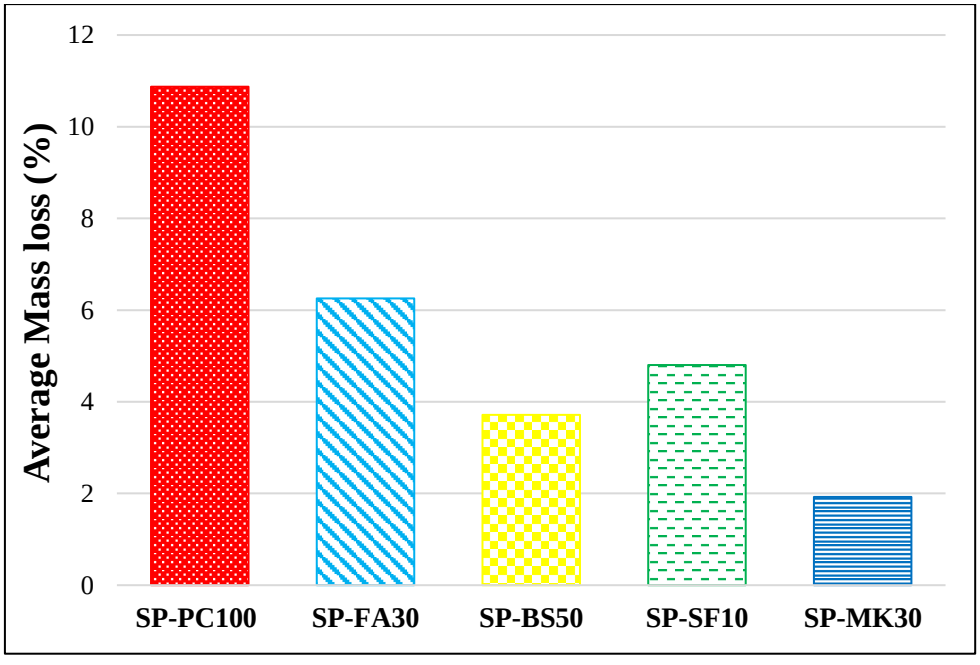

Figure 4. 47 Average Mass Loss Per Specimen

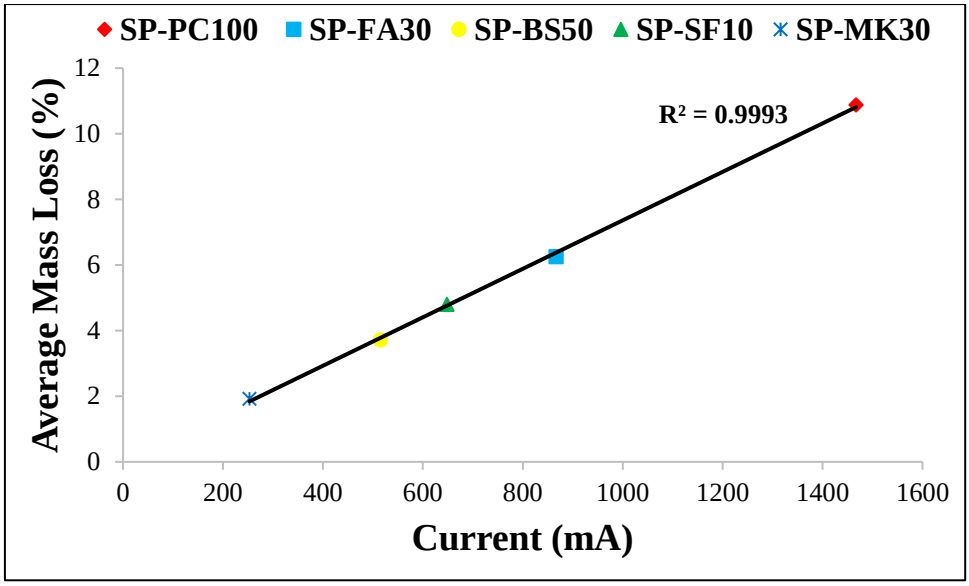

Figure 4. 48 Average Current vs Average Mass Loss

Table 4. 8 Gravimetric Analysis of Bars in SP-PC100

SP-PC100					
Bars	**Initial Mass**	**Final Mass**	**Mass Loss**	**% of Mass loss**	**Current (mA)**
Bar-1	244.47	195.26	49.21	20.13	2654.23
Bar-2	245.29	192.22	53.07	21.64	3221.59
Bar-3	244.25	205.29	38.96	15.95	1849.66
Bar-4	244.84	212.39	32.45	13.25	1637.40
Bar-5	245.57	201.94	43.63	17.77	2191.11
Bar-6	245.00	235.83	9.17	3.74	503.88
Bar-7	244.54	240.50	4.04	1.65	354.43
Bar-8	245.25	242.29	2.96	1.21	316.91
Bar-9	244.60	238.43	6.17	2.52	474.40

Table 4. 9 Gravimetric Analysis of Bars in SP-FA30

SP-FA30					
Bars	**Initial Mass**	**Final Mass**	**Mass Loss**	**% of Mass loss**	**Current (mA)**
Bar-1	245.52	230.50	15.02	6.12	743.93
Bar-2	244.23	231.02	13.21	5.41	742.17
Bar-3	244.45	232.43	12.02	4.92	656.23
Bar-4	244.44	236.86	7.58	3.10	403.08
Bar-5	244.12	222.95	21.17	8.67	1401.98
Bar-6	244.97	222.22	22.75	9.29	1192.63
Bar-7	244.27	221.84	22.43	9.18	1110.47
Bar-8	243.94	232.03	11.91	4.88	779.91
Bar-9	244.33	232.77	11.56	4.73	773.28

Table 4. 10 Gravimetric Analysis of Bars in SP-BS50

SP-BS50					
Bars	**Initial Mass**	**Final Mass**	**Mass Loss**	**% of Mass loss**	**Current (mA)**
Bar-1	244.74	222.33	22.41	9.16	1095.91
Bar-2	244.30	229.03	15.27	6.25	754.26
Bar-3	244.43	228.42	16.01	6.55	799.25
Bar-4	243.79	238.23	5.56	2.28	359.64
Bar-5	244.24	238.36	5.88	2.41	356.97
Bar-6	244.63	236.06	8.57	3.50	481.00
Bar-7	243.99	241.55	2.44	1.00	253.52
Bar-8	244.01	242.17	1.84	0.75	232.18
Bar-9	244.42	240.67	3.75	1.53	306.77

Table 4. 11 Gravimetric Analysis of Bars in SP-SF10

SP-SF10					
Bars	**Initial Mass**	**Final Mass**	**Mass Loss**	**% of Mass loss**	**Current (mA)**
Bar-1	243.96	220.60	23.36	9.58	1211.34
Bar-2	244.08	223.63	20.45	8.38	983.48
Bar-3	244.38	224.40	19.98	8.18	953.43
Bar-4	244.30	238.40	5.90	2.42	410.98
Bar-5	244.60	235.73	8.87	3.63	479.72
Bar-6	244.50	227.52	16.98	6.94	863.57
Bar-7	244.88	241.04	3.84	1.57	312.32
Bar-8	244.47	241.74	2.73	1.12	288.91
Bar-9	244.17	240.70	3.47	1.42	330.58

Table 4. 12 Gravimetric Analysis of Bars in SP-MK30

SP-MK30					
Bars	**Initial Mass**	**Final Mass**	**Mass Loss**	**% of Mass loss**	**Current (mA)**
Bar-1	243.96	236.50	7.46	3.06	359.81
Bar-2	244.55	238.36	6.19	2.53	257.06
Bar-3	243.65	237.47	6.18	2.54	309.83
Bar-4	244.45	239.56	4.89	2.00	245.53
Bar-5	244.14	238.38	5.76	2.36	274.89
Bar-6	244.45	240.05	4.40	1.80	292.50
Bar-7	244.69	242.40	2.29	0.94	161.75
Bar-8	244.18	241.51	2.67	1.09	177.49
Bar-9	244.10	241.63	2.47	1.01	197.80

4.4.2.7 Influence of Cover Depth and Binder Type

The influence of cover depth is seen with respect to the appearance of corrosion-induced cracks (time to cracking) and the rebar mass loss. The cover depth influenced the current flowing (connectivity) between the external cathode and the rebars. The higher the cover depth, the lower the connectivity and thus, the mass loss. From results of the logged inducing current and gravimetric analysis, it is evident that the cover depth influenced both results. The cover depth also influenced the time to cracking as was discussed under the evolution of the corrosion-induced crack. Of all specimens that cracked, the first crack appeared on bars at 15 mm cover depth. Thus, indicating that higher cover depth increases or extend the time to cracking. In natural corrosion environment, the higher the cover depth, the longer the time it takes corrosion agents to reach the rebars. The influence of binder type is mainly seen with respect to resistivity and durability perspectives of the specimens.

4.4.2.8 Relationship Between the Measured Crack Width and Cross-Section Loss

Generally, it was observed that the largest crack width did not necessarily occur at the maximum cross-section loss along the bars. This effect is the consequence of the corrosion product migrating away from the steel-concrete interface. As discussed in Section 2.4, the pressure exerted by the corrosion product on the surrounding concrete, the appearance of cracks as well as the relationship between the crack width and the corrosion level depend on the solubility of the corrosion products. Due to the solubility or diffusivity of the corrosion product, the quantitative investigation of this relationship between the cross-section loss and the corrosion-induced crack width was obstructed. Figure 4.49 shows the accumulation of the corrosion product at the surface of the ponding basin. However, it was cleared, that the cover-diameter ratio influenced the appearance of the corrosion-induced crack. The lower the ratio, the earlier cracks appeared.

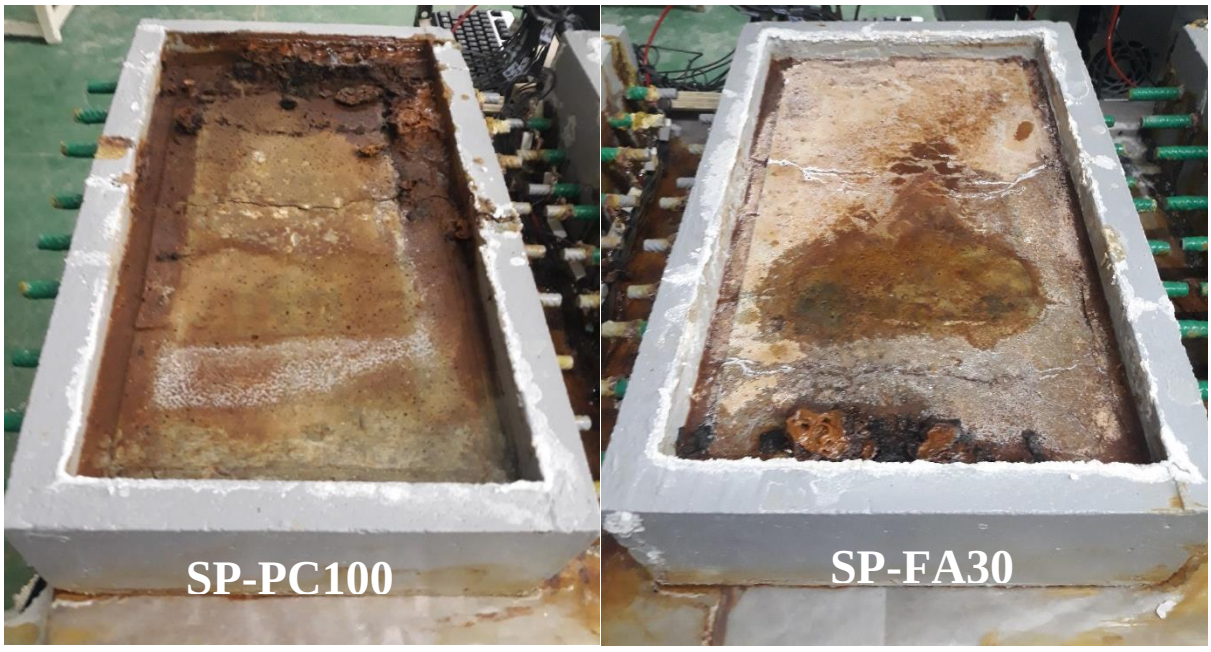

(a)

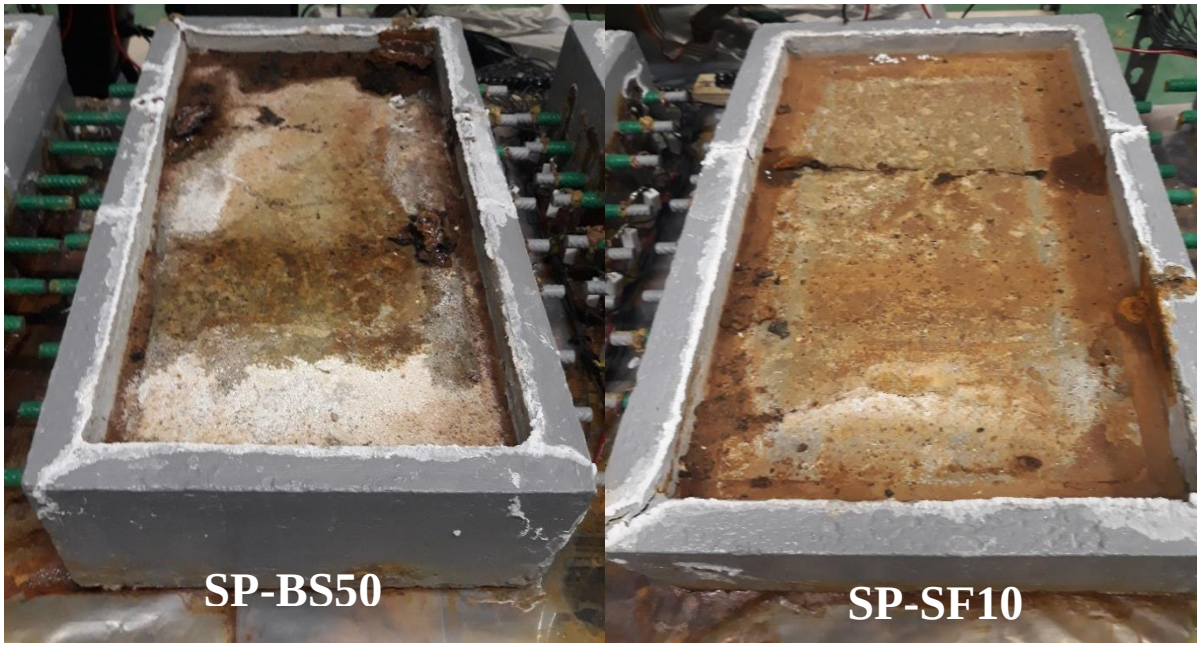

(b)

Figure 4. 49 Accumulation of Corrosion Product at the Surface of the Ponding Basin

4.5 SUMMARY OF EXPERIMENTAL RESULTS

The laboratory investigation aimed to study the relationship between the level of corrosion (cross-section loss) and the corrosion-induced crack width and, performance resistance of binder type against chloride-induced corrosion. Metakaolin and blast-furnace slag were the binders that performed the best at the age tested. These two materials exhibited better resistance against corrosion. Most especially, metakaolin, exhibiting excellent performance both in strength development and every aspect of durability. The blast-furnace slag performance was only seen in terms of durability. Regarding the overall performance against corrosion (time to cracking, crack width, mass loss and resistivity), all binary binders performed better than the control, in order of SP-MK30, SP-BS50, SP-SF10 and SP-FA30 (descending order of performance). The low rating of SP-SF10 and SP-FA30 is attributed to the particle grading of the silica fume and, the replacement level of the fly ash, respectively. The results of the accelerated corrosion test confirmed that the durability of concrete is directly linked to its resistivity, which is the controlling factor of corrosion propagation.

With regards to the relationship between corrosion level and the corrosion-induced crack width, the laboratory investigation showed that this relationship is dependent on the solubility of the corrosion product. The largest crack width did not occur at the maximum cross-section loss along the bars. This is attributed to the condition tested (present of chloride and enough moisture), which increases the solubility of the corrosion product, thus, permitting migration away from the steel-concrete interface. Consequently, the quantitative description of this relationship was obstructed. However, a parameter (cover-diameter ratio) was identified and could be useful depending on findings of the FEM analysis.

4.6 REFERENCES

1. Alexander, M.G., 2017. Durability Index Testing Procedure Manual.
2. Assouli, B., Ballivy, G. and Rivard, P., 2008. Influence of environmental parameters on application of standard ASTM C876-91: Half-cell potential measurements. Corrosion Engineering, Science and Technology, 43(1), pp.93-96.
3. Ha, T.H., Muralidharan, S., Bae, J.H., Ha, Y.C., Lee, H.G., Park, K.W. and Kim, D.K., 2007. Accelerated short-term techniques to evaluate the corrosion performance of steel in fly ash blended concrete. Building and Environment, 42(1), pp.78-85.
4. Ince, R., Gör, M., Eren, M.E. and Alyamaç, K.E., 2015. The effect of size on the splitting strength of cubic concrete members. Strain, 51(2), pp.135-146.
5. Ince, R., 2012. Determination of concrete fracture parameters based on peak-load method with diagonal split-tension cubes. Engineering Fracture Mechanics, 82, pp.100-114.
6. Mehta, P.K. and Monteiro, P.J., 2006. Concrete: microstructure, properties, and materials.
7. Owens, G. and Fulton, F. 2009. Fulton's concrete technology. Midrand: Cement & Concrete Institute.
8. Sabir, B.B., Wild, S. and Bai, J., 2001. Metakaolin and calcined clays as pozzolans for concrete: a review. Cement and concrete composites, 23(6), pp.441-454.
9. Sabir, B.B., Wild, S. and O'farrell, M., 1998. A water sorptivity test for mortar and concrete. Materials and Structures, 31(8), p.568.)
10. Siddique, R., 2011. Utilisation of silica fume in concrete: Review of hardened properties. Resources, Conservation and Recycling, 55(11), pp.923-932.
11. Siddique, R. and Khan, M.I., 2011. Supplementary cementing materials. Springer Science & Business Media.
12. Vu, D.D., Stroeven, P. and Bui, V.B., 2001. Strength and durability aspects of calcined kaolin-blended Portland cement mortar and concrete. Cement and Concrete Composites, 23(6), pp.471-478.

5 FINITE ELEMENT ANALYSIS

5.1 INTRODUCTION

With the development of computer-based simulation programs (FEA software), it is now possible to model system which previously seemed impossible. Finite element analysis (FEA) software has become an integral part of today's engineering analysis. It provides means by which the physical behaviour of complex phenomena, such as steel corrosion in concrete can be accurately represented. Thought the exact solutions for some engineering problems are unattainable but with the aid of FEA software, an approximation closer to the exact solution can be obtained. However, the accuracy of any finite element analysis depends on the following key points:

1. How realistic is the representation of the system being modelled to the physical or real conditions?
2. Meshing and element sizing of the model.
3. Boundary conditions and assumptions employed.

In this regard, this chapter presents a pre-analysis of the simulation based on the above-listed points. It outlines the geometry description and materials properties of the models, meshing and element sizing, boundary conditions and, the assumptions and theories employed in this analysis. This simulation of reinforcement corrosion in concrete was conducted in ANSYS 19.2 workbench student version. ANSYS is a general purpose commercial FEA software and can model a wide range of problem with greater degree of accuracy. ANSYS was selected based on its solver performance (meshing, contacts, and physics interaction) and user-friendly interface. It is worth noting that the simulations were conducted as plane stress two-dimensional (2D) boundary problem, and this approach was adopted to reduce processing time, improved the accuracy of the results and moreover, based on the solver limitation of the student vision. Like any mathematical modelling, this simulation aimed to structurally predict the behaviours (stresses and deformations) of the system being modelled (steel corrosion in concrete) and study the relationship between the pressure exerted by the expansive corrosion product on the surrounding concrete, which was applied as internal pressure, and the corresponding deformations and resultant stresses.

5.2 GEOMETRY AND MATERIAL PROPERTIES

The simulation considered three cases containing various samples. This was intended to improve the findings as well as verification and validation. Case I was based on the specimen properties (geometry and material descriptions) of the laboratory investigation. Case II was arbitrarily selected with material properties of the most used structural concrete and, Case III was selected from the literature, based on Andrade et al. (1993) & Molina et al. (1993) investigations.

5.2.1 Case I

As previously stated, this case was based on the specimens tested during the laboratory investigation. The geometry descriptions and material properties are the same as the laboratory experiment. The compressive strength, tensile strength and density were obtained during the experimental investigation and are presented in Table 5.1. The elastic modulus was deduced from the compressive strength according to the South African National Standard (SANS). Eq. – 5.1 gives the relationship from which the elastic modulus was estimated. It is important to note that Eq. – 5.1 can be used to estimate the elastic modulus of concrete at any age from three-day and above, provided the characteristic strength is equal or above 20 MPa (Owens and Fulton, 2009). Figure 5.1 shows the boundary conditions employed in modelling of Case I specimens.

$$E_{c,56} = K_0 + \alpha f_{cu,56} \qquad \text{---------- Eq. – 5.1}$$

Where $E_{c,56}$ is the elastic modulus at the 56th day after casting, K_0 the aggregate stiffness factor which is related to the elastic modulus of the aggregate, α the aggregate interaction factor and $f_{cu,56}$ the 56-day characteristic strength of the specimen obtained from Eq. – 5.2 assuming normal distribution. Note, the subscripts 56 is an indication of the age only.

$$f_{cu} = f_{c,56} - 1.65\sigma \qquad \text{---------- Eq. – 5.2}$$

Where $f_{c,56}$ is the average 56-day compressive strength and σ the standard deviation.

Table 5. 1 Properties of Case I specimens

Parameters	**SP-PC100**	**SP-FA30**	**SP-BS50**	**SP-SF10**	**SP-MK30**
Compressive strength [a] (MPa)	43.0	37.3	38.8	46.9	52.6
Tensile strength [b] (MPa)	4.4	3.9	4.1	4.6	4.9
Elastic Modulus (GPa)	31.67	30.18	30.64	32.68	34.11
Poisson's Ratio [c]	0.2	0.2	0.2	0.2	0.2
Density [d] (kg/m^3)	2434.4	2428.2	2431.3	2329.1	2432.6

[a] Average 56-day compressive strength obtained from the laboratory investigation
[b] Average 56-day splitting tensile strength obtained from the laboratory investigation
[c] Based on SANS recommended value (Owens and Fulton, 2009)
[d] Average 56-day saturated surface dry density of the cubes

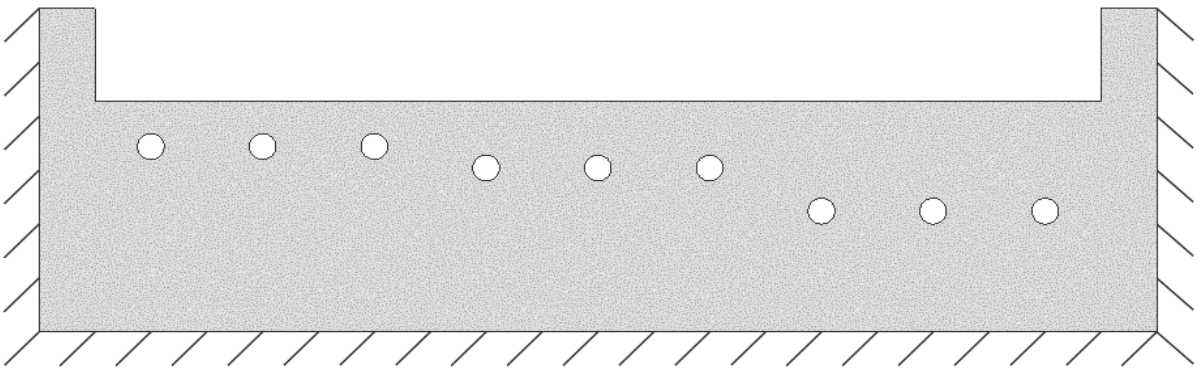

Figure 5. 1 Boundary Conditions of Case I Specimens

5.2.2 Case II

This case focused on the parametric studies of the simulation. It contained five specimens (concrete beams) singly reinforced, with dimensions of 400 x 100 x 150 mm and various sizes of rebar diameter per specimen. Figure 5.2, 5.3, and 5.4 show the longitudinal section, the cross-section and boundary conditions, respectively, of Case II specimens. This case considered more specimens to study the influence of varying the rebar diameter since the load was applied in steps (tabular) and could not be set as a parameter in ANSYS. The parameters studied were the influence of concrete cover depth, compressive and tensile strength, elastic modulus and rebar diameters on the resultant stresses and deformations. Material properties were the same for all specimens, and the properties of rust (corrosion product) were selected from the literature and are listed in Section 5.5. The concrete properties considered were those of normal-weight concrete with compressive strength ranging from 20.0 MPa to 40.0 MPa. For simplicity, the tensile strength of the specimens was considered 10% of the compressive strength, and the elastic modulus was derived from the compressive strength based on CEB-FIP Model Code (1990) for normal-weight concrete containing quartzitic aggregates (Eq. – 5.3), which assume direct dependency on the concrete compressive strength (Mehta and Monteiro, 2006). CEB-FIP Model has been selected because of its flexibility since this case is based on conceptual or imaginary specimens. CEB-FIP Model permits the estimation of the elastic modulus from either the average compressive strength or the characteristic compressive. Table 5.2 presents the material properties of the specimens for Case II.

$$E_C = 2.15 \times 10^4 \left(\frac{f_{cm}}{10}\right)^{\frac{1}{3}} \qquad \text{---------- Eq. – 5.3}$$

Where $\boldsymbol{E_C}$ is the elastic modulus of concrete and $\boldsymbol{f_{cm}}$ the average 28-day compressive strength (Mehta and Monteiro, 2006).

Table 5. 2 Material Properties of Case II

MATERIAL PROPERTIES		
Concrete		
Compressive Strength	20.0, 25.0, 30.0, 35.0, 40.0	MPa
Tensile Strength	2.0, 2.5, 3.0, 3.5, 4.0,	MPa
Density	2400	kg/m^3
Elastic Modulus	27.0, 29.0, 31.0, 33.0, 34.0	GPa
Poisson's Ratio	0.2	
Concrete Cover	20, 25, 30, 35, 40	mm
Specimen	**Rebar Diameter**	
SP-I	10 mm	
SP-II	12 mm	
SP-III	16 mm	
SP-IV	20 mm	
SP-V	25 mm	

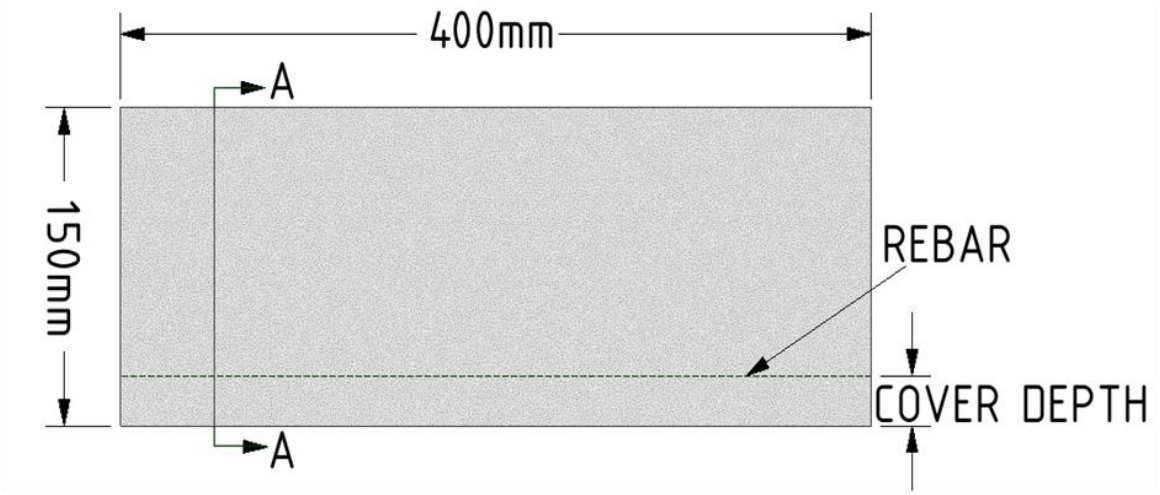

Figure 5. 2 Longitudinal Section of Case II Specimens

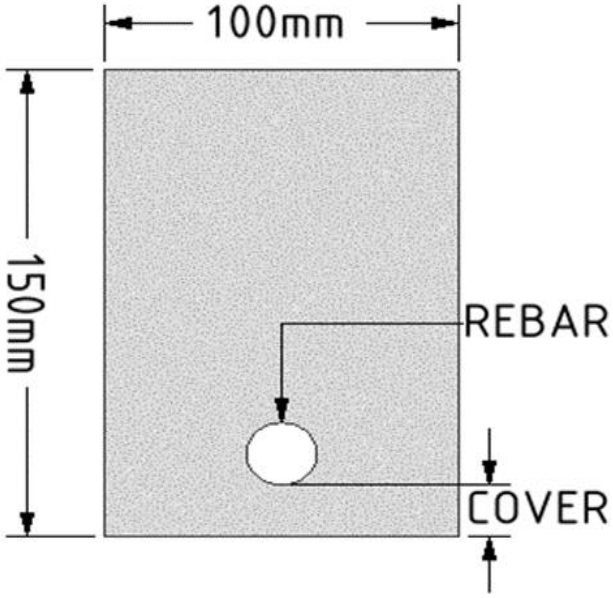

Figure 5. 3 Cross-section at A-A of the Longitudinal Section

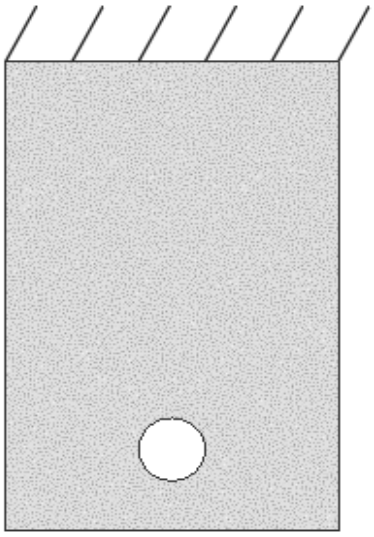

Figure 5. 4 Boundary Conditions of Case II Specimens

5.2.3 Case III

As previously mentioned, this case has adopted properties of Andrade et al. (1993) & Molina et al. (1993) specimens. The geometry descriptions and boundary conditions, and material properties are presented in Figure 5.5 – 5.7, and Table 5.3, respectively. Molina et al. adopted properties of liquid water (bulk modulus and Poisson's ratio) as the rust properties from which the elastic modulus of rust was obtained. This case was selected to study the influence of the rust properties on the finite element modelling, and for validation, as Andrade et al. (1993) experimental data are part of selected data for validation.

Table 5. 3 Material Properties of Case III

MATERIAL PROPERTIES	
Concrete	
Compressive strength	30.0 MPa
Splitting Tensile strength	3.55 MPa
Poisson's ratio	0.2
Elastic Modulus	36 GPa
Fracture Energy	200 Jm^{-2}
Shear Retention Factor	0.2
Steel	
Rebar diameter	16 mm
Elastic Modulus	210 GPa
Poisson's Ratio	0.3
Rust	
Elastic Modulus	12 MPa
Poisson's Ratio	0.499
Bulk modulus	2.0 GPa
Volume Expansion Ratio	2

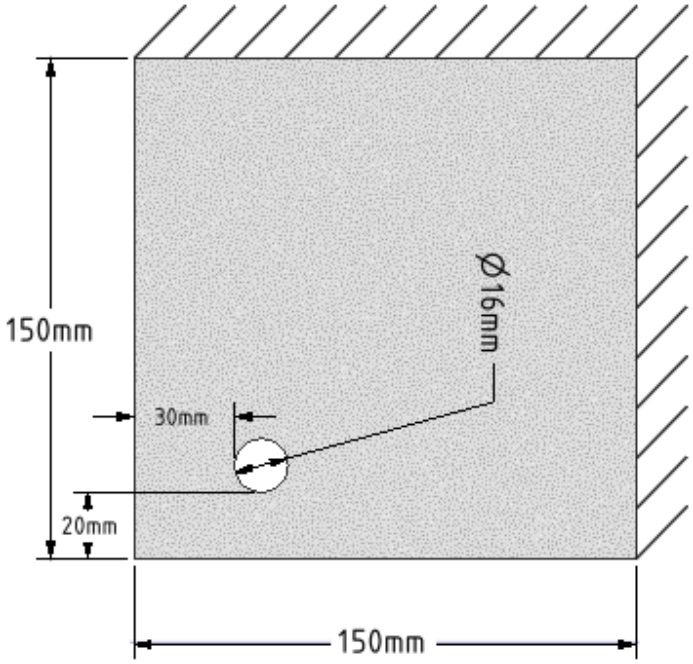

Figure 5. 5 Cross-Section and Boundary Conditions of Specimen-I (Case III)

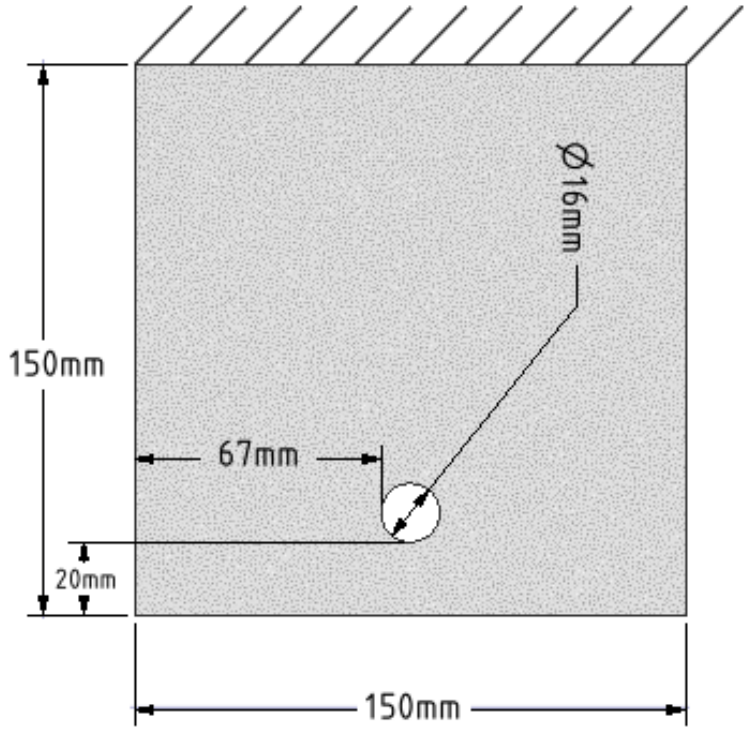

Figure 5. 6 Cross-Section and Boundary Conditions of Specimen-II & III (Case III)

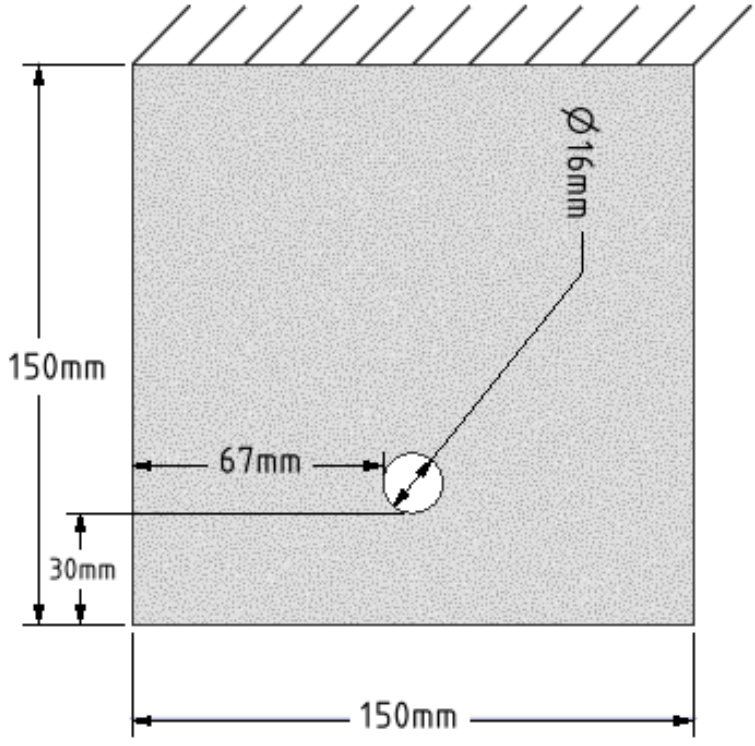

Figure 5. 7 Cross-Section and Boundary Conditions of Specimen-IV (Case III)

5.3 MESHING AND ELEMENT SIZING

Meshing plays a vital role in finite element analysis. Holding key points 1 & 3 constant as indicated in Section 5.1, the finer the mesh, the more realistic is the result or the closer the approximate value is to the exact solution. Meshing is also one of the means often used to verify finite element solutions because of the direct dependency of finite element analysis on the mesh quality. Thus, for this simulation, mesh refinement was also employed in the verification of the results. The primary mesh settings considered in this analysis are those presented below. The remaining settings were left as program controlled or as default settings. Figure 5.8 illustrates the mesh refinement considered for Case I.

- Element Order: Quadratic
- Size function: Proximity and Curvature
- Relevant Centre: Fine
- Maximum Size: 2.5 mm

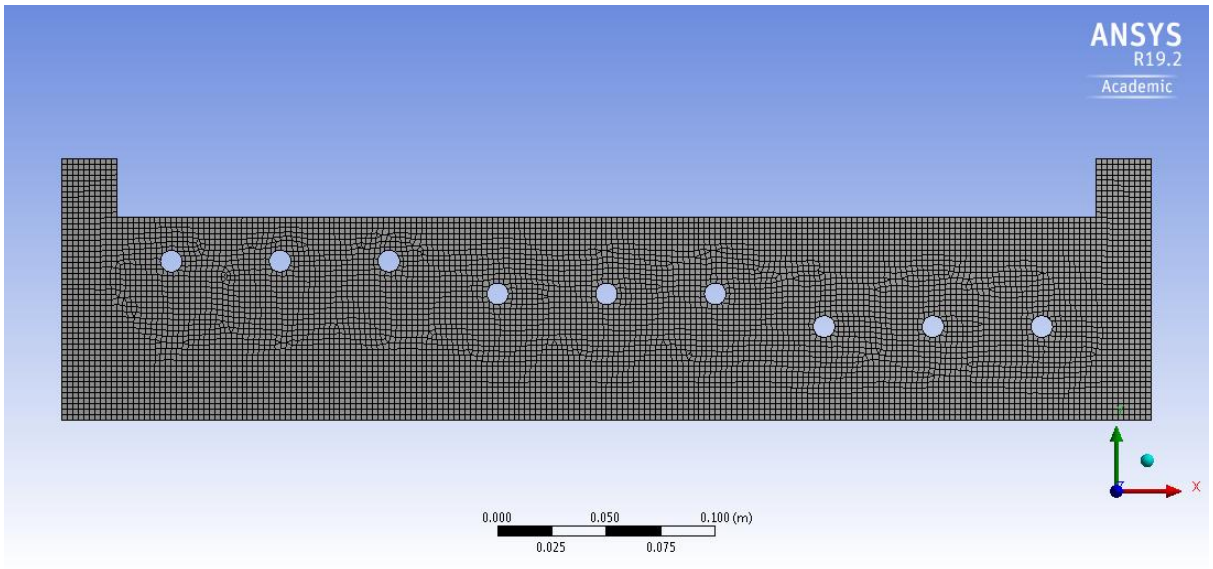

Figure 5. 8 Mesh Sizing

5.4 DAMAGE ANALYSIS

Concrete is quasi-brittle material, thus it allowable to model concrete as a linear elastic strain softening material up to the point of failure in tension or up to the development of cracks, after which the behaviour of concrete become orthogonal (Bangash, 1989). In this regard, the damage analysis used in this study is based on the below assumptions which are also valid for damage analysis and failure theories (Brittle failure theory, Mohr-Columb theory, etc.) use in ANSYS.

- Concrete is isotropic linear elastic material, and thus, it is defined by elastic modulus and Poisson's ratio (Shi, 2009).
- Crack initiates only at a point when the maximum principal stress at that point exceeds the tensile strength of the concrete, and the crack forms normal to the direction of the principal tensile stress (Shi, 2009).

5.5 LOAD ANALYSIS

Corrosion is not a standard load in FEM software; it is often modelled as internal pressure or radial expansion of the rebar. In this study, internal pressure was considered for accurately studying the relationship between the deformation and the applied load, which mimic the radius loss. This approach permits the evaluation of the rebar cross-section loss through the gradual application of the load (internal pressure), which was considered as the function of the rebar radius loss due to corrosion. The applied load was considered as the pressure developed in response to the change in volume of the original steel as the result of a change in its chemical compositions due to corrosion. The loads were applied in steps and are presented in the Appendix D. The derivation of applied load (pressure) is based on the following assumptions and findings of other researchers presented below. It is important to note that these assumptions have been considered for simplification.

- The rust distribution depends on the morphology of the corrosion process, which may occur as uniform or non-uniform corrosion of the rebar, hence, the deformation could be uniform or non-uniform.
- The type of corrosion product (rust) been developed is Ferric hydroxide $Fe(OH)_3$ and has the following properties:
    - Volume expansion ratio (n) = 4.00 (Jamali et al., 2013)
    - Molar mass = 0.532 (Jamali et al., 2013)
    - Density = 3.90 g/cm^3 (Jamali et al., 2013)
    - Modulus of Elasticity = 500 MPa (Chen and Leung, 2013)
    - Poisson's Ratio = 0.3 (Chen and Leung, 2013)
- The steel-concrete interface has no influence on the corrosion-induced crack width (Jamali et al., 2013).
- The rust does not penetrate the corrosion-induced crack before the crack reaches the concrete surface. This assumption is based on the finding of Zhao et al. (2012).

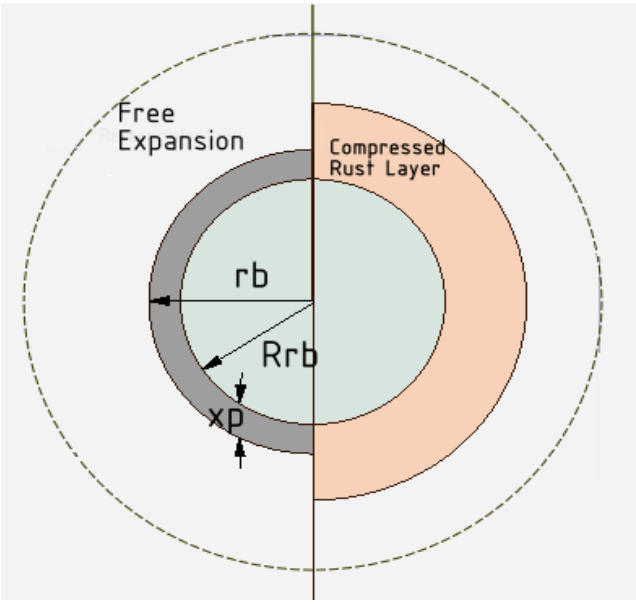

Figure 5. 9 Schematic of Uniform Corrosion; Adapted & modified from Oh et al. (2007)

5.5.1 DERIVATION OF THE APPLIED LOAD

The derivation of the applied load was done analytically for both uniform and non-uniform corrosion.

5.5.1.1 Uniform Corrosion

Consider Figure 5.9: Let $\boldsymbol{x_p}$ be the radius loss to corrosion (attack penetration), $\boldsymbol{r_b}$ the original radius of the rebar and $\boldsymbol{R_{rb}}$ the residual radius of the rebar. Assuming the expansion to be only in the radial direction:

The volume of steel loss to corrosion or being corroded (V_s)

$$V_s = \pi\left[{r_b}^2 - {R_{rb}}^2\right]h = \pi\left[{r_b}^2 - (r_b - x_p)^2\right]h \quad \text{---------- Eq. – 5.4}$$

Note: $R_{rb} = r_b - x_p$

The volume of free rust expansion (V_{rust})

$$V_{rust} = V_s \cdot n \quad \text{---------- Eq. – 5.5}$$

Where $\boldsymbol{n}$ is the volume expansion ratio.

Due to restrain imposed by the surrounding concrete and assuming no diffusion of the corrosion product (rust) into the surrounding concrete, the volume of the free rust expansion will be compressed. Thus, becoming the compressed volume of rust ($\boldsymbol{CV_{rust}}$).

$$CV_{rust} = V_{rust} \cdot \frac{1}{B_{rust}} \quad \text{---------- Eq. – 5.6}$$

Where ($\frac{\boldsymbol{1}}{\boldsymbol{B_{rust}}}$) is the compressibility coefficient of the corrosion product. The inverse of the bulk modulus ($\boldsymbol{B_{rust}}$) of the corrosion product was considered as the volume compressibility coefficient in this analysis. The bulk modulus of the corrosion product is obtained from:

$$B = \frac{E}{3(1-2v)}$$

Where E and v is the elastic modulus and the Poisson's ratio of the rust, respectively.
Therefore, the volumetric strain of rust is:

$$\varepsilon_{rust} = \frac{CV_{rust}}{V_{rust}} = \frac{1}{B_{rust}} \quad \text{---------- Eq. – 5.7}$$

Note: with the introduction of the compressibility coefficient, the volumetric strain is equal to the radial strain.

Thus, from Oh et al. (2007) proposed formula, the internal pressure (n/mm) acting along the circumference at the steel-concrete interface is obtained:

$$P = k_{rust} \cdot \varepsilon_{rust} \quad \text{---------- Eq. – 5.8}$$

Where k_{rust} is the stiffness of the compressed rust layer. The stiffness of the compressed rust layer is the function of its area or thickness and could be obtained with the assumption of a hollow cylinder. However, this approach is not applicable to non-uniform corrosion. Thus, for comparing the both derived pressures (uniform and non-uniform), the stiffness was considered

in terms of the compressed area multiplied by the elastic modulus of the corrosion product (rust).

$$k_{rust} = \frac{\pi n(r_b{}^2 - R_{rb}{}^2)}{B_{rust}} \cdot E_{rust} \qquad \text{---------- Eq. – 5.9}$$

Where E_{rust} is the elastic modulus of the corrosion product.

Note: the value of the height (***h***) used in this analysis is 1 mm and the internal line pressure (N/mm) acting along the circumference can be converted to N/mm^2 by dividing by ***h***.

5.5.1.2 Non-Uniform Corrosion

Assuming the ingress of corrosion agents to be one-directional as illustrated in Figure 5.10, half of the rebar circumference is exposed to corrosion agents, and corrosion begins at the section closer to the exposed surface. Thus, the residual shape of the half corroding section becomes elliptical (Malumbela et al., 2011). To quantify the residual area, the half section (semi-circle) of the rebar facing the direction of ingress of the corrosion agents is considered. Therefore, let $\Delta \boldsymbol{r_b}$ be the maximum radius loss to corrosion, $\boldsymbol{r_b}$ the original radius of the rebar and $\boldsymbol{R_{rb}}$ the residual radius of the rebar.

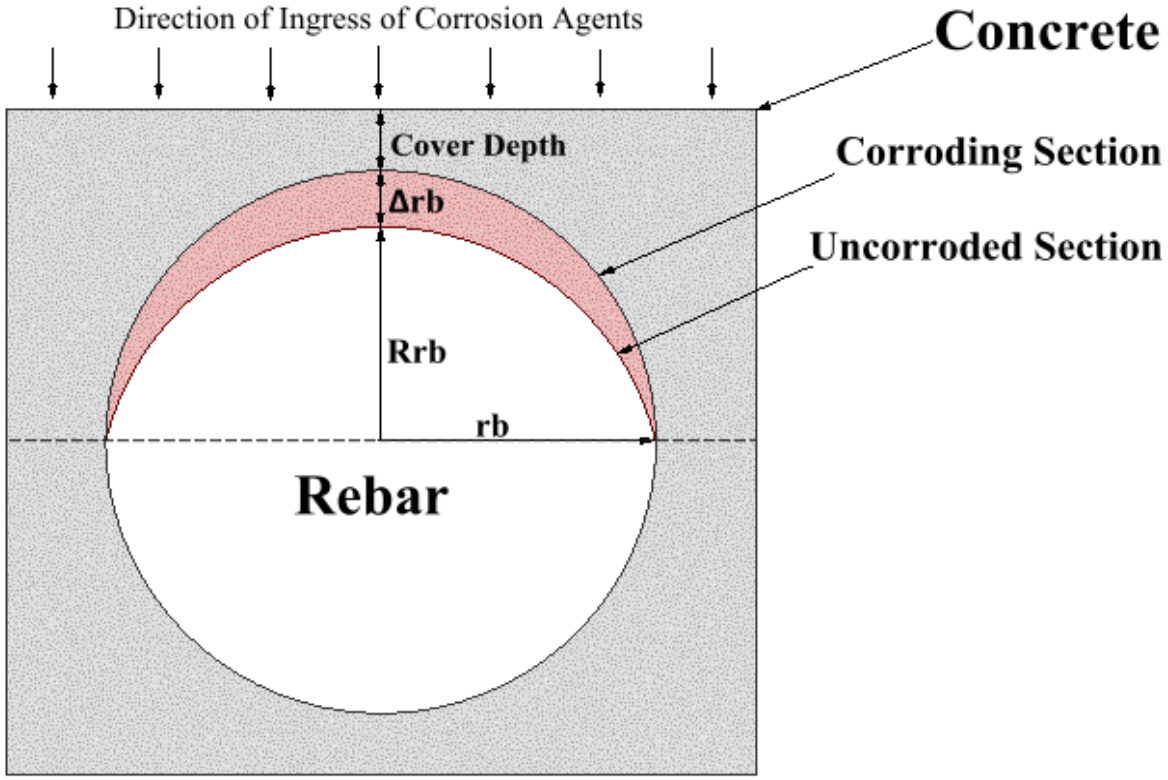

Figure 5. 10 Schematic of Non-Uniform Corrosion

The volume of steel being corroded (V_s) is:

$$V_s = \frac{\pi r_b{}^2 h}{2} - \frac{\pi(r_b - \Delta r_b) r_{bh}}{2} = \frac{\pi}{2}[r_b{}^2 - (r_b - \Delta r_b) r_b]h \qquad \text{---------- Eq. – 5.10}$$

Following the same approach from Eq. 5.5 to Eq. 5.9 will yield the pressure.

5.5.2 COMPARISON OF UNIFORM AND NON-UNIFORM PRESSURE

Since the developed pressure is directly proportional to the volume of steel being corroded, the comparison was made in terms of the volume of steel loss to corrosion. For comparison, similar assumption of the one-directional ingress of corrosion agents and the consideration of half section of the rebar facing the direction of ingress were employed to uniform corrosion. Based on the selected radius loss as indicated in Table 5.4 and with the assumption that the radius loss is constant for both cases ($\boldsymbol{x_p}$ or $\boldsymbol{\Delta r_b}$), it is shown that the assumption of uniform corrosion produces greater volume of steel loss.

Table 5. 4 Comparison of Uniform and Non-uniform corrosion

Steps	x_p *or* Δr_b (mm)	r_b (mm)	Uniform Corrosion	Non-uniform Corrosion
			$V_s\ (mm^3)$	$V_s\ (mm^3)$
1	0.01	6	0.1882	0.0942
2	0.02	6	0.3762	0.1884
3	0.05	6	0.9381	0.4710
4	0.10	6	1.8683	0.9420
5	1.50	6	24.7275	14.1300
6	2.00	6	31.4000	18.8400

5.6 BRIEF DESCRIPTION OF THE SIMULATION PROCEDURES

As stated earlier in Section 5.1, the simulation was conducted in ANSYS Workbench 19.2, student version. ANSYS Workbench offers a graphical user interface simulation environment which serves as the project workspace. This workspace enables the performance of several types of analysis, from structural to computational fluid dynamics, etc. As illustrated in the project schematics shown in Figure 5.11 to 5.13, the analysis was conducted as static structural analysis. The procedures of building the model consisted of defining the material properties in the Engineering data section, importing the geometry from Design Modeler and then modelling. The modelling was done in ANSYS Mechanical which is launched from workbench by clicking on the model icon in the schematic. In mechanical, the mesh setting was defined, the loads and boundary conditions applied as well as other desired setting, after which the solution was obtained. Due to the spacious nature of the ANSYS simulation results, the complete report of each case could not be presented in this paper. However, detailed discussions of the simulation results are presented in Chapter 6 and the full report of SP-PC100 of Case I is presented in Appendix D to further illustrates the procedures and settings considered in the simulation.

5.7 VERIFICATION AND VALIDATION

Verification of the simulation results was done by analytical calculations and by mesh refinement. The simulations validation was also done by comparing the results with experimental data of other researchers.

5.8 SUMMARY

This chapter presented discussions about the simulation procedures conducted in ANSYS 19.2 student version. All cases were modelled as two-dimensional (2D) planes stress geometry. Several assumptions were employed for the derivation of the applied pressure as well as the damage analysis for simplification of the entire simulation process. The comparison of the pressure derived based on uniform corrosion with that of non-uniform corrosion shows that at a given radius loss, non-uniform corrosion produces lesser pressure. This concurred with the discussion presented in Section 2.4. Thus, the approach of calculating the applied pressure and conducting the simulation based on the assumption of uniform corrosion was adopted in this investigation.

5.9 REFERENCES

1. Andrade, C., Alonso, C. and Molina, F.J., 1993. Cover cracking as a function of bar corrosion: Part I-Experimental test. Materials and structures, 26(8), pp.453-464.
2. Bangash, M.Y.H., 1989. Concrete and concrete structures: Numerical modelling and applications.
3. Chen, E. and Leung, C.K., 2015. Finite element modelling of concrete cover cracking due to non-uniform steel corrosion. Engineering Fracture Mechanics, 134, pp.61-78.
4. Chen, E. and Leung, C.K.Y., 2013. Numerical modelling of non-uniform steel corrosion development and its mechanical influences on reinforced concrete structures. In 8th International Conference on Fracture Mechanics of Concrete and Concrete Structures-FraMCoS-8, Toledo, Spanin.
5. Chen, X. and Liu, Y., 2014. Finite element modelling and simulation with ANSYS Workbench. CRC Press.
6. Chernin, L. and Val, D.V., 2011. Prediction of corrosion-induced cover cracking in reinforced concrete structures. Construction and Building Materials, 25(4), pp.1854-1869.
7. Chernin, L., Val, D.V. and Volokh, K.Y., 2010. Analytical modelling of concrete cover cracking caused by corrosion of reinforcement. Materials and Structures, 43(4), pp.543-556.
8. Chun-Qing, L., Melchers, R.E. and Jian-Jun, Z., 2006. Analytical model for corrosion-induced crack width in reinforced concrete structures. ACI Structural Journal, 103(4), p.479.
9. Dill, E.H., 2011. The finite element method for mechanics of solids with ANSYS applications. CRC Press.
10. Du, X., Jin, L. and Zhang, R., 2014. Modelling the cracking of cover concrete due to non-uniform corrosion of reinforcement. Corrosion Science, 89, pp.189-202.
11. Du, Y.G., Chan, A.H.C., Clark, L.A., Wang, X.T., Gurkalo, F. and Bartos, S., 2013. Finite element analysis of cracking and delamination of concrete beam due to steel corrosion. Engineering Structures, 56, pp.8-21.
12. Habibi, S., 2017. Finite Element Modelling of Corrosion Damaged Reinforced Concrete Structures, Master thesis, University of Toronto (Canada).

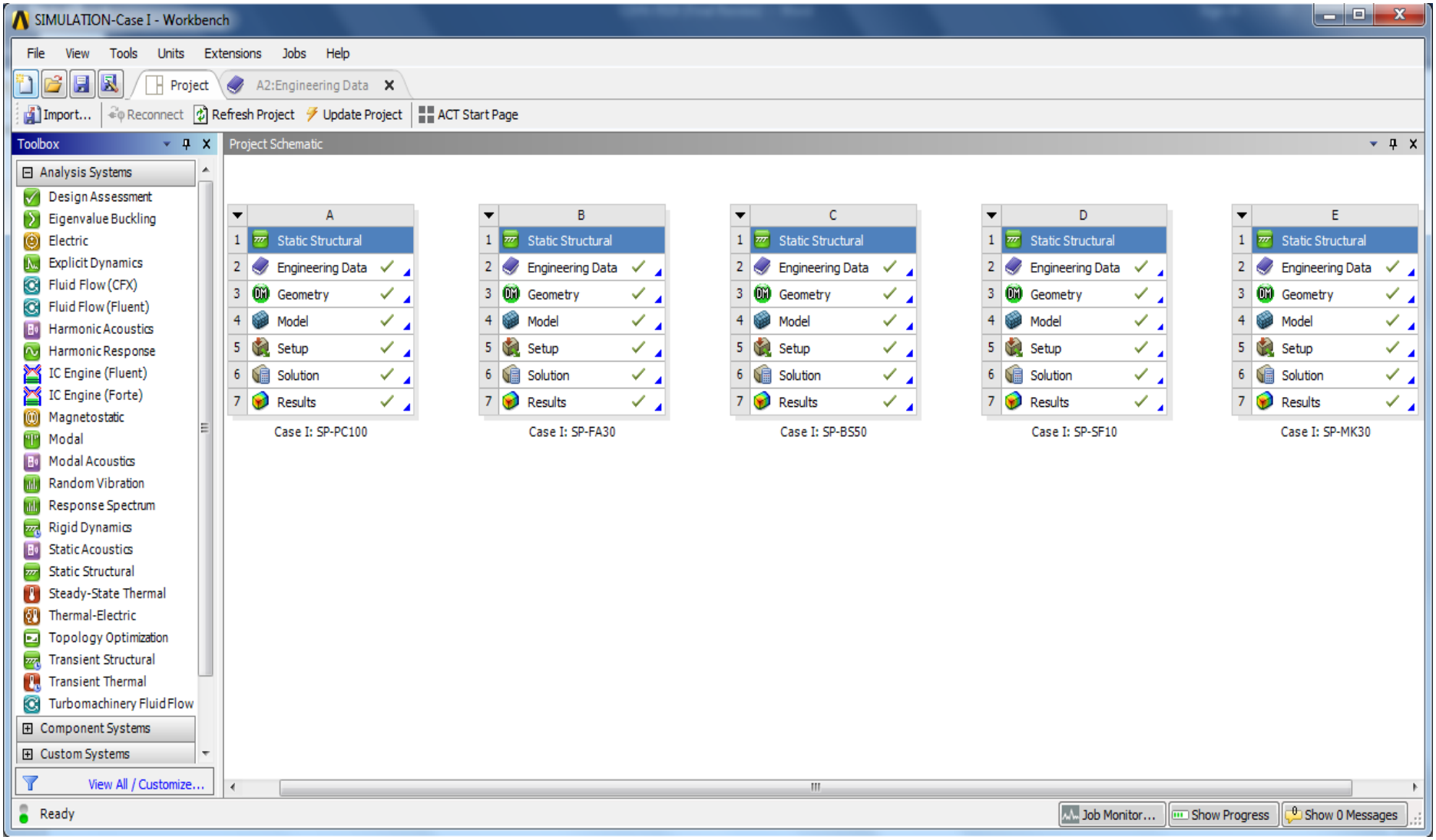

Figure 5. 11 Project Schematic of Case I

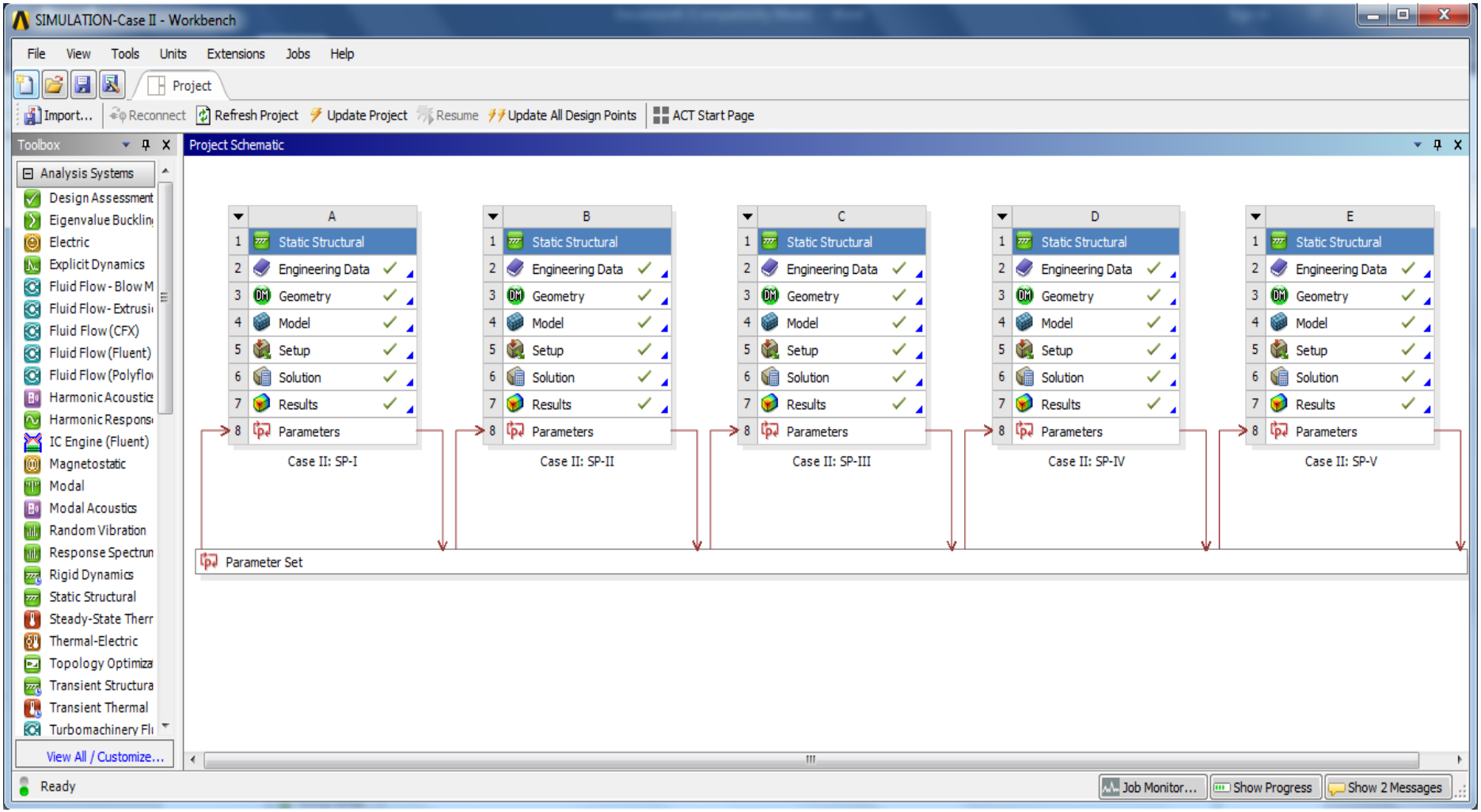

Figure 5. 12 Project Schematic of Case II

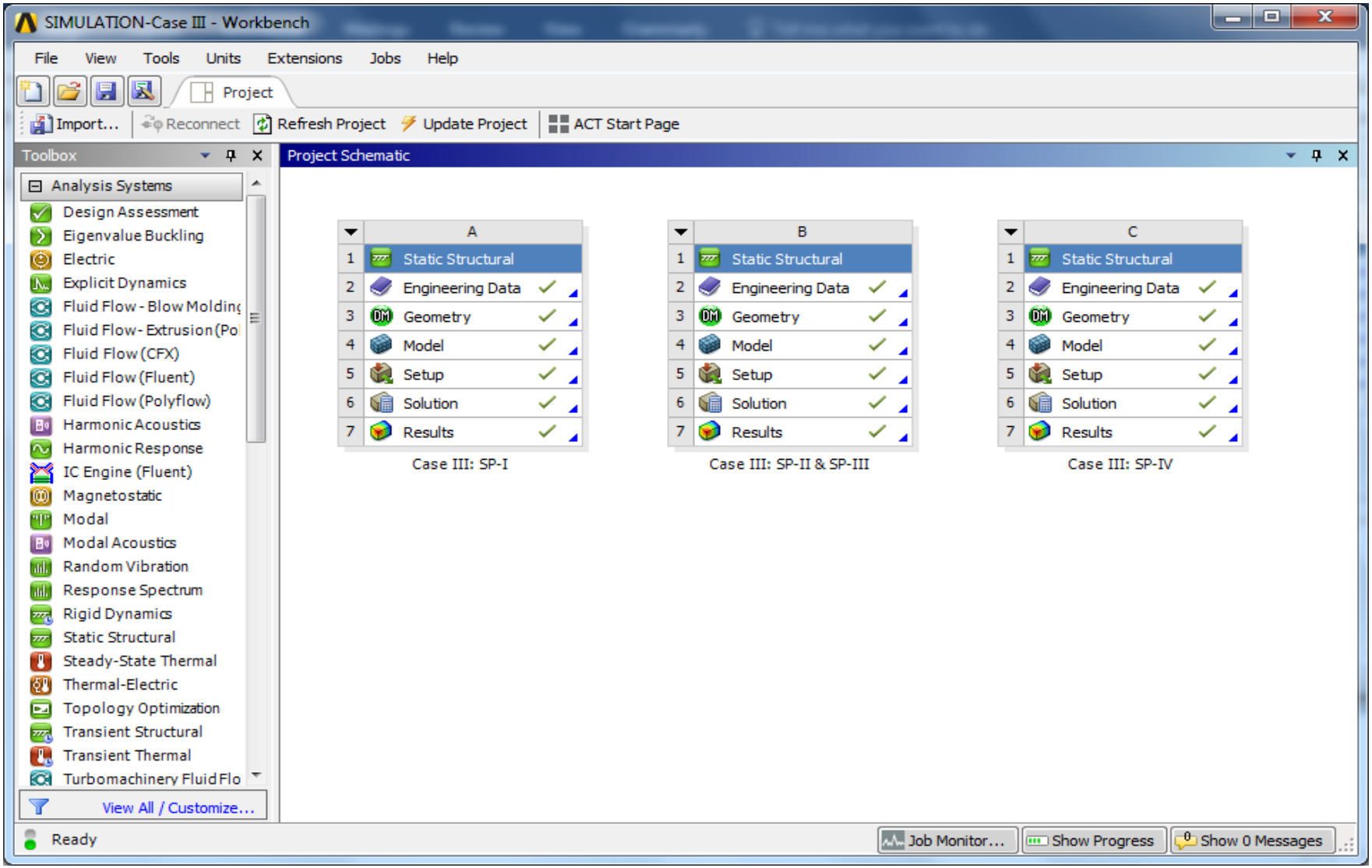

Figure 5. 13 Project Schematic of Case III

13. Jamali, A., Angst, U., Adey, B. and Elsener, B., 2013. Modelling of corrosion-induced concrete cover cracking: A critical analysis. Construction and Building Materials, 42, pp.225-237.
14. Kallias, A.N. and Rafiq, M.I., 2010. Finite element investigation of the structural response of corroded RC beams. Engineering Structures, 32(9), pp.2984-2994.
15. Kim, S.H.K. and Ann, K.Y., 2010. Modelling steel corrosion in concrete structures-part 2: A unified adaptive finite element model for simulation of steel corrosion. International Journal of Electrochemical Science, 5(3), pp.314-326.
16. Kwan, A.K.H. and Ma, F.J., 2016. Crack width analysis of reinforced concrete under direct tension by finite element method and crack queuing algorithm. Engineering Structures, 126, pp.618-627.
17. Malumbela, G., Alexander, M. and Moyo, P., 2011. Model for cover cracking of RC beams due to partial surface steel corrosion. Construction and Building Materials, 25(2), pp.987-991.
18. Mehta, P.K. and Monteiro, P.J., 2006. Concrete: microstructure, properties, and materials. 2006.
19. Molina, F.J., Alonso, C. and Andrade, C., 1993. Cover cracking as a function of rebar corrosion: part 2—numerical model. Materials and structures, 26(9), pp.532-548.
20. Muthulingam, S. and Rao, B.N., 2015. Non-uniform corrosion states of rebar in concrete under chloride environment. Corrosion Science, 93, pp.267-282.
21. Nakasone, Y., Yoshimoto, S. and Stolarski, T.A., Engineering Analysis with ANSYS Software (2007).
22. Oh, B.H., Kim, K.H., Jang, B.S., Kim, J.S. and Jang, S.Y., 2007. Realistic model for corrosion-induced cracking in reinforced concrete structures. In: Carpinteri, A., Gambarova, P. G., Ferro, G., & Plizzari, G. (eds) Proceedings of the 6th international conference on fracture mechanics of concrete and concrete structures, Catania, Italy, 17-22 June 2007: Fracture mechanics of concrete and concrete structures. London, Taylor & Francis.
23. Potisuk, T., Higgins, C.C., Miller, T.H. and Yim, S.C., 2011. Finite element analysis of reinforced concrete beams with corrosion subjected to shear. Advances in Civil Engineering, 2011.
24. Static Structural Analysis, 19.2 Documentation File. ANSYS Manual.
25. Shi, Z., 2009. Crack analysis in structural concrete: theory and applications. Butterworth-Heinemann.
26. Sutrisno, W., Hartana, I.K., Suprobo, P., Wahyuni, E. and Iranata, D., 2016. Analysis of Corrosion Induced Crack in Reinforced Concrete with Smeared Crack Approach. International Journal of Applied Engineering Research, 11(19), pp.9970-9974.
27. Zhang, J., Ling, X. and Guan, Z., 2017. Finite element modelling of concrete cover crack propagation due to non-uniform corrosion of reinforcement. Construction and Building Materials, 132, pp.487-499.
28. Zhao, Y., Yu, J., Hu, B. and Jin, W., 2012. Crack shape and rust distribution in corrosion-induced cracking concrete. Corrosion science, 55, pp.385-393.

6 RESULTS AND DISCUSSIONS OF THE FEA

6.1 INTRODUCTION

This chapter presents the simulation results and discussions, as well as the comparison of Case I simulation results with those obtained from the impressed current. The simulation was conducted with the intention of obtaining a clearer insight into the relationship between the stresses and deformation arising in concrete as the result of reinforcement corrosion. In the simulation, the pressure exerted by the corrosion product on the surrounding concrete was applied as internal pressure. The discussions presented in this chapter set the basis for the derivation of the proposed model.

6.2 RESULTS AND DISCUSSIONS

6.2.1 CASE I RESULT

The discussion of Case I simulation results is focused on comparing the results with those of the impressed current and the influence of the specimens' strength on the deformation response of the simulation. The results of Case I correlate well with the those of the impressed current regarding the influence of cover depth. For all specimens, the simulation results show higher deformation occurring at sections with the lowest cover depth (15 mm) and the maximum deformation occurring at Bar-3. These are in confirmative with results from the impressed current and can explain the reason the first crack appeared on bars at 15 mm cover depth for all specimens that cracked during the impressed current as well as partially justified why Bar-3 was the first to crack in SP-FA30, SP-BS50 and SP-SF10. A similar influence of the cover depth was observed with the internal stresses, with the maximum occurring at sections with 15 mm cover depth. Internal stresses comprise the normal, maximum principal, and von-Mises stresses develop in response or as the result of the applied pressure. This trend indicates that the stiffness of the concrete cover also depends on the depth of the cover.

With regards to the specimen's strength, the deformation varies according to the strength of the specimens. The specimen with the lowest strength exhibited the highest deformation, and the one with the highest strength exhibited the lowest deformation. An increase in strength increases the stiffness of the concrete cover, thus, reducing the deformation at a given applied pressure. To further explained the observed relationship between the deformation and the specimens' strength, images from Case I simulation have been included in ascending order of the specimens' strength (SP-FA30, SP-BS50, SP-PC100, SP-SF10 and SP-MK30). Figure 6.1 – 6.5 illustrate the decreasing trend of the maximum deformation due to the increase in strength per specimen.

The internal stresses were the same for all specimens as was the applied load. Thus, the variation in the specimens' strength only influences the deformation. Further discussions on the influence of the concrete cover depth are presented in the parametric studies.

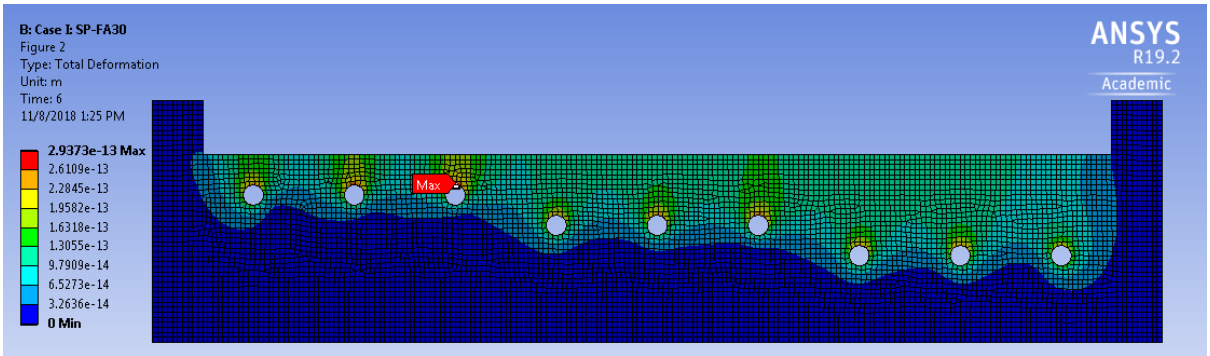

Figure 6. 1 Total Deformation of SP-FA30

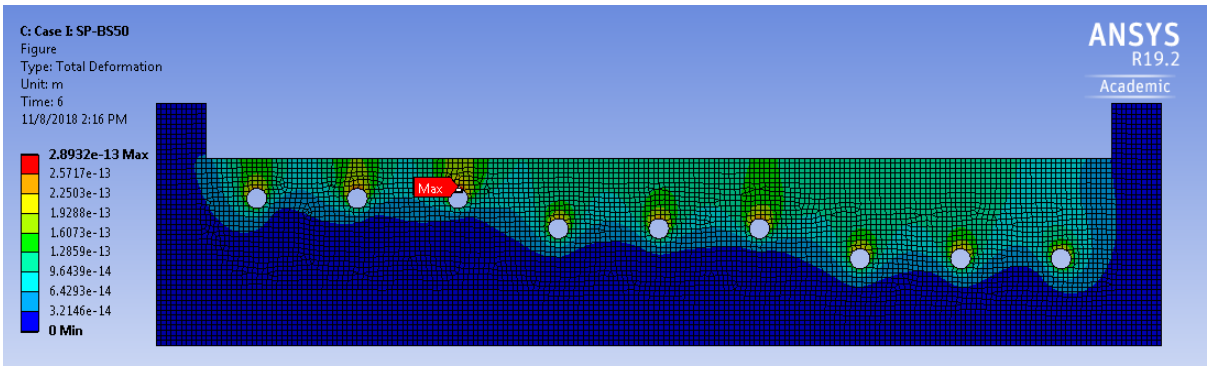

Figure 6. 2 Total Deformation of SP-BS50

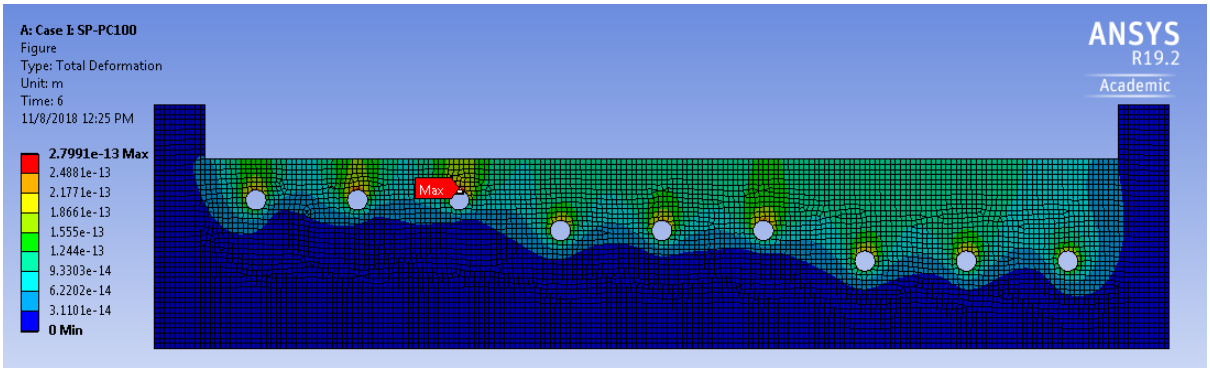

Figure 6. 3 Total Deformation of SP-PC100

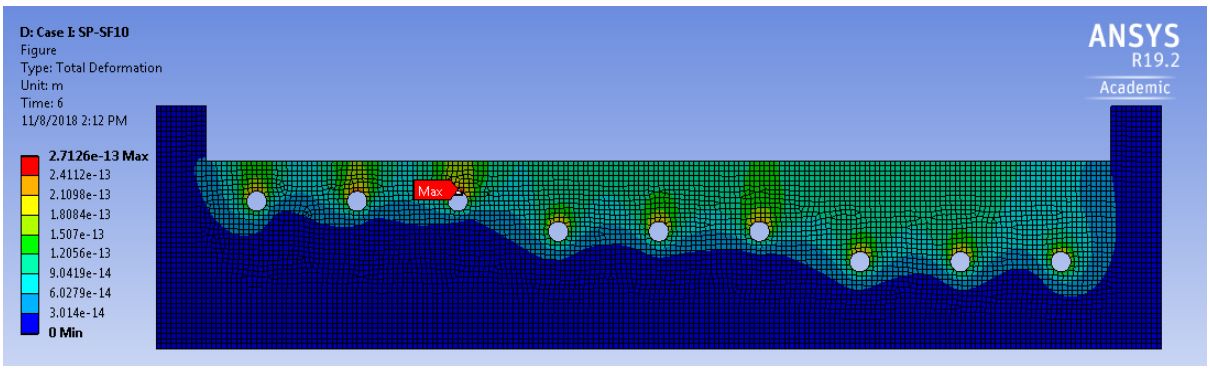

Figure 6. 4 Total Deformation of SP-SF10

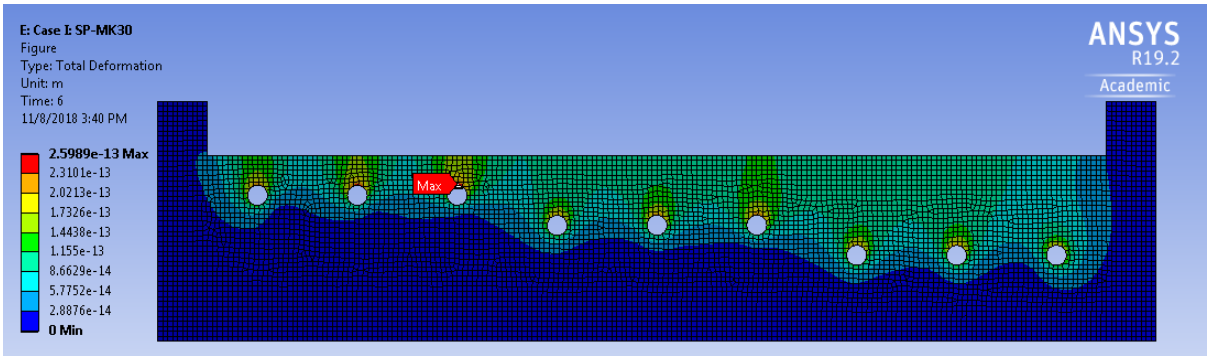

Figure 6. 5 Total Deformation of SP-MK30

6.2.2 PARAMETRIC STUDIES

The parametric analysis of this simulation was conducted with Case II. The parameters studied were the influence of concrete cover depth, tensile strength, modulus of elasticity and the rebar diameter. The below discussions present the parametric findings.

6.2.2.1 Concrete Cover Depth

The parametric analysis of the cover depth shows an inverse relationship between the concrete cover depth and the internal stresses (von-Mises, maximum principal, normal, etc.) as well as the deformation. At a given applied pressure, an increase in the depth of the concrete cover increases the stiffness (resistance to deformation) of the concrete cover, thus, reducing deformation and the internal stresses arising in response to the applied pressure. An increase in cover depth reduces internal stresses because of the increase in the area upon which the internal forces are acting. This finding is in confirmative with the findings of Pengwei et al. (2011) and other researchers. Figure 6.6 – 6.15 illustrate the observed relationships.

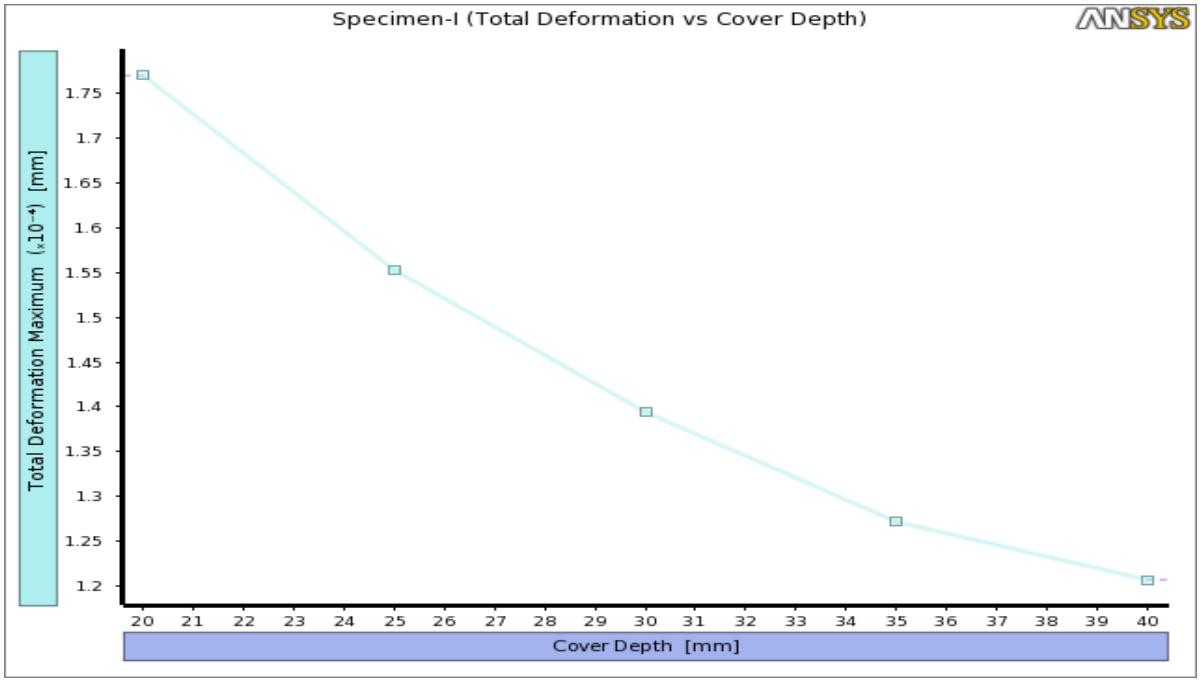

Figure 6. 6 Total Deformation vs Cover Depth (Case II, SP-I)

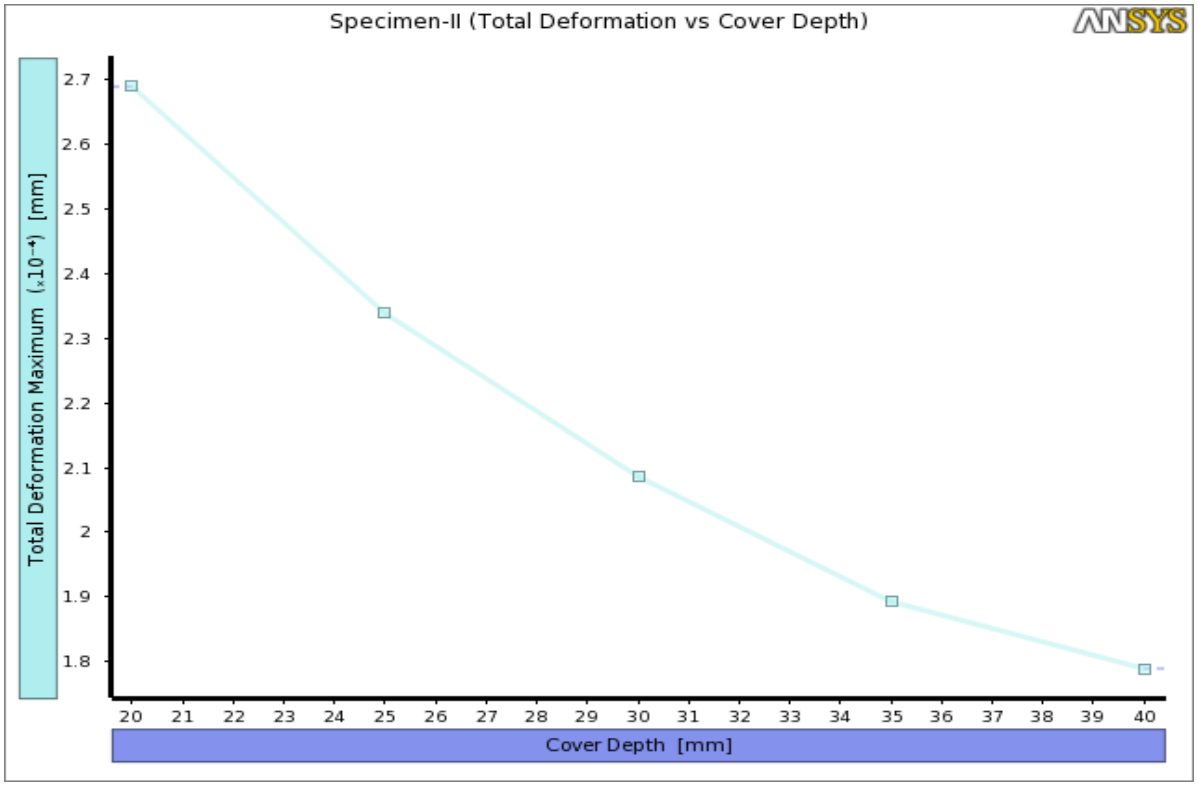

Figure 6. 7 Total Deformation vs Cover Depth (Case II, SP-II)

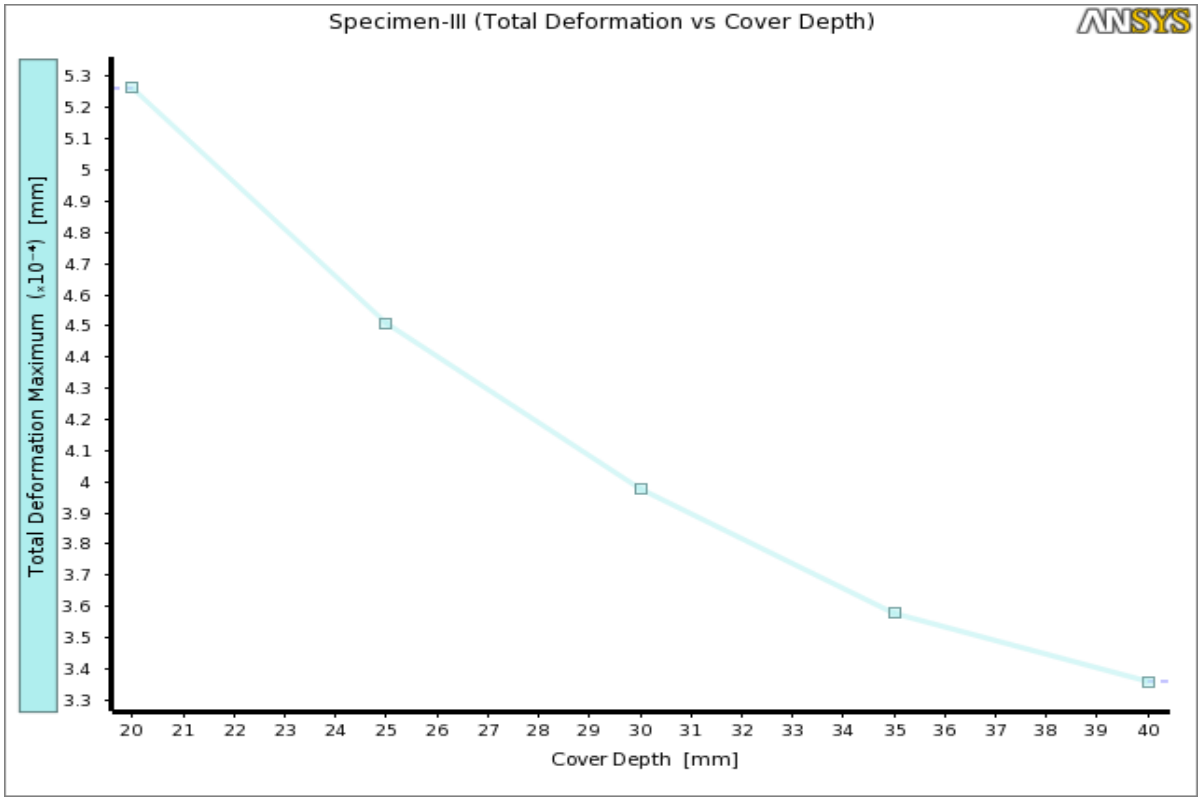

Figure 6. 8 Total Deformation vs Cover Depth (Case II, SP-III)

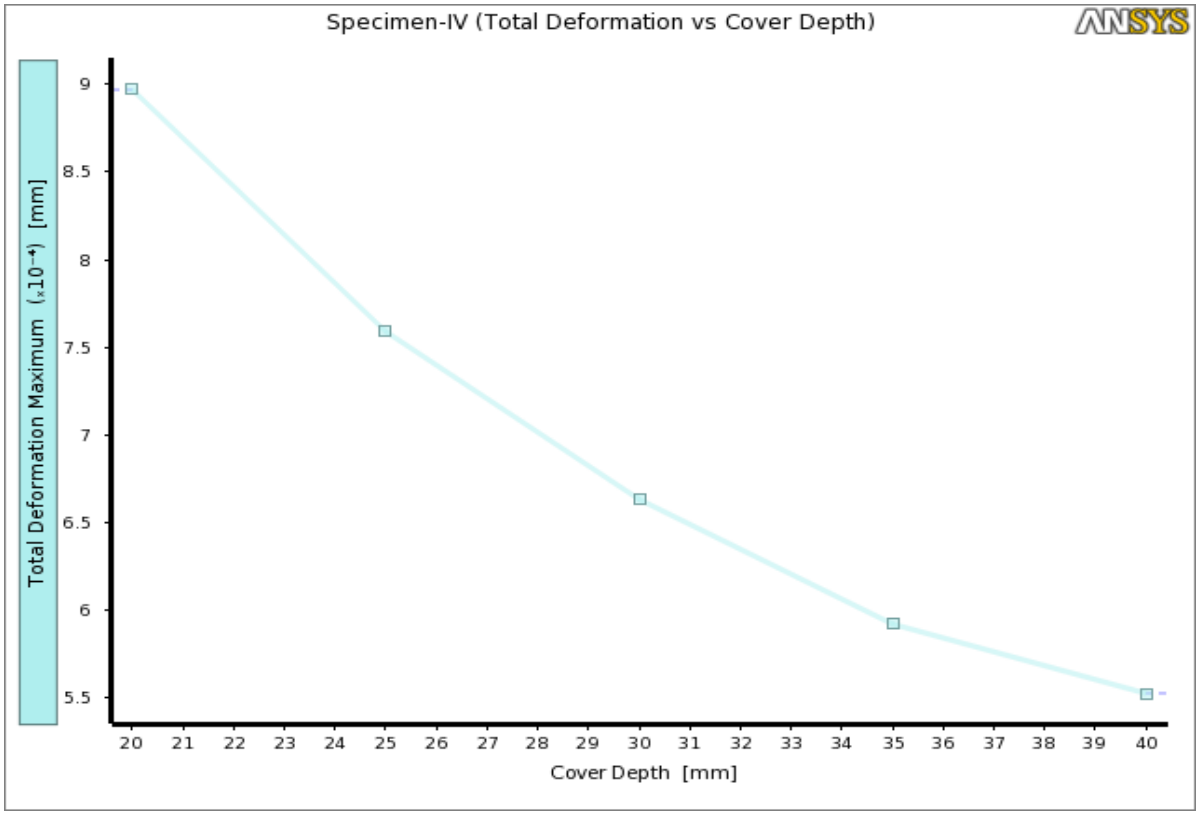

Figure 6. 9 Total Deformation vs Cover Depth (Case II, SP-IV)

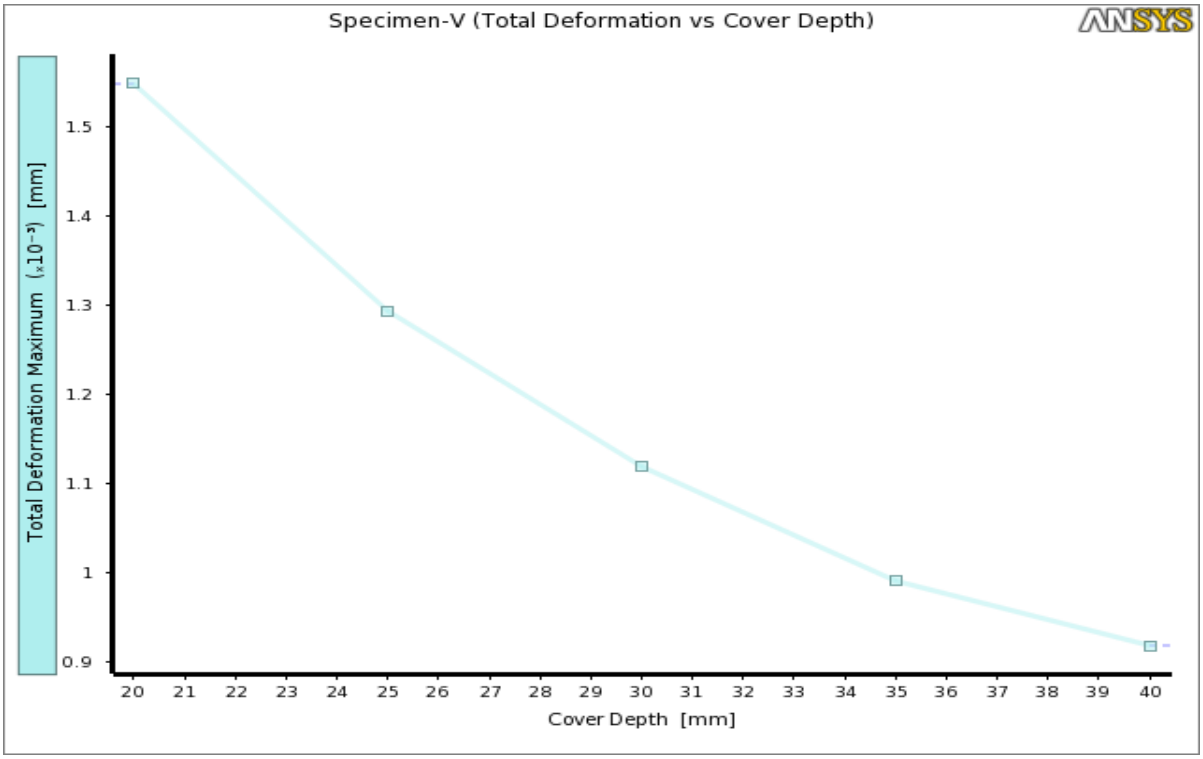

Figure 6. 10 Total Deformation vs Cover Depth (Case II, SP-V)

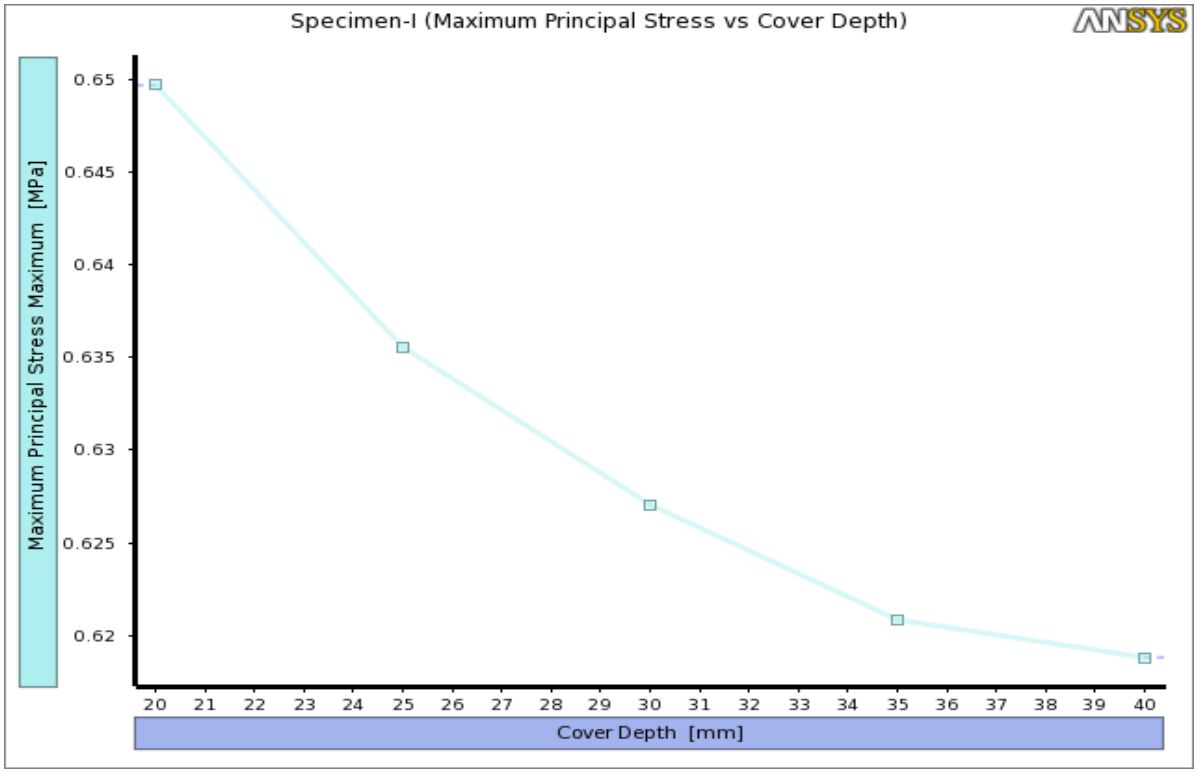

Figure 6. 11 Maximum Principal Stress vs Cover Depth (Case II, SP-I)

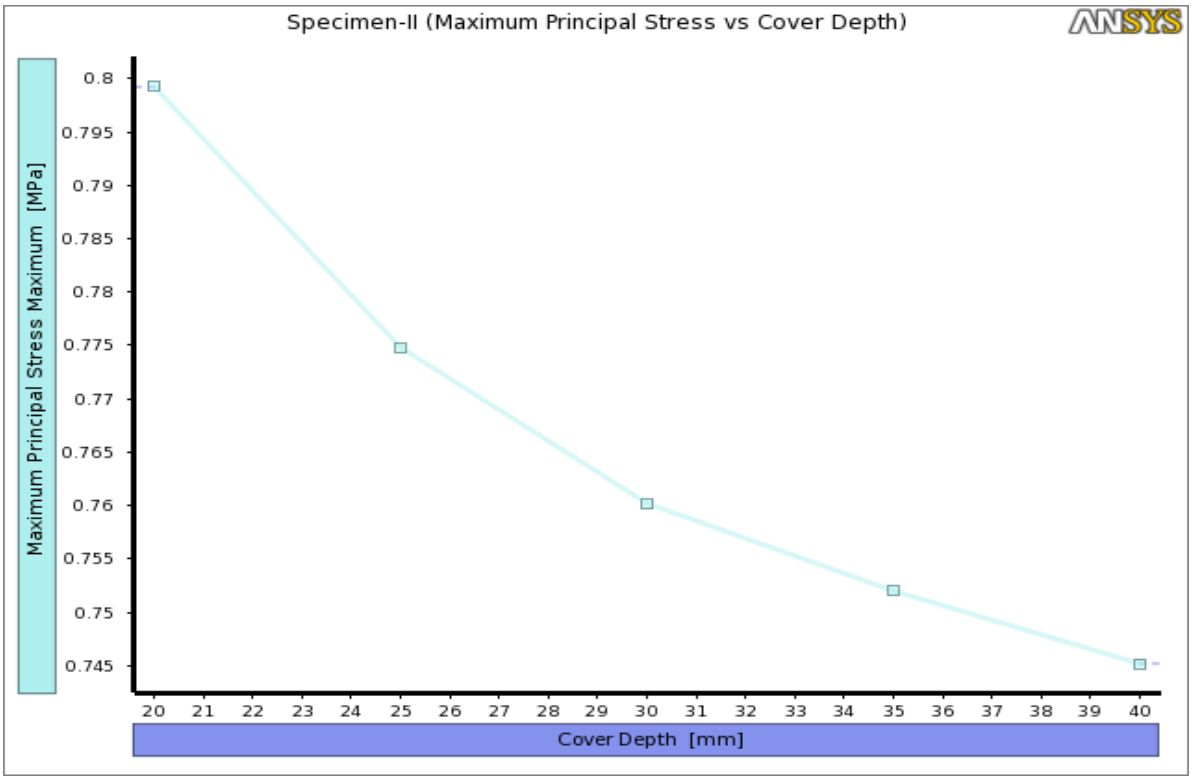

Figure 6. 12 Maximum Principal Stress vs Cover Depth (Case II, SP-II)

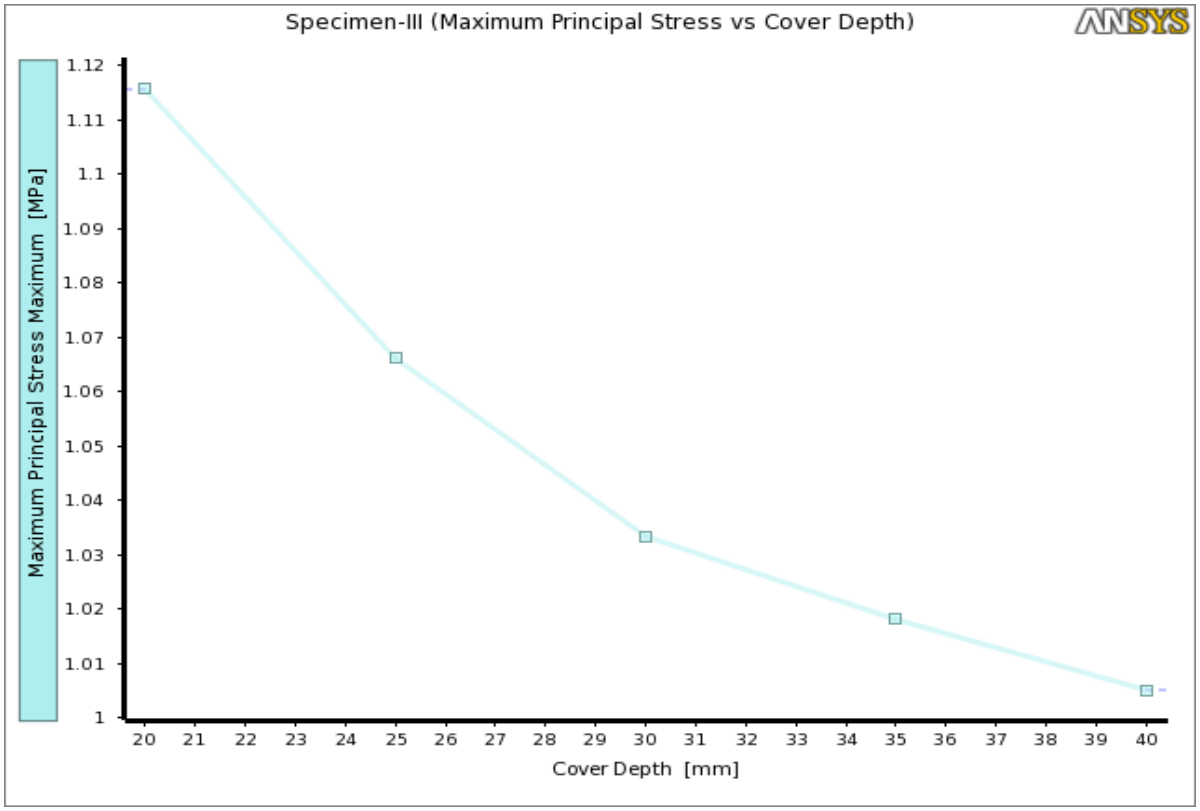

Figure 6. 13 Maximum Principal Stress vs Cover Depth (Case II, SP-III)

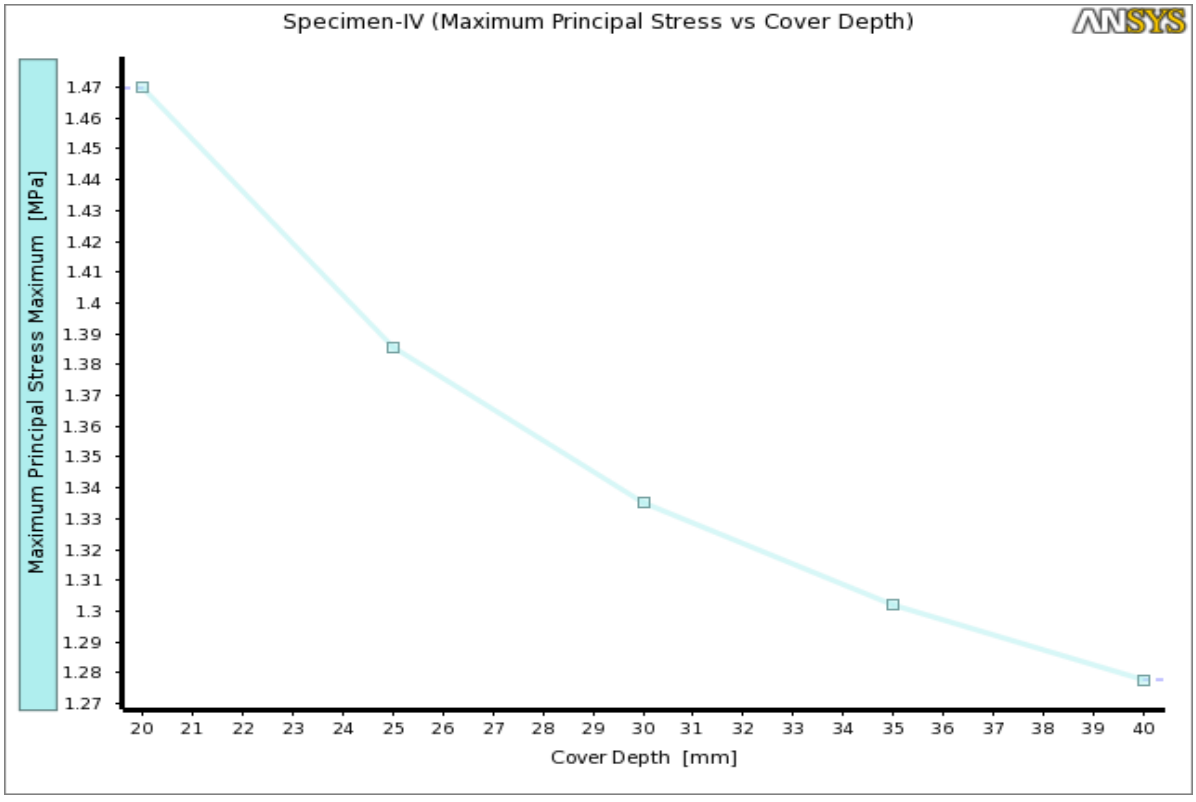

Figure 6. 14 Maximum Principal Stress vs Cover Depth (Case II, SP-IV)

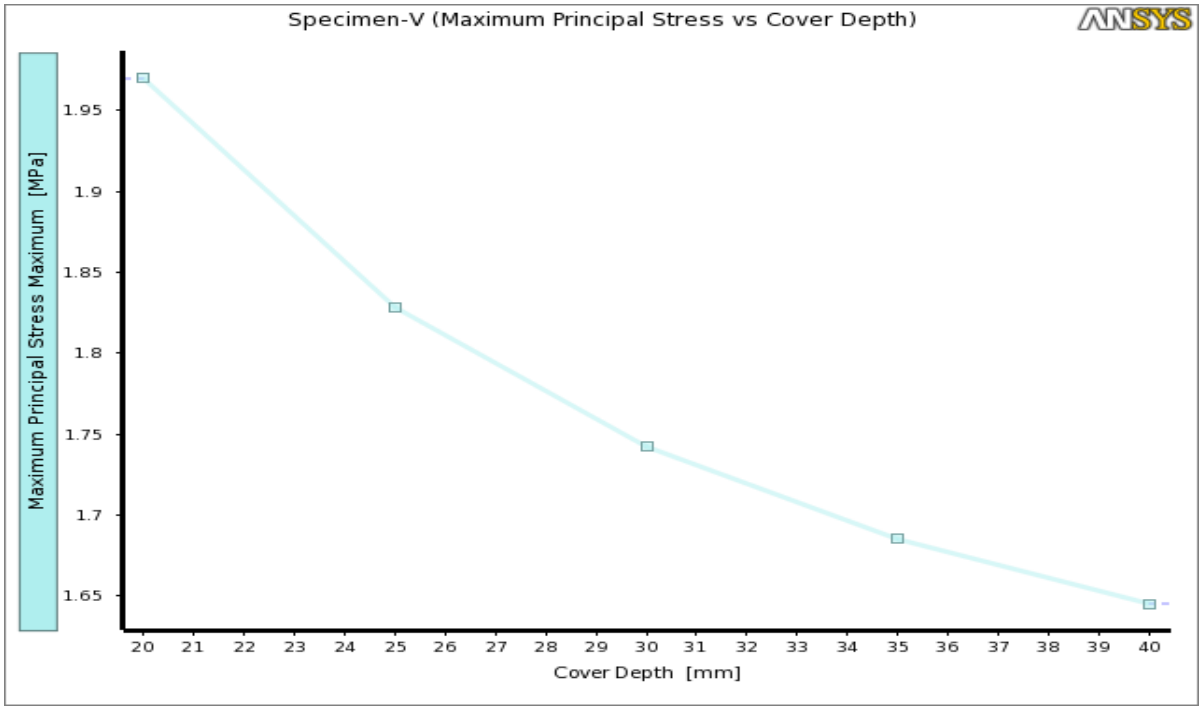

Figure 6. 15 Maximum Principal Stress vs Cover Depth (Case II, SP-V)

6.2.2.2 Concrete Tensile Strength

Concrete strength plays a vital role in preventing deformation and failure. Results of the parametric analysis show an inverse relationship between concrete tensile strength and the deformations. As illustrated in Figure 6.16 – 6.25, at a given applied pressure, an increase in the tensile strength increases the concrete cover resistance against the applied pressure leading to a reduction in deformations. Increase in tensile strength also increases the concrete cover stiffness. These results agree with most concrete failure theories and damage models.

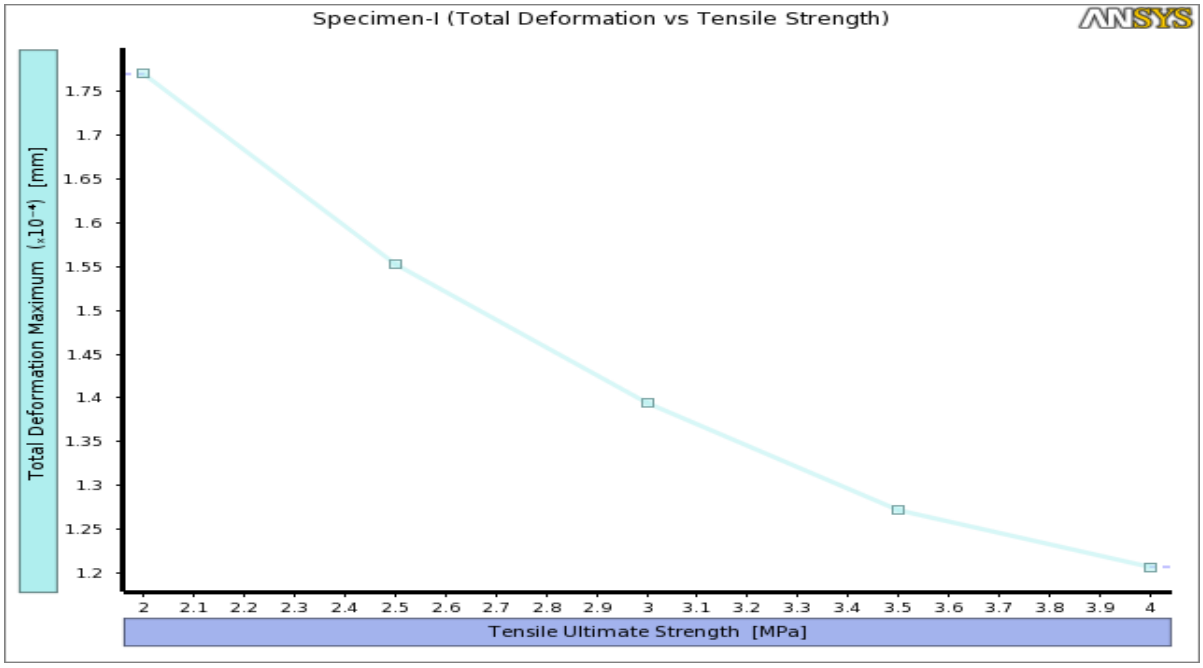

Figure 6. 16 Total Deformation vs Tensile Strength (Case II, SP-I)

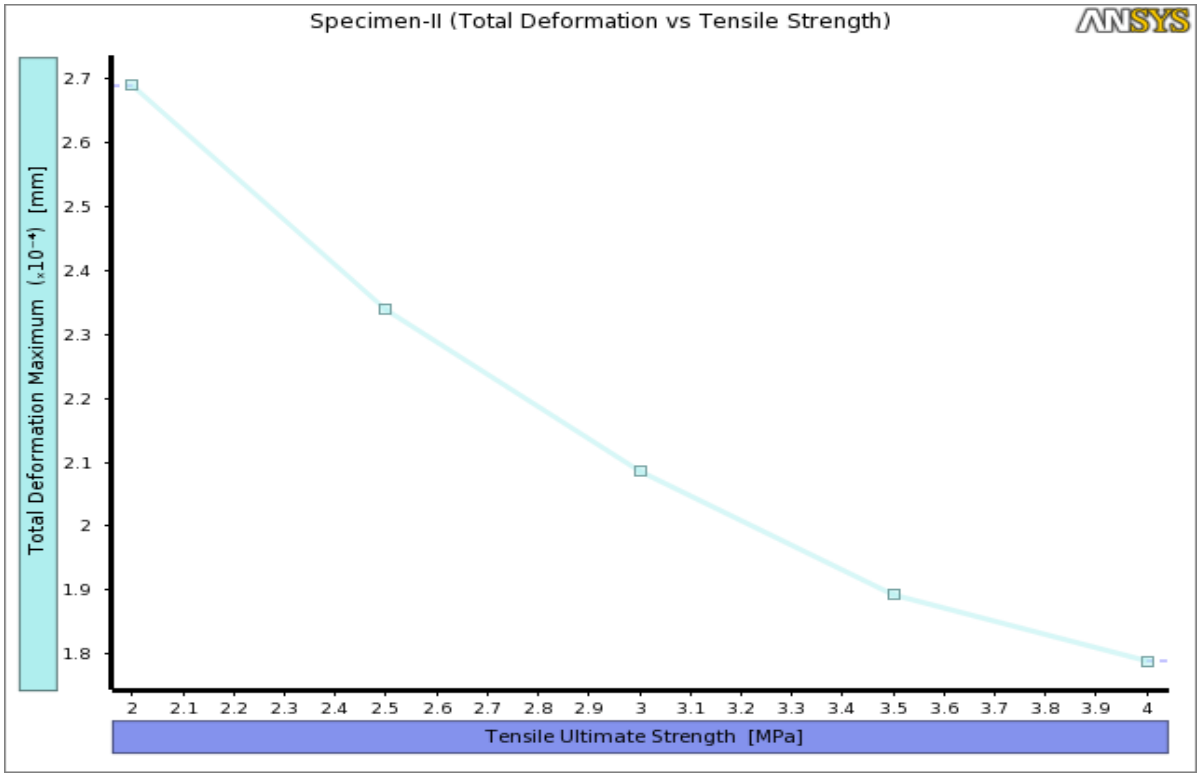

Figure 6. 17 Total Deformation vs Tensile Strength (Case II, SP-II)

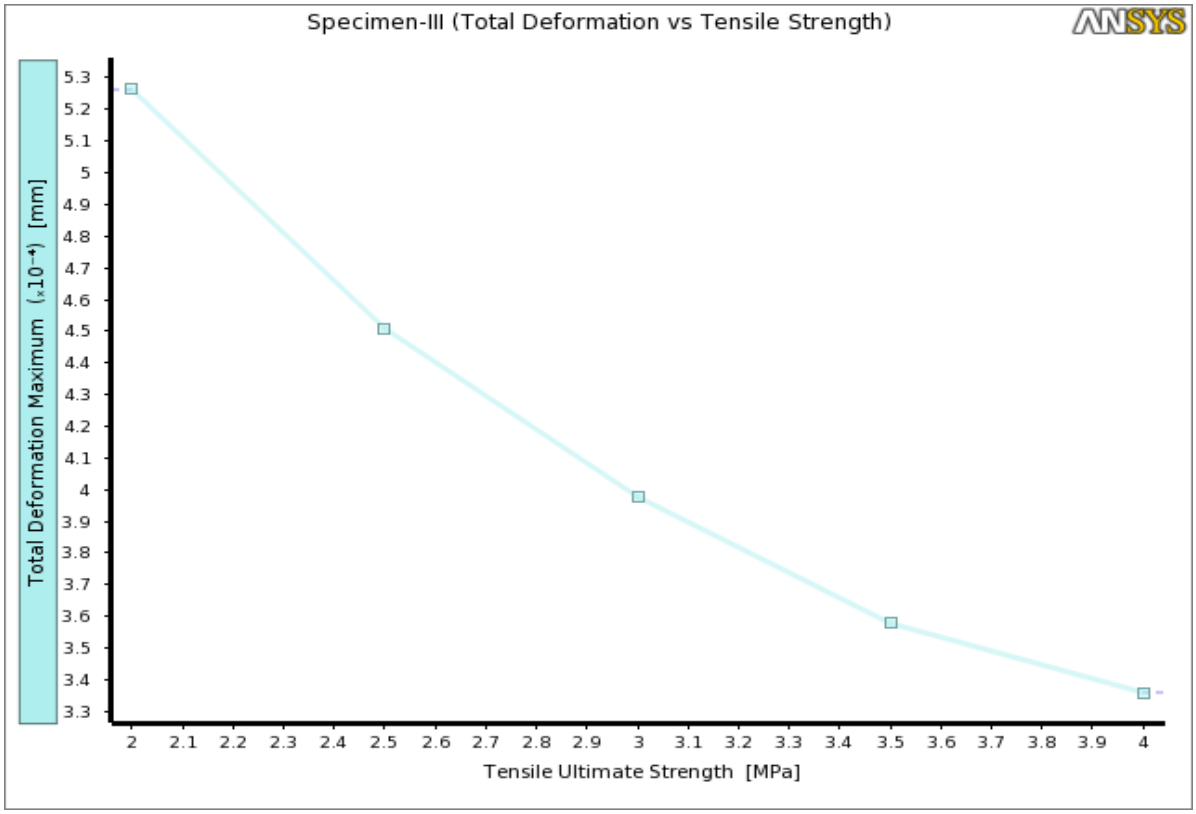

Figure 6. 18 Total Deformation vs Tensile Strength (Case II, SP-III)

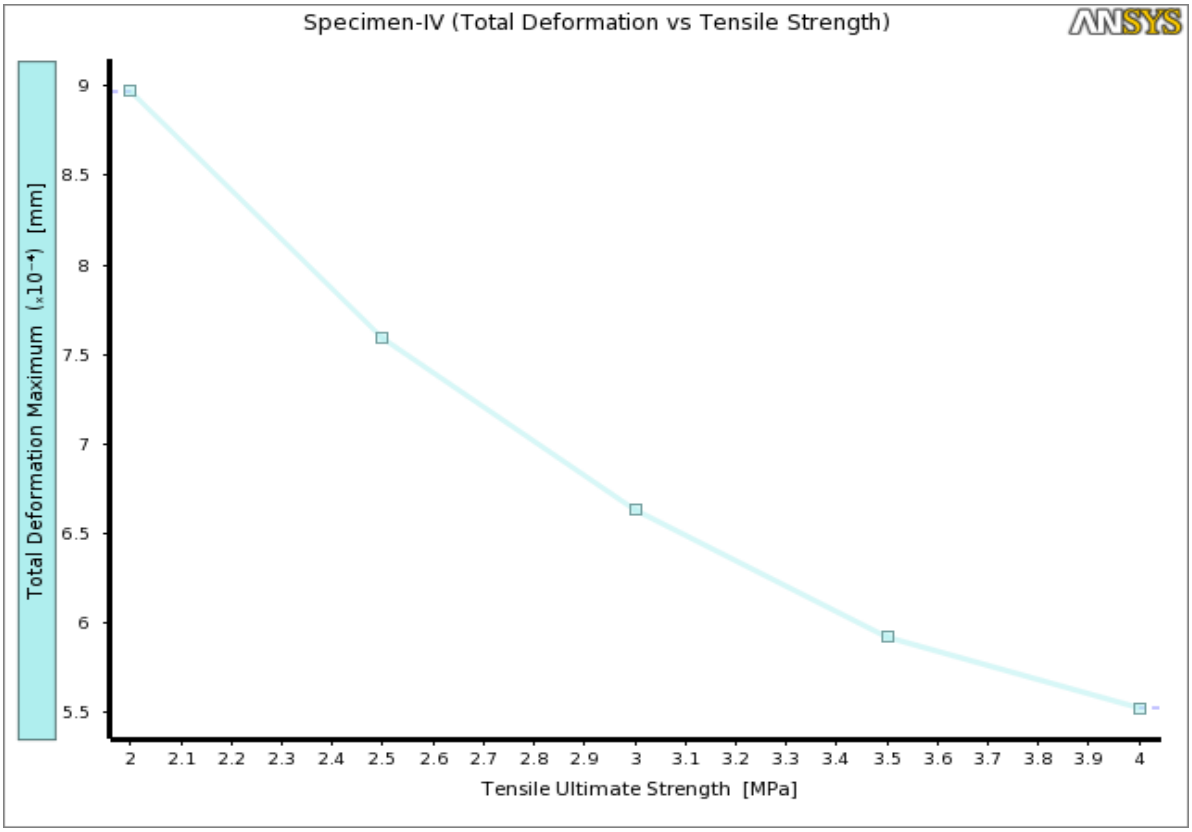

Figure 6. 19 Total Deformation vs Tensile Strength (Case II, SP-IV)

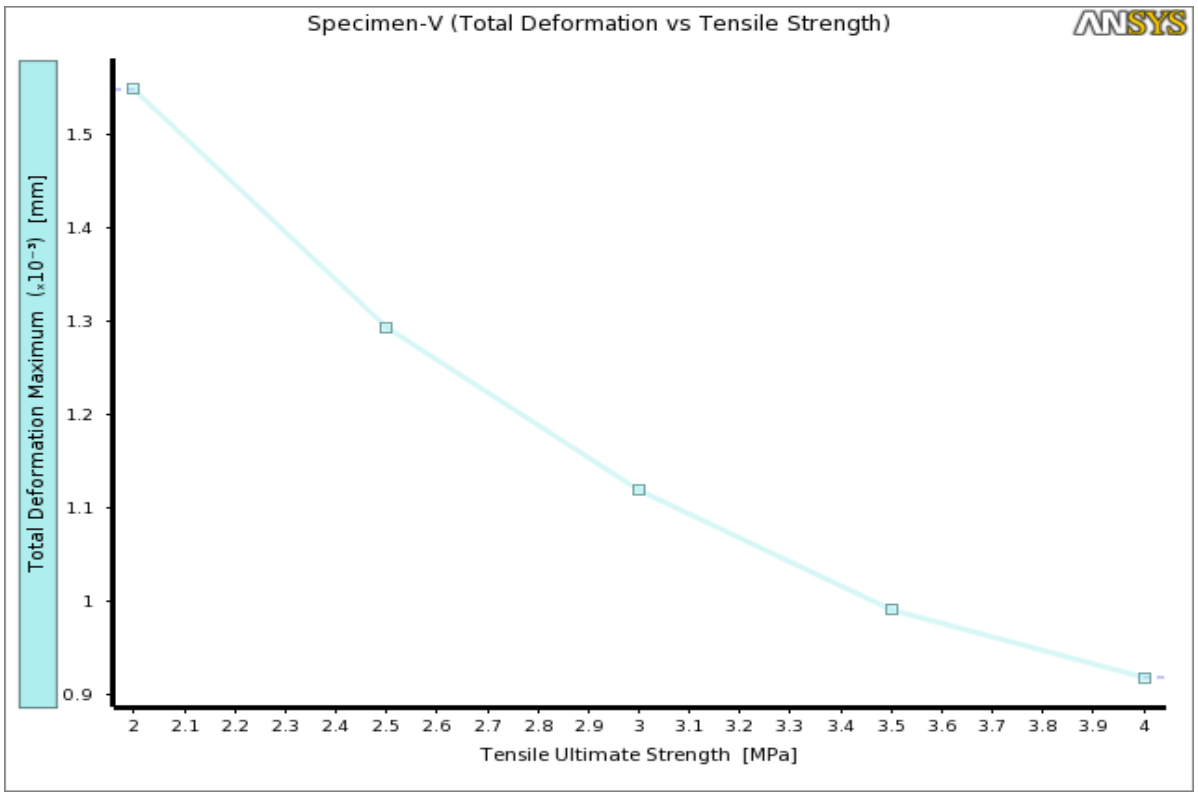

Figure 6. 20 Total Deformation vs Tensile Strength (Case II, SP-V)

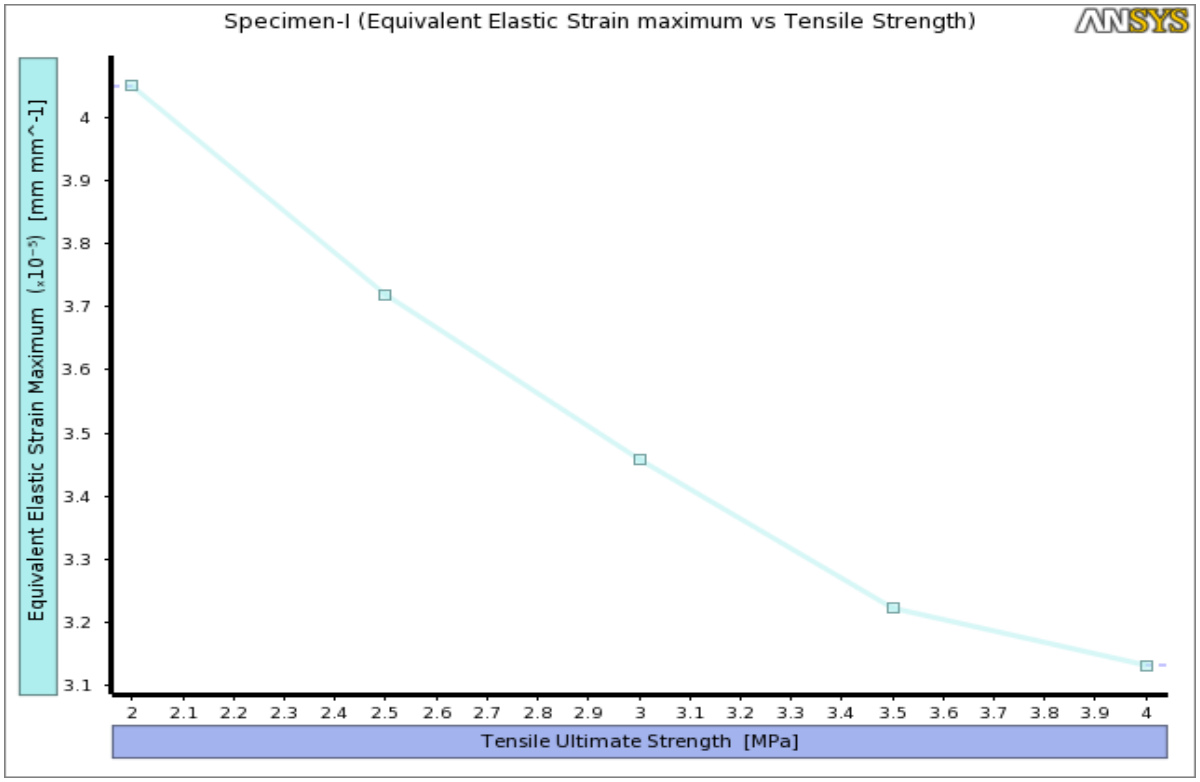

Figure 6. 21 Equivalent Elastic Strain (Max) vs Tensile Strength (Case II, SP-I)

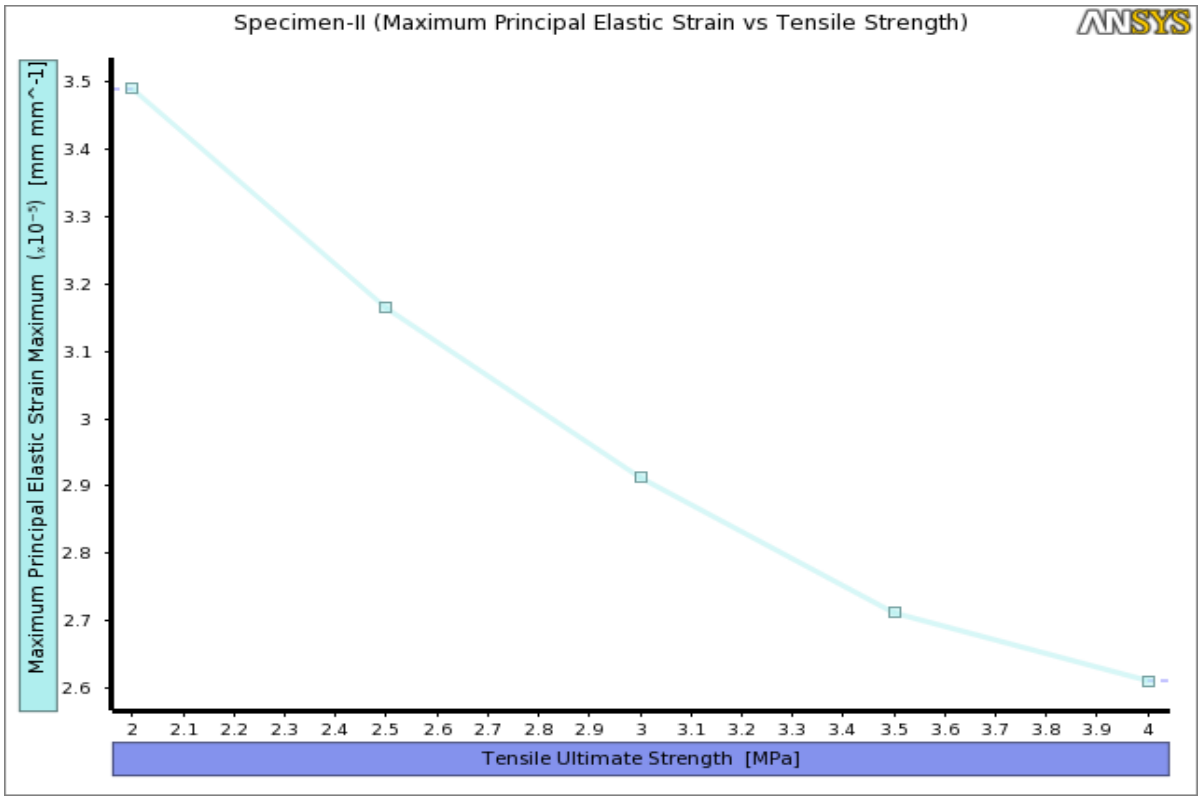

Figure 6. 22 Principal Elastic Strain (Max) vs Tensile Strength (Case II, SP-II)

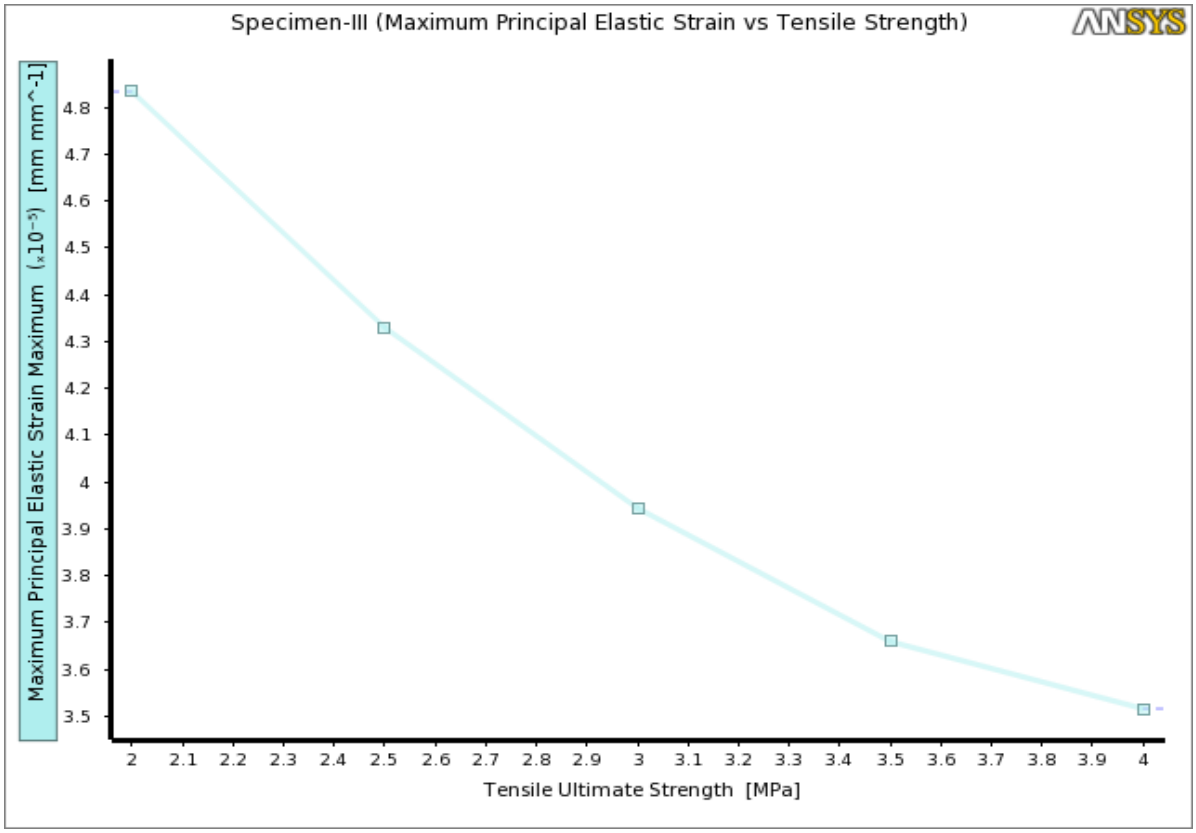

Figure 6. 23 Principal Elastic Strain (Max) vs Tensile Strength (Case II, SP-III)

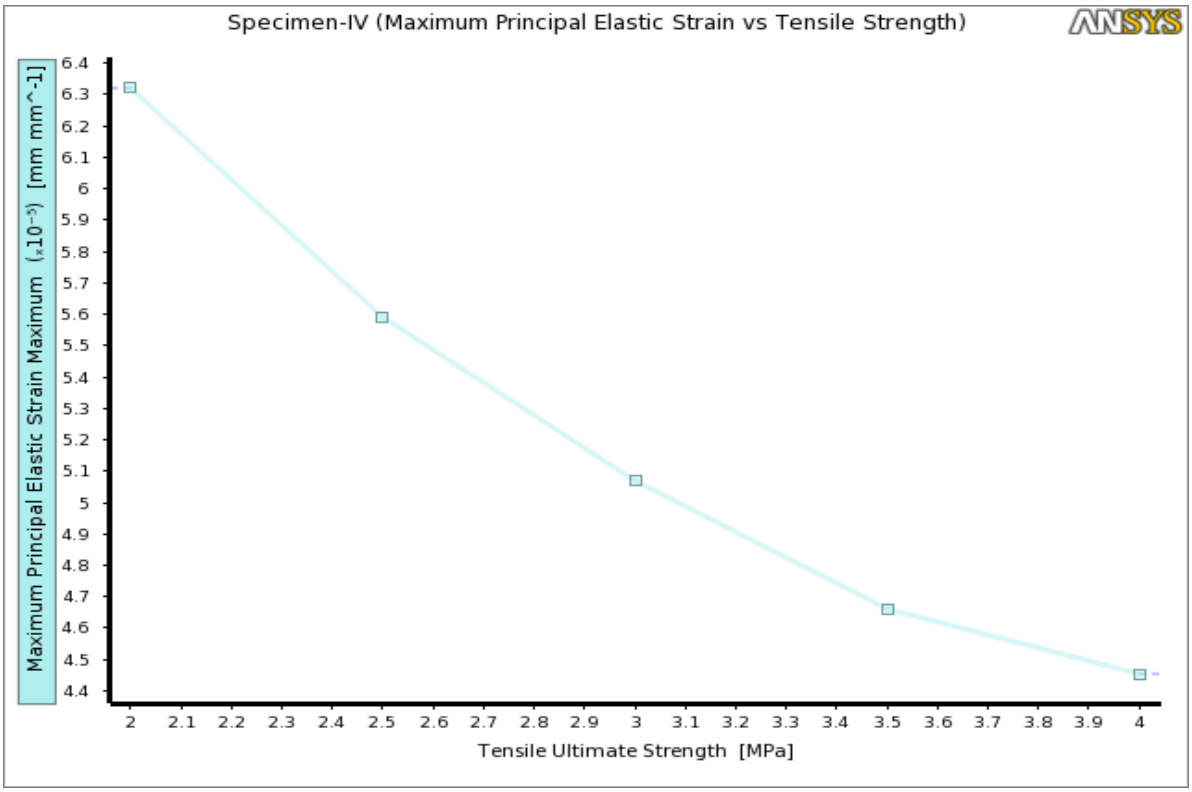

Figure 6. 24 Principal Elastic Strain (Max) vs Tensile Strength (Case II, SP-IV)

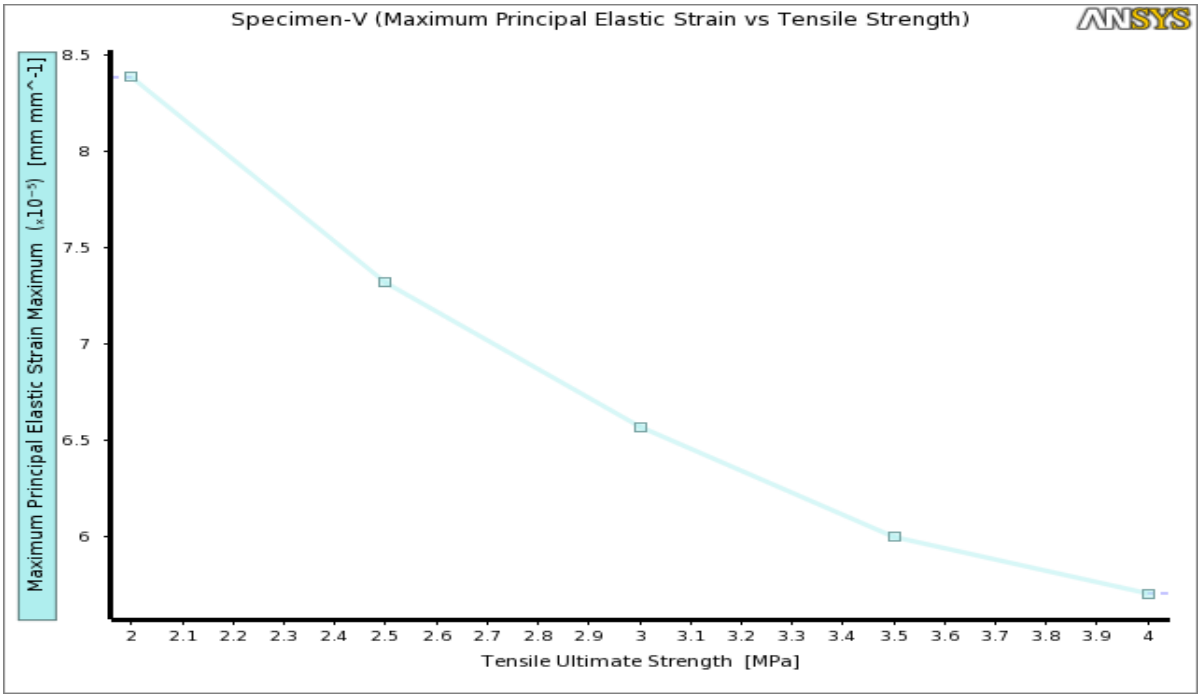

Figure 6. 25 Principal Elastic Strain (Max) vs Tensile Strength (Case II, SP-V)

6.2.2.3 Concrete's Modulus of Elasticity

Elastic Modulus is a property of a material that describes its stiffness. It describes the material ability to resist deformation. The stiffer a material, the lesser the deformation. The parametric analysis of the specimens' elastic modulus reproduced similar effect of an increase in stiffness mentioned above and is illustrated in Figure 6.26 – 6.29. An inverse relationship between the specimens' modulus of elasticity and the deformations is observed. At a given pressure, an increase in the elastic modulus decreases the deformations.

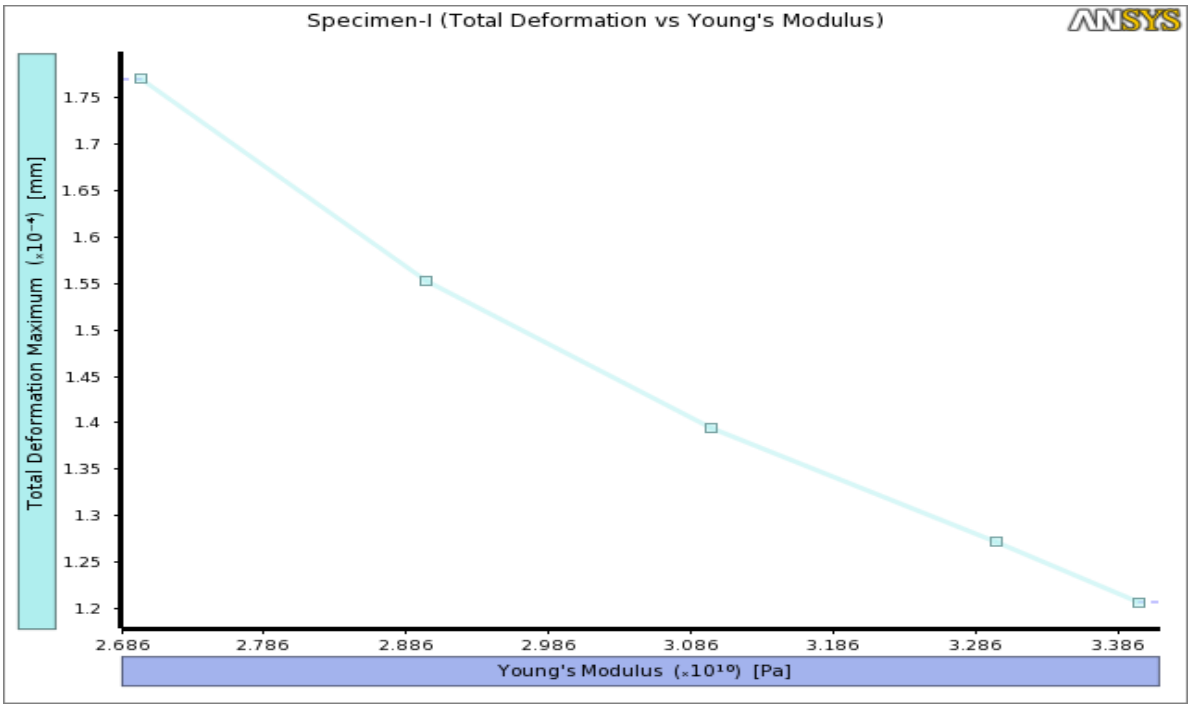

Figure 6. 26 Total Deformation vs Elastic Modulus (Case II, SP-I)

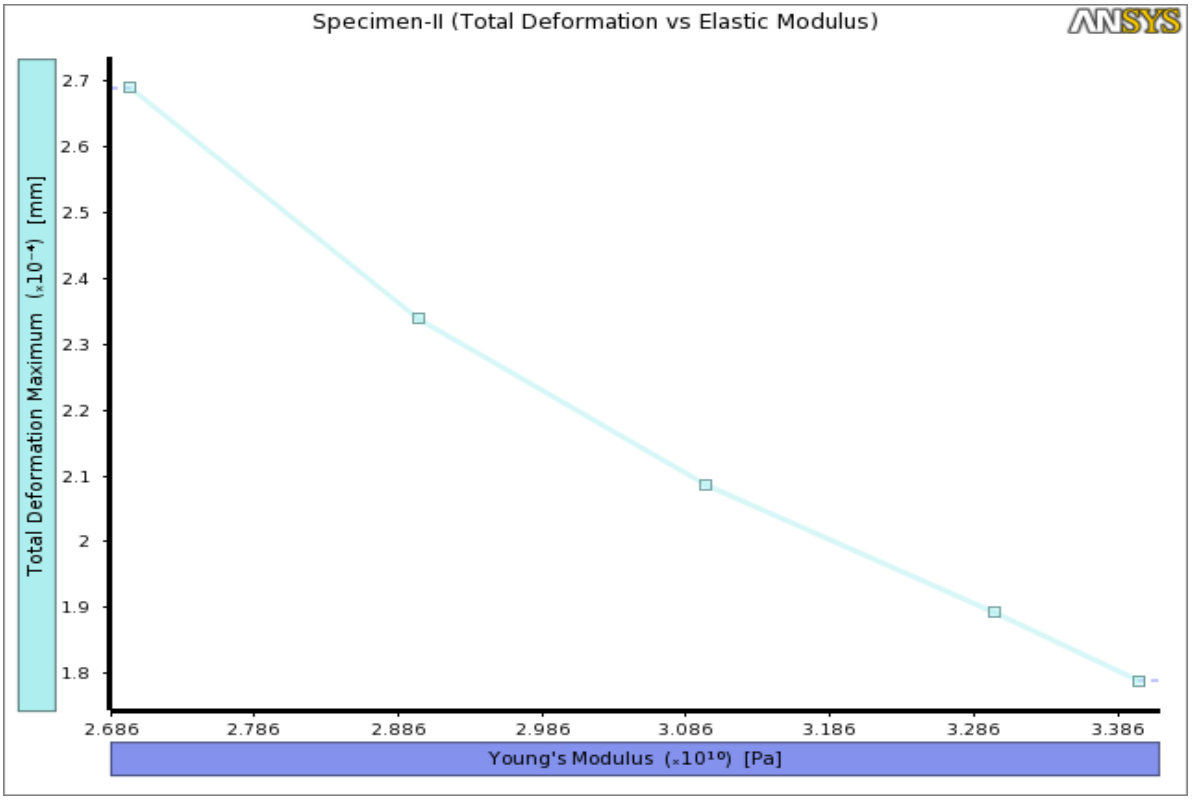

Figure 6. 27 Total Deformation vs Elastic Modulus (Case II, SP-II)

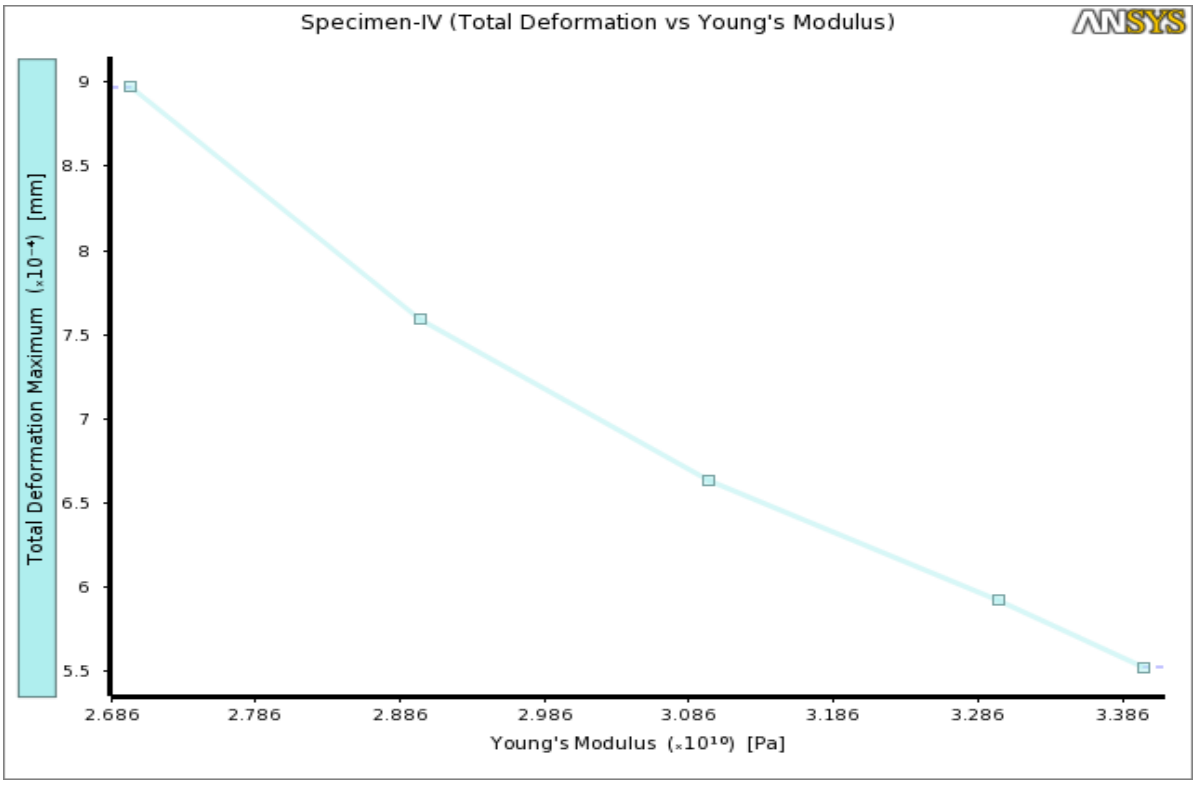

Figure 6. 28 Total Deformation vs Elastic Modulus (Case II, SP-IV)

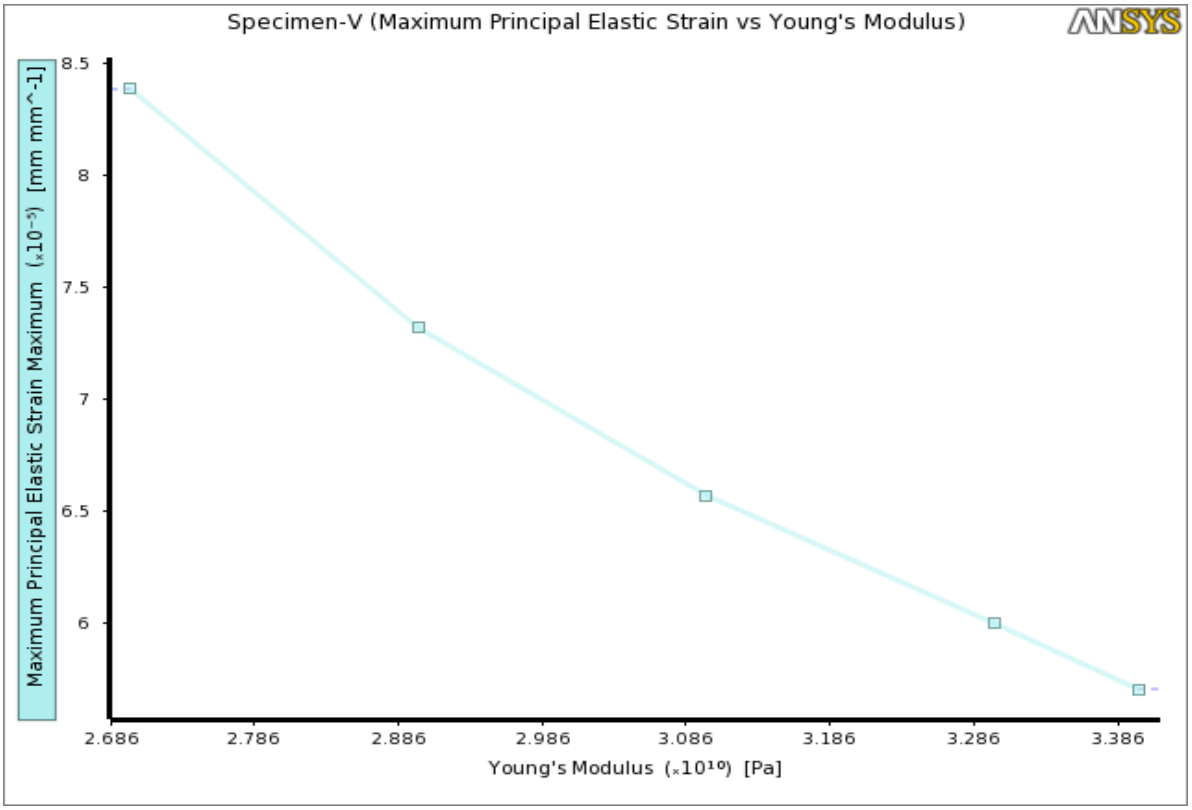

Figure 6. 29 Principal Elastic Strain (Max) vs Elastic Modulus (Case II, SP-V)

6.2.2.4 Rebar Diameter

In the context of steel corrosion in concrete, the internal pressure being developed as the result of corrosion mainly depend on the section (volume/area) of the rebar being convert to rust and the properties of rust (volume expansion ratio, elastic modulus, etc.). When other conditions are constant at a given attack penetration (e.g. 0.01mm), an increase in the diameter of the rebar will result in greater section being loss thus an increase in the internal pressure, which will lead to increase in deformations and internal stresses. This effect was evident in the derivation of the applied pressure presented in Chapter 5.

6.2.3 INFLUENCE OF RUST PROPERTIES

The influence of selected rust properties on the modelled system was studied through Case III. The primary effect was observed through the derivation of the applied pressure. The derived applied pressures in Case III are lesser than those of Case II with the same diameter. This effect was also reflected in the simulation results, showing smaller deformations. The observed influencing properties of rust are the volume expansion ratio, elastic modulus and Poisson's ratio. Therefore, the properties selected by Molina et al. (1993) may have had little influence on the system and probably should have been the reason for the poor agreement between their simulation results and their experimental results. The properties of the corrosion product used by Molina et al. (1993) were defined by the bulk modulus and Poisson's ratio of liquid water. Despite the minuteness of the rust properties on the modelled specimens of Case III, the

proportionality constant of the applied pressure and equivalent stress was the same as those of Case II specimen with the same diameter.

6.3 SUMMARY

This chapter presented the simulation results and discussions. Form the above discussions, the most influencing factor affecting deformations is the stiffness of the concrete cover which can be increased by either increasing the cover depth, the concrete strength (compressive and tensile) or the concrete elastic modulus. These results show some clear relationships form which appropriate formula can be established, linking the corrosion-induced crack width and residual cross-section of the corroding bar. From the three cases simulated, the following conclusion can be drawn:

1. The applied pressure is directly proportional to the deformations and the resultant stresses.
2. There exists a linear relationship between the deformations and the equivalent stresses.
3. The relationships and shape of plotted graphs are the same for all specimens within a given case.
4. The proportionality constant of the applied pressure to the equivalent stress is almost the same in all cases.
5. The proportionality constant of the equivalent stress to the equivalent strain equals the elastic modulus of the specimens, for all cases simulated.
6. The relationship between the applied pressure and the deformation in X-axis varies greatly.

7 DERIVATION OF THE PROPOSED MODEL

7.1 INTRODUCTION

This chapter presents the derivation of the proposed model and the validation against experimental data. The proposed model was derived analytically based on findings of the experimental and numerical investigations. The derivation employed similar assumptions listed in Chapter 5 as well as the assumption of uniform corrosion. Although steel corrosion in concrete is never uniform (Jang and Oh, 2010; Malumbela et al., 2011; Muthulingam and Rao, 2015) nor have a regular shape, but such consideration is necessary for the following reasons:

1. Simplification of the stress analysis (Zhao and Jin, 2016).
2. To avoid overestimation of the remaining cross-section of the corroding bar as was proven in Section 5.5.2.
3. The actual non-uniform shape or distribution of the corrosion product around the steel bar is unknown, and the non-uniformity is a unique property. There is little information available in the literature to characterise the actual non-uniform distribution of corrosion product around the rebar's circumference (Zhao and Jin, 2016). Therefore, the consideration of non-uniform corrosion is also based on assumptions of either elliptical shape or half-ellipse distribution, linearly decreased distribution or Gaussian distribution, which do not represent the actual non-uniform shape of steel corrosion in concrete.

7.2 DERIVATION

As in Section 5.4, assuming concrete to be an isotropic elastic material up to the point of failure in tension.

$$\sigma_{eq} = E_C \varepsilon_{eq} \qquad \text{---------- Eq. – 7.1}$$

Where $\boldsymbol{\sigma_{eq}}$ is the equivalent stress, $\boldsymbol{E_C}$ the elastic modulus of concrete and $\boldsymbol{\varepsilon_{eq}}$ the equivalent strain. When the equivalent stress exceeds the maximum tensile strength of the concrete, crack initiates thus, the equivalent strain within the crack zone becomes the strain at cracking ($\boldsymbol{\varepsilon_{cc}}$) (Bangash, 1989).

$$\sigma_{eq} = E_C \varepsilon_{cc} \qquad \text{---------- Eq. – 7.2}$$

The equivalent strain at cracking is proportional to the crack width with the assumption that no interlocking exists, thus, the shear goes to zero (Bangash, 1989). Form Bangash (1989), page 76 – 77, the proportionality constant is given as the volume containing the crack divided by the area of the crack. However, from results of the laboratory investigation and simulations, it was shown that the appearance of cracks and the deformation, respectively, strongly depend on the cover-diameter ratio. As was discussed in Chapter 4 & 6, respectively, the appearance of the first crack and the maximum deformation occurred at section of the specimens with the least cover depth. This is in confirmation with several experimental (Alonso et al.,1998) and

numerical (Jang and Oh, 2010) studies. Therefore, the cover-diameter ratio was considered the proportionality constant in this analysis and is expressed in Eq. – 7.3.

$$w = \frac{c}{D}\varepsilon_{cc} \qquad \text{---------- Eq. – 7.3}$$

Where $\boldsymbol{w}$ is the width of the crack, $\boldsymbol{c}$ the cover depth and $\boldsymbol{D}$ the rebar diameter. Making the strain at cracking ($\boldsymbol{\varepsilon_{cc}}$) the subject, Eq. – 7.3 becomes:

$$\varepsilon_{cc} = \frac{D}{c}w \qquad \text{---------- Eq. – 7.4}$$

Substituting Eq. – 7.4 into Eq. – 7.1 yields:

$$\sigma_{eq} = \frac{D}{c}E_C w \qquad \text{---------- Eq. – 7.5}$$

Note: Results from the finite element analysis showed that the applied pressure (internal pressure arising as the result of corrosion) is directly proportional to the equivalent stress.

$$P \approx \sigma_{eq}$$

Also, from the finite element analysis, the proportionality constant was observed to be closely related for all cases. The maximum value of 2.05 was adopted in this derivation.

$$P = 2.05\sigma_{eq}$$

$$P = 2.05\left[\frac{D}{c}\cdot E_C \cdot w\right] \qquad \text{---------- Eq. – 7.6}$$

Recall from Section 5.5, Eq. – 5.7 the applied pressure (P) is:

$$P = k_{rust}\cdot \varepsilon_{rust}$$

Where k_{rust} is the stiffness of the compressed rust layer and ε_{rust} the volumetric strain of the of the corrosion product (or rust layer).

To further recapitulate:

$$k_{rust} = \frac{\pi n({r_b}^2 - {R_{rb}}^2)}{B_{rust}}\cdot E_{rust}$$

Thus, the applied pressure becomes:

$$P = \frac{\pi n({r_b}^2 - {R_{rb}}^2)}{B_{rust}}\cdot E_{rust}\cdot \varepsilon_{rust} \qquad \text{---------- Eq. – 7.7}$$

Expressing $\boldsymbol{\varepsilon_{rust}}$ in terms of compressibility coefficient of the corrosion product, Eq. – 7.7 becomes:

$$P = \frac{\pi n({r_b}^2 - {R_{rb}}^2)}{B_{rust}}\cdot E_{rust}\cdot \frac{1}{B_{rust}} \qquad \text{---------- Eq. – 7.8}$$

Simplifying yields:

$$P = \frac{\pi n\left({r_b}^2 - {R_{rb}}^2\right)\cdot E_{rust}}{{B_{rust}}^2} \quad \text{---------- Eq. – 7.9}$$

Also, expressing $\boldsymbol{B_{rust}}$ in terms of the elastic modulus of rust and Poisson's ratio, and simplifying yields:

$$P = \frac{\pi n\left({r_b}^2 - {R_{rb}}^2\right)\cdot[3(1-2v)]^2}{E_{rust}} \quad \text{--------- Eq. – 7.10}$$

Recall from Section 6.2.3, the influencing properties of corrosion product were found to be the elastic modulus, Poisson's ratio and volume expansion ratio. There are consensuses among researchers regarding the volume expansion ratio of corrosion products and the Poisson's ratio than its elastic modulus. The elastic modulus of corrosion products reported in the literature varies greatly and depends on the environment. However, some researchers have estimated the elastic modulus of the corrosion products to be in the range of 0.1 to 0.5 GPa and, has been verified by Zhao and Jin (2016). In this regard, the influence of the rust elastic modulus in the above equation must be mitigated. Since the value adopted in Section 5.5 is 500 MPa or 0.5 GPa, the mitigation was done by rounding up the value to 1 GPa and keeping it constant. This approach allowed the proposed relationship to be dependent on the volume expansion ratio of the corrosion product and its Poisson's ratio. It should be noted that the corrosion-induced crack appears as a result of the rust expansion. The Poisson's ratio is usually considered the same as that of the steel being oxidised, hence 0.3 was adopted. Thus, substituting 1 GPa and 0.3 for $\boldsymbol{E_{rust}}$ and $\boldsymbol{v}$, respectively in Eq. – 7.10 yields:

$$P = 1.44\pi n({r_b}^2 - {R_{rb}}^2)GPa^{-1} \quad \text{--------- Eq. – 7.11}$$

Substituting for P into Eq. – 7.6 yields:

$$1.44\pi n({r_b}^2 - {R_{rb}}^2)GPa^{-1} = 2.05\left[\frac{D}{c}\cdot E_C \cdot w\right] \quad \text{--------- Eq. – 7.12}$$

Simplifying, the residual radius becomes:

$$R_{rb} = \sqrt{{r_b}^2 - \frac{2.05\left[\frac{D}{c}\cdot E_C\cdot w\right]GPa}{1.44\pi n}} \quad \text{--------- Eq. – 7.13}$$

To account for unit cancellation, GPa^2 is introduced in the denominator under the square root. Thus, Eq. – 7.13 becomes:

$$R_{rb} = \sqrt{{r_b}^2 - \frac{2.05\left[\frac{D}{c}\cdot E_C\cdot w\right]GPa}{1.44\pi n GPa^2}} \quad \text{--------- Eq. – 7.14}$$

The above equation presents an expression from which the residual radius can be estimated.

$\boldsymbol{R_{rb}}$ = residual radius of the rebar (mm)
$\boldsymbol{r_b}$ = original radius of the rebar (mm)
$\boldsymbol{E_c}$ = concrete elastic modulus (GPa)
$\boldsymbol{w}$ = width of the corrosion-induced crack (mm)
$\boldsymbol{n}$ = volume expansion ratio of the corrosion product

The concrete elastic modulus ($\boldsymbol{Ec}$) in Eq. – 7.14 can be estimated from the compressive strength when it is not known or specified. In fact, expressing the concrete elastic modulus in terms of the compressive strength is the most practical approach since the compressive strength is one of the properties of concrete usually specified and relatively easy to obtain, both in the laboratory and the field. Several codes (SANS, CEB-FIP, BS, IS, etc.) provide an accurate compressive strength – elastic modulus relationship and could be substituted directly for the elastic modulus in Eq. – 7.14.

In the above derivation, the residual section or remaining cross-section of the corroding is expressed in terms of the residual radius. With this approach, the model is applicable to both generalise and localise corrosion and, accommodates multi-directional ingress of corrosion agents thus, improving the versatility and accuracy.

7.3 VALIDATION OF THE DERIVED MODEL

The derived model was tested against results for the laboratory investigation and, experimental and analytical data from the literature. The results correlate well with a reasonable degree of accuracy. The summary of validations is presented here while the details are found in Appendix C. In the validation, the values of the volume expansion ratio and Poisson's ratio were the same as those used in the derivation of the applied pressure.

The validation of the derived model against data from the laboratory investigation showed the highest deviation, with the average percentages' errors of 10.8, 9.1, 6.6 and 8.7 % for SP-PC100, SP-FA30, SP-BS50 and SP-SF10, respectively. The deviation is attributed to the migration of the corrosion product away from the steel-concrete interface and accumulating at the surface of the ponding basin, as was discussed in Section 4.4.2.8. The migration of the corrosion product away from the steel-concrete interface not only reduces the pressure exerted on the surrounding concrete which influences the corrosion-induced crack width but also distort the relationship between the section loss and the corrosion-induced crack width. It is worth noting that the derivation of the model did not consider the effect of corrosion product migrating away from the steel-concrete interface, hence, could serve as a limitation. The migration effect is controlled by the solubility or diffusivity of the corrosion product and was not considered due to the complication involved. Despite the deviation, the percentage errors are still within the permissible range. The data used in the validation is the average of the crack width and cross-section loss measured at the various sections as described in Section 4.4.2.5.

The experimental data from the literature considered in the validation were those of Andrade et al. (1993) and Vidal et al. (2004) while the analytical data was that of Chen and Leung (2013). Except for Chen and Leung (2013), details of Andrade et al. (1993) and Vidal et al. (2004) works are discussed in Chapter 2. However, a brief description is first presented here before the summary of the correlations.

Andrade et al.'s (1993) experimental data were based on artificial accelerated corrosion test collected from four reinforced concrete beams (specimen I, II, III and IV). The dimensions of these specimens were 38 x 15 x 15 cm. Each specimen contained single rebar of 16 mm

diameter and with a concrete cover depth 2 or 3 cm. The applied currents were 100 and 10 $\mu A/cm^2$ for specimen I, II, III and IV, respectively, with the assumption that 100% of the current applied was consumed in the corrosion process. It is worth noting that the Authors calculated the radius loss (attack penetration) based on the above assumption. The validation of the derived model against Andrade et al.'s (1993) data showed good correlation with an average percentage error of 0.22%.

Vidal et al.'s (2004) experimental data were collected from two reinforced concrete beams that have been naturally corroded over the period of fourteen (14) and seventeen (17) years under loading. These beams were part of a long-term experimental program started in 1984, which consisted of thirty-six (36) reinforced concrete beams. The beams considered in this study have the dimension of 3000 x 150 x 280 mm, an average 28-day compressive strength of 45 MPa and an elastic modulus of 32 GPa. The beams were labelled Beam A and Beam B and, contained rebars of 16- and 12-mm diameter at concrete cover of 48 and 16 mm, respectively. The Data used in this validation was collected from Figure 10 of Vidal et al. (2004), with the aid of WebPlotDigitizer software. The validation of the derived model against Vidal et al.'s (2004) data showed an average percentage error of 1.05%.

Chen and Leung (2013) presented a model for corrosion-induced cracking which combines chloride diffusion process and the cracking of concrete cover. Their studies considered two specimens with the dimension of 150 x 150 mm containing single rebar of 20 mm diameter. Each specimen was analysed based on uniform and non-uniform corrosion cases. These specimens were assigned an elastic modulus of 36 GPa and concrete cover depth of 20 and 40 mm, respectively. The data was obtained from the finite element analysis of various penetration depths of both uniform and non-uniform corrosion which give the corresponding crack width. The validation of the derived model against Chen and Leung's (2013) analytical data showed the best correlation with an average percentage error of 0.14%. The best fitting is attributed to the absence of the effect of the corrosion product migrating away for from the steel-concrete interface.

7.4 SUMMARY

This chapter presented the derivation and validation of the proposed model. The derivation of the model was based on findings of the experimental and numerical investigations. From these findings, appropriate relationships and important parameters were identified as well as the proportionality constant of the applied pressure and the equivalent stresses. The applied pressure was found to have a direct dependency on the volume of steel being oxidised and the properties of the corrosion product (volume expansion ratio, Poisson's ratio and elastic modulus). A model was then derived from which corrosion damage can be quantified in terms of the residual cross-section of the corroding bar. This proposed model was tested against the author's experimental data and against other experimental and analytical data from the literature, and the results showed good correlation.

7.5 REFERENCES

1. Alonso, C., Andrade, C., Rodriguez, J. and Diez, J.M., 1998. Factors controlling cracking of concrete affected by reinforcement corrosion. Materials and structures, 31(7), pp.435-441.
2. Jang, B.S. and Oh, B.H., 2010. Effects of non-uniform corrosion on the cracking and service life of reinforced concrete structures. Cement and Concrete Research, 40(9), pp.1441-1450.
3. Malumbela, G., Alexander, M. and Moyo, P., 2011. Model for cover cracking of RC beams due to partial surface steel corrosion. Construction and Building Materials, 25(2), pp.987-991.
4. Muthulingam, S. and Rao, B.N., 2015. Non-uniform corrosion states of rebar in concrete under chloride environment. Corrosion Science, 93, pp.267-282.
5. Zhao, Y. and Jin, W., 2016. Steel Corrosion-Induced Concrete Cracking. Butterworth-Heinemann.

8 SUMMARY AND CONCLUSION

8.1 INTRODUCTION

This chapter presents the concluding remarks of this research. These include the summary of the procedures and findings, the conclusion and limitations, as well as recommendations for future studies.

8.2 SUMMARY

This research sets out to establish a model from which corrosion damage in reinforced concrete structures can be estimated in terms of the residual cross-section. A model, which will transition engineers and practitioners from the traditional approach of recommending repairs for corrosion-damaged concrete structures early than necessary or when the structure is beyond the limit state, to recommending appropriate repairs based on an informed decision of the residual cross-section of the corroding bar.

This study was conducted through experimental (laboratory) and numerical investigations of the relationship between the level of corrosion (cross-section loss) and corrosion-induced crack width. The laboratory experiment investigated the relationship between the corrosion-induced crack width and the corrosion level (section loss/mass loss) under chloride-induced corrosion with respect to binder type (performance resistance), and cover depth. While the numerical focused on the relationship between the pressure exerted by the expansive corrosion product on the surrounding concrete, and the corresponding deformation (corrosion-induced crack width). Experimentally, it was found that the relationship between the corrosion level and the corrosion-induced crack depends on the solubility of the corrosion product as well as the cover-diameter ratio. The numerical investigation found that the relationship between the applied pressure and the deformation depends mainly on the stiffness of the concrete cover, which also depends on the cover-diameter ratio, the concrete strength and its elastic modulus. Based on these findings, the model was derived analytically.

8.3 CONCLUSION

Based on the findings of these investigations, which agree with results from the literature, the following conclusion can be reached:

1. The resistance of concrete to corrosion depends mainly on the microstructural properties of the concrete, which also depends on the binder type.
2. The resistivity of concrete is directly linked to its durability properties.
3. A potentially durable concrete should have high resistivity.
4. The concrete resistivity is the main factor controlling the rate in which corrosion propagates.
5. The relationship between the cross-section loss of the rebar to corrosion and the corrosion-induced crack width depends on the solubility of the corrosion product.

6. The pressure being developed due to corrosion is directly proportional to the volume of the steel being oxidised and the solubility of the corrosion product.
7. From the simulation perspectives, the cover depth, concrete strength and elastic modulus are parameters that controlled deformation.

It is worth noting that the aim of this research was achieved as the validation and comparison showed good results. This derived model is applicable to structures in service, and the required input parameters are easily obtainable. However, this model is not without limitations, which are as the result of those variables and conditions not considered in the analysis and partially to some of the assumptions employed.

8.4 LIMITATIONS

The following are the limitations of this derived model:

1. Applicable only to the appearances of corrosion-induced crack.
2. Cannot be applied to structures in water-saturated conditions or cases where the solubility of the corrosion product is high.
3. The model accuracy also depends on properties (volume expansion ratio, and Poisson's ratio) of the corrosion product selected as well as the migration effect.
4. Not applicable to prestressed or post-stressed concrete.
5. Did not consider the influence of external load, secondary reinforcement (stirrup) on the growth of the crack width nor crack self-healing effect.
6. Do not account for the diffusivity or the migration of the corrosion product away from the steel-concrete interface.
7. Derived based on the consideration of elastic theory and other assumptions which may serve as limitations under some circumstances.

8.5 RECOMMENDATIONS FOR FUTURE RESEARCH

1. Modelling the diffusivity or migration of the corrosion product away from the steel-concrete interface.
2. The influence of fatigue, external loading, and secondary reinforcement (stirrup) on the evolution of the corrosion-induced crack width.
3. The behaviour of corroding reinforced concrete member under dynamic loading.

APPENDIX A DETAILS OF SOME MATERIALS

A1 SUPERPLASTICIZER

Description as indicated by the manufacturer:

- Brand Name : CHRYSO Fluid Premia 100
- Bulk Density : 1.065 ± 0.010
- pH : 7
- Dry extract : approx. 30%
- Na_2O equiv. : ≤ 1.60%
- Cl^- content : < 0.1%
- State : Liquid
- Colour : Milky orange brown

A2 AGGREGATES SIEVE ANALYSIS AND GRADING CURVES

Table A.1 Sieve Analysis of the Fine Aggregates

Sieve Size	Mass of Fine Aggregates Retained Mass per Test Sample: 300 g				Percentage (%) Retained	Cumulative Percentage (%) Retained	Percentage (%) Passing
	I	II	III	Average			
9.5 mm	0.00	0.00	0.00	0.00	0.00	0.00	100.00
4.75 mm	12.90	14.10	14.50	13.83	4.61	4.61	95.39
2.36 mm	37.90	43.90	43.70	41.83	13.94	18.56	81.44
1.18 mm	79.40	80.10	81.40	80.30	26.77	45.32	54.68
600 µm	79.70	71.60	78.40	76.57	25.52	70.84	29.16
300 µm	48.40	46.60	43.20	46.07	15.36	86.20	13.80
150 µm	24.20	25.40	23.50	24.37	8.12	94.32	5.68
75 µm	12.10	11.20	10.10	11.13	3.71	98.03	1.97
Pan	5.40	7.10	5.20	5.90	1.97	100.00	0.00

Table A.2 Sieve Analysis of the coarse Aggregates

Sieve Size	Mass of Coarse Aggregates Retained Mass per Test Sample: 500 g				Percentage (%) Retained	Cumulative Percentage (%) Retained	Percentage (%) Passing
	I	II	III	Average			
16.0 mm	0	0	0	0.00	0.00	0.00	100.00
13.2 mm	77.40	87.10	79.70	81.40	16.28	16.28	83.72
9.5 mm	302.00	310.30	306.60	306.30	61.26	77.54	22.46
6.7 mm	105.60	92.40	98.70	98.90	19.78	97.32	2.68
4.75 mm	12.70	8.20	11.50	10.80	2.16	99.48	0.52
Pan	2.30	2.00	3.50	2.60	0.52	100.00	0.00

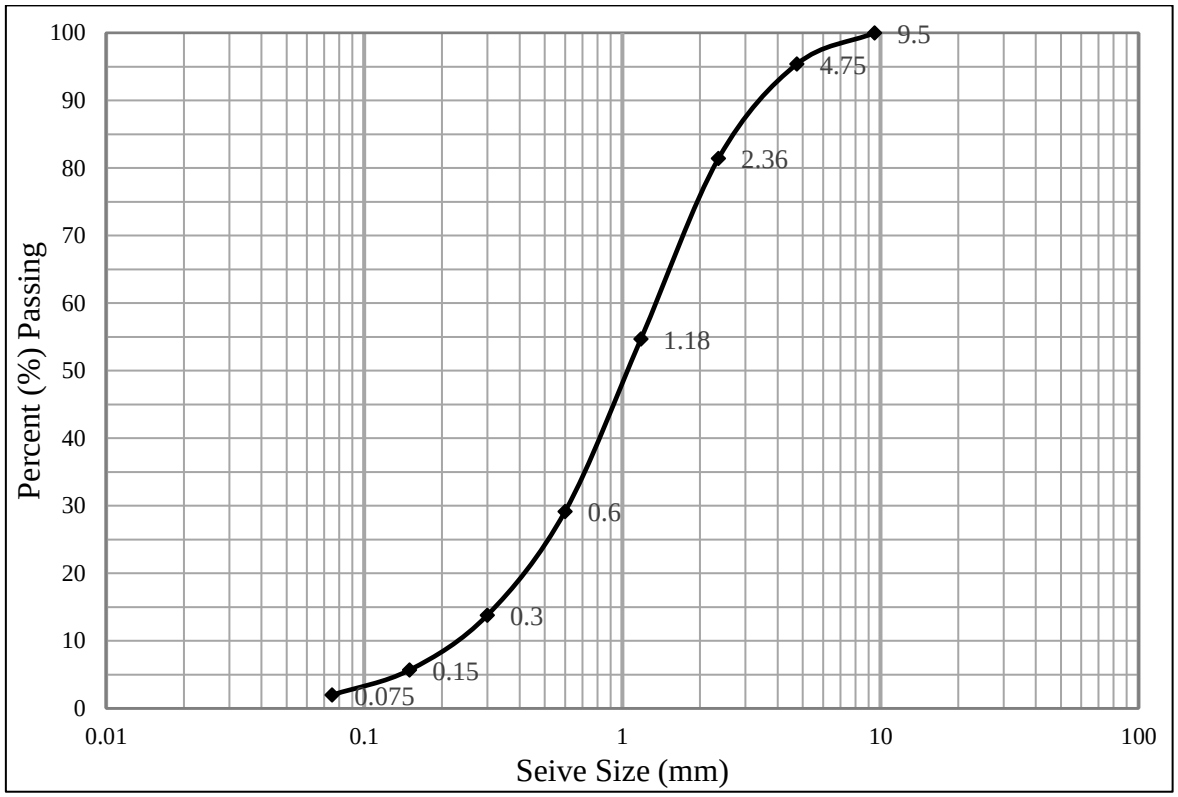

Figure A1 Fine Aggregate Grading Curve

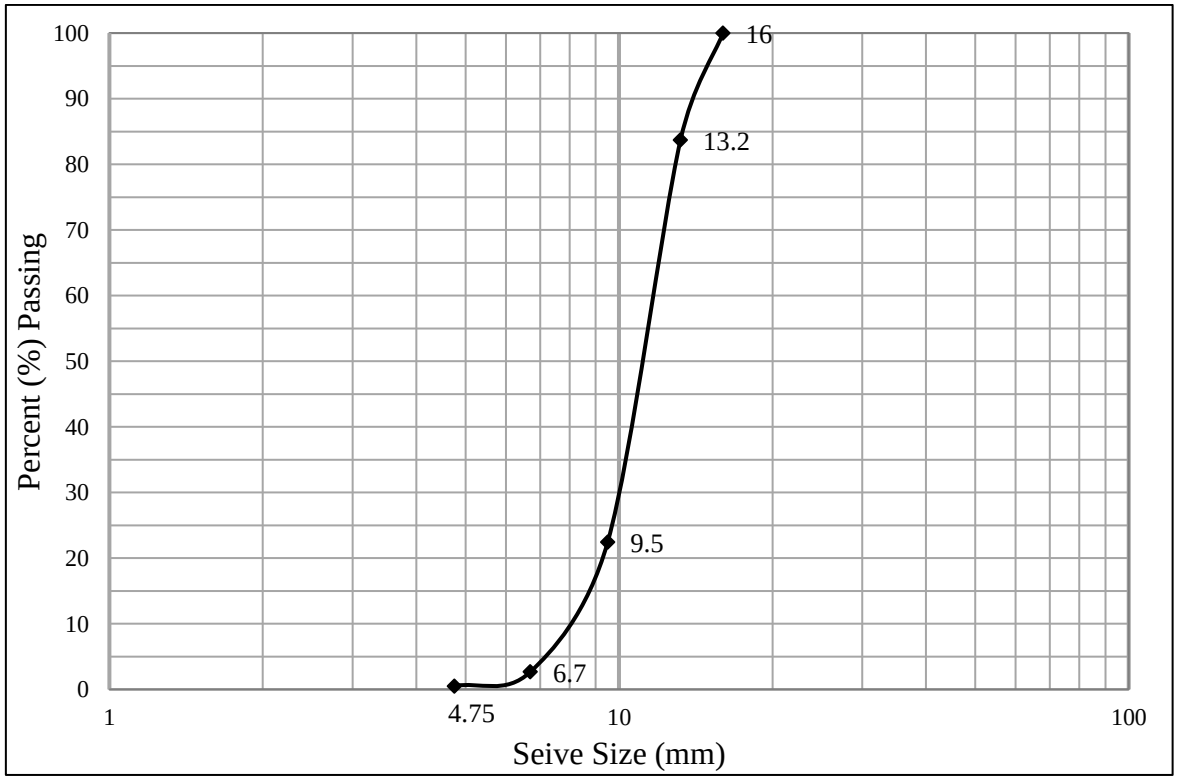

Figure A2 Coarse Aggregate Grading Curve

APPENDIX B DURABILITY INDEXES

B1 OXYGEN PERMEABILITY INDEX (OPI)

MIX 100% RHPC (OPI Test-1)							
Mean OPI:		**10.09**		**Variability Check:**		**Good**	
Mean k (m/s):		**8.088E-11**		**COV % (Mean k):**		**9.8**	
Sample 1		Sample 2		Sample 3		Sample 4	
Mean diameter (mm)	68.15	Mean diameter (mm)	68.25	Mean diameter (mm)	68.26	Mean diameter (mm)	68.29
Diameter 1 (mm)	68.12	Diameter 1 (mm)	68.26	Diameter 1 (mm)	68.32	Diameter 1 (mm)	68.26
Diameter 2 (mm)	68.22	Diameter 2 (mm)	68.20	Diameter 2 (mm)	68.20	Diameter 2 (mm)	68.28
Diameter 3 (mm)	68.16	Diameter 3 (mm)	68.18	Diameter 3 (mm)	68.26	Diameter 3 (mm)	68.26
Diameter 4 (mm)	68.10	Diameter 4 (mm)	68.36	Diameter 4 (mm)	68.24	Diameter 4 (mm)	68.34
Mean thickness (mm)	30.90	Mean thickness (mm)	30.29	Mean thickness (mm)	30.04	Mean thickness (mm)	31.85
Thickness 1 (mm)	30.74	Thickness 1 (mm)	30.08	Thickness 1 (mm)	29.86	Thickness 1 (mm)	31.68
Thickness 2 (mm)	31.00	Thickness 2 (mm)	30.52	Thickness 2 (mm)	30.14	Thickness 2 (mm)	31.92
Thickness 3 (mm)	30.80	Thickness 3 (mm)	30.02	Thickness 3 (mm)	30.04	Thickness 3 (mm)	31.80
Thickness 4 (mm)	31.04	Thickness 4 (mm)	30.54	Thickness 4 (mm)	30.12	Thickness 4 (mm)	31.98
Cell Volume (L)	5.00	Cell Volume (L)	5.00	Cell Volume (L)	5.00	Cell Volume (L)	5.00
k (m/s)	7.764E-11	k (m/s)	7.400E-11	k (m/s)	9.227E-11	k (m/s)	7.959E-11
r^2	0.9979	r^2	0.9978	r^2	0.9954	r^2	0.9960
r^2 Validity	Valid	r^2 Validity	Valid	r^2 Validity	Valid	r^2 Validity	Valid
OPI	10.11	OPI	10.13	OPI	10.03	OPI	10.10
Time	Pressure	Time	Pressure	Time	Pressure	Time	Pressure
hh:mm:ss	(kPa)	hh:mm:ss	(kPa)	hh:mm:ss	(kPa)	hh:mm:ss	(kPa)
11:07:34	101.85	11:07:34	103.56	11:07:34	101.92	11:07:34	102.29
11:12:34	101.30	11:12:34	103.02	11:12:34	101.18	11:12:34	101.73
11:17:34	100.76	11:17:34	102.49	11:17:34	100.51	11:17:34	101.19

11:22:34	100.31	11:22:34	102.04	11:22:34	99.92	11:22:34	100.68
11:27:34	99.80	11:27:34	101.53	11:27:34	99.24	11:27:34	100.13
11:32:34	99.34	11:32:34	101.06	11:32:34	98.66	11:32:34	99.63
11:37:34	98.82	11:37:34	100.56	11:37:34	98.05	11:37:34	99.14
11:42:34	98.37	11:42:34	100.11	11:42:34	97.46	11:42:34	98.66
11:47:34	97.89	11:47:34	99.63	11:47:34	96.85	11:47:34	98.16
11:52:34	97.43	11:52:34	99.16	11:52:34	96.25	11:52:34	97.66
11:57:34	97.00	11:57:34	98.73	11:57:34	95.68	11:57:34	97.22
12:02:34	96.59	12:02:34	98.32	12:02:34	95.17	12:02:34	96.80
12:07:34	96.14	12:07:34	97.87	12:07:34	94.64	12:07:34	96.35
12:12:34	95.70	12:12:34	97.43	12:12:34	94.06	12:12:34	95.90
12:17:34	95.31	12:17:34	97.04	12:17:34	93.59	12:17:34	95.46
12:22:34	94.90	12:22:34	96.64	12:22:34	93.08	12:22:34	95.06
12:27:34	94.50	12:27:34	96.25	12:27:34	92.60	12:27:34	94.68
12:32:34	94.08	12:32:34	95.82	12:32:34	92.09	12:32:34	94.24
12:37:34	93.73	12:37:34	95.48	12:37:34	91.64	12:37:34	93.90
12:42:34	93.34	12:42:34	95.09	12:42:34	91.18	12:42:34	93.51
12:47:34	92.90	12:47:34	94.65	12:47:34	90.71	12:47:34	93.07
12:52:34	92.52	12:52:34	94.27	12:52:34	90.24	12:52:34	92.73
12:57:34	92.17	12:57:34	93.92	12:57:34	89.78	12:57:34	92.37
13:02:34	91.80	13:02:34	93.54	13:02:34	89.35	13:02:34	91.99
13:07:34	91.41	13:07:34	93.15	13:07:34	88.86	13:07:34	91.60
13:12:34	90.98	13:12:34	92.75	13:12:34	88.42	13:12:34	91.18
13:17:34	90.63	13:17:34	92.40	13:17:34	88.00	13:17:34	90.84
13:22:34	90.33	13:22:34	92.10	13:22:34	87.62	13:22:34	90.54
13:27:34	89.99	13:27:34	91.76	13:27:34	87.22	13:27:34	90.19
13:32:34	89.56	13:32:34	91.33	13:32:34	86.77	13:32:34	89.76
13:37:34	89.24	13:37:34	91.01	13:37:34	86.37	13:37:34	89.45
13:42:34	88.85	13:42:34	90.64	13:42:34	85.93	13:42:34	89.07

13:47:34	88.47	13:47:34	90.27	13:47:34	85.54	13:47:34	88.70
13:52:34	88.06	13:52:34	89.86	13:52:34	85.08	13:52:34	88.29
13:57:34	87.67	13:57:34	89.49	13:57:34	84.67	13:57:34	87.93
14:02:34	87.28	14:02:34	89.10	14:02:34	84.23	14:02:34	87.56
14:07:34	86.94	14:07:34	88.76	14:07:34	83.82	14:07:34	87.22
14:12:34	86.58	14:12:34	88.40	14:12:34	83.44	14:12:34	86.89
14:17:34	86.22	14:17:34	88.04	14:17:34	83.01	14:17:34	86.52
14:22:34	85.85	14:22:34	87.67	14:22:34	82.58	14:22:34	86.17
14:27:34	85.49	14:27:34	87.31	14:27:34	82.17	14:27:34	85.81
14:32:34	85.10	14:32:34	86.92	14:32:34	81.74	14:32:34	85.48
14:37:34	84.76	14:37:34	86.58	14:37:34	81.35	14:37:34	85.14
14:42:34	84.42	14:42:34	86.24	14:42:34	80.91	14:42:34	84.79
14:47:34	84.06	14:47:34	85.88	14:47:34	80.50	14:47:34	84.43
14:52:34	83.68	14:52:34	85.50	14:52:34	80.07	14:52:34	84.11
14:57:34	83.37	14:57:34	85.19	14:57:34	79.71	14:57:34	83.80
15:02:34	82.96	15:02:34	84.78	15:02:34	79.27	15:02:34	83.39
15:07:34	82.67	15:07:34	84.49	15:07:34	78.90	15:07:34	83.10
15:12:34	82.32	15:12:34	84.14	15:12:34	78.51	15:12:34	82.75
15:17:34	81.91	15:17:34	83.74	15:17:34	78.10	15:17:34	82.37
15:22:34	81.56	15:22:34	83.39	15:22:34	77.68	15:22:34	82.02
15:27:34	81.26	15:27:34	83.09	15:27:34	77.34	15:27:34	81.74
15:32:34	80.96	15:32:34	82.79	15:32:34	76.94	15:32:34	81.44
15:37:34	80.66	15:37:34	82.49	15:37:34	76.60	15:37:34	81.09
15:42:34	80.28	15:42:34	82.11	15:42:34	76.22	15:42:34	80.71
15:47:34	80.01	15:47:34	81.85	15:47:34	75.87	15:47:34	80.40
15:52:34	79.65	15:52:34	81.49	15:52:34	75.49	15:52:34	80.04
15:57:34	79.36	15:57:34	81.20	15:57:34	75.14	15:57:34	79.75
16:02:34	79.04	16:02:34	80.88	16:02:34	74.80	16:02:34	79.42
16:07:34	78.78	16:07:34	80.64	16:07:34	74.48	16:07:34	79.18

16:12:34	78.46	16:12:34	80.33	16:12:34	74.16	16:12:34	78.87
16:17:34	78.13	16:17:34	80.00	16:17:34	73.81	16:17:34	78.54
16:22:34	77.88	16:22:34	79.75	16:22:34	73.48	16:22:34	78.29
16:27:34	77.60	16:27:34	79.47	16:27:34	73.18	16:27:34	78.01
16:32:34	77.32	16:32:34	79.19	16:32:34	72.86	16:32:34	77.73
16:37:34	77.00	16:37:34	78.87	16:37:34	72.53	16:37:34	77.42
16:42:34	76.73	16:42:34	78.60	16:42:34	72.24	16:42:34	77.14
16:47:34	76.42	16:47:34	78.28	16:47:34	71.92	16:47:34	76.89
16:52:34	76.15	16:52:34	78.01	16:52:34	71.58	16:52:34	76.69
16:57:34	75.89	16:57:34	77.74	16:57:34	71.32	16:57:34	76.48
17:02:34	75.64	17:02:34	77.45	17:02:34	70.99	17:02:34	76.29
17:07:34	75.43	17:07:34	77.23	17:07:34	70.74	17:07:34	76.14

MIX 100% RHPC (OPI Test-2)							
Mean OPI:		**10.12**		**Variability Check:**		**Good**	
Mean k (m/s):		**7.884E-11**		**COV % (Mean k):**		**30.1**	
Sample 1		Sample 2		Sample 3		Sample 4	
Mean diameter (mm)	68.13	Mean diameter (mm)	68.18	Mean diameter (mm)	68.20	Mean diameter (mm)	68.36
Diameter 1 (mm)	68.08	Diameter 1 (mm)	68.28	Diameter 1 (mm)	68.02	Diameter 1 (mm)	68.34
Diameter 2 (mm)	68.14	Diameter 2 (mm)	68.26	Diameter 2 (mm)	68.24	Diameter 2 (mm)	68.40
Diameter 3 (mm)	68.18	Diameter 3 (mm)	68.02	Diameter 3 (mm)	68.42	Diameter 3 (mm)	68.36
Diameter 4 (mm)	68.12	Diameter 4 (mm)	68.14	Diameter 4 (mm)	68.12	Diameter 4 (mm)	68.32
Mean thickness (mm)	31.21	Mean thickness (mm)	30.49	Mean thickness (mm)	30.69	Mean thickness (mm)	29.52
Thickness 1 (mm)	31.64	Thickness 1 (mm)	31.02	Thickness 1 (mm)	31.32	Thickness 1 (mm)	30.32
Thickness 2 (mm)	31.04	Thickness 2 (mm)	30.38	Thickness 2 (mm)	30.88	Thickness 2 (mm)	29.42
Thickness 3 (mm)	31.36	Thickness 3 (mm)	30.58	Thickness 3 (mm)	30.38	Thickness 3 (mm)	29.28

Thickness 4 (mm)	30.78	Thickness 4 (mm)	29.98	Thickness 4 (mm)	30.16	Thickness 4 (mm)	29.06
Cell Volume (L)	5.00	Cell Volume (L)	5.00	Cell Volume (L)	5.00	Cell Volume (L)	5.00
k (m/s)	5.398E-11	k (m/s)	1.103E-10	k (m/s)	8.097E-11	k (m/s)	7.015E-11
r^2	0.9990	r^2	0.9988	r^2	0.9951	r^2	0.9980
r^2 Validity	Valid	r^2 Validity	Valid	r^2 Validity	Valid	r^2 Validity	Valid
OPI	10.27	OPI	9.96	OPI	10.09	OPI	10.15
Time	Pressure	Time	Pressure	Time	Pressure	Time	Pressure
hh:mm:ss	(kPa)	hh:mm:ss	(kPa)	hh:mm:ss	(kPa)	hh:mm:ss	(kPa)
11:07:34	98.56	11:07:34	103.91	17:36:41	101.42	17:36:41	101.70
11:12:34	98.64	11:12:34	103.35	17:41:41	101.03	17:41:41	101.31
11:17:34	98.36	11:17:34	102.71	17:46:41	100.63	17:46:41	100.89
11:22:34	98.06	11:22:34	102.10	17:51:41	100.24	17:51:41	100.55
11:27:34	97.73	11:27:34	101.59	17:56:41	99.85	17:56:41	100.09
11:32:34	97.44	11:32:34	100.97	18:01:41	99.46	18:01:41	99.71
11:37:34	97.16	11:37:34	100.39	18:06:41	99.07	18:06:41	99.32
11:42:34	96.81	11:42:34	99.68	18:11:41	98.66	18:11:41	98.95
11:47:34	96.56	11:47:34	99.05	18:16:41	98.26	18:16:41	98.58
11:52:34	96.25	11:52:34	98.40	18:21:41	97.86	18:21:41	98.18
11:57:34	95.93	11:57:34	97.71	18:26:41	97.46	18:26:41	97.82
12:02:34	95.63	12:02:34	97.04	18:31:41	97.06	18:31:41	97.42
12:07:34	95.39	12:07:34	96.39	18:36:41	96.64	18:36:41	97.03
12:12:34	95.08	12:12:34	95.76	18:41:41	96.25	18:41:41	96.71
12:17:34	94.79	12:17:34	95.22	18:46:41	95.86	18:46:41	96.28
12:22:34	94.52	12:22:34	94.58	18:51:41	95.45	18:51:41	95.96
12:27:34	94.25	12:27:34	93.95	18:56:41	95.03	18:56:41	95.54
12:32:34	93.98	12:32:34	93.29	19:01:41	94.64	19:01:41	95.18
12:37:34	93.66	12:37:34	92.66	19:06:41	94.23	19:06:41	94.84
12:42:34	93.39	12:42:34	92.06	19:11:41	93.82	19:11:41	94.46
12:47:34	93.14	12:47:34	91.46	19:16:41	93.41	19:16:41	94.09

12:52:34	92.86	12:52:34	90.85	19:21:41	93.02	19:21:41	93.71
12:57:34	92.52	12:57:34	90.22	19:26:41	92.59	19:26:41	93.40
13:02:34	92.28	13:02:34	89.67	19:31:41	92.17	19:31:41	93.04
13:07:34	91.96	13:07:34	89.03	19:36:41	91.76	19:36:41	92.68
13:12:34	91.72	13:12:34	88.48	19:41:41	91.35	19:41:41	92.31
13:17:34	91.45	13:17:34	87.93	19:46:41	90.94	19:46:41	91.96
13:22:34	91.18	13:22:34	87.43	19:51:41	90.53	19:51:41	91.61
13:27:34	90.92	13:27:34	86.89	19:56:41	90.12	19:56:41	91.24
13:32:34	90.68	13:32:34	86.36	20:01:41	89.71	20:01:41	90.83
13:37:34	90.35	13:37:34	85.84	20:06:41	89.29	20:06:41	90.49
13:42:34	90.07	13:42:34	85.28	20:11:41	88.87	20:11:41	90.06
13:47:34	89.79	13:47:34	84.77	20:16:41	88.45	20:16:41	89.71
13:52:34	89.51	13:52:34	84.22	20:21:41	88.03	20:21:41	89.31
13:57:34	89.27	13:57:34	83.74	20:26:41	87.61	20:26:41	88.97
14:02:34	88.96	14:02:34	83.18	20:31:41	87.19	20:31:41	88.52
14:07:34	88.68	14:07:34	82.67	20:36:41	86.77	20:36:41	88.21
14:12:34	88.41	14:12:34	82.19	20:41:41	86.35	20:41:41	87.81
14:17:34	88.12	14:17:34	81.67	20:46:41	85.93	20:46:41	87.43
14:22:34	87.86	14:22:34	81.17	20:51:41	85.51	20:51:41	87.02
14:27:34	87.58	14:27:34	80.67	20:56:41	85.09	20:56:41	86.61
14:32:34	87.32	14:32:34	80.21	21:01:41	84.67	21:01:41	86.29
14:37:34	87.04	14:37:34	79.73	21:06:41	84.24	21:06:41	85.87
14:42:34	86.72	14:42:34	79.19	21:11:41	83.85	21:11:41	85.55
14:47:34	86.45	14:47:34	78.75	21:16:41	83.44	21:16:41	85.14
14:52:34	86.19	14:52:34	78.25	21:21:41	83.07	21:21:41	84.73
14:57:34	85.91	14:57:34	77.80	21:26:41	82.68	21:26:41	84.36
15:02:34	85.68	15:02:34	77.32	21:31:41	82.29	21:31:41	84.01
15:07:34	85.37	15:07:34	76.84	21:36:41	81.88	21:36:41	83.65
15:12:34	85.11	15:12:34	76.39	21:41:41	81.47	21:41:41	83.29

15:17:34	84.89	15:17:34	75.94	21:46:41	81.09	21:46:41	82.88
15:22:34	84.61	15:22:34	75.45	21:51:41	80.67	21:51:41	82.55
15:27:34	84.43	15:27:34	75.09	21:56:41	80.23	21:56:41	82.13
15:32:34	84.13	15:32:34	74.58	22:01:41	79.87	22:01:41	81.78
15:37:34	83.86	15:37:34	74.16	22:06:41	79.46	22:06:41	81.44
15:42:34	83.66	15:42:34	73.74	22:11:41	79.05	22:11:41	81.07
15:47:34	83.36	15:47:34	73.29	22:16:41	78.64	22:16:41	80.67
15:52:34	83.14	15:52:34	72.87	22:21:41	78.23	22:21:41	80.33
15:57:34	82.88	15:57:34	72.44	22:26:41	77.82	22:26:41	80.00
16:02:34	82.65	16:02:34	72.05	22:31:41	77.41	22:31:41	79.61
16:07:34	82.37	16:07:34	71.64	22:36:41	77.05	22:36:41	79.31
16:12:34	82.16	16:12:34	71.28	22:41:41	76.59	22:41:41	78.92
16:17:34	81.95	16:17:34	70.88	22:46:41	76.18	22:46:41	78.54
16:22:34	81.65	16:22:34	70.47	22:51:41	75.77	22:51:41	78.24
16:27:34	81.42	16:27:34	70.09	22:56:41	75.36	22:56:41	77.88
16:32:34	81.18	16:32:34	69.70	23:01:41	74.97	23:01:41	77.52
16:37:34	80.94	16:37:34	69.40	23:06:41	74.55	23:06:41	77.20
16:42:34	80.71	16:42:34	69.07	23:11:41	74.16	23:11:41	76.88
16:47:34	80.51	16:47:34	68.71	23:16:41	73.73	23:16:41	76.53
16:52:34	80.24	16:52:34	68.31	23:21:41	73.35	23:21:41	76.20
16:57:34	80.03	16:57:34	68.00	23:26:41	72.96	23:26:41	75.90
17:02:34	79.81	17:02:34	67.63	23:31:41	72.52	23:31:41	75.57
17:07:34	79.58	17:07:34	67.32	23:36:41	72.13	23:36:41	75.26

MIX 100% RHPC (OPI Test-3)							
Mean OPI:		**10.18**		**Variability Check:**		**Good**	
Mean k (m/s):		**6.879E-11**		**COV % (Mean k):**		**31.9**	
Sample 1		Sample 2		Sample 3		Sample 4	
Mean diameter (mm)	68.12	Mean diameter (mm)	68.27	Mean diameter (mm)	68.26	Mean diameter (mm)	68.25
Diameter 1 (mm)	68.02	Diameter 1 (mm)	68.32	Diameter 1 (mm)	68.30	Diameter 1 (mm)	68.16
Diameter 2 (mm)	68.08	Diameter 2 (mm)	68.12	Diameter 2 (mm)	68.28	Diameter 2 (mm)	68.26
Diameter 3 (mm)	68.26	Diameter 3 (mm)	68.38	Diameter 3 (mm)	68.34	Diameter 3 (mm)	68.28
Diameter 4 (mm)	68.10	Diameter 4 (mm)	68.24	Diameter 4 (mm)	68.12	Diameter 4 (mm)	68.30
Mean thickness (mm)	30.72	Mean thickness (mm)	31.42	Mean thickness (mm)	31.08	Mean thickness (mm)	28.69
Thickness 1 (mm)	30.78	Thickness 1 (mm)	31.12	Thickness 1 (mm)	31.42	Thickness 1 (mm)	29.74
Thickness 2 (mm)	30.62	Thickness 2 (mm)	31.54	Thickness 2 (mm)	31.10	Thickness 2 (mm)	28.34
Thickness 3 (mm)	31.42	Thickness 3 (mm)	31.62	Thickness 3 (mm)	31.52	Thickness 3 (mm)	28.60
Thickness 4 (mm)	30.04	Thickness 4 (mm)	31.38	Thickness 4 (mm)	30.26	Thickness 4 (mm)	28.06
Cell Volume (L)	5.00	Cell Volume (L)	5.00	Cell Volume (L)	5.00	Cell Volume (L)	5.00
k (m/s)	5.143E-11	k (m/s)	5.633E-11	k (m/s)	1.001E-10	k (m/s)	6.729E-11
r^2	0.9965	r^2	0.9984	r^2	0.9986	r^2	0.9975
r^2 Validity	Valid	r^2 Validity	Valid	r^2 Validity	Valid	r^2 Validity	Valid
OPI	10.29	OPI	10.25	OPI	10.00	OPI	10.17
Time	Pressure	Time	Pressure	Time	Pressure	Time	Pressure
hh:mm:ss	(kPa)	hh:mm:ss	(kPa)	hh:mm:ss	(kPa)	hh:mm:ss	(kPa)
17:36:41	102.47	17:36:41	100.27	17:36:41	102.21	17:36:41	102.55
17:41:41	102.12	17:41:41	99.85	17:41:41	101.77	17:41:41	102.10
17:46:41	101.76	17:46:41	99.45	17:46:41	101.27	17:46:41	101.63
17:51:41	101.48	17:51:41	99.09	17:51:41	100.75	17:51:41	101.27
17:56:41	101.27	17:56:41	98.78	17:56:41	100.22	17:56:41	100.85
18:01:41	101.04	18:01:41	98.42	18:01:41	99.67	18:01:41	100.45
18:06:41	100.84	18:06:41	98.06	18:06:41	99.15	18:06:41	100.02
18:11:41	100.55	18:11:41	97.66	18:11:41	98.66	18:11:41	99.67

18:16:41	100.33	18:16:41	97.35	18:16:41	98.08	18:16:41	99.29
18:21:41	100.11	18:21:41	97.06	18:21:41	97.57	18:21:41	98.91
18:26:41	99.91	18:26:41	96.74	18:26:41	97.01	18:26:41	98.52
18:31:41	99.71	18:31:41	96.40	18:31:41	96.47	18:31:41	98.14
18:36:41	99.49	18:36:41	96.10	18:36:41	95.98	18:36:41	97.77
18:41:41	98.90	18:41:41	95.78	18:41:41	95.46	18:41:41	97.44
18:46:41	98.43	18:46:41	95.54	18:46:41	94.92	18:46:41	97.03
18:51:41	97.99	18:51:41	95.26	18:51:41	94.42	18:51:41	96.71
18:56:41	97.63	18:56:41	95.02	18:56:41	93.89	18:56:41	96.31
19:01:41	97.26	19:01:41	94.78	19:01:41	93.41	19:01:41	95.98
19:06:41	96.82	19:06:41	94.52	19:06:41	92.93	19:06:41	95.65
19:11:41	96.50	19:11:41	94.19	19:11:41	92.43	19:11:41	95.31
19:16:41	96.20	19:16:41	93.90	19:16:41	91.87	19:16:41	94.91
19:21:41	95.93	19:21:41	93.66	19:21:41	91.42	19:21:41	94.57
19:26:41	95.66	19:26:41	93.36	19:26:41	90.90	19:26:41	94.23
19:31:41	95.40	19:31:41	93.08	19:31:41	90.39	19:31:41	93.87
19:36:41	95.14	19:36:41	92.82	19:36:41	89.90	19:36:41	93.53
19:41:41	94.90	19:41:41	92.56	19:41:41	89.40	19:41:41	93.16
19:46:41	94.63	19:46:41	92.33	19:46:41	88.97	19:46:41	92.85
19:51:41	94.34	19:51:41	92.06	19:51:41	88.49	19:51:41	92.50
19:56:41	94.08	19:56:41	91.79	19:56:41	87.98	19:56:41	92.14
20:01:41	93.88	20:01:41	91.53	20:01:41	87.50	20:01:41	91.76
20:06:41	93.60	20:06:41	91.25	20:06:41	87.02	20:06:41	91.43
20:11:41	93.34	20:11:41	91.04	20:11:41	86.59	20:11:41	91.08
20:16:41	93.09	20:16:41	90.70	20:16:41	86.09	20:16:41	90.69
20:21:41	92.82	20:21:41	90.47	20:21:41	85.66	20:21:41	90.34
20:26:41	92.58	20:26:41	90.16	20:26:41	85.14	20:26:41	89.97
20:31:41	92.37	20:31:41	89.94	20:31:41	84.67	20:31:41	89.57
20:36:41	92.09	20:36:41	89.63	20:36:41	84.19	20:36:41	89.23

20:41:41	91.84	20:41:41	89.39	20:41:41	83.73	20:41:41	88.87
20:46:41	91.59	20:46:41	89.13	20:46:41	83.26	20:46:41	88.49
20:51:41	91.30	20:51:41	88.79	20:51:41	82.72	20:51:41	88.07
20:56:41	91.04	20:56:41	88.57	20:56:41	82.28	20:56:41	87.71
21:01:41	90.75	21:01:41	88.28	21:01:41	81.81	21:01:41	87.35
21:06:41	90.56	21:06:41	88.04	21:06:41	81.32	21:06:41	86.94
21:11:41	90.28	21:11:41	87.73	21:11:41	80.83	21:11:41	86.59
21:16:41	90.09	21:16:41	87.46	21:16:41	80.33	21:16:41	86.19
21:21:41	89.87	21:21:41	87.25	21:21:41	79.89	21:21:41	85.81
21:26:41	89.58	21:26:41	86.99	21:26:41	79.43	21:26:41	85.45
21:31:41	89.37	21:31:41	86.66	21:31:41	78.93	21:31:41	85.06
21:36:41	89.11	21:36:41	86.45	21:36:41	78.53	21:36:41	84.73
21:41:41	88.90	21:41:41	86.15	21:41:41	78.02	21:41:41	84.34
21:46:41	88.66	21:46:41	85.95	21:46:41	77.59	21:46:41	83.96
21:51:41	88.41	21:51:41	85.66	21:51:41	77.12	21:51:41	83.61
21:56:41	88.23	21:56:41	85.43	21:56:41	76.64	21:56:41	83.19
22:01:41	88.02	22:01:41	85.16	22:01:41	76.17	22:01:41	82.81
22:06:41	87.74	22:06:41	84.93	22:06:41	75.76	22:06:41	82.49
22:11:41	87.56	22:11:41	84.63	22:11:41	75.24	22:11:41	82.08
22:16:41	87.31	22:16:41	84.42	22:16:41	74.82	22:16:41	81.71
22:21:41	87.09	22:21:41	84.11	22:21:41	74.32	22:21:41	81.32
22:26:41	86.84	22:26:41	83.86	22:26:41	73.88	22:26:41	80.99
22:31:41	86.66	22:31:41	83.63	22:31:41	73.42	22:31:41	80.59
22:36:41	86.40	22:36:41	83.37	22:36:41	73.02	22:36:41	80.27
22:41:41	86.23	22:41:41	83.14	22:41:41	72.55	22:41:41	79.87
22:46:41	86.01	22:46:41	82.94	22:46:41	72.15	22:46:41	79.52
22:51:41	85.74	22:51:41	82.69	22:51:41	71.73	22:51:41	79.19
22:56:41	85.54	22:56:41	82.46	22:56:41	71.29	22:56:41	78.82
23:01:41	85.36	23:01:41	82.23	23:01:41	70.90	23:01:41	78.47

23:06:41	85.13	23:06:41	81.97	23:06:41	70.48	23:06:41	78.12
23:11:41	84.94	23:11:41	81.68	23:11:41	70.03	23:11:41	77.75
23:16:41	84.75	23:16:41	81.45	23:16:41	69.63	23:16:41	77.40
23:21:41	84.56	23:21:41	81.23	23:21:41	69.24	23:21:41	77.05
23:26:41	84.32	23:26:41	81.04	23:26:41	68.89	23:26:41	76.76
23:31:41	84.13	23:31:41	80.83	23:31:41	68.48	23:31:41	76.42
23:36:41	83.97	23:36:41	80.57	23:36:41	68.12	23:36:41	76.07

MIX FA-30 (OPI Test-1)							
Mean OPI:		**10.19**		**Variability Check:**		**Good**	
Mean k (m/s):		**6.544E-11**		**COV % (Mean k):**		**8.7**	
Sample 1		Sample 2		Sample 3		Sample 4	
Mean diameter (mm)	68.49	Mean diameter (mm)	68.26	Mean diameter (mm)	68.42	Mean diameter (mm)	68.40
Diameter 1 (mm)	68.78	Diameter 1 (mm)	68.20	Diameter 1 (mm)	68.30	Diameter 1 (mm)	68.42
Diameter 2 (mm)	68.24	Diameter 2 (mm)	68.28	Diameter 2 (mm)	68.16	Diameter 2 (mm)	68.40
Diameter 3 (mm)	68.36	Diameter 3 (mm)	68.26	Diameter 3 (mm)	68.90	Diameter 3 (mm)	68.48
Diameter 4 (mm)	68.58	Diameter 4 (mm)	68.28	Diameter 4 (mm)	68.32	Diameter 4 (mm)	68.28
Mean thickness (mm)	30.74	Mean thickness (mm)	29.31	Mean thickness (mm)	29.91	Mean thickness (mm)	31.47
Thickness 1 (mm)	30.58	Thickness 1 (mm)	29.56	Thickness 1 (mm)	29.72	Thickness 1 (mm)	31.52
Thickness 2 (mm)	30.04	Thickness 2 (mm)	29.18	Thickness 2 (mm)	29.84	Thickness 2 (mm)	31.78
Thickness 3 (mm)	31.48	Thickness 3 (mm)	29.14	Thickness 3 (mm)	29.96	Thickness 3 (mm)	31.48
Thickness 4 (mm)	30.86	Thickness 4 (mm)	29.36	Thickness 4 (mm)	30.12	Thickness 4 (mm)	31.08
Cell Volume (L)	5.00	Cell Volume (L)	5.00	Cell Volume (L)	5.00	Cell Volume (L)	5.00
k (m/s)	5.756E-11	k (m/s)	7.068E-11	k (m/s)	6.520E-11	k (m/s)	6.833E-11
r^2	0.9982	r^2	0.9976	r^2	0.9962	r^2	0.9963
r^2 Validity	Valid	r^2 Validity	Valid	r^2 Validity	Valid	r^2 Validity	Valid
OPI	10.24	OPI	10.15	OPI	10.19	OPI	10.17

Time	Pressure	Time	Pressure	Time	Pressure	Time	Pressure
hh:mm:ss	(kPa)	hh:mm:ss	(kPa)	hh:mm:ss	(kPa)	hh:mm:ss	(kPa)
0:06:19	102.25	0:06:19	103.96	0:06:19	102.37	0:06:19	99.85
0:11:19	101.87	0:11:19	103.55	0:11:19	102.09	0:11:19	99.51
0:16:19	101.51	0:16:19	103.00	0:16:19	101.76	0:16:19	99.16
0:21:19	101.23	0:21:19	102.46	0:21:19	101.38	0:21:19	98.88
0:26:19	100.92	0:26:19	101.91	0:26:19	101.07	0:26:19	98.56
0:31:19	100.59	0:31:19	101.37	0:31:19	100.74	0:31:19	98.19
0:36:19	100.24	0:36:19	100.86	0:36:19	100.39	0:36:19	97.87
0:41:19	99.87	0:41:19	100.37	0:41:19	100.02	0:41:19	97.48
0:46:19	99.49	0:46:19	99.84	0:46:19	99.64	0:46:19	97.13
0:51:19	99.06	0:51:19	99.37	0:51:19	99.21	0:51:19	96.78
0:56:19	98.78	0:56:19	98.83	0:56:19	98.93	0:56:19	96.45
1:01:19	98.74	1:01:19	98.38	1:01:19	98.52	1:01:19	96.11
1:06:19	98.46	1:06:19	98.17	1:06:19	98.23	1:06:19	95.76
1:11:19	98.14	1:11:19	97.70	1:11:19	97.89	1:11:19	95.42
1:16:19	97.77	1:16:19	97.24	1:16:19	97.52	1:16:19	95.15
1:21:19	97.45	1:21:19	97.08	1:21:19	97.21	1:21:19	94.84
1:26:19	97.12	1:26:19	96.71	1:26:19	96.87	1:26:19	94.50
1:31:19	96.81	1:31:19	96.41	1:31:19	96.56	1:31:19	94.15
1:36:19	96.49	1:36:19	96.18	1:36:19	96.25	1:36:19	93.86
1:41:19	96.13	1:41:19	95.67	1:41:19	95.88	1:41:19	93.53
1:46:19	96.01	1:46:19	95.58	1:46:19	95.52	1:46:19	93.20
1:51:19	95.74	1:51:19	95.07	1:51:19	95.16	1:51:19	92.84
1:56:19	95.40	1:56:19	94.57	1:56:19	94.81	1:56:19	92.49
2:01:19	95.38	2:01:19	94.11	2:01:19	94.40	2:01:19	92.15
2:06:19	95.09	2:06:19	93.62	2:06:19	94.10	2:06:19	91.78
2:11:19	94.73	2:11:19	93.29	2:11:19	93.74	2:11:19	91.46
2:16:19	94.34	2:16:19	92.93	2:16:19	93.36	2:16:19	91.13

2:21:19	94.01	2:21:19	92.55	2:21:19	93.02	2:21:19	90.77
2:26:19	93.89	2:26:19	92.23	2:26:19	92.60	2:26:19	90.39
2:31:19	93.60	2:31:19	91.89	2:31:19	92.32	2:31:19	90.06
2:36:19	93.26	2:36:19	91.53	2:36:19	91.97	2:36:19	89.72
2:41:19	92.89	2:41:19	91.22	2:41:19	91.60	2:41:19	89.37
2:46:19	92.50	2:46:19	90.85	2:46:19	91.21	2:46:19	89.06
2:51:19	92.12	2:51:19	90.55	2:51:19	90.83	2:51:19	88.69
2:56:19	91.88	2:56:19	90.25	2:56:19	90.59	2:56:19	88.38
3:01:19	91.54	3:01:19	90.04	3:01:19	90.26	3:01:19	88.08
3:06:19	91.07	3:06:19	89.72	3:06:19	89.79	3:06:19	87.67
3:11:19	90.75	3:11:19	89.39	3:11:19	89.46	3:11:19	87.36
3:16:19	90.41	3:16:19	89.11	3:16:19	89.12	3:16:19	87.02
3:21:19	90.16	3:21:19	88.77	3:21:19	88.88	3:21:19	86.75
3:26:19	89.85	3:26:19	88.40	3:26:19	88.56	3:26:19	86.40
3:31:19	89.80	3:31:19	88.22	3:31:19	88.21	3:31:19	86.04
3:36:19	89.52	3:36:19	87.90	3:36:19	87.94	3:36:19	85.86
3:41:19	89.20	3:41:19	87.53	3:41:19	87.61	3:41:19	85.54
3:46:19	88.84	3:46:19	87.15	3:46:19	87.25	3:46:19	85.17
3:51:19	88.46	3:51:19	86.71	3:51:19	86.87	3:51:19	84.79
3:56:19	88.19	3:56:19	86.22	3:56:19	86.61	3:56:19	84.49
4:01:19	87.97	4:01:19	85.92	4:01:19	86.38	4:01:19	84.29
4:06:19	87.40	4:06:19	85.12	4:06:19	84.82	4:06:19	82.78
4:11:19	87.16	4:11:19	84.87	4:11:19	85.06	4:11:19	82.99
4:16:19	86.76	4:16:19	84.37	4:16:19	84.39	4:16:19	82.39
4:21:19	86.45	4:21:19	83.97	4:21:19	83.82	4:21:19	81.86
4:26:19	86.43	4:26:19	83.67	4:26:19	84.10	4:26:19	82.03
4:31:19	86.06	4:31:19	83.65	4:31:19	83.34	4:31:19	81.37
4:36:19	85.70	4:36:19	83.27	4:36:19	83.00	4:36:19	81.07
4:41:19	85.31	4:41:19	82.91	4:41:19	82.61	4:41:19	80.63

4:46:19	84.95	4:46:19	82.52	4:46:19	82.33	4:46:19	80.40
4:51:19	84.57	4:51:19	82.16	4:51:19	82.49	4:51:19	80.50
4:56:19	84.33	4:56:19	81.78	4:56:19	81.80	4:56:19	79.93
5:01:19	84.00	5:01:19	81.34	5:01:19	81.60	5:01:19	79.62
5:06:19	83.61	5:06:19	81.01	5:06:19	81.25	5:06:19	79.35
5:11:19	83.60	5:11:19	80.63	5:11:19	81.02	5:11:19	79.12
5:16:19	83.27	5:16:19	80.21	5:16:19	80.74	5:16:19	78.78
5:21:19	83.04	5:21:19	79.88	5:21:19	80.41	5:21:19	78.53
5:26:19	82.88	5:26:19	79.45	5:26:19	80.01	5:26:19	78.20
5:31:19	82.51	5:31:19	79.10	5:31:19	79.95	5:31:19	78.01
5:36:19	82.22	5:36:19	78.72	5:36:19	79.52	5:36:19	77.69
5:41:19	82.21	5:41:19	78.33	5:41:19	79.38	5:41:19	77.54
5:46:19	82.02	5:46:19	78.33	5:46:19	78.98	5:46:19	77.15
5:51:19	81.72	5:51:19	78.12	5:51:19	78.54	5:51:19	76.74
5:56:19	81.64	5:56:19	78.03	5:56:19	78.38	5:56:19	76.55
6:01:19	81.45	6:01:19	77.85	6:01:19	78.22	6:01:19	76.36
6:06:19	81.44	6:06:19	77.76	6:06:19	77.83	6:06:19	76.04

MIX FA-30 (OPI Test-2)							
Mean OPI:		**10.12**		**Variability Check:**		**Good**	
Mean k (m/s):		**7.630E-11**		**COV % (Mean k):**		**18.2**	
Sample 1		Sample 2		Sample 3		Sample 4	
Mean diameter (mm)	68.24	Mean diameter (mm)	68.35	Mean diameter (mm)	68.33	Mean diameter (mm)	68.18
Diameter 1 (mm)	68.18	Diameter 1 (mm)	68.56	Diameter 1 (mm)	68.36	Diameter 1 (mm)	68.04
Diameter 2 (mm)	68.32	Diameter 2 (mm)	68.26	Diameter 2 (mm)	68.28	Diameter 2 (mm)	68.34
Diameter 3 (mm)	68.26	Diameter 3 (mm)	68.34	Diameter 3 (mm)	68.30	Diameter 3 (mm)	68.20
Diameter 4 (mm)	68.20	Diameter 4 (mm)	68.24	Diameter 4 (mm)	68.38	Diameter 4 (mm)	68.12

Mean thickness (mm)	28.97	Mean thickness (mm)	30.06	Mean thickness (mm)	31.23	Mean thickness (mm)	29.59
Thickness 1 (mm)	29.32	Thickness 1 (mm)	29.62	Thickness 1 (mm)	31.84	Thickness 1 (mm)	30.06
Thickness 2 (mm)	28.52	Thickness 2 (mm)	30.06	Thickness 2 (mm)	31.64	Thickness 2 (mm)	28.78
Thickness 3 (mm)	29.38	Thickness 3 (mm)	29.50	Thickness 3 (mm)	31.32	Thickness 3 (mm)	29.92
Thickness 4 (mm)	28.64	Thickness 4 (mm)	31.04	Thickness 4 (mm)	30.10	Thickness 4 (mm)	29.60
Cell Volume (L)	5.00	Cell Volume (L)	5.00	Cell Volume (L)	5.00	Cell Volume (L)	5.00
k (m/s)	9.467E-11	k (m/s)	6.957E-11	k (m/s)	6.256E-11	k (m/s)	7.839E-11
r^2	0.9947	r^2	0.9972	r^2	0.9988	r^2	0.9962
r^2 Validity	Valid	r^2 Validity	Valid	r^2 Validity	Valid	r^2 Validity	Valid
OPI	10.02	OPI	10.16	OPI	10.20	OPI	10.11
Time	Pressure	Time	Pressure	Time	Pressure	Time	Pressure
hh:mm:ss	(kPa)	hh:mm:ss	(kPa)	hh:mm:ss	(kPa)	hh:mm:ss	(kPa)
0:06:19	103.44	0:06:19	102.11	6:32:06	100.33	6:32:06	102.83
0:11:19	102.93	0:11:19	101.66	6:37:06	99.90	6:37:06	102.18
0:16:19	102.44	0:16:19	101.14	6:42:06	99.56	6:42:06	101.75
0:21:19	101.88	0:21:19	100.57	6:47:06	99.06	6:47:06	101.42
0:26:19	101.43	0:26:19	100.27	6:52:06	98.73	6:52:06	100.89
0:31:19	101.05	0:31:19	99.97	6:57:06	98.44	6:57:06	100.57
0:36:19	100.63	0:36:19	99.63	7:02:06	98.11	7:02:06	100.17
0:41:19	100.25	0:41:19	99.06	7:07:06	97.61	7:07:06	99.89
0:46:19	99.70	0:46:19	98.79	7:12:06	97.37	7:12:06	99.53
0:51:19	99.40	0:51:19	98.29	7:17:06	97.19	7:17:06	99.23
0:56:19	98.84	0:56:19	98.20	7:22:06	96.61	7:22:06	98.92
1:01:19	98.27	1:01:19	97.73	7:27:06	96.27	7:27:06	98.32
1:06:19	97.61	1:06:19	97.16	7:32:06	95.97	7:32:06	98.12
1:11:19	97.02	1:11:19	96.65	7:37:06	95.41	7:37:06	97.82
1:16:19	96.50	1:16:19	96.17	7:42:06	95.38	7:42:06	97.74
1:21:19	95.94	1:21:19	95.68	7:47:06	95.13	7:47:06	97.50
1:26:19	95.35	1:26:19	95.17	7:52:06	94.85	7:52:06	96.88

1:31:19	94.72	1:31:19	94.63	7:57:06	94.44	7:57:06	96.36
1:36:19	94.15	1:36:19	94.34	8:02:06	94.15	8:02:06	95.74
1:41:19	93.58	1:41:19	94.01	8:07:06	93.81	8:07:06	95.25
1:46:19	93.00	1:46:19	93.68	8:12:06	93.44	8:12:06	94.62
1:51:19	92.39	1:51:19	93.32	8:17:06	93.13	8:17:06	94.05
1:56:19	91.80	1:56:19	92.97	8:22:06	92.79	8:22:06	93.43
2:01:19	91.25	2:01:19	92.63	8:27:06	92.48	8:27:06	92.91
2:06:19	90.61	2:06:19	92.26	8:32:06	92.17	8:32:06	92.19
2:11:19	90.02	2:11:19	91.94	8:37:06	91.80	8:37:06	91.65
2:16:19	89.46	2:16:19	91.61	8:42:06	91.64	8:42:06	91.30
2:21:19	89.45	2:21:19	91.25	8:47:06	91.58	8:47:06	90.73
2:26:19	88.87	2:26:19	90.87	8:52:06	91.23	8:52:06	90.70
2:31:19	88.26	2:31:19	90.54	8:57:06	90.82	8:57:06	90.16
2:36:19	87.67	2:36:19	90.20	9:02:06	90.52	9:02:06	89.96
2:41:19	87.07	2:41:19	89.85	9:07:06	90.16	9:07:06	89.41
2:46:19	86.57	2:46:19	89.54	9:12:06	89.88	9:12:06	88.93
2:51:19	85.96	2:51:19	89.17	9:17:06	89.54	9:17:06	88.39
2:56:19	85.37	2:56:19	88.86	9:22:06	89.12	9:22:06	88.00
3:01:19	84.82	3:01:19	88.56	9:27:06	88.84	9:27:06	87.99
3:06:19	84.23	3:06:19	88.15	9:32:06	88.49	9:32:06	87.59
3:11:19	83.64	3:11:19	87.84	9:37:06	88.12	9:37:06	87.13
3:16:19	83.11	3:16:19	87.50	9:42:06	88.03	9:42:06	86.73
3:21:19	82.58	3:21:19	87.23	9:47:06	87.65	9:47:06	86.37
3:26:19	82.00	3:26:19	86.88	9:52:06	87.41	9:52:06	85.95
3:31:19	81.43	3:31:19	86.52	9:57:06	87.08	9:57:06	85.47
3:36:19	81.04	3:36:19	86.34	10:02:06	87.01	10:02:06	85.06
3:41:19	80.52	3:41:19	86.02	10:07:06	86.68	10:07:06	84.56
3:46:19	79.96	3:46:19	85.65	10:12:06	86.34	10:12:06	84.15
3:51:19	79.37	3:51:19	85.27	10:17:06	86.10	10:17:06	83.72

3:56:19	78.83	3:56:19	84.78	10:22:06	85.78	10:22:06	83.30
4:01:19	78.46	4:01:19	84.41	10:27:06	85.43	10:27:06	82.82
4:06:19	77.90	4:06:19	84.07	10:32:06	85.03	10:32:06	82.44
4:11:19	77.89	4:11:19	83.83	10:37:06	84.69	10:37:06	82.02
4:16:19	77.44	4:16:19	83.49	10:42:06	84.32	10:42:06	81.65
4:21:19	76.78	4:21:19	83.31	10:47:06	84.28	10:47:06	81.18
4:26:19	76.71	4:26:19	82.99	10:52:06	84.06	10:52:06	80.72
4:31:19	76.38	4:31:19	82.83	10:57:06	83.75	10:57:06	80.39
4:36:19	75.93	4:36:19	82.44	11:02:06	83.40	11:02:06	79.99
4:41:19	75.35	4:41:19	82.03	11:07:06	82.96	11:07:06	79.57
4:46:19	74.95	4:46:19	81.85	11:12:06	82.63	11:12:06	79.21
4:51:19	74.80	4:51:19	81.46	11:17:06	82.33	11:17:06	78.85
4:56:19	74.14	4:56:19	81.05	11:22:06	82.00	11:22:06	78.45
5:01:19	73.63	5:01:19	80.57	11:27:06	81.63	11:27:06	78.10
5:06:19	73.24	5:06:19	80.22	11:32:06	81.35	11:32:06	77.72
5:11:19	72.86	5:11:19	79.83	11:37:06	80.98	11:37:06	77.35
5:16:19	72.82	5:16:19	79.36	11:42:06	80.74	11:42:06	77.05
5:21:19	72.46	5:21:19	79.02	11:47:06	80.39	11:47:06	76.66
5:26:19	72.27	5:26:19	78.99	11:52:06	79.98	11:52:06	76.46
5:31:19	71.89	5:31:19	78.88	11:57:06	79.74	11:57:06	76.21
5:36:19	71.78	5:36:19	78.51	12:02:06	79.64	12:02:06	76.03
5:41:19	71.55	5:41:19	78.30	12:07:06	79.50	12:07:06	76.02
5:46:19	71.52	5:46:19	78.28	12:12:06	79.44	12:12:06	75.86
5:51:19	71.39	5:51:19	78.06	12:17:06	79.20	12:17:06	75.61
5:56:19	71.14	5:56:19	78.05	12:22:06	79.19	12:22:06	75.49
6:01:19	71.07	6:01:19	77.92	12:27:06	79.07	12:27:06	75.28
6:06:19	70.93	6:06:19	77.92	12:32:06	78.79	12:32:06	75.27

MIX FA-30 (OPI Test-3)							
Mean OPI:		**10.15**		**Variability Check:**		**Good**	
Mean k (m/s):		**7.085E-11**		**COV % (Mean k):**		**11.8**	
Sample 1		Sample 2		Sample 3		Sample 4	
Mean diameter (mm)	68.31	Mean diameter (mm)	68.40	Mean diameter (mm)	68.56	Mean diameter (mm)	68.34
Diameter 1 (mm)	68.26	Diameter 1 (mm)	68.48	Diameter 1 (mm)	68.48	Diameter 1 (mm)	68.28
Diameter 2 (mm)	68.34	Diameter 2 (mm)	68.30	Diameter 2 (mm)	68.44	Diameter 2 (mm)	68.46
Diameter 3 (mm)	68.44	Diameter 3 (mm)	68.28	Diameter 3 (mm)	68.78	Diameter 3 (mm)	68.24
Diameter 4 (mm)	68.20	Diameter 4 (mm)	68.52	Diameter 4 (mm)	68.54	Diameter 4 (mm)	68.38
Mean thickness (mm)	29.05	Mean thickness (mm)	31.06	Mean thickness (mm)	30.59	Mean thickness (mm)	31.88
Thickness 1 (mm)	29.72	Thickness 1 (mm)	31.90	Thickness 1 (mm)	30.90	Thickness 1 (mm)	31.78
Thickness 2 (mm)	28.34	Thickness 2 (mm)	30.26	Thickness 2 (mm)	30.76	Thickness 2 (mm)	31.84
Thickness 3 (mm)	29.48	Thickness 3 (mm)	31.56	Thickness 3 (mm)	30.18	Thickness 3 (mm)	31.96
Thickness 4 (mm)	28.64	Thickness 4 (mm)	30.50	Thickness 4 (mm)	30.50	Thickness 4 (mm)	31.92
Cell Volume (L)	5.00	Cell Volume (L)	5.00	Cell Volume (L)	5.00	Cell Volume (L)	5.00
k (m/s)	6.586E-11	k (m/s)	7.233E-11	k (m/s)	8.195E-11	k (m/s)	6.326E-11
r^2	0.9902	r^2	0.9964	r^2	0.9959	r^2	0.9949
r^2 Validity	Valid	r^2 Validity	Valid	r^2 Validity	Valid	r^2 Validity	Valid
OPI	10.18	OPI	10.14	OPI	10.09	OPI	10.20
Time	Pressure	Time	Pressure	Time	Pressure	Time	Pressure
hh:mm:ss	(kPa)	hh:mm:ss	(kPa)	hh:mm:ss	(kPa)	hh:mm:ss	(kPa)
6:32:06	100.33	6:32:06	97.00	6:32:06	100.37	6:32:06	101.58
6:37:06	99.89	6:37:06	96.51	6:37:06	99.70	6:37:06	101.22
6:42:06	99.54	6:42:06	96.18	6:42:06	99.27	6:42:06	100.90
6:47:06	99.26	6:47:06	95.82	6:47:06	98.80	6:47:06	100.56
6:52:06	98.94	6:52:06	95.32	6:52:06	98.19	6:52:06	100.36
6:57:06	98.57	6:57:06	94.86	6:57:06	97.63	6:57:06	100.11
7:02:06	98.25	7:02:06	94.50	7:02:06	97.22	7:02:06	99.74
7:07:06	97.86	7:07:06	94.05	7:07:06	96.64	7:07:06	99.31

7:12:06	97.51	7:12:06	93.61	7:12:06	96.14	7:12:06	98.87
7:17:06	97.17	7:17:06	93.23	7:17:06	95.63	7:17:06	98.49
7:22:06	96.83	7:22:06	92.81	7:22:06	95.15	7:22:06	98.07
7:27:06	96.49	7:27:06	92.39	7:27:06	94.63	7:27:06	97.66
7:32:06	96.14	7:32:06	92.02	7:32:06	94.17	7:32:06	97.28
7:37:06	95.81	7:37:06	91.68	7:37:06	93.77	7:37:06	96.94
7:42:06	95.54	7:42:06	91.09	7:42:06	93.10	7:42:06	96.55
7:47:06	95.22	7:47:06	92.24	7:47:06	94.20	7:47:06	96.28
7:52:06	94.89	7:52:06	91.64	7:52:06	93.52	7:52:06	95.88
7:57:06	94.53	7:57:06	91.25	7:57:06	93.09	7:57:06	95.56
8:02:06	94.24	8:02:06	90.84	8:02:06	92.58	8:02:06	95.16
8:07:06	93.92	8:07:06	90.59	8:07:06	92.30	8:07:06	94.91
8:12:06	93.58	8:12:06	90.25	8:12:06	91.85	8:12:06	94.57
8:17:06	93.22	8:17:06	89.73	8:17:06	91.28	8:17:06	94.25
8:22:06	92.87	8:22:06	89.29	8:22:06	90.73	8:22:06	93.81
8:27:06	92.53	8:27:06	88.81	8:27:06	90.22	8:27:06	93.33
8:32:06	92.16	8:32:06	88.21	8:32:06	89.52	8:32:06	93.03
8:37:06	91.84	8:37:06	87.77	8:37:06	89.01	8:37:06	92.59
8:42:06	91.51	8:42:06	87.16	8:42:06	88.34	8:42:06	92.38
8:47:06	91.15	8:47:06	86.71	8:47:06	87.82	8:47:06	91.93
8:52:06	90.77	8:52:06	86.28	8:52:06	87.31	8:52:06	91.50
8:57:06	90.45	8:57:06	85.50	8:57:06	86.49	8:57:06	91.01
9:02:06	90.10	9:02:06	85.18	9:02:06	86.11	9:02:06	90.70
9:07:06	89.75	9:07:06	84.79	9:07:06	85.64	9:07:06	90.31
9:12:06	89.44	9:12:06	84.19	9:12:06	85.04	9:12:06	90.01
9:17:06	89.07	9:17:06	83.98	9:17:06	84.74	9:17:06	89.80
9:22:06	88.77	9:22:06	84.08	9:22:06	84.81	9:22:06	89.69
9:27:06	88.47	9:27:06	83.72	9:27:06	84.39	9:27:06	89.34
9:32:06	88.06	9:32:06	83.35	9:32:06	84.01	9:32:06	88.97

9:37:06	87.74	9:37:06	83.07	9:37:06	83.68	9:37:06	88.69
9:42:06	87.41	9:42:06	83.12	9:42:06	83.66	9:42:06	88.64
9:47:06	87.13	9:47:06	83.02	9:47:06	83.56	9:47:06	88.54
9:52:06	86.79	9:52:06	82.78	9:52:06	83.28	9:52:06	88.50
9:57:06	86.42	9:57:06	82.39	9:57:06	82.83	9:57:06	88.40
10:02:06	86.24	10:02:06	82.19	10:02:06	82.59	10:02:06	88.20
10:07:06	85.92	10:07:06	81.97	10:07:06	82.31	10:07:06	87.99
10:12:06	85.55	10:12:06	81.58	10:12:06	81.92	10:12:06	87.60
10:17:06	85.17	10:17:06	81.25	10:17:06	81.55	10:17:06	87.27
10:22:06	84.87	10:22:06	80.91	10:22:06	81.14	10:22:06	86.93
10:27:06	84.67	10:27:06	80.66	10:27:06	80.84	10:27:06	86.67
10:32:06	83.17	10:32:06	80.31	10:32:06	80.46	10:32:06	86.32
10:37:06	82.96	10:37:06	80.05	10:37:06	80.17	10:37:06	86.06
10:42:06	82.36	10:42:06	79.68	10:42:06	79.81	10:42:06	85.70
10:47:06	81.83	10:47:06	79.17	10:47:06	79.26	10:47:06	85.48
10:52:06	81.66	10:52:06	78.90	10:52:06	78.93	10:52:06	85.21
10:57:06	80.99	10:57:06	78.55	10:57:06	78.58	10:57:06	84.86
11:02:06	80.69	11:02:06	78.28	11:02:06	78.30	11:02:06	84.60
11:07:06	80.26	11:07:06	77.93	11:07:06	77.88	11:07:06	84.24
11:12:06	80.03	11:12:06	77.58	11:12:06	77.54	11:12:06	83.90
11:17:06	79.74	11:17:06	77.24	11:17:06	77.18	11:17:06	83.55
11:22:06	79.17	11:22:06	77.00	11:22:06	76.92	11:22:06	83.32
11:27:06	78.85	11:27:06	76.65	11:27:06	76.55	11:27:06	82.97
11:32:06	78.58	11:32:06	76.38	11:32:06	76.28	11:32:06	82.70
11:37:06	78.36	11:37:06	76.12	11:37:06	75.96	11:37:06	82.44
11:42:06	78.02	11:42:06	75.74	11:42:06	75.61	11:42:06	82.06
11:47:06	77.77	11:47:06	75.37	11:47:06	75.22	11:47:06	81.69
11:52:06	77.43	11:52:06	74.60	11:52:06	74.40	11:52:06	81.62
11:57:06	77.25	11:57:06	74.59	11:57:06	74.41	11:57:06	81.61

12:02:06	76.93	12:02:06	74.93	12:02:06	74.74	12:02:06	81.47
12:07:06	76.78	12:07:06	74.30	12:07:06	74.12	12:07:06	81.13
12:12:06	76.38	12:12:06	73.28	12:12:06	73.09	12:12:06	81.01
12:17:06	75.98	12:17:06	73.17	12:17:06	72.96	12:17:06	80.91
12:22:06	75.79	12:22:06	72.99	12:22:06	72.77	12:22:06	80.72
12:27:06	75.59	12:27:06	72.48	12:27:06	72.30	12:27:06	80.47
12:32:06	75.28	12:32:06	72.16	12:32:06	71.98	12:32:06	80.25

MIX GGBS-50 (OPI Test-1)							
Mean OPI:		**10.27**		**Variability Check:**		**Good**	
Mean k (m/s):		**5.427E-11**		**COV % (Mean k):**		**12.0**	
Sample 1		Sample 2		Sample 3		Sample 4	
Mean diameter (mm)	68.50	Mean diameter (mm)	68.53	Mean diameter (mm)	68.59	Mean diameter (mm)	68.69
Diameter 1 (mm)	68.58	Diameter 1 (mm)	68.52	Diameter 1 (mm)	68.50	Diameter 1 (mm)	68.74
Diameter 2 (mm)	68.46	Diameter 2 (mm)	68.50	Diameter 2 (mm)	68.56	Diameter 2 (mm)	68.84
Diameter 3 (mm)	68.48	Diameter 3 (mm)	68.58	Diameter 3 (mm)	68.62	Diameter 3 (mm)	68.54
Diameter 4 (mm)	68.46	Diameter 4 (mm)	68.52	Diameter 4 (mm)	68.66	Diameter 4 (mm)	68.62
Mean thickness (mm)	28.73	Mean thickness (mm)	28.36	Mean thickness (mm)	28.68	Mean thickness (mm)	30.25
Thickness 1 (mm)	28.64	Thickness 1 (mm)	28.82	Thickness 1 (mm)	29.08	Thickness 1 (mm)	30.30
Thickness 2 (mm)	29.48	Thickness 2 (mm)	28.08	Thickness 2 (mm)	28.08	Thickness 2 (mm)	30.00
Thickness 3 (mm)	28.40	Thickness 3 (mm)	28.52	Thickness 3 (mm)	29.06	Thickness 3 (mm)	30.54
Thickness 4 (mm)	28.40	Thickness 4 (mm)	28.02	Thickness 4 (mm)	28.48	Thickness 4 (mm)	30.16
Cell Volume (L)	5.00	Cell Volume (L)	5.00	Cell Volume (L)	5.00	Cell Volume (L)	5.00
k (m/s)	5.788E-11	k (m/s)	5.951E-11	k (m/s)	4.496E-11	k (m/s)	5.475E-11
r^2	0.9967	r^2	0.9975	r^2	0.9949	r^2	0.9986
r^2 Validity	Valid	r^2 Validity	Valid	r^2 Validity	Valid	r^2 Validity	Valid
OPI	10.24	OPI	10.23	OPI	10.35	OPI	10.26

Time	Pressure	Time	Pressure	Time	Pressure	Time	Pressure
hh:mm:ss	(kPa)	hh:mm:ss	(kPa)	hh:mm:ss	(kPa)	hh:mm:ss	(kPa)
23:52:35	102.26	23:52:35	102.96	23:52:35	102.83	23:52:35	97.98
23:57:35	101.97	23:57:35	102.57	23:57:35	102.82	23:57:35	97.89
0:02:35	101.61	0:02:35	102.21	0:02:35	102.43	0:02:35	97.61
0:07:35	101.28	0:07:35	101.78	0:07:35	102.10	0:07:35	97.25
0:12:35	100.99	0:12:35	101.39	0:12:35	101.77	0:12:35	96.87
0:17:35	100.66	0:17:35	100.96	0:17:35	101.52	0:17:35	96.54
0:22:35	100.27	0:22:35	100.57	0:22:35	101.31	0:22:35	96.17
0:27:35	99.84	0:27:35	100.14	0:27:35	101.05	0:27:35	95.90
0:32:35	99.49	0:32:35	99.79	0:32:35	100.77	0:32:35	95.53
0:37:35	99.08	0:37:35	99.38	0:37:35	100.52	0:37:35	95.20
0:42:35	98.73	0:42:35	99.03	0:42:35	100.27	0:42:35	94.89
0:47:35	98.34	0:47:35	98.64	0:47:35	100.13	0:47:35	94.63
0:52:35	97.97	0:52:35	98.27	0:52:35	99.80	0:52:35	94.39
0:57:35	97.63	0:57:35	97.83	0:57:35	99.45	0:57:35	94.06
1:02:35	97.26	1:02:35	97.46	1:02:35	99.41	1:02:35	93.93
1:07:35	96.96	1:07:35	97.16	1:07:35	99.28	1:07:35	93.71
1:12:35	96.74	1:12:35	96.74	1:12:35	98.83	1:12:35	93.25
1:17:35	96.67	1:17:35	96.66	1:17:35	98.41	1:17:35	92.82
1:22:35	96.38	1:22:35	96.28	1:22:35	98.20	1:22:35	92.55
1:27:35	96.00	1:27:35	95.90	1:27:35	98.14	1:27:35	92.34
1:32:35	95.70	1:32:35	95.49	1:32:35	97.75	1:32:35	92.12
1:37:35	95.32	1:37:35	95.12	1:37:35	97.43	1:37:35	91.69
1:42:35	95.19	1:42:35	94.99	1:42:35	97.16	1:42:35	91.21
1:47:35	94.98	1:47:35	94.98	1:47:35	96.84	1:47:35	90.84
1:52:35	94.68	1:52:35	94.78	1:52:35	96.56	1:52:35	90.61
1:57:35	94.38	1:57:35	94.47	1:57:35	96.51	1:57:35	90.46
2:02:35	94.02	2:02:35	94.12	2:02:35	96.19	2:02:35	90.05

2:07:35	93.76	2:07:35	93.86	2:07:35	95.70	2:07:35	89.75
2:12:35	93.39	2:12:35	93.48	2:12:35	95.15	2:12:35	89.42
2:17:35	93.03	2:17:35	93.13	2:17:35	95.01	2:17:35	89.12
2:22:35	92.67	2:22:35	92.76	2:22:35	94.80	2:22:35	88.85
2:27:35	92.28	2:27:35	92.38	2:27:35	94.52	2:27:35	88.51
2:32:35	91.96	2:32:35	92.06	2:32:35	94.49	2:32:35	88.40
2:37:35	91.57	2:37:35	91.67	2:37:35	94.23	2:37:35	88.15
2:42:35	91.21	2:42:35	91.31	2:42:35	94.01	2:42:35	87.83
2:47:35	90.99	2:47:35	90.89	2:47:35	93.90	2:47:35	87.67
2:52:35	90.76	2:52:35	90.65	2:52:35	93.75	2:52:35	87.60
2:57:35	90.44	2:57:35	90.44	2:57:35	93.55	2:57:35	87.39
3:02:35	90.07	3:02:35	90.07	3:02:35	93.35	3:02:35	87.12
3:07:35	89.72	3:07:35	89.72	3:07:35	93.22	3:07:35	86.87
3:12:35	89.34	3:12:35	89.34	3:12:35	93.01	3:12:35	86.59
3:17:35	89.00	3:17:35	89.09	3:17:35	92.47	3:17:35	86.35
3:22:35	88.81	3:22:35	88.91	3:22:35	92.26	3:22:35	86.29
3:27:35	88.57	3:27:35	88.67	3:27:35	91.99	3:27:35	86.01
3:32:35	88.24	3:32:35	88.34	3:32:35	91.73	3:32:35	85.66
3:37:35	87.83	3:37:35	87.93	3:37:35	91.15	3:37:35	85.27
3:42:35	87.38	3:42:35	87.48	3:42:35	91.02	3:42:35	85.06
3:47:35	87.02	3:47:35	87.12	3:47:35	90.83	3:47:35	84.73
3:52:35	86.63	3:52:35	86.73	3:52:35	90.62	3:52:35	84.52
3:57:35	86.24	3:57:35	86.34	3:57:35	90.41	3:57:35	84.22
4:02:35	85.86	4:02:35	85.96	4:02:35	90.16	4:02:35	83.92
4:07:35	85.55	4:07:35	85.55	4:07:35	89.82	4:07:35	83.59
4:12:35	85.26	4:12:35	85.26	4:12:35	89.46	4:12:35	83.25
4:17:35	84.90	4:17:35	84.90	4:17:35	89.08	4:17:35	82.90
4:22:35	84.60	4:22:35	84.60	4:22:35	88.75	4:22:35	82.77
4:27:35	84.15	4:27:35	84.34	4:27:35	88.30	4:27:35	82.47

4:32:35	83.78	4:32:35	83.98	4:32:35	87.93	4:32:35	82.24
4:37:35	83.46	4:37:35	83.66	4:37:35	87.87	4:37:35	82.15
4:42:35	83.20	4:42:35	83.20	4:42:35	87.46	4:42:35	81.75
4:47:35	83.08	4:47:35	82.78	4:47:35	87.31	4:47:35	81.47
4:52:35	82.77	4:52:35	82.47	4:52:35	86.88	4:52:35	81.03
4:57:35	82.36	4:57:35	82.06	4:57:35	86.64	4:57:35	80.70
5:02:35	82.05	5:02:35	81.64	5:02:35	86.38	5:02:35	80.35
5:07:35	81.69	5:07:35	81.29	5:07:35	86.03	5:07:35	80.05
5:12:35	81.43	5:12:35	81.23	5:12:35	85.81	5:12:35	79.72
5:17:35	81.06	5:17:35	80.85	5:17:35	85.42	5:17:35	79.34
5:22:35	80.71	5:22:35	80.51	5:22:35	85.38	5:22:35	79.24
5:27:35	80.40	5:27:35	80.20	5:27:35	85.30	5:27:35	79.24
5:32:35	80.21	5:32:35	80.01	5:32:35	85.05	5:32:35	79.00
5:37:35	79.85	5:37:35	79.65	5:37:35	84.72	5:37:35	78.62
5:42:35	79.59	5:42:35	79.59	5:42:35	84.55	5:42:35	78.32
5:47:35	79.43	5:47:35	79.33	5:47:35	84.54	5:47:35	78.24
5:52:35	79.38	5:52:35	79.28	5:52:35	84.48	5:52:35	78.07

MIX GGBS-50 (OPI Test-2)							
Mean OPI:		**10.25**		**Variability Check:**		**Good**	
Mean k (m/s):		**5.686E-11**		**COV % (Mean k):**		**9.9**	
Sample 1		Sample 2		Sample 3		Sample 4	
Mean diameter (mm)	68.53	Mean diameter (mm)	68.67	Mean diameter (mm)	68.65	Mean diameter (mm)	68.64
Diameter 1 (mm)	68.56	Diameter 1 (mm)	68.64	Diameter 1 (mm)	68.72	Diameter 1 (mm)	68.72
Diameter 2 (mm)	68.60	Diameter 2 (mm)	68.86	Diameter 2 (mm)	68.64	Diameter 2 (mm)	68.70
Diameter 3 (mm)	68.48	Diameter 3 (mm)	68.70	Diameter 3 (mm)	68.54	Diameter 3 (mm)	68.62
Diameter 4 (mm)	68.46	Diameter 4 (mm)	68.48	Diameter 4 (mm)	68.70	Diameter 4 (mm)	68.52

Mean thickness (mm)	29.75	Mean thickness (mm)	29.56	Mean thickness (mm)	29.05	Mean thickness (mm)	29.72
Thickness 1 (mm)	29.54	Thickness 1 (mm)	29.32	Thickness 1 (mm)	29.66	Thickness 1 (mm)	29.72
Thickness 2 (mm)	29.84	Thickness 2 (mm)	29.84	Thickness 2 (mm)	29.42	Thickness 2 (mm)	29.48
Thickness 3 (mm)	29.52	Thickness 3 (mm)	29.50	Thickness 3 (mm)	28.60	Thickness 3 (mm)	29.58
Thickness 4 (mm)	30.08	Thickness 4 (mm)	29.56	Thickness 4 (mm)	28.52	Thickness 4 (mm)	30.10
Cell Volume (L)	5.00	Cell Volume (L)	5.00	Cell Volume (L)	5.00	Cell Volume (L)	5.00
k (m/s)	5.700E-11	k (m/s)	5.222E-11	k (m/s)	5.350E-11	k (m/s)	6.470E-11
r^2	0.9986	r^2	0.9968	r^2	0.9956	r^2	0.9952
r^2 Validity	Valid	r^2 Validity	Valid	r^2 Validity	Valid	r^2 Validity	Valid
OPI	10.24	OPI	10.28	OPI	10.27	OPI	10.19
Time	Pressure	Time	Pressure	Time	Pressure	Time	Pressure
hh:mm:ss	(kPa)	hh:mm:ss	(kPa)	hh:mm:ss	(kPa)	hh:mm:ss	(kPa)
23:52:35	100.78	23:52:35	102.70	6:17:43	102.56	6:17:43	103.13
23:57:35	100.37	23:57:35	102.25	6:22:43	102.13	6:22:43	102.68
0:02:35	100.03	0:02:35	101.94	6:27:43	101.74	6:27:43	102.17
0:07:35	99.63	0:07:35	101.49	6:32:43	101.31	6:32:43	101.72
0:12:35	99.27	0:12:35	101.19	6:37:43	100.92	6:37:43	101.28
0:17:35	98.82	0:17:35	100.90	6:42:43	100.49	6:42:43	100.84
0:22:35	98.45	0:22:35	100.61	6:47:43	100.14	6:47:43	100.41
0:27:35	98.15	0:27:35	100.30	6:52:43	99.73	6:52:43	100.00
0:32:35	97.74	0:32:35	100.04	6:57:43	99.38	6:57:43	99.61
0:37:35	97.66	0:37:35	99.69	7:02:43	98.99	7:02:43	99.20
0:42:35	97.27	0:42:35	99.41	7:07:43	98.62	7:07:43	98.77
0:47:35	96.90	0:47:35	99.09	7:12:43	98.18	7:12:43	98.35
0:52:35	96.49	0:52:35	98.75	7:17:43	97.81	7:17:43	97.95
0:57:35	96.11	0:57:35	98.34	7:22:43	97.51	7:22:43	97.57
1:02:35	95.98	1:02:35	98.03	7:27:43	97.09	7:27:43	97.48
1:07:35	95.98	1:07:35	97.77	7:32:43	97.01	7:32:43	97.12
1:12:35	95.78	1:12:35	97.47	7:37:43	96.63	7:37:43	96.75

1:17:35	95.47	1:17:35	97.09	7:42:43	96.25	7:42:43	96.67
1:22:35	95.12	1:22:35	96.84	7:47:43	96.04	7:47:43	96.29
1:27:35	94.85	1:27:35	96.45	7:52:43	95.66	7:52:43	95.92
1:32:35	94.48	1:32:35	96.19	7:57:43	95.54	7:57:43	95.43
1:37:35	94.13	1:37:35	95.90	8:02:43	95.53	8:02:43	95.03
1:42:35	93.76	1:42:35	95.58	8:07:43	95.33	8:07:43	94.92
1:47:35	93.37	1:47:35	95.30	8:12:43	95.02	8:12:43	94.54
1:52:35	93.05	1:52:35	94.98	8:17:43	94.67	8:17:43	94.05
1:57:35	92.66	1:57:35	94.68	8:22:43	94.40	8:22:43	93.74
2:02:35	92.30	2:02:35	94.32	8:27:43	94.03	8:27:43	93.37
2:07:35	92.28	2:07:35	94.06	8:32:43	93.68	8:32:43	92.96
2:12:35	92.05	2:12:35	93.76	8:37:43	93.31	8:37:43	92.59
2:17:35	91.83	2:17:35	93.45	8:42:43	92.87	8:42:43	92.23
2:22:35	91.46	2:22:35	93.18	8:47:43	92.66	8:47:43	91.89
2:27:35	91.11	2:27:35	92.90	8:52:43	92.55	8:52:43	91.51
2:32:35	90.73	2:32:35	92.62	8:57:43	92.34	8:57:43	91.21
2:37:35	90.49	2:37:35	92.34	9:02:43	91.98	9:02:43	90.88
2:42:35	90.31	2:42:35	92.05	9:07:43	91.96	9:07:43	90.50
2:47:35	90.06	2:47:35	91.82	9:12:43	91.81	9:12:43	90.14
2:52:35	89.74	2:52:35	91.57	9:17:43	91.78	9:17:43	89.88
2:57:35	89.52	2:57:35	91.31	9:22:43	91.55	9:22:43	89.37
3:02:35	89.38	3:02:35	90.98	9:27:43	91.20	9:27:43	89.00
3:07:35	89.02	3:07:35	90.81	9:32:43	91.20	9:32:43	88.63
3:12:35	88.62	3:12:35	90.52	9:37:43	90.84	9:37:43	88.26
3:17:35	88.24	3:17:35	90.20	9:42:43	90.45	9:42:43	88.26
3:22:35	87.85	3:22:35	89.96	9:47:43	90.05	9:47:43	88.02
3:27:35	87.45	3:27:35	89.68	9:52:43	89.69	9:52:43	87.63
3:32:35	87.16	3:32:35	89.48	9:57:43	89.53	9:57:43	87.19
3:37:35	86.79	3:37:35	89.16	10:02:43	89.23	10:02:43	86.76

3:42:35	86.49	3:42:35	88.92	10:07:43	88.86	10:07:43	86.35
3:47:35	86.24	3:47:35	88.69	10:12:43	88.48	10:12:43	85.93
3:52:35	85.87	3:52:35	88.43	10:17:43	88.13	10:17:43	85.57
3:57:35	85.56	3:57:35	88.18	10:22:43	87.80	10:22:43	85.16
4:02:35	85.09	4:02:35	87.94	10:27:43	87.44	10:27:43	84.77
4:07:35	84.87	4:07:35	87.72	10:32:43	87.08	10:32:43	84.27
4:12:35	84.56	4:12:35	87.44	10:37:43	86.79	10:37:43	83.94
4:17:35	84.16	4:17:35	87.18	10:42:43	86.48	10:42:43	83.57
4:22:35	83.94	4:22:35	86.97	10:47:43	86.13	10:47:43	83.32
4:27:35	83.58	4:27:35	86.75	10:52:43	85.99	10:52:43	83.29
4:32:35	83.52	4:32:35	86.46	10:57:43	85.73	10:57:43	82.87
4:37:35	83.15	4:37:35	86.23	11:02:43	85.43	11:02:43	82.56
4:42:35	82.80	4:42:35	86.04	11:07:43	85.08	11:07:43	82.52
4:47:35	82.49	4:47:35	85.82	11:12:43	84.80	11:12:43	82.34
4:52:35	82.30	4:52:35	85.52	11:17:43	84.60	11:17:43	82.02
4:57:35	81.95	4:57:35	85.33	11:22:43	84.28	11:22:43	81.84
5:02:35	81.88	5:02:35	85.12	11:27:43	83.98	11:27:43	81.51
5:07:35	81.63	5:07:35	84.84	11:32:43	83.80	11:32:43	81.34
5:12:35	81.57	5:12:35	84.66	11:37:43	83.48	11:37:43	81.30
5:17:35	81.40	5:17:35	84.39	11:42:43	83.30	11:42:43	80.97
5:22:35	81.11	5:22:35	84.22	11:47:43	82.96	11:47:43	80.76
5:27:35	80.96	5:27:35	83.93	11:52:43	82.80	11:52:43	80.60
5:32:35	80.31	5:32:35	83.72	11:57:43	82.56	11:57:43	80.56
5:37:35	80.23	5:37:35	83.64	12:02:43	82.24	12:02:43	80.43
5:42:35	79.78	5:42:35	83.43	12:07:43	82.01	12:07:43	80.25
5:47:35	79.50	5:47:35	83.15	12:12:43	81.87	12:12:43	80.22
5:52:35	79.46	5:52:35	83.07	12:17:43	81.77	12:17:43	80.04

MIX GGBS-50 (OPI Test-3)							
Mean OPI:		**10.19**		**Variability Check:**		**Good**	
Mean k (m/s):		**6.458E-11**		**COV % (Mean k):**		**14.1**	
Sample 1		Sample 2		Sample 3		Sample 4	
Mean diameter (mm)	68.65	Mean diameter (mm)	68.69	Mean diameter (mm)	68.57	Mean diameter (mm)	68.69
Diameter 1 (mm)	68.56	Diameter 1 (mm)	68.68	Diameter 1 (mm)	68.68	Diameter 1 (mm)	68.68
Diameter 2 (mm)	68.56	Diameter 2 (mm)	68.56	Diameter 2 (mm)	68.68	Diameter 2 (mm)	68.64
Diameter 3 (mm)	68.76	Diameter 3 (mm)	68.88	Diameter 3 (mm)	68.48	Diameter 3 (mm)	68.80
Diameter 4 (mm)	68.70	Diameter 4 (mm)	68.62	Diameter 4 (mm)	68.42	Diameter 4 (mm)	68.64
Mean thickness (mm)	30.27	Mean thickness (mm)	30.22	Mean thickness (mm)	30.05	Mean thickness (mm)	30.04
Thickness 1 (mm)	30.00	Thickness 1 (mm)	30.12	Thickness 1 (mm)	29.40	Thickness 1 (mm)	30.26
Thickness 2 (mm)	30.34	Thickness 2 (mm)	30.08	Thickness 2 (mm)	30.04	Thickness 2 (mm)	28.76
Thickness 3 (mm)	30.96	Thickness 3 (mm)	30.42	Thickness 3 (mm)	30.10	Thickness 3 (mm)	30.92
Thickness 4 (mm)	29.76	Thickness 4 (mm)	30.26	Thickness 4 (mm)	30.66	Thickness 4 (mm)	30.22
Cell Volume (L)	5.00	Cell Volume (L)	5.00	Cell Volume (L)	5.00	Cell Volume (L)	5.00
k (m/s)	5.290E-11	k (m/s)	6.267E-11	k (m/s)	6.838E-11	k (m/s)	7.435E-11
r^2	0.9970	r^2	0.9993	r^2	0.9959	r^2	0.9945
r^2 Validity	Valid	r^2 Validity	Valid	r^2 Validity	Valid	r^2 Validity	Valid
OPI	10.28	OPI	10.20	OPI	10.17	OPI	10.13
Time	Pressure	Time	Pressure	Time	Pressure	Time	Pressure
hh:mm:ss	(kPa)	hh:mm:ss	(kPa)	hh:mm:ss	(kPa)	hh:mm:ss	(kPa)
6:17:43	103.47	6:17:43	101.07	6:17:43	102.18	6:17:43	101.78
6:22:43	102.95	6:22:43	100.56	6:22:43	101.48	6:22:43	101.33
6:27:43	102.76	6:27:43	100.46	6:27:43	101.01	6:27:43	100.82
6:32:43	102.31	6:32:43	100.14	6:32:43	100.51	6:32:43	100.80
6:37:43	102.01	6:37:43	99.71	6:37:43	100.06	6:37:43	100.27
6:42:43	101.71	6:42:43	99.26	6:42:43	99.53	6:42:43	99.85
6:47:43	101.42	6:47:43	98.87	6:47:43	99.14	6:47:43	99.52
6:52:43	101.12	6:52:43	98.58	6:52:43	98.63	6:52:43	98.95

6:57:43	100.86	6:57:43	98.17	6:57:43	98.22	6:57:43	98.32
7:02:43	100.51	7:02:43	97.96	7:02:43	97.56	7:02:43	97.74
7:07:43	100.23	7:07:43	97.55	7:07:43	97.19	7:07:43	97.11
7:12:43	99.91	7:12:43	97.08	7:12:43	96.70	7:12:43	96.51
7:17:43	99.57	7:17:43	96.75	7:17:43	96.32	7:17:43	95.92
7:22:43	99.16	7:22:43	96.59	7:22:43	95.90	7:22:43	95.46
7:27:43	98.85	7:27:43	96.34	7:27:43	95.53	7:27:43	94.88
7:32:43	98.59	7:32:43	96.02	7:32:43	95.23	7:32:43	94.38
7:37:43	98.29	7:37:43	95.73	7:37:43	94.82	7:37:43	93.99
7:42:43	97.91	7:42:43	95.32	7:42:43	94.74	7:42:43	93.47
7:47:43	97.65	7:47:43	94.99	7:47:43	94.35	7:47:43	93.03
7:52:43	97.27	7:52:43	94.71	7:52:43	93.98	7:52:43	92.51
7:57:43	97.01	7:57:43	94.34	7:57:43	93.57	7:57:43	91.91
8:02:43	96.72	8:02:43	94.05	8:02:43	93.19	8:02:43	91.85
8:07:43	96.39	8:07:43	93.64	8:07:43	93.07	8:07:43	91.51
8:12:43	96.12	8:12:43	93.21	8:12:43	93.06	8:12:43	91.04
8:17:43	95.80	8:17:43	92.78	8:17:43	92.86	8:17:43	90.67
8:22:43	95.49	8:22:43	92.36	8:22:43	92.55	8:22:43	90.40
8:27:43	95.14	8:27:43	91.98	8:27:43	92.20	8:27:43	90.19
8:32:43	94.88	8:32:43	91.58	8:32:43	91.93	8:32:43	89.82
8:37:43	94.58	8:37:43	91.37	8:37:43	91.56	8:37:43	89.48
8:42:43	94.26	8:42:43	90.97	8:42:43	91.21	8:42:43	88.99
8:47:43	94.00	8:47:43	90.90	8:47:43	90.84	8:47:43	88.65
8:52:43	93.71	8:52:43	90.58	8:52:43	90.45	8:52:43	88.43
8:57:43	93.44	8:57:43	90.32	8:57:43	90.13	8:57:43	88.08
9:02:43	93.16	9:02:43	89.93	9:02:43	89.74	9:02:43	87.87
9:07:43	92.87	9:07:43	89.62	9:07:43	89.38	9:07:43	87.53
9:12:43	92.64	9:12:43	89.39	9:12:43	88.96	9:12:43	87.52
9:17:43	92.39	9:17:43	89.04	9:17:43	88.73	9:17:43	87.24

9:22:43	92.13	9:22:43	88.67	9:22:43	88.51	9:22:43	86.86
9:27:43	91.79	9:27:43	88.33	9:27:43	88.14	9:27:43	86.65
9:32:43	91.62	9:32:43	87.98	9:32:43	87.79	9:32:43	86.25
9:37:43	91.34	9:37:43	87.57	9:37:43	87.41	9:37:43	86.01
9:42:43	91.02	9:42:43	87.20	9:42:43	87.17	9:42:43	85.58
9:47:43	90.77	9:47:43	86.84	9:47:43	86.99	9:47:43	85.13
9:52:43	90.50	9:52:43	86.48	9:52:43	86.74	9:52:43	84.70
9:57:43	90.29	9:57:43	86.18	9:57:43	86.42	9:57:43	84.23
10:02:43	89.98	10:02:43	85.80	10:02:43	86.00	10:02:43	83.84
10:07:43	89.74	10:07:43	85.47	10:07:43	85.56	10:07:43	83.42
10:12:43	89.50	10:12:43	85.14	10:12:43	85.20	10:12:43	83.00
10:17:43	89.25	10:17:43	85.14	10:17:43	84.80	10:17:43	82.78
10:22:43	89.00	10:22:43	84.85	10:22:43	84.42	10:22:43	82.40
10:27:43	88.76	10:27:43	84.52	10:27:43	84.03	10:27:43	81.99
10:32:43	88.54	10:32:43	84.19	10:32:43	83.63	10:32:43	81.59
10:37:43	88.26	10:37:43	83.84	10:37:43	83.34	10:37:43	81.21
10:42:43	88.00	10:42:43	83.47	10:42:43	82.98	10:42:43	80.82
10:47:43	87.78	10:47:43	83.19	10:47:43	82.67	10:47:43	80.42
10:52:43	87.57	10:52:43	82.81	10:52:43	82.42	10:52:43	80.02
10:57:43	87.28	10:57:43	82.51	10:57:43	82.05	10:57:43	79.69
11:02:43	87.05	11:02:43	82.13	11:02:43	81.74	11:02:43	79.48
11:07:43	86.86	11:07:43	81.89	11:07:43	81.27	11:07:43	79.13
11:12:43	86.64	11:12:43	81.55	11:12:43	80.85	11:12:43	78.76
11:17:43	86.34	11:17:43	81.24	11:17:43	80.54	11:17:43	78.47
11:22:43	86.15	11:22:43	80.88	11:22:43	80.14	11:22:43	78.38
11:27:43	85.94	11:27:43	80.65	11:27:43	79.72	11:27:43	78.04
11:32:43	85.65	11:32:43	80.29	11:32:43	79.36	11:32:43	77.95
11:37:43	85.48	11:37:43	80.04	11:37:43	79.30	11:37:43	77.58
11:42:43	85.21	11:42:43	79.73	11:42:43	78.93	11:42:43	77.31

11:47:43	85.04	11:47:43	79.39	11:47:43	78.58	11:47:43	77.14
11:52:43	84.75	11:52:43	79.13	11:52:43	78.27	11:52:43	76.86
11:57:43	84.53	11:57:43	78.80	11:57:43	78.08	11:57:43	76.55
12:02:43	84.46	12:02:43	78.49	12:02:43	77.73	12:02:43	76.18
12:07:43	84.25	12:07:43	78.24	12:07:43	77.66	12:07:43	75.88
12:12:43	83.97	12:12:43	78.07	12:12:43	77.41	12:12:43	75.83
12:17:43	83.89	12:17:43	78.04	12:17:43	77.35	12:17:43	75.68

MIX SF-10 (OPI Test-1)							
Mean OPI:		**10.09**		**Variability Check:**		**Good**	
Mean k (m/s):		**8.875E-11**		**COV % (Mean k):**		**48.3**	
Sample 1		Sample 2		Sample 3		Sample 4	
Mean diameter (mm)	68.63	Mean diameter (mm)	68.62	Mean diameter (mm)	68.57	Mean diameter (mm)	68.59
Diameter 1 (mm)	68.66	Diameter 1 (mm)	68.62	Diameter 1 (mm)	68.56	Diameter 1 (mm)	68.68
Diameter 2 (mm)	68.58	Diameter 2 (mm)	68.62	Diameter 2 (mm)	68.60	Diameter 2 (mm)	68.66
Diameter 3 (mm)	68.64	Diameter 3 (mm)	68.72	Diameter 3 (mm)	68.54	Diameter 3 (mm)	68.54
Diameter 4 (mm)	68.62	Diameter 4 (mm)	68.50	Diameter 4 (mm)	68.56	Diameter 4 (mm)	68.48
Mean thickness (mm)	30.25	Mean thickness (mm)	30.24	Mean thickness (mm)	31.08	Mean thickness (mm)	29.69
Thickness 1 (mm)	30.26	Thickness 1 (mm)	29.98	Thickness 1 (mm)	31.46	Thickness 1 (mm)	29.40
Thickness 2 (mm)	30.28	Thickness 2 (mm)	29.88	Thickness 2 (mm)	30.82	Thickness 2 (mm)	30.30
Thickness 3 (mm)	30.10	Thickness 3 (mm)	30.32	Thickness 3 (mm)	31.26	Thickness 3 (mm)	29.14
Thickness 4 (mm)	30.36	Thickness 4 (mm)	30.76	Thickness 4 (mm)	30.78	Thickness 4 (mm)	29.90
Cell Volume (L)	5.00	Cell Volume (L)	5.00	Cell Volume (L)	5.00	Cell Volume (L)	5.00
k (m/s)	1.495E-10	k (m/s)	5.672E-11	k (m/s)	6.062E-11	k (m/s)	8.813E-11
r^2	0.9998	r^2	0.9998	r^2	0.9952	r^2	0.9982
r^2 Validity	Valid	r^2 Validity	Valid	r^2 Validity	Valid	r^2 Validity	Valid
OPI	9.83	OPI	10.25	OPI	10.22	OPI	10.05

Time	Pressure	Time	Pressure	Time	Pressure	Time	Pressure
hh:mm:ss	(kPa)	hh:mm:ss	(kPa)	hh:mm:ss	(kPa)	hh:mm:ss	(kPa)
21:06:39	104.32	21:06:39	104.51	21:06:39	102.40	21:06:39	103.02
21:11:39	103.33	21:11:39	104.21	21:11:39	102.07	21:11:39	102.50
21:16:39	102.23	21:16:39	103.91	21:16:39	101.80	21:16:39	101.96
21:21:39	101.30	21:21:39	103.54	21:21:39	101.38	21:21:39	101.45
21:26:39	100.21	21:26:39	103.17	21:26:39	101.07	21:26:39	100.91
21:31:39	99.16	21:31:39	102.80	21:31:39	100.65	21:31:39	100.33
21:36:39	98.18	21:36:39	102.51	21:36:39	100.30	21:36:39	99.77
21:41:39	97.53	21:41:39	102.10	21:41:39	100.02	21:41:39	99.34
21:46:39	97.13	21:46:39	101.78	21:46:39	99.67	21:46:39	98.76
21:51:39	96.20	21:51:39	101.44	21:51:39	99.28	21:51:39	98.29
21:56:39	95.58	21:56:39	101.09	21:56:39	98.99	21:56:39	97.76
22:01:39	94.61	22:01:39	100.73	22:01:39	98.66	22:01:39	97.24
22:06:39	93.71	22:06:39	100.38	22:06:39	98.26	22:06:39	96.76
22:11:39	92.90	22:11:39	100.16	22:11:39	98.40	22:11:39	96.73
22:16:39	92.21	22:16:39	99.85	22:16:39	98.07	22:16:39	96.23
22:21:39	91.67	22:21:39	99.54	22:21:39	97.83	22:21:39	95.72
22:26:39	90.84	22:26:39	99.20	22:26:39	97.48	22:26:39	95.29
22:31:39	89.90	22:31:39	98.87	22:31:39	97.22	22:31:39	94.80
22:36:39	89.16	22:36:39	98.63	22:36:39	96.87	22:36:39	94.33
22:41:39	88.31	22:41:39	98.31	22:41:39	96.58	22:41:39	93.90
22:46:39	87.70	22:46:39	97.98	22:46:39	96.34	22:46:39	93.41
22:51:39	86.94	22:51:39	97.71	22:51:39	95.98	22:51:39	92.95
22:56:39	86.05	22:56:39	97.37	22:56:39	95.76	22:56:39	92.52
23:01:39	85.33	23:01:39	97.11	23:01:39	95.41	23:01:39	92.10
23:06:39	84.77	23:06:39	96.80	23:06:39	95.17	23:06:39	91.62
23:11:39	84.05	23:11:39	96.52	23:11:39	94.82	23:11:39	91.17
23:16:39	83.16	23:16:39	96.12	23:16:39	94.51	23:16:39	90.69

23:21:39	82.44	23:21:39	95.88	23:21:39	94.15	23:21:39	90.18
23:26:39	81.87	23:26:39	95.57	23:26:39	93.83	23:26:39	89.73
23:31:39	81.43	23:31:39	95.20	23:31:39	93.57	23:31:39	89.27
23:36:39	80.70	23:36:39	94.89	23:36:39	93.06	23:36:39	88.65
23:41:39	79.92	23:41:39	94.52	23:41:39	92.79	23:41:39	88.27
23:46:39	79.26	23:46:39	94.29	23:46:39	92.51	23:46:39	87.88
23:51:39	78.46	23:51:39	93.96	23:51:39	92.25	23:51:39	87.39
23:56:39	77.81	23:56:39	93.69	23:56:39	91.95	23:56:39	87.03
0:01:39	77.08	0:01:39	93.42	0:01:39	91.69	0:01:39	86.55
0:06:39	76.52	0:06:39	92.81	0:06:39	90.18	0:06:39	85.02
0:11:39	75.92	0:11:39	92.56	0:11:39	89.87	0:11:39	84.65
0:16:39	75.16	0:16:39	92.24	0:16:39	89.65	0:16:39	84.23
0:21:39	74.47	0:21:39	91.89	0:21:39	89.15	0:21:39	83.66
0:26:39	73.87	0:26:39	91.65	0:26:39	88.88	0:26:39	83.29
0:31:39	73.36	0:31:39	91.32	0:31:39	88.58	0:31:39	82.85
0:36:39	72.67	0:36:39	91.03	0:36:39	88.34	0:36:39	82.44
0:41:39	72.06	0:41:39	90.75	0:41:39	88.00	0:41:39	82.05
0:46:39	71.36	0:46:39	90.42	0:46:39	87.72	0:46:39	81.59
0:51:39	70.77	0:51:39	90.14	0:51:39	87.36	0:51:39	81.18
0:56:39	70.08	0:56:39	89.85	0:56:39	87.24	0:56:39	80.88
1:01:39	69.50	1:01:39	89.53	1:01:39	86.77	1:01:39	80.36
1:06:39	68.89	1:06:39	89.26	1:06:39	86.51	1:06:39	79.94
1:11:39	68.44	1:11:39	88.96	1:11:39	86.24	1:11:39	79.53
1:16:39	67.80	1:16:39	88.62	1:16:39	86.01	1:16:39	79.19
1:21:39	67.27	1:21:39	88.36	1:21:39	85.74	1:21:39	78.84
1:26:39	66.63	1:26:39	88.08	1:26:39	85.52	1:26:39	78.44
1:31:39	66.07	1:31:39	87.79	1:31:39	85.26	1:31:39	78.09
1:36:39	65.57	1:36:39	87.56	1:36:39	84.94	1:36:39	77.69
1:41:39	65.00	1:41:39	87.28	1:41:39	84.69	1:41:39	77.34

1:46:39	64.44	1:46:39	87.01	1:46:39	84.52	1:46:39	77.02
1:51:39	63.89	1:51:39	86.80	1:51:39	84.26	1:51:39	76.59
1:56:39	63.33	1:56:39	86.51	1:56:39	84.06	1:56:39	76.27
2:01:39	62.80	2:01:39	86.21	2:01:39	83.74	2:01:39	75.91
2:06:39	62.31	2:06:39	86.02	2:06:39	83.51	2:06:39	75.54
2:11:39	61.76	2:11:39	85.70	2:11:39	83.28	2:11:39	75.23
2:16:39	61.23	2:16:39	85.44	2:16:39	82.93	2:16:39	74.76
2:21:39	60.70	2:21:39	85.14	2:21:39	82.68	2:21:39	74.45
2:26:39	60.07	2:26:39	84.77	2:26:39	82.41	2:26:39	74.02
2:31:39	59.76	2:31:39	84.78	2:31:39	83.10	2:31:39	74.49
2:36:39	59.33	2:36:39	84.27	2:36:39	81.98	2:36:39	73.45
2:41:39	58.80	2:41:39	83.98	2:41:39	81.75	2:41:39	73.11
2:46:39	58.32	2:46:39	83.76	2:46:39	81.52	2:46:39	72.71
2:51:39	57.83	2:51:39	83.44	2:51:39	81.19	2:51:39	72.36
2:56:39	57.27	2:56:39	83.11	2:56:39	80.96	2:56:39	72.02
3:01:39	56.84	3:01:39	82.91	3:01:39	80.67	3:01:39	71.62
3:06:39	56.32	3:06:39	82.63	3:06:39	80.45	3:06:39	71.25

MIX SF-10 (OPI Test-2)							
Mean OPI:		**9.99**		**Variability Check:**		**Good**	
Mean k (m/s):		**1.039E-10**		**COV % (Mean k):**		**15.4**	
Sample 1		Sample 2		Sample 3		Sample 4	
Mean diameter (mm)	68.59	Mean diameter (mm)	68.78	Mean diameter (mm)	68.67	Mean diameter (mm)	68.61
Diameter 1 (mm)	68.58	Diameter 1 (mm)	68.82	Diameter 1 (mm)	68.76	Diameter 1 (mm)	68.64
Diameter 2 (mm)	68.68	Diameter 2 (mm)	68.74	Diameter 2 (mm)	68.62	Diameter 2 (mm)	68.64
Diameter 3 (mm)	68.56	Diameter 3 (mm)	68.72	Diameter 3 (mm)	68.60	Diameter 3 (mm)	68.60
Diameter 4 (mm)	68.52	Diameter 4 (mm)	68.84	Diameter 4 (mm)	68.70	Diameter 4 (mm)	68.56

Mean thickness (mm)	29.45	Mean thickness (mm)	29.28	Mean thickness (mm)	28.83	Mean thickness (mm)	31.57
Thickness 1 (mm)	29.46	Thickness 1 (mm)	28.96	Thickness 1 (mm)	28.90	Thickness 1 (mm)	31.98
Thickness 2 (mm)	29.14	Thickness 2 (mm)	28.92	Thickness 2 (mm)	28.72	Thickness 2 (mm)	31.18
Thickness 3 (mm)	29.86	Thickness 3 (mm)	29.78	Thickness 3 (mm)	28.54	Thickness 3 (mm)	31.70
Thickness 4 (mm)	29.34	Thickness 4 (mm)	29.46	Thickness 4 (mm)	29.14	Thickness 4 (mm)	31.40
Cell Volume (L)	5.00	Cell Volume (L)	5.00	Cell Volume (L)	5.00	Cell Volume (L)	5.00
k (m/s)	1.077E-10	k (m/s)	8.133E-11	k (m/s)	1.193E-10	k (m/s)	1.073E-10
r^2	0.9988	r^2	0.9998	r^2	0.9962	r^2	0.9998
r^2 Validity	Valid	r^2 Validity	Valid	r^2 Validity	Valid	r^2 Validity	Valid
OPI	9.97	OPI	10.09	OPI	9.92	OPI	9.97
Time	Pressure	Time	Pressure	Time	Pressure	Time	Pressure
hh:mm:ss	(kPa)	hh:mm:ss	(kPa)	hh:mm:ss	(kPa)	hh:mm:ss	(kPa)
21:06:39	104.29	21:06:39	103.11	3:50:40	103.31	3:50:40	103.47
21:11:39	103.61	21:11:39	102.60	3:55:40	102.72	3:55:40	102.95
21:16:39	102.91	21:16:39	102.08	4:00:40	101.98	4:00:40	102.29
21:21:39	102.28	21:21:39	101.61	4:05:40	101.31	4:05:40	101.75
21:26:39	101.59	21:26:39	101.06	4:10:40	100.73	4:10:40	101.23
21:31:39	100.88	21:31:39	100.54	4:15:40	99.95	4:15:40	100.57
21:36:39	100.23	21:36:39	100.06	4:20:40	99.30	4:20:40	99.99
21:41:39	99.64	21:41:39	99.53	4:25:40	98.71	4:25:40	99.46
21:46:39	98.96	21:46:39	99.03	4:30:40	98.04	4:30:40	98.88
21:51:39	98.38	21:51:39	98.56	4:35:40	97.31	4:35:40	98.26
21:56:39	97.69	21:56:39	98.02	4:40:40	96.74	4:40:40	97.74
22:01:39	97.07	22:01:39	97.52	4:45:40	96.13	4:45:40	97.24
22:06:39	96.49	22:06:39	97.06	4:50:40	95.44	4:50:40	96.59
22:11:39	96.31	22:11:39	96.69	4:55:40	94.79	4:55:40	96.07
22:16:39	95.72	22:16:39	96.22	5:00:40	94.18	5:00:40	95.50
22:21:39	95.07	22:21:39	95.72	5:05:40	93.50	5:05:40	94.91
22:26:39	94.53	22:26:39	95.26	5:10:40	92.92	5:10:40	94.39

22:31:39	93.92	22:31:39	94.79	5:15:40	92.21	5:15:40	93.81
22:36:39	93.38	22:36:39	94.40	5:20:40	91.65	5:20:40	93.28
22:41:39	92.84	22:41:39	93.95	5:25:40	91.06	5:25:40	92.79
22:46:39	92.20	22:46:39	93.46	5:30:40	90.45	5:30:40	92.22
22:51:39	91.68	22:51:39	93.06	5:35:40	89.80	5:35:40	91.69
22:56:39	91.10	22:56:39	92.58	5:40:40	89.21	5:40:40	91.15
23:01:39	90.61	23:01:39	92.21	5:45:40	88.56	5:45:40	90.61
23:06:39	90.01	23:06:39	91.74	5:50:40	87.94	5:50:40	90.07
23:11:39	89.50	23:11:39	91.35	5:55:40	87.32	5:55:40	89.50
23:16:39	88.87	23:16:39	90.85	6:00:40	86.67	6:00:40	88.98
23:21:39	88.31	23:21:39	90.45	6:05:40	86.06	6:05:40	88.41
23:26:39	87.76	23:26:39	90.01	6:10:40	85.42	6:10:40	87.89
23:31:39	87.18	23:31:39	89.54	6:15:40	84.82	6:15:40	87.38
23:36:39	86.49	23:36:39	89.08	6:20:40	84.25	6:20:40	86.84
23:41:39	86.01	23:41:39	88.65	6:25:40	83.62	6:25:40	86.30
23:46:39	85.55	23:46:39	88.28	6:30:40	83.07	6:30:40	85.85
23:51:39	84.94	23:51:39	87.83	6:35:40	82.47	6:35:40	85.35
23:56:39	84.49	23:56:39	87.44	6:40:40	81.80	6:40:40	84.77
0:01:39	83.94	0:01:39	87.04	6:45:40	81.18	6:45:40	84.26
0:06:39	82.35	0:06:39	86.35	6:50:40	80.66	6:50:40	83.82
0:11:39	81.91	0:11:39	85.99	6:55:40	79.96	6:55:40	83.24
0:16:39	81.37	0:16:39	85.54	7:00:40	79.39	7:00:40	82.75
0:21:39	80.73	0:21:39	85.12	7:05:40	78.81	7:05:40	82.30
0:26:39	80.31	0:26:39	84.78	7:10:40	78.25	7:10:40	81.83
0:31:39	79.77	0:31:39	84.35	7:15:40	77.59	7:15:40	81.31
0:36:39	79.28	0:36:39	83.94	7:20:40	77.03	7:20:40	80.85
0:41:39	78.83	0:41:39	83.59	7:25:40	76.36	7:25:40	80.29
0:46:39	78.29	0:46:39	83.14	7:30:40	75.80	7:30:40	79.80
0:51:39	77.83	0:51:39	82.76	7:35:40	75.16	7:35:40	79.30

0:56:39	77.45	0:56:39	82.36	7:40:40	74.58	7:40:40	78.83
1:01:39	76.87	1:01:39	81.95	7:45:40	74.06	7:45:40	78.42
1:06:39	76.40	1:06:39	81.57	7:50:40	73.45	7:50:40	77.89
1:11:39	75.89	1:11:39	81.14	7:55:40	72.92	7:55:40	77.48
1:16:39	75.47	1:16:39	80.74	8:00:40	72.26	8:00:40	76.94
1:21:39	75.09	1:21:39	80.41	8:05:40	71.73	8:05:40	76.51
1:26:39	74.58	1:26:39	79.99	8:10:40	71.14	8:10:40	76.03
1:31:39	74.19	1:31:39	79.65	8:15:40	70.59	8:15:40	75.63
1:36:39	73.75	1:36:39	79.30	8:20:40	69.98	8:20:40	75.11
1:41:39	73.32	1:41:39	78.93	8:25:40	69.39	8:25:40	74.68
1:46:39	72.92	1:46:39	78.56	8:30:40	68.82	8:30:40	74.22
1:51:39	72.44	1:51:39	78.21	8:35:40	68.31	8:35:40	73.82
1:56:39	72.06	1:56:39	77.84	8:40:40	67.73	8:40:40	73.38
2:01:39	71.63	2:01:39	77.49	8:45:40	67.15	8:45:40	72.86
2:06:39	71.21	2:06:39	77.17	8:50:40	66.65	8:50:40	72.50
2:11:39	70.85	2:11:39	76.80	8:55:40	66.14	8:55:40	72.13
2:16:39	70.35	2:16:39	76.43	9:00:40	65.53	9:00:40	71.56
2:21:39	69.95	2:21:39	76.06	9:05:40	65.02	9:05:40	71.17
2:26:39	69.45	2:26:39	75.62	9:10:40	64.44	9:10:40	70.75
2:31:39	69.87	2:31:39	75.47	9:15:40	63.88	9:15:40	70.31
2:36:39	68.80	2:36:39	74.96	9:20:40	63.45	9:20:40	69.93
2:41:39	68.39	2:41:39	74.59	9:25:40	62.84	9:25:40	69.46
2:46:39	67.96	2:46:39	74.25	9:30:40	62.43	9:30:40	69.14
2:51:39	67.56	2:51:39	73.89	9:35:40	61.83	9:35:40	68.67
2:56:39	67.15	2:56:39	73.49	9:40:40	61.34	9:40:40	68.24
3:01:39	66.73	3:01:39	73.18	9:45:40	60.89	9:45:40	67.88
3:06:39	66.31	3:06:39	72.81	9:50:40	60.42	9:50:40	67.55

MIX SF-10 (OPI Test-3)							
Mean OPI:		**9.95**		**Variability Check:**		**Good**	
Mean k (m/s):		**1.146E-10**		**COV % (Mean k):**		**20.5**	
Sample 1		Sample 2		Sample 3		Sample 4	
Mean diameter (mm)	68.72	Mean diameter (mm)	68.47	Mean diameter (mm)	68.62	Mean diameter (mm)	68.75
Diameter 1 (mm)	68.64	Diameter 1 (mm)	68.44	Diameter 1 (mm)	68.74	Diameter 1 (mm)	68.92
Diameter 2 (mm)	68.88	Diameter 2 (mm)	68.68	Diameter 2 (mm)	68.66	Diameter 2 (mm)	68.76
Diameter 3 (mm)	68.68	Diameter 3 (mm)	68.60	Diameter 3 (mm)	68.68	Diameter 3 (mm)	68.82
Diameter 4 (mm)	68.66	Diameter 4 (mm)	68.14	Diameter 4 (mm)	68.40	Diameter 4 (mm)	68.50
Mean thickness (mm)	29.18	Mean thickness (mm)	28.95	Mean thickness (mm)	31.19	Mean thickness (mm)	31.21
Thickness 1 (mm)	28.88	Thickness 1 (mm)	28.58	Thickness 1 (mm)	31.96	Thickness 1 (mm)	30.90
Thickness 2 (mm)	29.72	Thickness 2 (mm)	29.12	Thickness 2 (mm)	30.46	Thickness 2 (mm)	31.60
Thickness 3 (mm)	28.86	Thickness 3 (mm)	28.88	Thickness 3 (mm)	31.64	Thickness 3 (mm)	30.34
Thickness 4 (mm)	29.26	Thickness 4 (mm)	29.22	Thickness 4 (mm)	30.68	Thickness 4 (mm)	31.98
Cell Volume (L)	5.00	Cell Volume (L)	5.00	Cell Volume (L)	5.00	Cell Volume (L)	5.00
k (m/s)	1.095E-10	k (m/s)	8.543E-11	k (m/s)	1.221E-10	k (m/s)	1.413E-10
r^2	0.9997	r^2	0.9998	r^2	0.9985	r^2	0.9999
r^2 Validity	Valid	r^2 Validity	Valid	r^2 Validity	Valid	r^2 Validity	Valid
OPI	9.96	OPI	10.07	OPI	9.91	OPI	9.85
Time	Pressure	Time	Pressure	Time	Pressure	Time	Pressure
hh:mm:ss	(kPa)	hh:mm:ss	(kPa)	hh:mm:ss	(kPa)	hh:mm:ss	(kPa)
3:50:40	103.52	3:50:40	102.41	3:50:40	103.68	3:50:40	102.78
3:55:40	102.84	3:55:40	101.92	3:55:40	103.12	3:55:40	102.03
4:00:40	102.12	4:00:40	101.40	4:00:40	102.44	4:00:40	101.20
4:05:40	101.46	4:05:40	100.84	4:05:40	101.73	4:05:40	100.38
4:10:40	101.29	4:10:40	100.86	4:10:40	101.61	4:10:40	99.73
4:15:40	100.17	4:15:40	99.86	4:15:40	100.47	4:15:40	98.84
4:20:40	99.61	4:20:40	99.51	4:20:40	99.97	4:20:40	98.10
4:25:40	98.86	4:25:40	98.95	4:25:40	99.33	4:25:40	97.37

4:30:40	98.24	4:30:40	98.47	4:30:40	98.69	4:30:40	96.61
4:35:40	97.66	4:35:40	98.04	4:35:40	98.07	4:35:40	95.82
4:40:40	96.87	4:40:40	97.43	4:40:40	97.36	4:40:40	95.11
4:45:40	96.47	4:45:40	97.13	4:45:40	96.86	4:45:40	94.38
4:50:40	95.59	4:50:40	96.46	4:50:40	96.11	4:50:40	93.64
4:55:40	94.96	4:55:40	95.90	4:55:40	95.41	4:55:40	92.91
5:00:40	94.33	5:00:40	95.47	5:00:40	94.85	5:00:40	92.21
5:05:40	93.73	5:05:40	95.00	5:05:40	94.22	5:05:40	91.47
5:10:40	93.09	5:10:40	94.51	5:10:40	93.60	5:10:40	90.79
5:15:40	92.49	5:15:40	94.00	5:15:40	92.94	5:15:40	90.06
5:20:40	91.99	5:20:40	93.65	5:20:40	92.46	5:20:40	89.38
5:25:40	91.34	5:25:40	93.09	5:25:40	91.78	5:25:40	88.71
5:30:40	90.73	5:30:40	92.65	5:30:40	91.20	5:30:40	88.01
5:35:40	90.12	5:35:40	92.11	5:35:40	90.55	5:35:40	87.33
5:40:40	89.47	5:40:40	91.64	5:40:40	89.94	5:40:40	86.65
5:45:40	88.98	5:45:40	91.19	5:45:40	89.33	5:45:40	85.92
5:50:40	88.40	5:50:40	90.75	5:50:40	88.76	5:50:40	85.27
5:55:40	87.65	5:55:40	90.20	5:55:40	88.08	5:55:40	84.60
6:00:40	87.16	6:00:40	89.72	6:00:40	87.47	6:00:40	83.92
6:05:40	86.61	6:05:40	89.35	6:05:40	86.93	6:05:40	83.24
6:10:40	86.05	6:10:40	88.87	6:10:40	86.30	6:10:40	82.57
6:15:40	85.49	6:15:40	88.37	6:15:40	85.69	6:15:40	81.92
6:20:40	84.89	6:20:40	87.97	6:20:40	85.16	6:20:40	81.29
6:25:40	84.33	6:25:40	87.44	6:25:40	84.48	6:25:40	80.62
6:30:40	83.77	6:30:40	87.03	6:30:40	83.99	6:30:40	80.04
6:35:40	83.21	6:35:40	86.59	6:35:40	83.40	6:35:40	79.41
6:40:40	82.66	6:40:40	86.12	6:40:40	82.74	6:40:40	78.72
6:45:40	82.19	6:45:40	85.72	6:45:40	82.22	6:45:40	78.10
6:50:40	81.54	6:50:40	85.22	6:50:40	81.66	6:50:40	77.52

6:55:40	81.07	6:55:40	84.76	6:55:40	80.97	6:55:40	76.84
7:00:40	80.48	7:00:40	84.32	7:00:40	80.40	7:00:40	76.23
7:05:40	79.96	7:05:40	83.83	7:05:40	79.81	7:05:40	75.64
7:10:40	79.45	7:10:40	83.45	7:10:40	79.33	7:10:40	75.06
7:15:40	79.22	7:15:40	83.24	7:15:40	78.91	7:15:40	74.43
7:20:40	78.59	7:20:40	82.70	7:20:40	78.27	7:20:40	73.83
7:25:40	77.97	7:25:40	82.15	7:25:40	77.57	7:25:40	73.20
7:30:40	77.56	7:30:40	81.85	7:30:40	77.12	7:30:40	72.63
7:35:40	76.95	7:35:40	81.33	7:35:40	76.49	7:35:40	72.03
7:40:40	76.49	7:40:40	80.92	7:40:40	75.95	7:40:40	71.46
7:45:40	75.98	7:45:40	80.46	7:45:40	75.38	7:45:40	70.90
7:50:40	75.48	7:50:40	80.12	7:50:40	74.91	7:50:40	70.34
7:55:40	74.93	7:55:40	79.59	7:55:40	74.28	7:55:40	69.78
8:00:40	74.57	8:00:40	79.33	8:00:40	73.84	8:00:40	69.19
8:05:40	73.86	8:05:40	78.69	8:05:40	73.14	8:05:40	68.65
8:10:40	73.42	8:10:40	78.34	8:10:40	72.65	8:10:40	68.10
8:15:40	73.09	8:15:40	78.02	8:15:40	72.20	8:15:40	67.56
8:20:40	72.65	8:20:40	77.65	8:20:40	71.70	8:20:40	67.00
8:25:40	72.24	8:25:40	77.25	8:25:40	71.15	8:25:40	66.45
8:30:40	71.73	8:30:40	76.80	8:30:40	70.58	8:30:40	65.89
8:35:40	71.21	8:35:40	76.38	8:35:40	70.08	8:35:40	65.41
8:40:40	70.96	8:40:40	76.17	8:40:40	69.72	8:40:40	64.88
8:45:40	70.34	8:45:40	75.74	8:45:40	69.11	8:45:40	64.33
8:50:40	69.99	8:50:40	75.30	8:50:40	68.70	8:50:40	63.87
8:55:40	69.92	8:55:40	75.30	8:55:40	68.50	8:55:40	63.39
9:00:40	68.94	9:00:40	74.46	9:00:40	67.56	9:00:40	62.80
9:05:40	68.51	9:05:40	74.09	9:05:40	67.12	9:05:40	62.33
9:10:40	68.09	9:10:40	73.64	9:10:40	66.55	9:10:40	61.79
9:15:40	67.73	9:15:40	73.32	9:15:40	66.10	9:15:40	61.28

9:20:40	67.23	9:20:40	72.94	9:20:40	65.65	9:20:40	60.85
9:25:40	66.97	9:25:40	72.68	9:25:40	65.24	9:25:40	60.33
9:30:40	66.57	9:30:40	72.36	9:30:40	64.86	9:30:40	59.91
9:35:40	66.17	9:35:40	71.95	9:35:40	64.31	9:35:40	59.37
9:40:40	65.78	9:40:40	71.69	9:40:40	63.94	9:40:40	58.93
9:45:40	65.45	9:45:40	71.42	9:45:40	63.57	9:45:40	58.50
9:50:40	65.04	9:50:40	70.95	9:50:40	63.04	9:50:40	58.04

MIX MK-30 (OPI Test-1)							
Mean OPI:		**10.42**		**Variability Check:**		**Good**	
Mean k (m/s):		**3.810E-11**		**COV % (Mean k):**		**18.0**	
Sample 1		Sample 2		Sample 3		Sample 4	
Mean diameter (mm)	68.48	Mean diameter (mm)	68.76	Mean diameter (mm)	68.73	Mean diameter (mm)	68.71
Diameter 1 (mm)	68.42	Diameter 1 (mm)	68.64	Diameter 1 (mm)	68.98	Diameter 1 (mm)	68.90
Diameter 2 (mm)	68.46	Diameter 2 (mm)	68.80	Diameter 2 (mm)	68.66	Diameter 2 (mm)	68.84
Diameter 3 (mm)	68.50	Diameter 3 (mm)	68.86	Diameter 3 (mm)	68.68	Diameter 3 (mm)	68.54
Diameter 4 (mm)	68.52	Diameter 4 (mm)	68.72	Diameter 4 (mm)	68.58	Diameter 4 (mm)	68.54
Mean thickness (mm)	29.04	Mean thickness (mm)	30.33	Mean thickness (mm)	30.29	Mean thickness (mm)	29.64
Thickness 1 (mm)	28.66	Thickness 1 (mm)	29.84	Thickness 1 (mm)	30.58	Thickness 1 (mm)	29.24
Thickness 2 (mm)	29.40	Thickness 2 (mm)	30.14	Thickness 2 (mm)	30.58	Thickness 2 (mm)	30.06
Thickness 3 (mm)	28.74	Thickness 3 (mm)	30.56	Thickness 3 (mm)	29.96	Thickness 3 (mm)	28.82
Thickness 4 (mm)	29.34	Thickness 4 (mm)	30.76	Thickness 4 (mm)	30.02	Thickness 4 (mm)	30.44
Cell Volume (L)	5.00	Cell Volume (L)	5.00	Cell Volume (L)	5.00	Cell Volume (L)	5.00
k (m/s)	2.994E-11	k (m/s)	3.496E-11	k (m/s)	4.344E-11	k (m/s)	4.406E-11
r^2	0.9991	r^2	0.9994	r^2	0.9978	r^2	0.9981
r^2 Validity	Valid	r^2 Validity	Valid	r^2 Validity	Valid	r^2 Validity	Valid
OPI	10.52	OPI	10.46	OPI	10.36	OPI	10.36

Time	Pressure	Time	Pressure	Time	Pressure	Time	Pressure
hh:mm:ss	(kPa)	hh:mm:ss	(kPa)	hh:mm:ss	(kPa)	hh:mm:ss	(kPa)
21:15:02	102.90	21:15:02	104.53	21:15:02	102.85	21:15:02	103.61
21:20:02	102.71	21:20:02	104.31	21:20:02	102.61	21:20:02	103.36
21:25:02	102.60	21:25:02	104.16	21:25:02	102.30	21:25:02	103.07
21:30:02	102.39	21:30:02	103.93	21:30:02	102.11	21:30:02	102.85
21:35:02	102.20	21:35:02	103.74	21:35:02	101.78	21:35:02	102.44
21:40:02	102.03	21:40:02	103.55	21:40:02	101.56	21:40:02	102.20
21:45:02	101.86	21:45:02	103.34	21:45:02	101.36	21:45:02	102.07
21:50:02	101.67	21:50:02	103.16	21:50:02	101.21	21:50:02	101.83
21:55:02	101.51	21:55:02	102.98	21:55:02	100.92	21:55:02	101.51
22:00:02	101.31	22:00:02	102.77	22:00:02	100.72	22:00:02	101.29
22:05:02	101.12	22:05:02	102.53	22:05:02	100.47	22:05:02	101.09
22:10:02	100.93	22:10:02	102.32	22:10:02	100.23	22:10:02	100.82
22:15:02	100.81	22:15:02	102.18	22:15:02	99.95	22:15:02	100.53
22:20:02	100.57	22:20:02	101.92	22:20:02	99.79	22:20:02	100.34
22:25:02	100.47	22:25:02	101.76	22:25:02	99.49	22:25:02	100.08
22:30:02	100.29	22:30:02	101.55	22:30:02	99.25	22:30:02	99.84
22:35:02	100.03	22:35:02	101.31	22:35:02	99.08	22:35:02	99.59
22:40:02	99.88	22:40:02	101.13	22:40:02	98.81	22:40:02	99.33
22:45:02	99.68	22:45:02	100.91	22:45:02	98.59	22:45:02	99.09
22:50:02	99.51	22:50:02	100.70	22:50:02	98.35	22:50:02	98.84
22:55:02	99.24	22:55:02	100.43	22:55:02	98.12	22:55:02	98.60
23:00:02	99.07	23:00:02	100.20	23:00:02	97.85	23:00:02	98.37
23:05:02	98.86	23:05:02	100.00	23:05:02	97.59	23:05:02	98.05
23:10:02	98.74	23:10:02	99.81	23:10:02	97.29	23:10:02	97.82
23:15:02	98.44	23:15:02	99.51	23:15:02	97.06	23:15:02	97.55
23:20:02	98.24	23:20:02	99.27	23:20:02	96.67	23:20:02	97.18
23:25:02	98.11	23:25:02	99.09	23:25:02	96.41	23:25:02	96.94

23:30:02	97.92	23:30:02	98.88	23:30:02	96.06	23:30:02	96.57
23:35:02	97.69	23:35:02	98.62	23:35:02	95.74	23:35:02	96.25
23:40:02	97.47	23:40:02	98.41	23:40:02	95.39	23:40:02	95.82
23:45:02	97.31	23:45:02	98.20	23:45:02	95.17	23:45:02	95.66
23:50:02	97.10	23:50:02	97.96	23:50:02	94.92	23:50:02	95.41
23:55:02	96.82	23:55:02	97.70	23:55:02	94.64	23:55:02	95.05
0:00:02	96.85	0:00:02	97.67	0:00:02	94.78	0:00:02	95.20
0:05:02	96.64	0:05:02	97.43	0:05:02	94.60	0:05:02	95.03
0:10:02	96.57	0:10:02	97.33	0:10:02	94.38	0:10:02	94.76
0:15:02	96.43	0:15:02	97.14	0:15:02	94.19	0:15:02	94.60
0:20:02	96.25	0:20:02	96.99	0:20:02	94.02	0:20:02	94.35
0:25:02	96.06	0:25:02	96.75	0:25:02	93.85	0:25:02	94.21
0:30:02	95.92	0:30:02	96.58	0:30:02	93.66	0:30:02	94.01
0:35:02	95.85	0:35:02	96.48	0:35:02	93.40	0:35:02	93.76
0:40:02	95.69	0:40:02	96.28	0:40:02	93.22	0:40:02	93.59
0:45:02	95.49	0:45:02	96.08	0:45:02	92.94	0:45:02	93.28
0:50:02	95.32	0:50:02	95.91	0:50:02	92.68	0:50:02	92.95
0:55:02	95.13	0:55:02	95.70	0:55:02	92.66	0:55:02	92.93
1:00:02	95.03	1:00:02	95.56	1:00:02	92.31	1:00:02	92.58
1:05:02	94.78	1:05:02	95.28	1:05:02	91.99	1:05:02	92.30
1:10:02	94.41	1:10:02	94.91	1:10:02	91.01	1:10:02	91.27
1:15:02	94.25	1:15:02	94.73	1:15:02	90.80	1:15:02	91.05
1:20:02	94.19	1:20:02	94.60	1:20:02	90.55	1:20:02	90.86
1:25:02	94.08	1:25:02	94.50	1:25:02	90.59	1:25:02	90.81
1:30:02	93.94	1:30:02	94.30	1:30:02	90.34	1:30:02	90.63
1:35:02	93.78	1:35:02	94.11	1:35:02	90.20	1:35:02	90.47
1:40:02	93.53	1:40:02	93.89	1:40:02	89.94	1:40:02	90.14
1:45:02	93.45	1:45:02	93.76	1:45:02	89.48	1:45:02	89.70
1:50:02	93.28	1:50:02	93.55	1:50:02	89.33	1:50:02	89.58

1:55:02	93.10	1:55:02	93.39	1:55:02	89.17	1:55:02	89.33
2:00:02	92.98	2:00:02	93.25	2:00:02	88.98	2:00:02	89.11
2:05:02	92.92	2:05:02	93.12	2:05:02	88.75	2:05:02	88.92
2:10:02	92.72	2:10:02	92.94	2:10:02	88.63	2:10:02	88.75
2:15:02	92.58	2:15:02	92.77	2:15:02	88.41	2:15:02	88.54
2:20:02	92.39	2:20:02	92.52	2:20:02	88.10	2:20:02	88.30
2:25:02	92.20	2:25:02	92.36	2:25:02	87.90	2:25:02	88.00
2:30:02	92.07	2:30:02	92.15	2:30:02	87.73	2:30:02	87.92
2:35:02	91.95	2:35:02	92.01	2:35:02	87.69	2:35:02	87.88
2:40:02	91.69	2:40:02	91.76	2:40:02	87.51	2:40:02	87.65
2:45:02	91.61	2:45:02	91.64	2:45:02	87.48	2:45:02	87.67
2:50:02	91.33	2:50:02	91.36	2:50:02	87.04	2:50:02	87.17
2:55:02	91.19	2:55:02	91.22	2:55:02	86.86	2:55:02	86.94
3:00:02	91.04	3:00:02	91.03	3:00:02	86.63	3:00:02	86.71
3:05:02	90.79	3:05:02	90.75	3:05:02	86.23	3:05:02	86.39
3:10:02	90.66	3:10:02	90.60	3:10:02	85.96	3:10:02	86.07
3:15:02	90.48	3:15:02	90.40	3:15:02	85.76	3:15:02	85.88

MIX MK-30 (OPI Test-2)							
Mean OPI:		**10.36**		**Variability Check:**		**Good**	
Mean k (m/s):		**4.422E-11**		**COV % (Mean k):**		**9.5**	
Sample 1		Sample 2		Sample 3		Sample 4	
Mean diameter (mm)	68.56	Mean diameter (mm)	68.62	Mean diameter (mm)	68.72	Mean diameter (mm)	68.80
Diameter 1 (mm)	68.48	Diameter 1 (mm)	68.60	Diameter 1 (mm)	68.70	Diameter 1 (mm)	68.90
Diameter 2 (mm)	68.76	Diameter 2 (mm)	68.64	Diameter 2 (mm)	68.70	Diameter 2 (mm)	68.98
Diameter 3 (mm)	68.40	Diameter 3 (mm)	68.72	Diameter 3 (mm)	68.78	Diameter 3 (mm)	68.66
Diameter 4 (mm)	68.58	Diameter 4 (mm)	68.50	Diameter 4 (mm)	68.70	Diameter 4 (mm)	68.64

Mean thickness (mm)	31.75	Mean thickness (mm)	31.46	Mean thickness (mm)	31.18	Mean thickness (mm)	30.68
Thickness 1 (mm)	31.98	Thickness 1 (mm)	31.18	Thickness 1 (mm)	31.54	Thickness 1 (mm)	31.14
Thickness 2 (mm)	31.54	Thickness 2 (mm)	31.84	Thickness 2 (mm)	31.52	Thickness 2 (mm)	30.58
Thickness 3 (mm)	31.98	Thickness 3 (mm)	31.18	Thickness 3 (mm)	30.98	Thickness 3 (mm)	30.60
Thickness 4 (mm)	31.50	Thickness 4 (mm)	31.64	Thickness 4 (mm)	30.66	Thickness 4 (mm)	30.38
Cell Volume (L)	5.00	Cell Volume (L)	5.00	Cell Volume (L)	5.00	Cell Volume (L)	5.00
k (m/s)	4.017E-11	k (m/s)	4.282E-11	k (m/s)	4.384E-11	k (m/s)	5.005E-11
r^2	0.9973	r^2	0.9991	r^2	0.9907	r^2	0.9969
r^2 Validity	Valid	r^2 Validity	Valid	r^2 Validity	Valid	r^2 Validity	Valid
OPI	10.40	OPI	10.37	OPI	10.36	OPI	10.30
Time	Pressure	Time	Pressure	Time	Pressure	Time	Pressure
hh:mm:ss	(kPa)	hh:mm:ss	(kPa)	hh:mm:ss	(kPa)	hh:mm:ss	(kPa)
21:15:02	102.87	21:15:02	104.52	3:44:27	103.68	3:44:27	104.57
21:20:02	102.67	21:20:02	104.26	3:49:27	103.46	3:49:27	104.36
21:25:02	102.46	21:25:02	104.03	3:54:27	103.31	3:54:27	104.15
21:30:02	102.25	21:30:02	103.75	3:59:27	103.09	3:59:27	103.92
21:35:02	101.89	21:35:02	103.46	4:04:27	102.87	4:04:27	103.67
21:40:02	101.69	21:40:02	103.21	4:09:27	102.66	4:09:27	103.39
21:45:02	101.59	21:45:02	103.01	4:14:27	102.40	4:14:27	103.07
21:50:02	101.37	21:50:02	102.75	4:19:27	102.22	4:19:27	102.82
21:55:02	101.12	21:55:02	102.53	4:24:27	102.02	4:24:27	102.54
22:00:02	100.94	22:00:02	102.29	4:29:27	101.77	4:29:27	102.27
22:05:02	100.75	22:05:02	102.04	4:34:27	101.52	4:34:27	101.97
22:10:02	100.51	22:10:02	101.79	4:39:27	101.31	4:39:27	101.73
22:15:02	100.30	22:15:02	101.59	4:44:27	101.11	4:44:27	101.44
22:20:02	100.11	22:20:02	101.32	4:49:27	100.86	4:49:27	101.19
22:25:02	99.94	22:25:02	101.14	4:54:27	100.67	4:54:27	100.92
22:30:02	99.75	22:30:02	100.91	4:59:27	100.46	4:59:27	100.60
22:35:02	99.50	22:35:02	100.61	5:04:27	100.23	5:04:27	100.35

22:40:02	99.30	22:40:02	100.39	5:09:27	100.02	5:09:27	100.11
22:45:02	99.09	22:45:02	100.15	5:14:27	99.77	5:14:27	99.82
22:50:02	98.90	22:50:02	99.92	5:19:27	99.55	5:19:27	99.50
22:55:02	98.67	22:55:02	99.64	5:24:27	99.29	5:24:27	99.22
23:00:02	98.48	23:00:02	99.40	5:29:27	99.08	5:29:27	99.02
23:05:02	98.21	23:05:02	99.16	5:34:27	98.84	5:34:27	98.66
23:10:02	98.05	23:10:02	98.95	5:39:27	98.59	5:39:27	98.39
23:15:02	97.77	23:15:02	98.63	5:44:27	98.35	5:44:27	98.12
23:20:02	97.44	23:20:02	98.36	5:49:27	98.09	5:49:27	97.86
23:25:02	97.25	23:25:02	98.14	5:54:27	97.88	5:54:27	97.54
23:30:02	96.94	23:30:02	97.89	5:59:27	97.58	5:59:27	97.19
23:35:02	96.65	23:35:02	97.62	6:04:27	97.34	6:04:27	96.90
23:40:02	96.25	23:40:02	97.31	6:09:27	97.08	6:09:27	96.65
23:45:02	96.13	23:45:02	97.10	6:14:27	96.87	6:14:27	96.36
23:50:02	95.91	23:50:02	96.84	6:19:27	96.59	6:19:27	96.07
23:55:02	95.55	23:55:02	96.52	6:24:27	96.33	6:24:27	95.80
0:00:02	95.78	0:00:02	96.44	6:29:27	96.16	6:29:27	95.47
0:05:02	95.62	0:05:02	96.21	6:34:27	95.89	6:34:27	95.15
0:10:02	95.42	0:10:02	96.00	6:39:27	95.71	6:39:27	94.93
0:15:02	95.28	0:15:02	95.81	6:44:27	95.48	6:44:27	94.64
0:20:02	95.06	0:20:02	95.58	6:49:27	95.27	6:49:27	94.39
0:25:02	94.92	0:25:02	95.35	6:54:27	95.00	6:54:27	94.09
0:30:02	94.76	0:30:02	95.15	6:59:27	94.71	6:59:27	93.74
0:35:02	94.58	0:35:02	95.00	7:04:27	94.52	7:04:27	93.48
0:40:02	94.43	0:40:02	94.79	7:09:27	94.30	7:09:27	93.23
0:45:02	94.15	0:45:02	94.55	7:14:27	94.01	7:14:27	92.92
0:50:02	93.87	0:50:02	94.33	7:19:27	93.79	7:19:27	92.62
0:55:02	93.85	0:55:02	94.14	7:24:27	93.53	7:24:27	92.41
1:00:02	93.57	1:00:02	93.95	7:29:27	93.31	7:29:27	92.12

1:05:02	93.29	1:05:02	93.68	7:34:27	92.94	7:34:27	91.81
1:10:02	92.27	1:10:02	93.27	7:39:27	92.59	7:39:27	91.57
1:15:02	92.08	1:15:02	93.07	7:44:27	92.39	7:44:27	91.37
1:20:02	91.98	1:20:02	92.93	7:49:27	92.13	7:49:27	91.08
1:25:02	91.96	1:25:02	92.77	7:54:27	91.96	7:54:27	90.87
1:30:02	91.83	1:30:02	92.59	7:59:27	91.68	7:59:27	90.55
1:35:02	91.68	1:35:02	92.38	8:04:27	91.40	8:04:27	90.25
1:40:02	91.36	1:40:02	92.13	8:09:27	91.10	8:09:27	89.95
1:45:02	90.99	1:45:02	91.94	8:14:27	90.88	8:14:27	89.67
1:50:02	90.89	1:50:02	91.76	8:19:27	90.56	8:19:27	89.36
1:55:02	90.65	1:55:02	91.54	8:24:27	90.34	8:24:27	89.09
2:00:02	90.48	2:00:02	91.36	8:29:27	90.07	8:29:27	88.74
2:05:02	90.36	2:05:02	91.23	8:34:27	89.80	8:34:27	88.46
2:10:02	90.20	2:10:02	91.02	8:39:27	89.47	8:39:27	88.14
2:15:02	90.04	2:15:02	90.84	8:44:27	89.27	8:44:27	87.94
2:20:02	89.81	2:20:02	90.62	8:49:27	89.03	8:49:27	87.77
2:25:02	89.56	2:25:02	90.40	8:54:27	88.75	8:54:27	87.47
2:30:02	89.52	2:30:02	90.23	8:59:27	88.48	8:59:27	87.19
2:35:02	89.54	2:35:02	90.06	9:04:27	88.24	9:04:27	86.96
2:40:02	89.30	2:40:02	89.80	9:09:27	87.90	9:09:27	86.54
2:45:02	89.40	2:45:02	89.69	9:14:27	87.63	9:14:27	86.20
2:50:02	88.88	2:50:02	89.36	9:19:27	87.31	9:19:27	85.92
2:55:02	88.73	2:55:02	89.17	9:24:27	87.04	9:24:27	85.62
3:00:02	88.51	3:00:02	88.94	9:29:27	86.80	9:29:27	85.38
3:05:02	88.21	3:05:02	88.69	9:34:27	86.47	9:34:27	85.16
3:10:02	87.94	3:10:02	88.48	9:39:27	86.21	9:39:27	84.97
3:15:02	87.79	3:15:02	88.26	9:44:27	85.99	9:44:27	84.80

MIX MK-30 (OPI Test-3)							
Mean OPI:		**10.35**		**Variability Check:**		**Good**	
Mean k (m/s):		**4.549E-11**		**COV % (Mean k):**		**18.8**	
Sample 1		Sample 2		Sample 3		Sample 4	
Mean diameter (mm)	68.71	Mean diameter (mm)	68.49	Mean diameter (mm)	68.79	Mean diameter (mm)	68.57
Diameter 1 (mm)	68.66	Diameter 1 (mm)	68.48	Diameter 1 (mm)	68.68	Diameter 1 (mm)	68.58
Diameter 2 (mm)	68.72	Diameter 2 (mm)	68.74	Diameter 2 (mm)	68.90	Diameter 2 (mm)	68.48
Diameter 3 (mm)	68.78	Diameter 3 (mm)	68.52	Diameter 3 (mm)	68.86	Diameter 3 (mm)	68.72
Diameter 4 (mm)	68.68	Diameter 4 (mm)	68.20	Diameter 4 (mm)	68.72	Diameter 4 (mm)	68.50
Mean thickness (mm)	30.18	Mean thickness (mm)	31.24	Mean thickness (mm)	30.01	Mean thickness (mm)	30.97
Thickness 1 (mm)	30.58	Thickness 1 (mm)	30.80	Thickness 1 (mm)	29.82	Thickness 1 (mm)	31.74
Thickness 2 (mm)	30.18	Thickness 2 (mm)	31.72	Thickness 2 (mm)	30.28	Thickness 2 (mm)	30.66
Thickness 3 (mm)	30.14	Thickness 3 (mm)	30.76	Thickness 3 (mm)	29.72	Thickness 3 (mm)	30.62
Thickness 4 (mm)	29.82	Thickness 4 (mm)	31.68	Thickness 4 (mm)	30.20	Thickness 4 (mm)	30.84
Cell Volume (L)	5.00	Cell Volume (L)	5.00	Cell Volume (L)	5.00	Cell Volume (L)	5.00
k (m/s)	3.512E-11	k (m/s)	5.465E-11	k (m/s)	4.979E-11	k (m/s)	4.239E-11
r^2	0.9955	r^2	0.9980	r^2	0.9906	r^2	0.9986
r^2 Validity	Valid	r^2 Validity	Valid	r^2 Validity	Valid	r^2 Validity	Valid
OPI	10.45	OPI	10.26	OPI	10.30	OPI	10.37
Time	Pressure	Time	Pressure	Time	Pressure	Time	Pressure
hh:mm:ss	(kPa)	hh:mm:ss	(kPa)	hh:mm:ss	(kPa)	hh:mm:ss	(kPa)
3:44:27	102.64	3:44:27	103.13	3:44:27	103.99	3:44:27	103.87
3:49:27	102.56	3:49:27	102.86	3:49:27	103.84	3:49:27	103.64
3:54:27	102.43	3:54:27	102.60	3:54:27	103.69	3:54:27	103.45
3:59:27	102.22	3:59:27	102.28	3:59:27	103.46	3:59:27	103.19
4:04:27	101.96	4:04:27	101.93	4:04:27	103.12	4:04:27	102.92
4:09:27	101.73	4:09:27	101.66	4:09:27	102.82	4:09:27	102.70
4:14:27	101.54	4:14:27	101.34	4:14:27	102.49	4:14:27	102.46
4:19:27	101.16	4:19:27	101.08	4:19:27	102.19	4:19:27	102.23

4:24:27	100.99	4:24:27	100.75	4:24:27	101.94	4:24:27	101.98
4:29:27	100.78	4:29:27	100.44	4:29:27	101.60	4:29:27	101.73
4:34:27	100.67	4:34:27	100.17	4:34:27	101.38	4:34:27	101.50
4:39:27	100.40	4:39:27	99.84	4:39:27	101.12	4:39:27	101.24
4:44:27	100.19	4:44:27	99.54	4:44:27	100.85	4:44:27	101.03
4:49:27	99.94	4:49:27	99.26	4:49:27	100.49	4:49:27	100.77
4:54:27	99.80	4:54:27	98.96	4:54:27	100.25	4:54:27	100.57
4:59:27	99.53	4:59:27	98.61	4:59:27	100.01	4:59:27	100.30
5:04:27	99.43	5:04:27	98.33	5:04:27	99.81	5:04:27	100.03
5:09:27	99.13	5:09:27	97.96	5:09:27	99.49	5:09:27	99.78
5:14:27	99.17	5:14:27	97.69	5:14:27	99.33	5:14:27	99.54
5:19:27	98.83	5:19:27	97.32	5:19:27	99.03	5:19:27	99.27
5:24:27	98.72	5:24:27	97.01	5:24:27	98.78	5:24:27	98.98
5:29:27	98.47	5:29:27	96.68	5:29:27	98.49	5:29:27	98.73
5:34:27	98.30	5:34:27	96.39	5:34:27	98.23	5:34:27	98.48
5:39:27	98.05	5:39:27	95.99	5:39:27	97.84	5:39:27	98.22
5:44:27	97.85	5:44:27	95.71	5:44:27	97.67	5:44:27	97.93
5:49:27	97.59	5:49:27	95.40	5:49:27	97.30	5:49:27	97.68
5:54:27	97.39	5:54:27	95.17	5:54:27	97.06	5:54:27	97.50
5:59:27	97.21	5:59:27	94.83	5:59:27	96.67	5:59:27	97.23
6:04:27	96.93	6:04:27	94.49	6:04:27	96.42	6:04:27	96.95
6:09:27	96.79	6:09:27	94.14	6:09:27	96.07	6:09:27	96.66
6:14:27	96.51	6:14:27	93.82	6:14:27	95.82	6:14:27	96.42
6:19:27	96.30	6:19:27	93.61	6:19:27	95.45	6:19:27	96.21
6:24:27	96.16	6:24:27	93.34	6:24:27	95.29	6:24:27	95.93
6:29:27	96.02	6:29:27	93.07	6:29:27	95.03	6:29:27	95.82
6:34:27	95.80	6:34:27	92.74	6:34:27	94.69	6:34:27	95.54
6:39:27	95.57	6:39:27	92.43	6:39:27	94.40	6:39:27	95.35
6:44:27	95.41	6:44:27	92.11	6:44:27	94.16	6:44:27	95.12

6:49:27	95.35	6:49:27	91.87	6:49:27	94.01	6:49:27	94.91
6:54:27	95.20	6:54:27	91.57	6:54:27	93.78	6:54:27	94.67
6:59:27	95.04	6:59:27	91.28	6:59:27	93.40	6:59:27	94.46
7:04:27	94.69	7:04:27	90.96	7:04:27	93.02	7:04:27	94.26
7:09:27	94.62	7:09:27	90.72	7:09:27	92.89	7:09:27	94.06
7:14:27	94.44	7:14:27	90.51	7:14:27	92.53	7:14:27	93.86
7:19:27	94.29	7:19:27	90.24	7:19:27	92.37	7:19:27	93.63
7:24:27	94.29	7:24:27	89.99	7:24:27	92.17	7:24:27	93.42
7:29:27	94.04	7:29:27	89.66	7:29:27	91.86	7:29:27	93.20
7:34:27	93.74	7:34:27	89.35	7:34:27	91.39	7:34:27	92.92
7:39:27	93.45	7:39:27	89.16	7:39:27	91.10	7:39:27	92.64
7:44:27	93.30	7:44:27	88.90	7:44:27	90.89	7:44:27	92.43
7:49:27	93.30	7:49:27	88.63	7:49:27	90.65	7:49:27	92.27
7:54:27	93.06	7:54:27	88.42	7:54:27	90.44	7:54:27	92.11
7:59:27	92.94	7:59:27	88.13	7:59:27	90.20	7:59:27	91.89
8:04:27	92.55	8:04:27	87.89	8:04:27	89.69	8:04:27	91.69
8:09:27	92.37	8:09:27	87.74	8:09:27	89.37	8:09:27	91.49
8:14:27	92.23	8:14:27	87.53	8:14:27	89.19	8:14:27	91.34
8:19:27	91.99	8:19:27	87.23	8:19:27	88.72	8:19:27	91.11
8:24:27	91.76	8:24:27	86.93	8:24:27	88.50	8:24:27	90.87
8:29:27	91.58	8:29:27	86.71	8:29:27	88.23	8:29:27	90.70
8:34:27	91.43	8:34:27	86.46	8:34:27	87.85	8:34:27	90.55
8:39:27	90.56	8:39:27	86.24	8:39:27	86.93	8:39:27	90.34
8:44:27	90.70	8:44:27	86.05	8:44:27	87.06	8:44:27	90.17
8:49:27	90.91	8:49:27	85.88	8:49:27	87.14	8:49:27	89.99
8:54:27	90.95	8:54:27	85.64	8:54:27	86.98	8:54:27	89.78
8:59:27	90.77	8:59:27	85.44	8:59:27	86.72	8:59:27	89.61
9:04:27	90.66	9:04:27	85.19	9:04:27	86.42	9:04:27	89.42
9:09:27	89.86	9:09:27	85.00	9:09:27	85.67	9:09:27	89.20

9:14:27	89.55	9:14:27	84.76	9:14:27	85.27	9:14:27	89.04
9:19:27	88.93	9:19:27	84.55	9:19:27	84.56	9:19:27	88.80
9:24:27	88.76	9:24:27	84.37	9:24:27	84.22	9:24:27	88.63
9:29:27	88.60	9:29:27	84.15	9:29:27	84.02	9:29:27	88.45
9:34:27	88.51	9:34:27	83.96	9:34:27	83.85	9:34:27	88.23
9:39:27	88.24	9:39:27	83.75	9:39:27	83.42	9:39:27	88.06
9:44:27	88.08	9:44:27	83.58	9:44:27	83.21	9:44:27	87.89

B2 WATER SORPTIVITY INDEX AND POROSITY

MIX 100% RHPC (WSI & Porosity Test-1)				
				Variability
Av. Sorptivity:	**5.53**	**COV:**	**11.7**	**Good**
Av. Porosity:	**12.00**	**COV:**	**12.0**	**High**
	Sample 1	Sample 2	Sample 3	Sample 4
Diameter (mm)	68.15	68.25	68.26	68.29
Thickness (mm)	30.90	30.29	30.04	31.85
Time (min)	Mass (g)	Mass (g)	Mass (g)	Mass (g)
0	261.94	259.37	258.13	285.87
3	262.65	260.04	258.99	286.54
5	262.82	260.19	259.17	286.67
7	262.97	260.29	259.33	286.76
9	263.09	260.39	259.47	286.86
12	263.24	260.51	259.62	286.96
16	263.41	260.66	259.84	287.10
20	263.62	260.85	260.06	287.22
25	263.75	260.97	260.21	287.35
Saturated Mass (g)	276.52	273.31	272.02	297.35
R^2 (Must be >0.98)	0.9983	0.9970	0.9984	0.9997
Range	3-25 min	3-25 min	3-25 min	3-25 min
Sorptivity (mm/hr$^{0.5}$)	**5.60**	**4.82**	**6.37**	**5.31**
Porosity (%)	**12.94**	**12.58**	**12.64**	**9.84**

MIX 100% RHPC (WSI & Porosity Test-2)				
				Variability
Av. Sorptivity:	**5.80**	**COV:**	**10.8**	**Good**
Av. Porosity:	**12.80**	**COV:**	**7.0**	**Good**
	Sample 1	Sample 2	Sample 3	Sample 4
Diameter (mm)	68.13	68.18	68.20	68.36
Thickness (mm)	31.21	30.49	30.69	29.52
Time (min)	Mass (g)	Mass (g)	Mass (g)	Mass (g)
0	262.84	263.55	259.30	249.66
3	263.70	264.49	259.95	250.44
5	263.86	264.65	260.12	250.62
7	264.01	264.81	260.24	250.75
9	264.12	264.94	260.35	250.87
12	264.27	265.12	260.50	251.04
16	264.45	265.33	260.69	251.23
20	264.62	265.53	260.83	251.40
25	264.78	265.74	261.03	251.57
Saturated Mass (g)	278.00	277.27	272.52	264.54
R^2 (Must be >0.98)	0.9997	0.9989	0.9992	0.9997
Range	3-25 min	3-25 min	3-25 min	3-25 min
Sorptivity (mm/hr$^{0.5}$)	**5.30**	**6.65**	**5.88**	**5.35**
Porosity (%)	**13.33**	**12.33**	**11.79**	**13.74**

MIX 100% RHPC (WSI & Porosity Test-3)				
				Variability
Av. Sorptivity:	**6.18**	**COV:**	**6.2**	**Good**
Av. Porosity:	**11.66**	**COV:**	**7.4**	**Good**
	Sample 1	Sample 2	Sample 3	Sample 4
Diameter (mm)	68.12	68.27	68.26	68.25
Thickness (mm)	30.72	31.42	31.08	28.69
Time (min)	Mass (g)	Mass (g)	Mass (g)	Mass (g)
0	252.89	271.64	267.57	252.43
3	253.76	272.40	268.37	253.14
5	253.96	272.57	268.53	253.28
7	254.11	272.70	268.67	253.39
9	254.25	272.82	268.78	253.49
12	254.44	272.98	268.95	253.64
16	254.65	273.17	269.14	253.82
20	254.85	273.31	269.28	253.95
25	255.03	273.50	269.45	254.10
Saturated Mass (g)	267.38	284.40	280.45	264.24
R^2 (Must be >0.98)	0.9996	0.9998	0.9995	0.9990
Range	3-25 min	3-25 min	3-25 min	3-25 min
Sorptivity (mm/hr$^{0.5}$)	**6.45**	**6.41**	**6.24**	**5.62**
Porosity (%)	**12.95**	**11.10**	**11.33**	**11.25**

MIX FA-30 (WSI & Porosity Test-1)				
				Variability
Av. Sorptivity:	**7.93**	**COV:**	**6.6**	**Good**
Av. Porosity:	**13.38**	**COV:**	**2.5**	**Good**
	Sample 1	Sample 2	Sample 3	Sample 4
Diameter (mm)	68.49	68.26	68.42	68.40
Thickness (mm)	30.74	29.31	29.91	31.47
Time (min)	Mass (g)	Mass (g)	Mass (g)	Mass (g)
0	261.46	252.36	255.06	266.73
3	262.44	253.37	256.16	267.94
5	262.70	253.62	256.43	268.21
7	262.90	253.83	256.62	268.42
9	263.08	254.00	256.80	268.63
12	263.32	254.25	257.02	268.87
16	263.58	254.52	257.28	269.15
20	263.81	254.76	257.49	269.39
25	264.06	255.04	257.72	269.65
Saturated Mass (g)	276.93	266.48	270.09	281.79
R^2 (Must be >0.98)	0.9998	0.9999	0.9992	0.9996
Range	3-25 min	3-25 min	3-25 min	3-25 min
Sorptivity (mm/hr$^{0.5}$)	**7.64**	**8.22**	**7.35**	**8.51**
Porosity (%)	**13.66**	**13.17**	**13.67**	**13.03**

MIX FA-30 (WSI & Porosity Test-2)				
				Variability
Av. Sorptivity:	**7.56**	**COV:**	**9.2**	**Good**
Av. Porosity:	**13.80**	**COV:**	**1.9**	**Good**
	Sample 1	Sample 2	Sample 3	Sample 4
Diameter (mm)	68.24	68.35	68.33	68.18
Thickness (mm)	28.97	30.06	31.23	29.59
Time (min)	Mass (g)	Mass (g)	Mass (g)	Mass (g)
0	248.33	256.24	263.27	250.07
3	249.41	257.32	264.11	251.14
5	249.62	257.54	264.33	251.35
7	249.80	257.74	264.52	251.57
9	249.97	257.93	264.69	251.79
12	250.18	258.17	264.90	252.03
16	250.43	258.47	265.14	252.30
20	250.65	258.73	265.38	252.55
25	250.89	259.02	265.63	252.81
Saturated Mass (g)	263.19	271.29	279.33	264.67
R^2 (Must be >0.98)	0.9997	0.9987	0.9997	0.9990
Range	3-25 min	3-25 min	3-25 min	3-25 min
Sorptivity (mm/hr$^{0.5}$)	**6.89**	**8.14**	**7.01**	**8.18**
Porosity (%)	**14.03**	**13.65**	**14.03**	**13.52**

MIX FA-30 (WSI & Porosity Test-3)				
				Variability
Av. Sorptivity:	**6.88**	**COV:**	**5.2**	**Good**
Av. Porosity:	**14.03**	**COV:**	**3.6**	**Good**
	Sample 1	Sample 2	Sample 3	Sample 4
Diameter (mm)	68.31	68.40	68.56	68.34
Thickness (mm)	29.05	31.06	30.59	31.88
Time (min)	Mass (g)	Mass (g)	Mass (g)	Mass (g)
0	243.19	265.19	261.12	269.06
3	244.17	266.25	262.10	270.15
5	244.37	266.44	262.29	270.35
7	244.56	266.62	262.48	270.54
9	244.73	266.79	262.65	270.70
12	244.96	267.01	262.87	270.91
16	245.20	267.24	263.12	271.14
20	245.43	267.46	263.33	271.36
25	245.69	267.71	263.60	271.61
Saturated Mass (g)	257.72	280.97	276.80	286.33
R^2 (Must be >0.98)	0.9994	0.9993	0.9991	0.9997
Range	3-25 min	3-25 min	3-25 min	3-25 min
Sorptivity (mm/hr$^{0.5}$)	**7.26**	**6.88**	**6.99**	**6.40**
Porosity (%)	**13.65**	**13.83**	**13.89**	**14.77**

MIX GGBS-50 (WSI & Porosity Test-1)				
				Variability
Av. Sorptivity:	**5.26**	**COV:**	**8.3**	**Good**
Av. Porosity:	**11.84**	**COV:**	**3.1**	**Good**
	Sample 1	Sample 2	Sample 3	Sample 4
Diameter (mm)	68.50	68.53	68.59	68.69
Thickness (mm)	28.73	28.36	28.68	30.25
Time (min)	Mass (g)	Mass (g)	Mass (g)	Mass (g)
0	249.97	246.77	252.57	264.63
3	250.67	247.56	253.25	265.45
5	250.83	247.70	253.41	265.61
7	250.97	247.83	253.55	265.76
9	251.11	247.96	253.68	265.89
12	251.21	248.04	253.78	266.01
16	251.37	248.20	253.95	266.18
20	251.50	248.32	254.09	266.31
25	251.66	248.45	254.25	266.47
Saturated Mass (g)	262.65	259.55	265.08	277.34
R^2 (Must be >0.98)	0.9970	0.9965	0.9982	0.9980
Range	3-25 min	3-25 min	3-25 min	3-25 min
Sorptivity (mm/hr$^{0.5}$)	**5.26**	**4.68**	**5.38**	**5.73**
Porosity (%)	**11.98**	**12.22**	**11.81**	**11.34**

MIX GGBS-50 (WSI & Porosity Test-2)				
				Variability
Av. Sorptivity:	**4.81**	**COV:**	**13.3**	**Caution**
Av. Porosity:	**12.04**	**COV:**	**1.6**	**Good**
	Sample 1	Sample 2	Sample 3	Sample 4
Diameter (mm)	68.53	68.67	68.65	68.64
Thickness (mm)	29.75	29.56	29.05	29.72
Time (min)	Mass (g)	Mass (g)	Mass (g)	Mass (g)
0	260.44	252.88	251.21	261.51
3	261.25	253.57	251.88	262.23
5	261.44	253.70	252.03	262.36
7	261.58	253.80	252.13	262.50
9	261.73	253.90	252.25	262.62
12	261.85	254.00	252.36	262.75
16	262.01	254.12	252.50	262.90
20	262.16	254.23	252.61	263.01
25	262.33	254.37	252.71	263.14
Saturated Mass (g)	273.71	266.24	263.85	274.84
R^2 (Must be >0.98)	0.9971	0.9991	0.9959	0.9966
Range	3-25 min	3-25 min	3-25 min	3-25 min
Sorptivity (mm/hr$^{0.5}$)	**5.65**	**4.13**	**4.57**	**4.89**
Porosity (%)	**12.10**	**12.21**	**11.76**	**12.12**

MIX GGBS-50 (WSI & Porosity Test-3)				
				Variability
Av. Sorptivity:	**4.93**	**COV:**	**17.2**	**Caution**
Av. Porosity:	**12.13**	**COV:**	**4.3**	**Good**
	Sample 1	Sample 2	Sample 3	Sample 4
Diameter (mm)	68.65	68.69	68.57	68.69
Thickness (mm)	30.27	30.22	30.05	30.04
Time (min)	Mass (g)	Mass (g)	Mass (g)	Mass (g)
0	257.65	257.45	262.08	257.19
3	258.42	258.08	262.83	257.93
5	258.59	258.20	262.99	258.07
7	258.73	258.29	263.13	258.20
9	258.86	258.39	263.26	258.33
12	259.00	258.50	263.37	258.44
16	259.20	258.63	263.54	258.61
20	259.32	258.69	263.65	258.73
25	259.50	258.80	263.80	258.87
Saturated Mass (g)	271.55	271.47	274.69	270.81
R^2 (Must be >0.98)	0.9990	0.9943	0.9967	0.9982
Range	3-25 min	3-25 min	3-25 min	3-25 min
Sorptivity (mm/hr$^{0.5}$)	**5.57**	**3.72**	**5.46**	**4.96**
Porosity (%)	**12.41**	**12.52**	**11.37**	**12.23**

MIX SF-10 (WSI & Porosity Test-1)				
				Variability
Av. Sorptivity:	**4.39**	**COV:**	**16.7**	**Caution**
Av. Porosity:	**14.05**	**COV:**	**19.5**	**High**
	Sample 1	Sample 2	Sample 3	Sample 4
Diameter (mm)	68.63	68.62	68.57	68.59
Thickness (mm)	30.25	30.24	31.08	29.69
Time (min)	Mass (g)	Mass (g)	Mass (g)	Mass (g)
0	238.13	254.37	262.15	251.95
3	239.03	255.20	263.00	252.58
5	239.22	255.35	263.17	252.69
7	239.42	255.49	263.30	252.80
9	239.49	255.58	263.40	252.86
12	239.64	255.71	263.56	252.98
16	239.80	255.86	263.73	253.10
20	239.96	256.00	263.89	253.21
25	240.12	256.14	264.03	253.33
Saturated Mass (g)	258.42	268.24	276.88	266.00
R^2 (Must be >0.98)	0.9949	0.9992	0.9994	0.9994
Range	3-25 min	3-25 min	3-25 min	3-25 min
Sorptivity (mm/hr$^{0.5}$)	**3.77**	**4.84**	**5.19**	**3.76**
Porosity (%)	**18.13**	**12.41**	**12.84**	**12.81**

MIX SF-10 (WSI & Porosity Test-2)				
				Variability
Av. Sorptivity:	**3.90**	**COV:**	**8.9**	**Good**
Av. Porosity:	**14.07**	**COV:**	**5.2**	**Good**
	Sample 1	Sample 2	Sample 3	Sample 4
Diameter (mm)	68.59	68.78	68.67	68.61
Thickness (mm)	29.45	29.28	28.83	31.57
Time (min)	Mass (g)	Mass (g)	Mass (g)	Mass (g)
0	242.88	251.86	243.94	260.05
3	243.56	252.50	244.68	260.78
5	243.68	252.60	244.86	260.93
7	243.79	252.71	244.97	261.05
9	243.87	252.80	245.08	261.15
12	243.99	252.92	245.23	261.28
16	244.12	253.05	245.37	261.43
20	244.21	253.15	245.51	261.55
25	244.33	253.27	245.64	261.69
Saturated Mass (g)	258.54	265.98	259.22	277.08
R^2 (Must be >0.98)	0.9986	0.9989	0.9981	0.9994
Range	3-25 min	3-25 min	3-25 min	3-25 min
Sorptivity (mm/hr$^{0.5}$)	**3.45**	**3.86**	**4.28**	**3.99**
Porosity (%)	**14.39**	**12.98**	**14.31**	**14.59**

MIX SF-10 (WSI & Porosity Test-3)				
				Variability
Av. Sorptivity:	**3.82**	**COV:**	**8.6**	**Good**
Av. Porosity:	**13.64**	**COV:**	**3.8**	**Good**
	Sample 1	Sample 2	Sample 3	Sample 4
Diameter (mm)	68.72	68.47	68.62	68.75
Thickness (mm)	29.18	28.95	31.19	31.21
Time (min)	Mass (g)	Mass (g)	Mass (g)	Mass (g)
0	245.32	239.68	267.14	261.43
3	246.12	240.37	267.73	262.19
5	246.28	240.50	267.85	262.32
7	246.39	240.60	267.94	262.42
9	246.49	240.69	268.02	262.51
12	246.63	240.80	268.12	262.62
16	246.78	240.93	268.23	262.75
20	246.91	241.04	268.34	262.87
25	247.07	241.17	268.45	263.00
Saturated Mass (g)	260.45	254.27	282.00	277.66
R^2 (Must be >0.98)	0.9998	0.9998	0.9997	0.9999
Range	3-25 min	3-25 min	3-25 min	3-25 min
Sorptivity (mm/hr$^{0.5}$)	**4.30**	**3.74**	**3.56**	**3.67**
Porosity (%)	**13.98**	**13.69**	**12.88**	**14.01**

MIX MK-30 (WSI & Porosity Test-1)				
				Variability
Av. Sorptivity:	**5.54**	**COV:**	**4.5**	**Good**
Av. Porosity:	**10.60**	**COV:**	**1.1**	**Good**
	Sample 1	Sample 2	Sample 3	Sample 4
Diameter (mm)	68.48	68.76	68.73	68.71
Thickness (mm)	29.04	30.33	30.29	29.64
Time (min)	Mass (g)	Mass (g)	Mass (g)	Mass (g)
0	249.86	262.50	263.69	259.87
3	250.65	263.26	264.53	260.68
5	250.81	263.43	264.69	260.84
7	250.95	263.56	264.83	260.97
9	251.04	263.65	264.93	261.07
12	251.19	263.78	265.08	261.21
16	251.31	263.90	265.23	261.36
20	251.42	264.03	265.34	261.50
25	251.55	264.15	265.47	261.63
Saturated Mass (g)	261.36	274.40	275.45	271.53
R^2 (Must be >0.98)	0.9946	0.9958	0.9965	0.9989
Range	3-25 min	3-25 min	3-25 min	3-25 min
Sorptivity (mm/hr$^{0.5}$)	**5.35**	**5.30**	**5.76**	**5.74**
Porosity (%)	**10.76**	**10.57**	**10.47**	**10.61**

MIX MK-30 (WSI & Porosity Test-2)				
				Variability
Av. Sorptivity:	**4.64**	**COV:**	**10.9**	**Good**
Av. Porosity:	**9.88**	**COV:**	**2.2**	**Good**
	Sample 1	Sample 2	Sample 3	Sample 4
Diameter (mm)	68.56	68.62	68.72	68.80
Thickness (mm)	31.75	31.46	31.18	30.68
Time (min)	Mass (g)	Mass (g)	Mass (g)	Mass (g)
0	279.89	279.97	274.87	270.61
3	280.61	280.68	275.59	271.21
5	280.73	280.80	275.72	271.34
7	280.82	280.89	275.84	271.43
9	280.89	280.97	275.93	271.50
12	280.99	281.09	276.04	271.59
16	281.11	281.19	276.17	271.69
20	281.20	281.29	276.29	271.77
25	281.29	281.40	276.41	271.86
Saturated Mass (g)	291.83	291.26	286.29	281.72
R^2 (Must be >0.98)	0.9983	0.9987	0.9991	0.9950
Range	3-25 min	3-25 min	3-25 min	3-25 min
Sorptivity (mm/hr$^{0.5}$)	**4.31**	**4.75**	**5.30**	**4.19**
Porosity (%)	**10.19**	**9.71**	**9.88**	**9.74**

MIX MK-30 (WSI & Porosity Test-3)				
				Variability
Av. Sorptivity:	**4.75**	**COV:**	**12.1**	**Good**
Av. Porosity:	**9.66**	**COV:**	**3.4**	**Good**
	Sample 1	Sample 2	Sample 3	Sample 4
Diameter (mm)	68.71	68.49	68.79	68.57
Thickness (mm)	30.18	31.24	30.01	30.97
Time (min)	Mass (g)	Mass (g)	Mass (g)	Mass (g)
0	270.37	278.02	264.67	275.04
3	271.03	278.70	265.38	275.76
5	271.18	278.84	265.52	275.88
7	271.29	278.94	265.64	275.97
9	271.36	278.99	265.71	276.03
12	271.48	279.09	265.82	276.12
16	271.60	279.21	265.96	276.21
20	271.72	279.30	266.07	276.29
25	271.84	279.40	266.17	276.36
Saturated Mass (g)	280.95	289.02	275.99	285.89
R^2 (Must be >0.98)	0.9984	0.9963	0.9974	0.9931
Range	3-25 min	3-25 min	3-25 min	3-25 min
Sorptivity ($mm/hr^{0.5}$)	**5.39**	**4.62**	**4.97**	**4.03**
Porosity (%)	**9.45**	**9.56**	**10.15**	**9.49**

B3 CHLORIDE CONDUCTIVITY INDEX (CCI)

MIX 100% RHPC (CCI Test-1)

Sample 1		Sample 2		Sample 3		Sample 4	
Thickness	Diameter	Thickness	Diameter	Thickness	Diameter	Thickness	Diameter
31.20	68.16	30.58	68.48	30.28	68.34	30.44	68.32
31.36	68.30	30.22	68.46	30.58	68.10	29.74	68.38
30.78	68.42	30.10	68.42	30.68	68.26	30.12	68.04
31.08	68.22	31.28	68.48	30.78	68.40	27.52	68.16
31.11	**68.28**	**30.55**	**68.46**	**30.58**	**68.28**	**29.46**	**68.23**

Chloride Conductivity

Sample	Oven dry mass, M_D (g)	Saturated mass, M_S (g)	Thickness (mm)	Diameter (mm)	Voltage (V)	Current (mA)	Conductivity (mS/cm)
Sample 1	272.59	286.33	31.11	68.28	10.78	153.0	1.21
Sample 2	268.42	281.41	30.55	68.46	10.26	159.0	1.29
Sample 3	267.69	280.98	30.58	68.28	10.45	154.0	1.23
Sample 4	246.94	263.33	29.46	68.23	10.81	210.0	1.57
						Average:	1.32
						COV:	12.52

Porosity

Sample	M_S - M_D (g)	Area (mm^2)	Porosity (n) (%)
Sample 1	13.74	3661.59	4.58
Sample 2	12.99	3681.46	4.30
Sample 3	13.29	3661.59	4.43
Sample 4	16.39	3656.23	5.48
		Average:	4.70
		COV:	11.35

SUMMARY						
						VARIABILITY
AV. CCI	**1.32**	S.D.	**0.17**	COV.	**12.52**	**Good**
AV. Porosity	**4.70**	S.D.	**0.17**	COV.	**11.35**	

MIX 100% RHPC (CCI Test-2)

Sample 1		Sample 2		Sample 3		Sample 4	
Thickness	Diameter	Thickness	Diameter	Thickness	Diameter	Thickness	Diameter
30.90	68.66	29.52	68.18	30.88	68.34	31.42	68.20
30.64	68.24	28.72	68.44	30.02	68.32	30.02	68.32
31.38	68.28	30.08	68.20	31.70	68.16	31.88	68.10
30.88	68.52	30.12	68.56	30.68	68.68	30.32	68.16
30.95	**68.43**	**29.61**	**68.35**	**30.82**	**68.38**	**30.91**	**68.20**

Chloride Conductivity

Sample	Oven dry mass, M_D (g)	Saturated mass, M_S (g)	Thickness (mm)	Diameter (mm)	Voltage (V)	Current (mA)	Conductivity (mS/cm)
Sample 1	265.19	280.10	30.95	68.43	10.11	196.0	1.63
Sample 2	250.22	263.87	29.61	68.35	10.56	168.0	1.28
Sample 3	261.46	276.42	30.82	68.38	10.61	162.0	1.28
Sample 4	249.90	267.32	30.91	68.20	10.63	206.0	1.64
						Average:	1.46
						COV:	13.97

Porosity

Sample	M_S - M_D (g)	Area (mm^2)	Porosity (n) (%)
Sample 1	14.91	3677.70	4.94
Sample 2	13.65	3669.10	4.54
Sample 3	14.96	3672.32	4.96
Sample 4	17.42	3653.01	5.83
		Average:	5.07
		COV:	10.73

SUMMARY						
						VARIABILITY
AV. CCI	**1.46**	S.D.	**0.20**	COV.	**13.97**	**Good**
AV. Porosity	**5.07**	S.D.	**0.20**	COV.	**10.73**	

MIX 100% RHPC (CCI Test-3)

Sample 1		Sample 2		Sample 3		Sample 4	
Thickness	Diameter	Thickness	Diameter	Thickness	Diameter	Thickness	Diameter
30.22	68.28	31.10	68.32	29.76	68.02	31.56	68.08
28.58	68.18	31.96	68.26	29.66	68.32	30.92	68.22
30.04	68.26	31.86	68.12	29.82	68.18	31.18	68.44
28.28	68.16	31.98	68.02	30.26	68.44	30.34	68.24
29.28	**68.22**	**31.73**	**68.18**	**29.88**	**68.24**	**31.00**	**68.25**

Chloride Conductivity

Sample	Oven dry mass, M_D (g)	Saturated mass, M_S (g)	Thickness (mm)	Diameter (mm)	Voltage (V)	Current (mA)	Conductivity (mS/cm)
Sample 1	250.49	263.37	29.28	68.22	10.76	178.0	1.33
Sample 2	275.30	289.72	31.73	68.18	10.21	180.0	1.53
Sample 3	259.15	272.64	29.88	68.24	10.61	151.0	1.16
Sample 4	259.01	275.16	31.00	68.25	10.46	186.0	1.51
						Average:	1.38
						COV:	12.50

Porosity

Sample	M_S - M_D (g)	Area (mm^2)	Porosity (n) (%)
Sample 1	12.88	3655.69	4.30
Sample 2	14.42	3651.41	4.83
Sample 3	13.49	3657.84	4.50
Sample 4	16.15	3658.37	5.39
		Average:	4.76
		COV:	9.98

SUMMARY						
						VARIABILITY
AV. CCI	**1.38**	S.D.	**0.17**	COV.	**12.50**	**Good**
AV. Porosity	**4.76**	S.D.	**0.17**	COV.	**9.98**	

MIX FA-30 (CCI Test-1)

Sample 1		Sample 2		Sample 3		Sample 4	
Thickness	Diameter	Thickness	Diameter	Thickness	Diameter	Thickness	Diameter
31.88	68.40	29.74	68.44	29.60	68.36	31.78	68.48
30.98	68.54	29.94	68.40	29.18	68.44	31.42	68.58
31.62	68.48	31.16	68.14	29.68	68.46	31.54	68.42
31.24	68.32	30.58	68.26	29.38	68.64	31.20	68.44
31.43	**68.44**	**30.36**	**68.31**	**29.46**	**68.48**	**31.49**	**68.48**

Chloride Conductivity

Sample	Oven dry mass, M_D (g)	Saturated mass, M_S (g)	Thickness (mm)	Diameter (mm)	Voltage (V)	Current (mA)	Conductivity (mS/cm)
Sample 1	269.76	286.08	31.43	68.44	10.91	187.0	1.46
Sample 2	257.75	274.21	30.36	68.31	10.37	216.0	1.73
Sample 3	251.96	267.31	29.46	68.48	10.57	181.0	1.37
Sample 4	269.40	285.27	31.49	68.48	10.98	202.0	1.57
						Average:	1.53
						COV:	9.95

Porosity

Sample	M_S - M_D (g)	Area (mm^2)	Porosity (n) (%)
Sample 1	16.32	3678.77	5.40
Sample 2	16.46	3665.34	5.48
Sample 3	15.35	3683.07	5.07
Sample 4	15.87	3683.61	5.24
		Average:	5.30
		COV:	3.40

SUMMARY						
						VARIABILITY
AV. CCI	**1.53**	S.D.	**0.15**	COV.	**9.95**	**Poor**
AV. Porosity	**5.30**	S.D.	**0.15**	COV.	**3.40**	

MIX FA-30 (CCI Test-2)

Sample 1		Sample 2		Sample 3		Sample 4	
Thickness	Diameter	Thickness	Diameter	Thickness	Diameter	Thickness	Diameter
31.98	68.48	28.98	68.46	29.96	68.42	29.16	68.30
31.86	68.26	29.04	68.22	30.02	68.32	29.18	68.54
31.66	68.88	28.68	68.48	29.48	68.34	29.80	68.62
31.58	68.42	28.82	68.40	29.50	68.46	29.88	68.34
31.77	**68.51**	**28.88**	**68.39**	**29.74**	**68.39**	**29.51**	**68.45**

Chloride Conductivity

Sample	Oven dry mass, M_D (g)	Saturated mass, M_S (g)	Thickness (mm)	Diameter (mm)	Voltage (V)	Current (mA)	Conductivity (mS/cm)
Sample 1	272.82	288.72	31.77	68.51	10.85	175.0	1.39
Sample 2	247.00	261.87	28.88	68.39	10.74	204.0	1.49
Sample 3	251.78	266.98	29.74	68.39	10.71	209.0	1.58
Sample 4	246.80	262.41	29.51	68.45	10.88	189.0	1.39
						Average:	1.46
						COV:	6.22

Porosity

Sample	M_S - M_D (g)	Area (mm^2)	Porosity (n) (%)
Sample 1	15.90	3686.84	5.25
Sample 2	14.87	3673.93	4.93
Sample 3	15.20	3673.40	5.04
Sample 4	15.61	3680.38	5.16
		Average:	5.10
		COV:	2.70

SUMMARY						
						VARIABILITY
AV. CCI	**1.46**	S.D.	**0.09**	COV.	**6.22**	**Good**
AV. Porosity	**5.10**	S.D.	**0.09**	COV.	**2.70**	

MIX FA-30 (CCI Test-3)

Sample 1		Sample 2		Sample 3		Sample 4	
Thickness	Diameter	Thickness	Diameter	Thickness	Diameter	Thickness	Diameter
31.20	68.48	30.50	68.56	29.32	68.16	31.44	68.50
30.46	68.44	30.62	68.64	29.56	68.38	29.80	68.28
30.82	68.42	30.48	68.58	29.28	68.30	31.90	68.42
29.72	68.60	30.64	68.54	29.54	68.08	30.94	68.36
30.55	**68.49**	**30.56**	**68.58**	**29.43**	**68.23**	**31.02**	**68.39**

Chloride Conductivity

Sample	Oven dry mass, M_D (g)	Saturated mass, M_S (g)	Thickness (mm)	Diameter (mm)	Voltage (V)	Current (mA)	Conductivity (mS/cm)
Sample 1	261.77	277.23	30.55	68.49	10.52	199.0	1.57
Sample 2	260.14	276.58	30.56	68.58	10.67	206.0	1.60
Sample 3	251.23	266.14	29.43	68.23	10.90	223.0	1.65
Sample 4	257.10	274.62	31.02	68.39	10.21	219.0	1.81
						Average:	1.66
						COV:	6.55

Porosity

Sample	M_S - M_D (g)	Area (mm^2)	Porosity (n) (%)
Sample 1	15.46	3684.15	5.11
Sample 2	16.44	3694.38	5.41
Sample 3	14.91	3656.76	4.98
Sample 4	17.52	3673.93	5.81
		Average:	5.33
		COV:	6.94

SUMMARY						
						VARIABILITY
AV. CCI	**1.66**	S.D.	**0.11**	COV.	**6.55**	**Poor**
AV. Porosity	**5.33**	S.D.	**0.11**	COV.	**6.94**	

MIX GGBS-50 (CCI Test-1)

Sample 1		Sample 2		Sample 3		Sample 4	
Thickness	Diameter	Thickness	Diameter	Thickness	Diameter	Thickness	Diameter
30.82	68.42	31.98	68.78	30.14	68.70	28.64	68.74
31.12	68.74	30.54	68.52	28.86	68.52	28.84	68.82
31.14	68.96	31.48	68.86	28.92	68.58	29.42	68.72
31.38	68.54	30.78	68.66	28.50	68.66	30.28	68.84
31.12	**68.67**	**31.20**	**68.71**	**29.11**	**68.62**	**29.30**	**68.78**

Chloride Conductivity

Sample	Oven dry mass, M_D (g)	Saturated mass, M_S (g)	Thickness (mm)	Diameter (mm)	Voltage (V)	Current (mA)	Conductivity (mS/cm)
Sample 1	270.08	283.93	31.12	68.67	10.92	67.0	0.52
Sample 2	264.41	279.25	31.20	68.71	10.75	83.0	0.65
Sample 3	250.79	264.46	29.11	68.62	10.83	89.0	0.65
Sample 4	251.10	265.00	29.30	68.78	10.86	84.0	0.61
						Average:	0.61
						COV:	10.35

Porosity

Sample	M_S - M_D (g)	Area (mm^2)	Porosity (n) (%)
Sample 1	13.85	3703.54	4.54
Sample 2	14.84	3707.86	4.85
Sample 3	13.67	3698.15	4.49
Sample 4	13.90	3715.96	4.53
		Average:	4.60
		COV:	3.66

SUMMARY						
						VARIABILITY
AV. CCI	**0.61**	S.D.	**0.06**	COV.	**10.35**	**Excellent**
AV. Porosity	**4.60**	S.D.	**0.06**	COV.	**3.66**	

MIX GGBS-50 (CCI Test-2)

Sample 1		Sample 2		Sample 3		Sample 4	
Thickness	Diameter	Thickness	Diameter	Thickness	Diameter	Thickness	Diameter
30.08	68.56	28.52	68.62	30.52	68.74	29.36	68.60
30.16	68.56	29.54	68.42	30.30	68.70	29.22	68.76
30.32	68.54	29.14	68.62	31.32	68.98	29.22	68.72
30.58	68.56	28.96	68.64	30.70	68.82	29.08	68.22
30.29	**68.56**	**29.04**	**68.58**	**30.71**	**68.81**	**29.22**	**68.58**

Chloride Conductivity

Sample	Oven dry mass, M_D (g)	Saturated mass, M_S (g)	Thickness (mm)	Diameter (mm)	Voltage (V)	Current (mA)	Conductivity (mS/cm)
Sample 1	258.58	271.90	30.29	68.56	10.81	68.0	0.52
Sample 2	242.66	256.66	29.04	68.58	10.99	76.0	0.54
Sample 3	266.26	280.78	30.71	68.81	10.85	81.0	0.62
Sample 4	245.39	260.12	29.22	68.58	10.70	84.0	0.62
						Average:	0.57
						COV:	9.15

Porosity

Sample	M_S - M_D (g)	Area (mm^2)	Porosity (n) (%)
Sample 1	13.32	3691.68	4.39
Sample 2	14.00	3693.84	4.61
Sample 3	14.52	3719.20	4.73
Sample 4	14.73	3693.84	4.85
		Average:	4.64
		COV:	4.23

SUMMARY						
						VARIABILITY
AV. CCI	**0.57**	S.D.	**0.05**	COV.	**9.15**	**Excellent**
AV. Porosity	**4.64**	S.D.	**0.05**	COV.	**4.23**	

MIX GGBS-50 (CCI Test-3)

Sample 1		Sample 2		Sample 3		Sample 4	
Thickness	Diameter	Thickness	Diameter	Thickness	Diameter	Thickness	Diameter
31.00	68.78	30.08	68.68	29.90	68.74	30.48	68.72
30.18	68.72	30.06	68.60	30.56	68.78	31.00	68.84
31.26	68.58	29.40	68.62	31.12	68.90	30.52	68.66
30.16	68.64	29.90	68.74	30.56	68.92	30.80	68.78
30.65	**68.68**	**29.86**	**68.66**	**30.54**	**68.84**	**30.70**	**68.75**

Chloride Conductivity

Sample	Oven dry mass, M_D (g)	Saturated mass, M_S (g)	Thickness (mm)	Diameter (mm)	Voltage (V)	Current (mA)	Conductivity (mS/cm)
Sample 1	263.58	277.73	30.65	68.68	10.86	77.0	0.59
Sample 2	252.34	267.43	29.86	68.66	10.90	84.0	0.62
Sample 3	264.80	278.64	30.54	68.84	10.75	82.0	0.63
Sample 4	261.70	275.69	30.70	68.75	10.71	72.0	0.56
						Average:	0.60
						COV:	5.49

Porosity

Sample	M_S - M_D (g)	Area (mm^2)	Porosity (n) (%)
Sample 1	14.15	3705.16	4.63
Sample 2	15.09	3703.00	4.95
Sample 3	13.84	3721.90	4.50
Sample 4	13.99	3712.71	4.57
		Average:	4.66
		COV:	4.22

SUMMARY						
						VARIABILITY
AV. CCI	**0.60**	S.D.	**0.03**	COV.	**5.49**	**Excellent**
AV. Porosity	**4.66**	S.D.	**0.03**	COV.	**4.22**	

MIX SF-10 (CCI Test-1)

Sample 1		Sample 2		Sample 3		Sample 4	
Thickness	Diameter	Thickness	Diameter	Thickness	Diameter	Thickness	Diameter
29.98	68.74	30.72	68.64	30.56	68.72	28.54	68.72
29.42	68.72	31.16	68.66	31.12	68.52	28.62	68.64
29.12	68.80	31.08	68.58	30.08	68.70	29.12	68.64
29.52	68.76	31.10	68.78	30.38	68.64	29.24	68.78
29.51	**68.76**	**31.02**	**68.67**	**30.54**	**68.65**	**28.88**	**68.70**

Chloride Conductivity

Sample	Oven dry mass, M_D (g)	Saturated mass, M_S (g)	Thickness (mm)	Diameter (mm)	Voltage (V)	Current (mA)	Conductivity (mS/cm)
Sample 1	254.32	269.00	29.51	68.76	10.92	103.0	0.75
Sample 2	247.58	267.22	31.02	68.67	10.63	145.0	1.14
Sample 3	252.17	269.41	30.54	68.65	10.92	125.0	0.94
Sample 4	239.81	257.10	28.88	68.70	10.55	121.0	0.89
						Average:	0.93
						COV:	17.42

Porosity

Sample	M_S - M_D (g)	Area (mm^2)	Porosity (n) (%)
Sample 1	14.68	3713.25	4.79
Sample 2	19.64	3703.54	6.44
Sample 3	17.24	3701.38	5.65
Sample 4	17.29	3706.78	5.66
		Average:	5.64
		COV:	11.92

SUMMARY						
						VARIABILITY
AV. CCI	**0.93**	S.D.	**0.13**	COV.	**17.42**	**Good**
AV. Porosity	**5.64**	S.D.	**0.13**	COV.	**11.92**	

MIX SF-10 (CCI Test-2)

Sample 1		Sample 2		Sample 3		Sample 4	
Thickness	Diameter	Thickness	Diameter	Thickness	Diameter	Thickness	Diameter
29.60	68.62	28.92	68.78	28.92	68.60	30.56	68.68
29.00	68.62	29.42	68.84	28.62	68.72	30.82	68.60
29.44	68.64	29.06	68.72	28.40	68.64	29.98	68.72
28.98	68.60	28.48	68.72	29.12	68.70	30.42	68.78
29.26	**68.62**	**28.97**	**68.77**	**28.77**	**68.67**	**30.45**	**68.70**

Chloride Conductivity

Sample	Oven dry mass, M_D (g)	Saturated mass, M_S (g)	Thickness (mm)	Diameter (mm)	Voltage (V)	Current (mA)	Conductivity (mS/cm)
Sample 1	246.60	261.61	29.26	68.62	10.98	114.0	0.82
Sample 2	241.32	257.18	28.97	68.77	10.86	124.0	0.89
Sample 3	233.86	251.79	28.77	68.67	10.73	160.0	1.16
Sample 4	260.07	275.50	30.45	68.70	10.69	105.0	0.81
						Average:	0.92
						COV:	17.79

Porosity

Sample	M_S - M_D (g)	Area (mm^2)	Porosity (n) (%)
Sample 1	15.01	3698.69	4.93
Sample 2	15.86	3714.34	5.17
Sample 3	17.93	3703.54	5.88
Sample 4	15.43	3706.78	5.05
		Average:	5.26
		COV:	8.07

SUMMARY						
						VARIABILITY
AV. CCI	**0.92**	S.D.	**0.16**	COV.	**17.79**	**Good**
AV. Porosity	**5.26**	S.D.	**0.16**	COV.	**8.07**	

MIX SF-10 (CCI Test-3)

Sample 1		Sample 2		Sample 3		Sample 4	
Thickness	Diameter	Thickness	Diameter	Thickness	Diameter	Thickness	Diameter
29.72	68.74	28.58	68.56	30.76	68.98	29.22	68.54
30.08	68.76	28.38	68.66	31.58	68.76	29.74	68.54
30.34	68.56	28.62	68.52	30.66	68.70	29.26	68.60
30.56	68.70	28.56	68.44	31.42	68.68	29.28	68.68
30.18	**68.69**	**28.54**	**68.55**	**31.11**	**68.78**	**29.38**	**68.59**

Chloride Conductivity

Sample	Oven dry mass, M_D (g)	Saturated mass, M_S (g)	Thickness (mm)	Diameter (mm)	Voltage (V)	Current (mA)	Conductivity (mS/cm)
Sample 1	246.83	265.46	30.18	68.69	10.67	138.0	1.05
Sample 2	233.28	250.20	28.54	68.55	10.81	139.0	0.99
Sample 3	265.47	281.36	31.11	68.78	10.46	106.0	0.85
Sample 4	238.39	257.21	29.38	68.59	10.43	107.0	0.82
						Average:	0.93
						COV:	12.29

Porosity

Sample	M_S - M_D (g)	Area (mm^2)	Porosity (n) (%)
Sample 1	18.63	3706.24	6.10
Sample 2	16.92	3690.61	5.57
Sample 3	15.89	3715.96	5.18
Sample 4	18.82	3695.45	6.19
		Average:	5.76
		COV:	8.19

SUMMARY						
						VARIABILITY
AV. CCI	**0.93**	S.D.	**0.11**	COV.	**12.29**	**Good**
AV. Porosity	**5.76**	S.D.	**0.11**	COV.	**8.19**	

MIX MK-30 (CCI Test-1)

Sample 1		Sample 2		Sample 3		Sample 4	
Thickness	Diameter	Thickness	Diameter	Thickness	Diameter	Thickness	Diameter
29.78	68.74	31.18	68.64	31.04	68.68	29.64	68.60
30.08	68.46	31.76	68.60	31.48	68.80	29.50	68.64
29.84	68.52	31.58	68.74	30.98	68.50	30.30	68.72
29.70	68.72	30.94	68.56	31.68	68.64	30.32	68.64
29.85	**68.61**	**31.37**	**68.64**	**31.30**	**68.66**	**29.94**	**68.65**

Chloride Conductivity

Sample	Oven dry mass, M_D (g)	Saturated mass, M_S (g)	Thickness (mm)	Diameter (mm)	Voltage (V)	Current (mA)	Conductivity (mS/cm)
Sample 1	259.42	271.04	29.85	68.61	10.67	48.0	0.36
Sample 2	267.17	280.18	31.37	68.64	10.66	53.0	0.42
Sample 3	267.82	281.09	31.30	68.66	10.62	58.0	0.46
Sample 4	264.64	276.66	29.94	68.65	10.71	50.0	0.38
						Average:	0.41
						COV:	10.99

Porosity

Sample	M_S - M_D (g)	Area (mm^2)	Porosity (n) (%)
Sample 1	11.62	3697.61	3.82
Sample 2	13.01	3700.30	4.27
Sample 3	13.27	3702.46	4.35
Sample 4	12.02	3701.92	3.94
		Average:	4.09
		COV:	6.25

SUMMARY						
						VARIABILITY
AV. CCI	**0.41**	S.D.	**0.04**	COV.	**10.99**	**Excellent**
AV. Porosity	**4.09**	S.D.	**0.04**	COV.	**6.25**	

MIX MK-30 (CCI Test-2)

Sample 1		Sample 2		Sample 3		Sample 4	
Thickness	Diameter	Thickness	Diameter	Thickness	Diameter	Thickness	Diameter
31.98	68.64	30.78	68.54	29.98	68.78	31.90	68.60
31.16	68.74	31.12	68.66	29.86	68.74	30.92	68.62
31.70	68.76	30.90	68.78	30.08	68.68	31.86	68.56
30.96	68.58	31.28	68.60	30.12	68.66	30.64	68.56
31.45	**68.68**	**31.02**	**68.65**	**30.01**	**68.72**	**31.33**	**68.59**

Chloride Conductivity

Sample	Oven dry mass, M_D (g)	Saturated mass, M_S (g)	Thickness (mm)	Diameter (mm)	Voltage (V)	Current (mA)	Conductivity (mS/cm)
Sample 1	269.84	283.35	31.45	68.68	10.60	55.0	0.44
Sample 2	275.79	286.92	31.02	68.65	10.70	47.0	0.37
Sample 3	259.49	271.49	30.01	68.72	10.71	47.0	0.36
Sample 4	268.21	281.34	31.33	68.59	10.61	51.0	0.41
						Average:	0.39
						COV:	9.88

Porosity

Sample	M_S - M_D (g)	Area (mm^2)	Porosity (n) (%)
Sample 1	13.51	3705.16	4.42
Sample 2	11.13	3701.38	3.65
Sample 3	12.00	3708.94	3.92
Sample 4	13.13	3694.92	4.32
		Average:	4.08
		COV:	8.77

SUMMARY						
						VARIABILITY
AV. CCI	**0.39**	S.D.	**0.04**	COV.	**9.88**	**Excellent**
AV. Porosity	**4.08**	S.D.	**0.04**	COV.	**8.77**	

MIX MK-30 (CCI Test-3)

Sample 1		Sample 2		Sample 3		Sample 4	
Thickness	Diameter	Thickness	Diameter	Thickness	Diameter	Thickness	Diameter
30.84	68.64	31.82	68.68	31.74	68.60	30.52	68.64
31.62	68.58	31.56	68.72	31.38	68.74	29.90	68.68
30.98	68.60	31.68	68.84	31.64	68.64	30.38	68.62
31.80	68.52	31.72	68.78	31.32	68.66	29.92	68.66
31.31	**68.59**	**31.70**	**68.76**	**31.52**	**68.66**	**30.18**	**68.65**

Chloride Conductivity

Sample	Oven dry mass, M_D (g)	Saturated mass, M_S (g)	Thickness (mm)	Diameter (mm)	Voltage (V)	Current (mA)	Conductivity (mS/cm)
Sample 1	276.22	288.67	31.31	68.59	10.63	48.0	0.38
Sample 2	282.76	294.04	31.70	68.76	10.69	44.0	0.35
Sample 3	272.64	285.84	31.52	68.66	10.92	55.0	0.43
Sample 4	266.79	279.89	30.18	68.65	10.79	62.0	0.47
						Average:	0.41
						COV:	12.61

Porosity

Sample	M_S - M_D (g)	Area (mm^2)	Porosity (n) (%)
Sample 1	12.45	3694.92	4.09
Sample 2	11.28	3713.25	3.68
Sample 3	13.20	3703.00	4.33
Sample 4	13.10	3701.92	4.30
		Average:	4.10
		COV:	7.24

SUMMARY						
						VARIABILITY
AV. CCI	**0.41**	S.D.	**0.05**	COV.	**12.61**	**Excellent**
AV. Porosity	**4.10**	S.D.	**0.05**	COV.	**7.24**	

APPENDIX C DETAILS OF RESISTIVITY AND HCP

C1 RESISTIVITY

Table C1 Resistivity of the Specimens

Resistivity (kΩcm)											
	Cyclic Ponding Period										After Impressed Current
Cycle	**0**	**1**	**2**	**3**	**4**	**5**	**6**	**7**	**8**	**9**	
SP-PC100	4.42	7.65	7.08	9.22	6.97	6.15	7.68	7.52	9.05	7.62	3.40
SP-FA30	5.97	6.10	8.55	8.68	10.22	9.23	9.25	9.42	9.95	8.52	5.25
SP-BS50	4.13	6.55	13.45	14.80	18.98	24.52	21.03	21.40	19.57	18.48	9.38
SP-SF10	6.22	8.08	11.07	12.28	17.68	18.23	18.47	17.62	14.77	12.65	9.03
SP-MK30	6.90	12.72	22.27	27.57	27.65	28.33	28.68	25.85	23.22	20.18	21.17

C2 HALF-CELL POTENTIAL MEASUREMENT

Table C2 Half-Cell Potential of Bars in SP-PC100

Half-Cell Potential (mV, CSE) of Bars in SP-PC100											
	Cyclic Ponding Period										After Impressed Current
Cycle	**0**	**1**	**2**	**3**	**4**	**5**	**6**	**7**	**8**	**9**	
Bar-1	-75	-97	-107	-114	-119	-119	-118	-277	-380	-376	-462
Bar-2	-92	-100	-116	-126	-128	-129	-135	-271	-375	-371	-612
Bar-3	-87	-101	-119	-123	-129	-126	-136	-272	-370	-365	-657
Bar-4	-88	-106	-119	-123	-130	-122	-131	-275	-355	-344	-618
Bar-5	-87	-104	-113	-120	-129	-119	-124	-272	-346	-342	-747
Bar-6	-96	-106	-112	-110	-119	-113	-117	-271	-345	-325	-783
Bar-7	-88	-95	-108	-115	-121	-121	-121	-273	-332	-327	-884
Bar-8	-89	-96	-116	-127	-128	-127	-122	-271	-334	-327	-806
Bar-9	-80	-95	-108	-118	-122	-120	-120	-270	-334	-325	-787

Table C3 Half-Cell Potential of Bars in SP-FA30

Half-Cell Potential (mV, CSE) of Bars in SP-FA30											
	Cyclic Ponding Period										After Impressed Current
Cycle	**0**	**1**	**2**	**3**	**4**	**5**	**6**	**7**	**8**	**9**	
Bar-1	-77	-116	-142	-122	-135	-130	-218	-267	-403	-390	-827
Bar-2	-79	-112	-134	-114	-125	-133	-166	-266	-403	-388	-704
Bar-3	-85	-132	-141	-128	-142	-140	-147	-261	-395	-385	-756
Bar-4	-85	-118	-134	-112	-125	-130	-126	-263	-378	-360	-734
Bar-5	-91	-126	-143	-124	-134	-138	-134	-262	-370	-352	-707
Bar-6	-93	-131	-137	-116	-125	-124	-118	-260	-371	-353	-610
Bar-7	-82	-118	-136	-113	-132	-130	-129	-262	-358	-336	-531
Bar-8	-75	-125	-132	-115	-129	-130	-129	-253	-348	-331	-607
Bar-9	-76	-116	-120	-106	-118	-121	-125	-234	-333	-322	-598

Table C4 Half-Cell Potential of Bars in SP-BS50

Half-Cell Potential (mV, CSE) of Bars in SP-BS50											
	Cyclic Ponding Period										After Impressed Current
Cycle	**0**	**1**	**2**	**3**	**4**	**5**	**6**	**7**	**8**	**9**	
Bar-1	-98	-129	-148	-133	-230	-211	-254	-227	-292	-282	-582
Bar-2	-118	-148	-256	-216	-242	-205	-306	-227	-295	-284	-583
Bar-3	-112	-146	-167	-224	-272	-255	-337	-224	-295	-284	-581
Bar-4	-110	-149	-178	-158	-181	-184	-177	-233	-273	-262	-614
Bar-5	-105	-149	-183	-155	-178	-185	-183	-229	-271	-257	-656
Bar-6	-117	-154	-184	-163	-187	-187	-193	-221	-257	-251	-653
Bar-7	-114	-149	-176	-154	-177	-182	-190	-220	-248	-231	-641
Bar-8	-103	-139	-159	-133	-152	-151	-148	-214	-244	-227	-681
Bar-9	-88	-121	-136	-115	-130	-126	-124	-217	-237	-225	-694

Table C5 Half-Cell Potential of Bars in SP-SF10

Half-Cell Potential (mV, CSE) of Bars in SP-SF10											
	Cyclic Ponding Period										After Impressed Current
Cycle	**0**	**1**	**2**	**3**	**4**	**5**	**6**	**7**	**8**	**9**	
Bar-1	-88	-121	-126	-115	-138	-128	-119	-137	-255	-250	-588
Bar-2	-84	-124	-137	-118	-154	-133	-137	-137	-254	-251	-586
Bar-3	-77	-129	-146	-127	-157	-146	-143	-138	-252	-248	-635
Bar-4	-90	-133	-148	-125	-144	-130	-124	-148	-245	-252	-734
Bar-5	-100	-119	-124	-110	-129	-117	-114	-144	-241	-247	-642
Bar-6	-91	-127	-135	-124	-142	-132	-131	-145	-240	-244	-648
Bar-7	-125	-173	-164	-130	-156	-140	-142	-148	-248	-235	-561
Bar-8	-97	-125	-135	-114	-137	-126	-121	-145	-247	-232	-596
Bar-9	-76	-117	-119	-130	-130	-127	-119	-138	-240	-229	-585

Table C6 Half-Cell Potential of Bars in SP-MK30

Half-Cell Potential (mV, CSE) of Bars in SP-MK30											
	Cyclic Ponding Period										After Impressed Current
Cycle	**0**	**1**	**2**	**3**	**4**	**5**	**6**	**7**	**8**	**9**	
Bar-1	-77	-148	-173	-159	-156	-165	-236	-317	-380	-381	-517
Bar-2	-65	-124	-147	-145	-168	-173	-199	-328	-375	-380	-572
Bar-3	-60	-117	-127	-121	-147	-170	-206	-310	-369	-378	-514
Bar-4	-65	-127	-146	-137	-134	-140	-119	-292	-355	-334	-531
Bar-5	-67	-128	-137	-134	-136	-144	-122	-283	-346	-330	-553
Bar-6	-63	-124	-138	-131	-135	-143	-119	-279	-339	-331	-567
Bar-7	-58	-118	-133	-122	-133	-141	-120	-270	-332	-302	-616
Bar-8	-61	-115	-122	-114	-119	-131	-121	-268	-334	-299	-625
Bar-9	-69	-130	-138	-135	-140	-157	-138	-269	-334	-297	-585

APPENDIX D SUPPLEMENTAL RESULTS OF MODELLING

D1 APPLIED PRESSURE FOR ALL CASES

DIAMETER 10 mm								
Steps	x_p (mm)	r_b (mm)	V_s (mm^3)	V_{rust} (mm^3)	CV_{rust} (mm^3)	ε_{rust}	k_{rust}	P (MPa)
1	0.01	5	0.3137	1.2547	0.0030	0.0024	1.5057	0.0036
2	0.02	5	0.6267	2.5070	0.0060	0.0024	3.0084	0.0072
3	25%	5	34.3438	137.3750	0.3297	0.0024	164.8500	0.3956
4	50%	5	58.8750	235.5000	0.5652	0.0024	282.6000	0.6782
5	75%	5	73.5938	294.3750	0.7065	0.0024	353.2500	0.8478
6	100%	5	78.5000	314.0000	0.7536	0.0024	376.8000	0.9043

DIAMETER 12 mm								
Steps	x_p (mm)	r_b (mm)	V_s (mm^3)	V_{rust} (mm^3)	CV_{rust} (mm^3)	ε_{rust}	k_{rust}	P (MPa)
1	0.01	6	0.3765	1.5059	0.0036	0.0024	1.8071	0.0043
2	0.02	6	0.7523	3.0094	0.0072	0.0024	3.6113	0.0087
3	25%	6	49.4550	197.820	0.4748	0.0024	237.3840	0.5697
4	50%	6	84.7800	339.120	0.8139	0.0024	406.9440	0.9767
5	75%	6	105.975	423.900	1.0174	0.0024	508.6800	1.2208
6	100%	6	113.040	452.160	1.0852	0.0024	542.5920	1.3022

DIAMETER 16 mm								
Steps	x_p (mm)	r_b (mm)	V_s (mm^3)	V_{rust} (mm^3)	CV_{rust} (mm^3)	ε_{rust}	k_{rust}	P (MPa)
1	0.01	8	0.5021	2.0083	0.0048	0.0024	2.4100	0.0058
2	0.02	8	1.0035	4.0142	0.0096	0.0024	4.8170	0.0116
3	25%	8	87.9200	351.680	0.8440	0.0024	422.0160	1.0128
4	50%	8	150.720	602.880	1.4469	0.0024	723.4560	1.7363
5	75%	8	188.400	753.600	1.8086	0.0024	904.3200	2.1704
6	100%	8	200.960	803.840	1.9292	0.0024	964.6080	2.3151

DIAMETER 20 mm								
Steps	x_p (mm)	r_b (mm)	V_s (mm^3)	V_{rust} (mm^3)	CV_{rust} (mm^3)	ε_{rust}	k_{rust}	P (MPa)
1	0.01	10	0.6277	2.5107	0.0060	0.0024	3.0129	0.0072
2	0.02	10	1.2547	5.0190	0.0120	0.0024	6.0228	0.0145
3	25%	10	137.375	549.5000	1.3188	0.0024	659.4000	1.5826
4	50%	10	235.500	942.0000	2.2608	0.0024	1130.4000	2.7130
5	75%	10	294.375	1177.500	2.8260	0.0024	1413.0000	3.3912
6	100%	10	314.000	1256.000	3.0144	0.0024	1507.2000	3.6173

DIAMETER 25 mm								
Steps	x_p (mm)	r_b (mm)	V_s (mm^3)	V_{rust} (mm^3)	CV_{rust} (mm^3)	ε_{rust}	k_{rust}	P (MPa)
1	0.01	12.5	0.7847	3.1387	0.0075	0.0024	3.7665	0.0090
2	0.02	12.5	1.5687	6.2750	0.0151	0.0024	7.5300	0.0181
3	25%	12.5	214.6484	858.5938	2.0606	0.0024	1030.3125	2.4728
4	50%	12.5	367.9688	1471.875	3.5325	0.0024	1766.2500	4.2390
5	75%	12.5	459.9609	1839.8438	4.4156	0.0024	2207.8125	5.2988
6	100%	12.5	490.625	1962.500	4.7100	0.0024	2355.0000	5.6520

D2 RESULTS OF THE VALIDATION

LABORATORY INVESTIGATION

SP-PC100										
$\boldsymbol{Bars}$	$\boldsymbol{D}$ $(\boldsymbol{mm})$	$\boldsymbol{c}$ $(\boldsymbol{mm})$	$\frac{\boldsymbol{D}}{\boldsymbol{c}}$	$\boldsymbol{r_b}$ $(\boldsymbol{mm})$	$\boldsymbol{w}$ $(\boldsymbol{mm})$	$\boldsymbol{E_c}$ $(\boldsymbol{GPa})$	$\boldsymbol{x_p}$ $(\boldsymbol{mm})$	$\boldsymbol{R_{rb}}$ $(\boldsymbol{mm})$	**Based on Derived Model**	
									$\boldsymbol{R_{rb}}$	$\boldsymbol{Error}$(%)
Bar-1	10	15	0.67	5	0.85	31.67	0.86	4.14	4.79	15.83%
Bar-2	10	15	0.67	5	1.23	31.67	0.80	4.21	4.70	11.72%
Bar-3	10	15	0.67	5	0.40	31.67	0.50	4.51	4.90	8.84%
Bar-4	10	30	0.33	5	0.10	31.67	0.57	4.43	4.99	12.60%
Bar-5	10	30	0.33	5	1.53	31.67	0.81	4.19	4.81	14.83%
Bar-6	10	30	0.33	5	0.85	31.67	0.06	4.94	4.90	0.82%

SP-FA30										
$\boldsymbol{Bars}$	$\boldsymbol{D}$ $(\boldsymbol{mm})$	$\boldsymbol{c}$ $(\boldsymbol{mm})$	$\boldsymbol{\frac{D}{c}}$	$\boldsymbol{r_b}$ $(\boldsymbol{mm})$	$\boldsymbol{w}$ $(\boldsymbol{mm})$	$\boldsymbol{E_c}$ $(\boldsymbol{GPa})$	$\boldsymbol{x_p}$ $(\boldsymbol{mm})$	$\boldsymbol{R_{rb}}$ $(\boldsymbol{mm})$	$\boldsymbol{Based\ on\ Derived\ Model}$	
									$\boldsymbol{R_{rb}}$	$\boldsymbol{Error}(\%)$
Bar-1	10	15	0.67	5	0.18	30.18	0.38	4.63	4.96	7.22%
Bar-2	10	15	0.67	5	0.26	30.18	0.63	4.38	4.94	12.92%
Bar-3	10	15	0.67	5	0.19	30.18	0.32	4.68	4.96	5.93%
Bar-5	10	30	0.33	5	0.07	30.18	0.37	4.63	4.99	7.88%
Bar-6	10	30	0.33	5	0.03	30.18	0.52	4.48	5.00	11.66%

SP-BS50										
$\boldsymbol{Bars}$	$\boldsymbol{D}$ $(\boldsymbol{mm})$	$\boldsymbol{c}$ $(\boldsymbol{mm})$	$\boldsymbol{\frac{D}{c}}$	$\boldsymbol{r_b}$ $(\boldsymbol{mm})$	$\boldsymbol{w}$ $(\boldsymbol{mm})$	$\boldsymbol{E_c}$ $(\boldsymbol{GPa})$	$\boldsymbol{x_p}$ $(\boldsymbol{mm})$	$\boldsymbol{R_{rb}}$ $(\boldsymbol{mm})$	$\boldsymbol{Based\ on\ Derived\ Model}$	
									$\boldsymbol{R_{rb}}$	$\boldsymbol{Error}(\%)$
Bar-1	10	15	0.67	5	0.11	30.64	0.46	4.54	4.98	9.66%
Bar-2	10	15	0.67	5	0.06	30.64	0.35	4.65	4.99	7.30%
Bar-3	10	15	0.67	5	0.09	30.64	0.35	4.66	4.98	6.96%
Bar-6	10	30	0.33	5	0.23	30.64	0.15	4.85	4.97	2.54%

SP-SF10										
$\boldsymbol{Bars}$	$\boldsymbol{D}$ $(\boldsymbol{mm})$	$\boldsymbol{c}$ $(\boldsymbol{mm})$	$\boldsymbol{\frac{D}{c}}$	$\boldsymbol{r_b}$ $(\boldsymbol{mm})$	$\boldsymbol{w}$ $(\boldsymbol{mm})$	$\boldsymbol{E_c}$ $(\boldsymbol{GPa})$	$\boldsymbol{x_p}$ $(\boldsymbol{mm})$	$\boldsymbol{R_{rb}}$ $(\boldsymbol{mm})$	$\boldsymbol{Based\ on\ Derived\ Model}$	
									$\boldsymbol{R_{rb}}$	$\boldsymbol{Error}(\%)$
Bar-1	10	15	0.67	5	0.17	32.68	0.52	4.48	4.96	10.73%
Bar-2	10	15	0.67	5	0.35	32.68	0.59	4.41	4.91	11.40%
Bar-3	10	15	0.67	5	0.12	32.68	0.35	4.66	4.97	6.80%
Bar-6	10	30	0.33	5	1.20	32.68	0.41	4.59	4.85	5.71%

ANDRADE ET AL.'S (1993) EXPERIMENTAL DATA

Specimen-I									
D (mm)	c (mm)	$\frac{D}{c}$	r_b (mm)	w (mm)	E_c (GPa)	x_p (mm)	R_{rb} (mm)	$\boldsymbol{Based\ on\ Derived\ Model}$	
								R_{rb}	$Error(\%)$
16	20	0.8	8	0.05	36	0.0179	7.9821	7.9898	0.10%
16	20	0.8	8	0.2	36	0.0467	7.9533	7.9591	0.07%
16	20	0.8	8	0.1	36	0.0467	7.9533	7.9796	0.33%
16	20	0.8	8	0.25	36	0.1075	7.8925	7.9489	0.71%
16	20	0.8	8	0.3	36	0.1075	7.8925	7.9386	0.58%
16	20	0.8	8	0.4	36	0.1075	7.8925	7.9180	0.32%

Specimen-II									
D (mm)	c (mm)	$\frac{D}{c}$	r_b (mm)	w (mm)	E_c (GPa)	x_p (mm)	R_{rb} (mm)	***Based on Derived Model***	
								R_{rb}	$Error(\%)$
16	20	0.8	8	0.1	36	0.02136	7.9786	7.9796	0.01%
16	20	0.8	8	0.2	36	0.04696	7.9530	7.9591	0.08%
16	20	0.8	8	0.35	36	0.11416	7.8858	7.9283	0.54%
16	20	0.8	8	0.5	36	0.01496	7.9850	7.8973	1.10%

Specimen-III									
D (mm)	c (mm)	$\frac{D}{c}$	r_b (mm)	w (mm)	E_c (GPa)	x_p (mm)	R_{rb} (mm)	***Based on Derived Model***	
								R_{rb}	$Error(\%)$
16	20	0.8	8	0.08	36	0.0245	7.9755	7.9837	0.10%
16	20	0.8	8	0.1	36	0.0373	7.9627	7.9796	0.21%
16	20	0.8	8	0.2	36	0.0501	7.9499	7.9591	0.12%
16	20	0.8	8	0.2	36	0.0597	7.9403	7.9591	0.24%
16	20	0.8	8	0.25	36	0.0725	7.9275	7.9489	0.27%
16	20	0.8	8	0.3	36	0.0853	7.9147	7.9386	0.30%
16	20	0.8	8	0.4	36	0.10456	7.8954	7.9180	0.29%
16	20	0.8	8	0.5	36	0.1365	7.8635	7.8973	0.43%

Specimen-IV									
D (mm)	c (mm)	$\frac{D}{c}$	r_b (mm)	w (mm)	E_c (GPa)	x_p (mm)	R_{rb} (mm)	***Based on Derived Model***	
								R_{rb}	***Error***$(\%)$
16	30	0.5333	8	0.05	36	0.01809	7.9819	7.9932	0.14%
16	30	0.5333	8	0.08	36	0.02127	7.9787	7.9891	0.13%
16	30	0.5333	8	0.08	36	0.02286	7.9771	7.9891	0.15%
16	30	0.5333	8	0.1	36	0.02509	7.9749	7.9864	0.14%
16	30	0.5333	8	0.2	36	0.0324	7.9676	7.9728	0.06%
16	30	0.5333	8	0.2	36	0.03876	7.9612	7.9728	0.15%
16	30	0.5333	8	0.25	36	0.04194	7.9581	7.9659	0.10%

VIDAL ET AL.'S (2004) EXPERIMENTAL DATA

BEAM-A Reinforcement in Tensile Zone									
D (mm)	c (mm)	$\frac{D}{c}$	r_b (mm)	w (mm)	E_c (GPa)	x_p (mm)	R_{rb} (mm)	***Based on Derived Model***	
								R_{rb}	$Error(\%)$
16	48	0.333	8	0.30	32	0.0431	7.9569	7.9773	0.26%
16	48	0.333	8	0.30	32	0.0516	7.9484	7.9773	0.36%
16	48	0.333	8	0.60	32	0.0610	7.9390	7.9546	0.20%
16	48	0.333	8	0.70	32	0.0842	7.9158	7.9470	0.39%
16	48	0.333	8	0.50	32	0.0840	7.9160	7.9622	0.58%
16	48	0.333	8	0.81	32	0.0932	7.9068	7.9386	0.40%
16	48	0.333	8	0.60	32	0.1073	7.8928	7.9546	0.78%
16	48	0.333	8	1.00	32	0.1169	7.8831	7.9242	0.52%
16	48	0.333	8	0.80	32	0.1221	7.8779	7.9394	0.78%
16	48	0.333	8	1.30	32	0.1220	7.8781	7.9013	0.29%
16	48	0.333	8	1.50	32	0.1301	7.8699	7.8860	0.20%
16	48	0.333	8	1.50	32	0.1371	7.8629	7.8860	0.29%
16	48	0.333	8	1.80	32	0.1395	7.8605	7.8630	0.03%

BEAM-A Reinforcement in Compression Zone									
D (mm)	c (mm)	$\frac{D}{c}$	r_b (mm)	w (mm)	E_c (GPa)	x_p (mm)	R_{rb} (mm)	***Based on Derived Model***	
								R_{rb}	$Error(\%)$
8	48	0.167	4	0.0064	32	0.0302	3.9698	3.9995	0.75%

BEAM-B Reinforcement in Tensile Zone									
D (mm)	c (mm)	$\frac{D}{c}$	r_b (mm)	w (mm)	E_c (GPa)	x_p (mm)	R_{rb} (mm)	***Based on Derived Model***	
								R_{rb}	$Error(\%)$
12	16	0.750	6	0.0008	32	0.0277	5.9723	5.9998	0.46%
12	16	0.750	6	0.102	32	0.0355	5.9645	5.9768	0.21%
12	16	0.750	6	0.004	32	0.0466	5.9534	5.9991	0.77%
12	16	0.750	6	0.3043	32	0.0415	5.9585	5.9306	0.47%
12	16	0.750	6	0.2569	32	0.0482	5.9518	5.9415	0.17%
12	16	0.750	6	0.3518	32	0.0491	5.9509	5.9197	0.52%
12	16	0.750	6	0.3518	32	0.0813	5.9187	5.9197	0.02%
12	16	0.750	6	0.4024	32	0.0914	5.9086	5.9081	0.01%
12	16	0.750	6	0.3549	32	0.1077	5.8923	5.9190	0.45%

BEAM-B Reinforcement in Compressive Zone									
D (mm)	c (mm)	$\frac{D}{c}$	r_b (mm)	w (mm)	E_c (GPa)	x_p (mm)	R_{rb} (mm)	***Based on Derived Model***	
								R_{rb}	$Error(\%)$
6	16	0.375	3	0.0000	32	0.0070	2.9930	3.0000	0.23%
6	16	0.375	3	0.0000	32	0.0481	2.9519	3.0000	1.63%
6	16	0.375	3	0.0000	32	0.0567	2.9433	3.0000	1.93%
6	16	0.375	3	0.1450	32	0.0547	2.9453	2.9670	0.74%
6	16	0.375	3	0.0000	32	0.0666	2.9334	3.0000	2.27%
6	16	0.375	3	0.0505	32	0.0804	2.9196	2.9885	2.36%
6	16	0.375	3	0.0000	32	0.1100	2.8900	3.0000	3.81%
6	16	0.375	3	0.1480	32	0.1150	2.8850	2.9663	2.82%
6	16	0.375	3	0.2080	32	0.1480	2.8520	2.9525	3.52%
6	16	0.375	3	0.2520	32	0.2350	2.7650	2.9423	6.41%

CHEN AND LEUNG'S (2013) ANALYTICAL DATA

Uniform Corrosion @ Cover depth of 20 mm									
D (mm)	c (mm)	$\frac{D}{c}$	r_b (mm)	w (mm)	E_c (GPa)	x_p (mm)	R_{rb} (mm)	***Based on Derived Model***	
								$\boldsymbol{R_{rb}}$	$\boldsymbol{Error}(\%)$
20	20	1	10	0.099	36	0.016	9.9840	9.9798	0.04%
20	20	1	10	0.138	36	0.024	9.9760	9.9718	0.04%
20	20	1	10	0.165	36	0.032	9.9680	9.9663	0.02%
20	20	1	10	0.225	36	0.044	9.9560	9.9540	0.02%
20	20	1	10	0.28	36	0.056	9.9440	9.9427	0.01%
20	20	1	10	0.338	36	0.064	9.9360	9.9308	0.05%
20	20	1	10	0.366	36	0.072	9.9280	9.9251	0.03%
20	20	1	10	0.406	36	0.08	9.9200	9.9169	0.03%
20	20	1	10	0.463	36	0.092	9.9080	9.9051	0.03%
20	20	1	10	0.497	36	0.1	9.9000	9.8981	0.02%

Non-uniform Corrosion @ Cover depth of 20 mm									
D (mm)	c (mm)	$\frac{D}{c}$	r_b (mm)	w (mm)	E_c (GPa)	x_p (mm)	R_{rb} (mm)	***Based on Derived Model***	
								$\boldsymbol{R_{rb}}$	***Error***(%)
20	20	1	10	0.137	36	0.024	9.9760	9.9720	0.04%
20	20	1	10	0.191	36	0.036	9.9640	9.9610	0.03%
20	20	1	10	0.257	36	0.048	9.9520	9.9475	0.05%
20	20	1	10	0.307	36	0.06	9.9400	9.9372	0.03%
20	20	1	10	0.385	36	0.072	9.9280	9.9212	0.07%
20	20	1	10	0.436	36	0.084	9.9160	9.9107	0.05%

Uniform Corrosion @ Cover depth of 40 mm									
D (mm)	c (mm)	$\frac{D}{c}$	r_b (mm)	w (mm)	E_c (GPa)	x_p (mm)	R_{rb} (mm)	***Based on Derived Model***	
								$\boldsymbol{R_{rb}}$	***Error***(%)
20	40	0.5	10	0.099	36	0.016	9.9840	9.9899	0.06%
20	40	0.5	10	0.138	36	0.024	9.9760	9.9859	0.10%
20	40	0.5	10	0.165	36	0.032	9.9680	9.9832	0.15%
20	40	0.5	10	0.225	36	0.044	9.9560	9.9770	0.21%
20	40	0.5	10	0.28	36	0.056	9.9440	9.9714	0.28%
20	40	0.5	10	0.338	36	0.064	9.9360	9.9655	0.30%
20	40	0.5	10	0.366	36	0.072	9.9280	9.9626	0.35%
20	40	0.5	10	0.406	36	0.08	9.9200	9.9585	0.39%
20	40	0.5	10	0.463	36	0.092	9.9080	9.9527	0.45%
20	40	0.5	10	0.497	36	0.1	9.9000	9.9492	0.50%

Non-uniform Corrosion @ Cover depth of 40 mm									
D (mm)	c (mm)	$\frac{D}{c}$	r_b (mm)	w (mm)	E_c (GPa)	x_p (mm)	R_{rb} (mm)	***Based on Derived Model***	
								$\boldsymbol{R_{rb}}$	***Error***(%)
20	40	0.5	10	0.204	36	0.034	9.9660	9.9792	0.13%
20	40	0.5	10	0.328	36	0.048	9.9520	9.9665	0.15%
20	40	0.5	10	0.452	36	0.068	9.9320	9.9538	0.22%
20	40	0.5	10	0.568	36	0.088	9.9120	9.9419	0.30%

Note: Crack width for non-uniform corrosion is the average value

D3 SIMULATION RESULTS OF CASE I, SP-1

Case I: SP-1

Units

TABLE 1

Unit System	Metric (m, kg, N, s, V, A) Degrees rad/s Celsius
Angle	Degrees
Rotational Velocity	rad/s
Temperature	Celsius

Model (A4)

Geometry

TABLE 2
Model (A4) > Geometry

Object Name	*Geometry*
State	Fully Defined
Definition	
Source	C:\Users\Lenovo\Documents\ANSYS-Research Project\SIMULATION-Case I_files\dp0\SYS\DM\SYS.agdb
Type	DesignModeler
Length Unit	Meters
Element Control	Program Controlled
2D Behaviour	Plane Stress
Display Style	Body Color
Bounding Box	
Length X	0.5 m
Length Y	0.12 m
Properties	
Volume	4.7143e-005 m³
Mass	0.11477 kg
Surface Area(approx.)	4.7143e-002 m²
Scale Factor Value	1.
Statistics	
Bodies	1
Active Bodies	1
Nodes	23856
Elements	7756
Mesh Metric	None
Update Options	
Assign Default Material	No
Basic Geometry Options	
Parameters	Independent
Parameter Key	
Attributes	Yes
Attribute Key	
Named Selections	Yes
Named Selection Key	
Material Properties	Yes

Advanced Geometry Options	
Use Associativity	Yes
Coordinate Systems	Yes
Coordinate System Key	
Reader Mode Saves Updated File	No
Use Instances	Yes
Smart CAD Update	Yes
Compare Parts On Update	No
Analysis Type	2-D
Clean Bodies On Import	No
Stitch Surfaces On Import	No
Decompose Disjoint Geometry	Yes
Enclosure and Symmetry Processing	Yes

TABLE 3
Model (A4) > Geometry > Parts

Object Name	*Surface Body*
State	Meshed
Graphics Properties	
Visible	Yes
Transparency	1
Definition	
Suppressed	No
Stiffness Behaviour	Flexible
Coordinate System	Default Coordinate System
Reference Temperature	By Environment
Thickness	1.e-003 m
Thickness Mode	Refresh on Update
Behaviour	None
Material	
Assignment	Concrete NL
Nonlinear Effects	Yes
Thermal Strain Effects	Yes
Bounding Box	
Length X	0.5 m
Length Y	0.12 m
Properties	
Volume	4.7143e-005 m³
Mass	0.11477 kg
Centroid X	0.25 m
Centroid Y	4.8046e-002 m
Centroid Z	0. m
Moment of Inertia Ip1	9.2848e-005 kg·m²
Moment of Inertia Ip2	2.5153e-003 kg·m²
Moment of Inertia Ip3	2.6082e-003 kg·m²
Surface Area(approx.)	4.7143e-002 m²
Statistics	
Nodes	23856
Elements	7756
Mesh Metric	None

Coordinate Systems

TABLE 4
Model (A4) > Coordinate Systems > Coordinate System

Object Name	*Global Coordinate System*
State	Fully Defined
Definition	
Type	Cartesian
Coordinate System ID	0.
Origin	
Origin X	0. m
Origin Y	0. m
Directional Vectors	
X-Axis Data	[1. 0.]
Y-Axis Data	[0. 1.]

Mesh

TABLE 5
Model (A4) > Mesh

Object Name	*Mesh*
State	Solved
Display	
Display Style	Use Geometry Setting
Defaults	
Physics Preference	Mechanical
Element Order	Quadratic
Element Size	2.5e-003 m
Sizing	
Use Adaptive Sizing	No
Growth Rate	Default (1.2)
Mesh Defeaturing	Yes
Defeature Size	Default (1.25e-005 m)
Capture Curvature	Yes
Curvature Min Size	Default (2.5e-005 m)
Curvature Normal Angle	Default (30.0°)
Capture Proximity	Yes
Proximity Min Size	Default (2.5e-005 m)
Num Cells Across Gap	Default (3)
Proximity Size Function Sources	Faces and Edges
Bounding Box Diagonal	0.5142 m
Average Surface Area	4.7147e-002 m²
Minimum Edge Length	2.5e-002 m
Quality	
Check Mesh Quality	Yes, Errors
Error Limits	Standard Mechanical
Target Quality	Default (0.050000)
Smoothing	Medium
Mesh Metric	None
Inflation	
Use Automatic Inflation	None
Inflation Option	Smooth Transition
Transition Ratio	0.272
Maximum Layers	2

Growth Rate	1.2
Inflation Algorithm	Pre
View Advanced Options	No
Advanced	
Number of CPUs for Parallel Part Meshing	Program Controlled
Straight Sided Elements	No
Rigid Body Behaviour	Dimensionally Reduced
Triangle Surface Mesher	Program Controlled
Topology Checking	No
Use Sheet Thickness for Pinch	No
Pinch Tolerance	Default (2.25e-005 m)
Generate Pinch on Refresh	No
Sheet Loop Removal	No
Statistics	
Nodes	23856
Elements	7756

FIGURE 1
Model (A4) > Mesh > Meshing

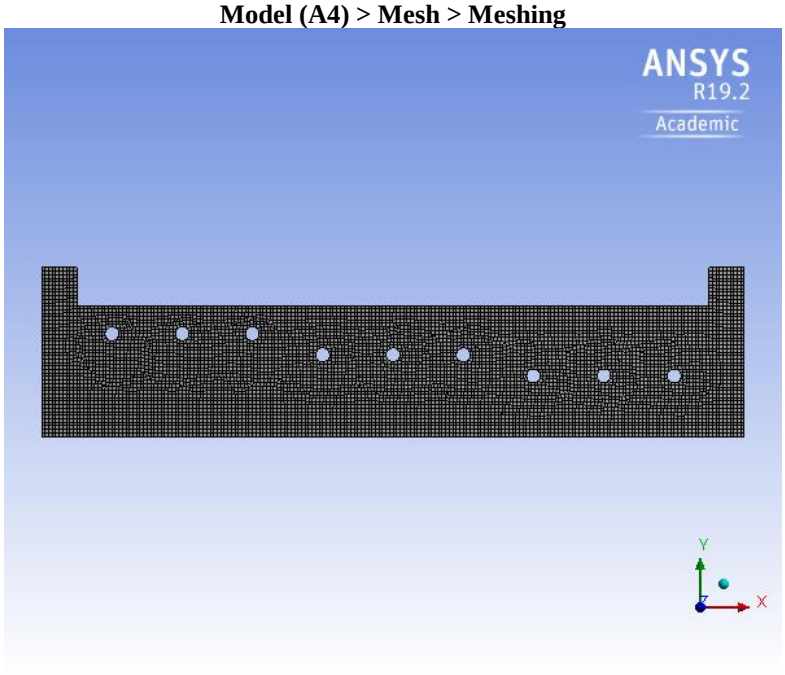

Static Structural (A5)

TABLE 6
Model (A4) > Analysis

Object Name	*Static Structural (A5)*
State	Solved
Definition	
Physics Type	Structural
Analysis Type	Static Structural
Solver Target	Mechanical APDL
Options	
Environment Temperature	22. °C
Generate Input Only	No

TABLE 7
Model (A4) > Static Structural (A5) > Analysis Settings

Object Name	*Analysis Settings*
State	Fully Defined
Step Controls	
Number Of Steps	6.
Current Step Number	1.
Step End Time	1. s
Auto Time Stepping	Program Controlled
Solver Controls	
Solver Type	Program Controlled
Weak Springs	Off
Solver Pivot Checking	Program Controlled
Large Deflection	On
Inertia Relief	Off
Rotor dynamics Controls	
Coriolis Effect	Off
Restart Controls	
Generate Restart Points	Program Controlled
Retain Files After Full Solve	No
Combine Restart Files	Program Controlled
Nonlinear Controls	
Newton-Raphson Option	Full
Force Convergence	Program Controlled
Moment Convergence	Program Controlled
Displacement Convergence	Program Controlled
Rotation Convergence	Program Controlled
Line Search	Program Controlled
Stabilization	Off
Output Controls	
Stress	Yes
Strain	Yes
Nodal Forces	No
Contact Miscellaneous	No
General Miscellaneous	No
Store Results At	All-Time Points
Analysis Data Management	
Solver Files Directory	C:\Users\Lenovo\Documents\ANSYS-Research Project\SIMULATION-Case I_files\dp0\SYS\MECH\
Future Analysis	None
Scratch Solver Files Directory	
Save MAPDL db	No
Contact Summary	Program Controlled
Delete Unneeded Files	Yes
Nonlinear Solution	Yes
Solver Units	Active System
Solver Unit System	mks

TABLE 8
Model (A4) > Static Structural (A5) > Analysis Settings
Step-Specific "Step Controls"

Step	Step End Time
1	1. s
2	2. s
3	3. s
4	4. s
5	5. s
6	6. s

FIGURE 2
Model (A4) > Static Structural (A5) > Boundary Conditions

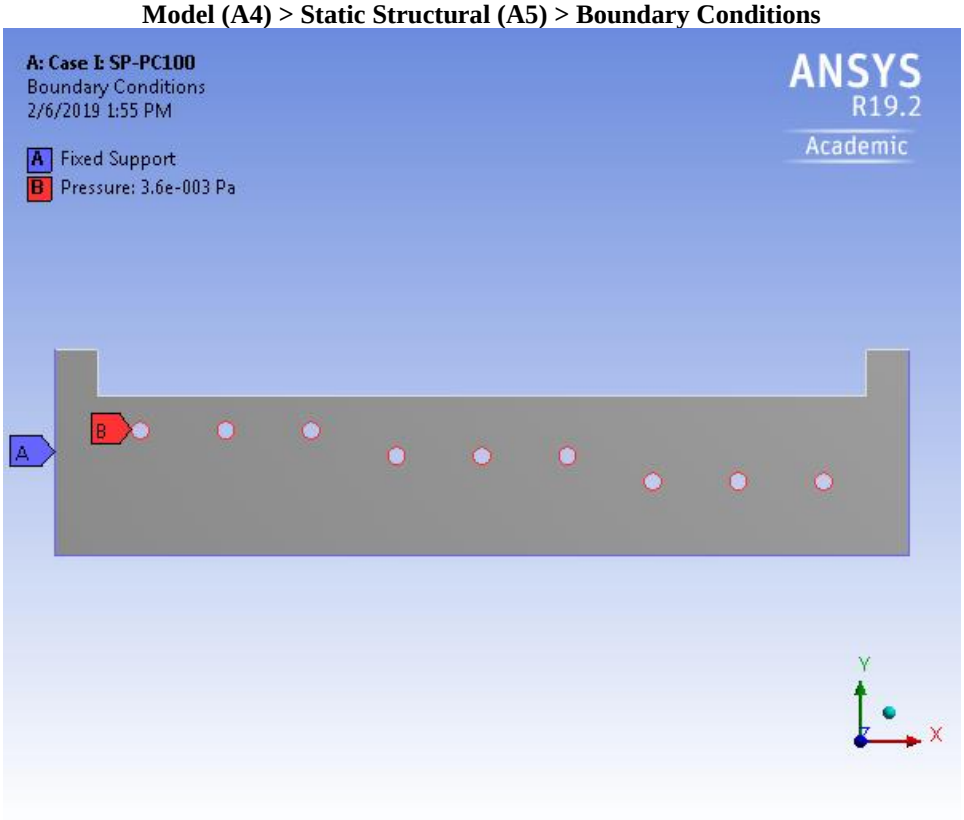

TABLE 9
Model (A4) > Static Structural (A5) > Loads

Object Name	*Fixed Support*	*Pressure*
State	Fully Defined	
Scope		
Scoping Method	Geometry Selection	
Geometry	3 Edges	9 Edges
Definition		
Type	Fixed Support	Pressure
Suppressed	No	
Define By		Normal To
Applied By		Direct
Magnitude		Tabular Data
Tabular Data		
Independent Variable		Time

FIGURE 3
Model (A4) > Static Structural (A5) > Pressure

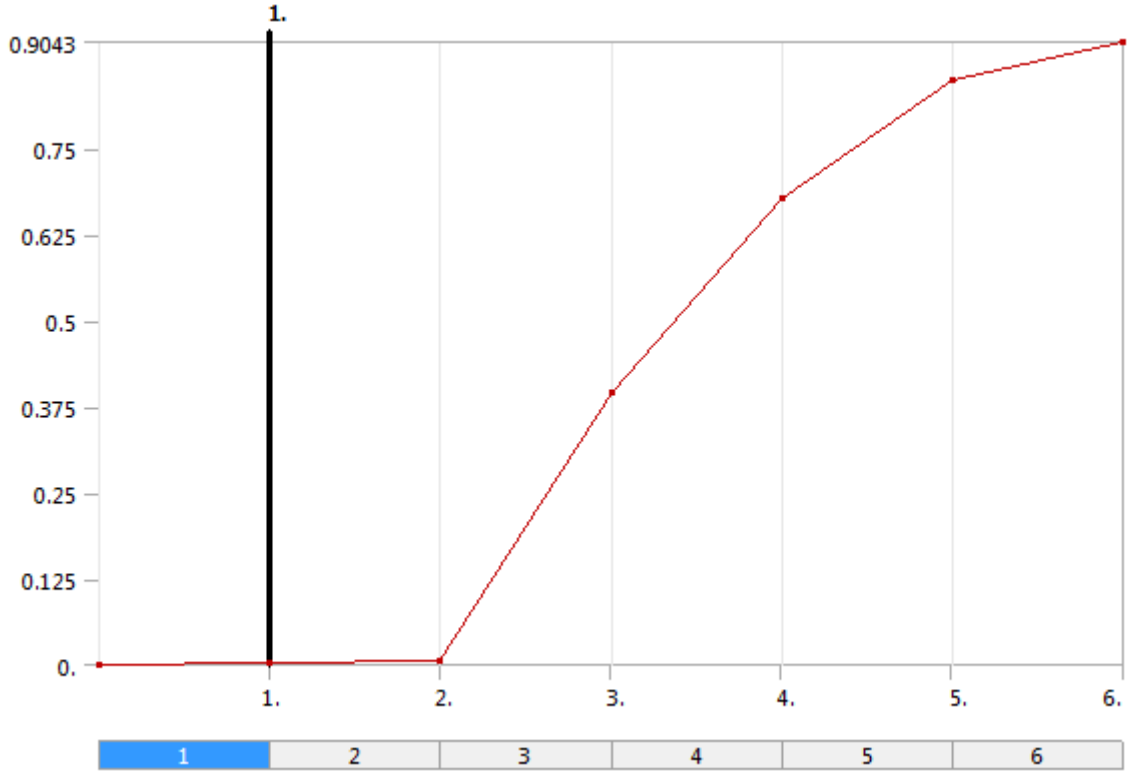

TABLE 10
Model (A4) > Static Structural (A5) > Pressure

Steps	Time [s]	Pressure [Pa]
1	0.	0.
	1.	3.6e-003
2	2.	7.2e-003
3	3.	0.3956
4	4.	0.6782
5	5.	0.8478
6	6.	0.9043

Solution (A6)

TABLE 11
Model (A4) > Static Structural (A5) > Solution

Object Name	*Solution (A6)*
State	Solved
Adaptive Mesh Refinement	
Max Refinement Loops	1.
Refinement Depth	2.
Information	
Status	Done
MAPDL Elapsed Time	1 m 17 s
MAPDL Memory Used	319. MB
MAPDL Result File Size	33.5 MB
Post Processing	
Beam Section Results	No
On-Demand Stress/Strain	No

TABLE 12
Model (A4) > Static Structural (A5) > Solution (A6) > Solution Information

Object Name	*Solution Information*
State	Solved
Solution Information	
Solution Output	Solver Output
Newton-Raphson Residuals	0
Identify Element Violations	0
Update Interval	2.5 s
Display Points	All
FE Connection Visibility	
Activate Visibility	Yes
Display	All FE Connectors
Draw Connections Attached To	All Nodes
Line Color	Connection Type
Visible on Results	No
Line Thickness	Single
Display Type	Lines

TABLE 13
Model (A4) > Static Structural (A5) > Solution (A6) > Results

Object Name	*Total Deformation*	*Equivalent Stress*	*Maximum Principal Stress*	*Normal Stress*	*Equivalent Elastic Strain*	*Maximum Principal Elastic Strain*	*Normal Elastic Strain*	*Directional Deformation*
State	Solved							
Scope								
Scoping Method	Geometry Selection							
Geometry	All Bodies							
Definition								
Type	Total Deformation	Equivalent (von-Mises) Stress	Maximum Principal Stress	Normal Stress	Equivalent Elastic Strain	Maximum Principal Elastic Strain	Normal Elastic Strain	Directional Deformation
By	Time							
Display Time	Last							
Calculate Time History	Yes							
Identifier								
Suppressed	No							
Orientation				X Axis			X Axis	
Coordinate System				Global Coordinate System			Global Coordinate System	
Results								
Minimum	0. m	2.5969e-005 Pa	0. Pa	-0.90715 Pa	8.2074e-016 m/m	1.7568e-016 m/m	-3.5664e-011 m/m	-1.7343e-013 m
Maximum	2.7991e-013 m	1.7872 Pa	1.1236 Pa	0.84516 Pa	5.6445e-011 m/m	4.1397e-011 m/m	3.247e-011 m/m	1.6984e-013 m

Average	4.4747e-014 m	0.1004 Pa	5.7051e-002 Pa	-1.3178e-002 Pa	3.2235e-012 m/m	2.1694e-012 m/m	-4.9163e-013 m/m	1.9974e-015 m
Minimum Occurs On	Surface Body							
Maximum Occurs On	Surface Body							
Minimum Value Over Time								
Minimum	0. m	1.0338e-007 Pa	0. Pa	-0.90715 Pa	3.2674e-018 m/m	6.9939e-019 m/m	-3.5664e-011 m/m	-1.7343e-013 m
Maximum	0. m	2.5969e-005 Pa	0. Pa	-3.6113e-003 Pa	8.2074e-016 m/m	1.7568e-016 m/m	-1.4198e-013 m/m	-6.9044e-016 m
Maximum Value Over Time								
Minimum	1.1143e-015 m	7.115e-003 Pa	4.4729e-003 Pa	3.3646e-003 Pa	2.2471e-013 m/m	1.648e-013 m/m	1.2926e-013 m/m	6.7613e-016 m
Maximum	2.7991e-013 m	1.7872 Pa	1.1236 Pa	0.84516 Pa	5.6445e-011 m/m	4.1397e-011 m/m	3.247e-011 m/m	1.6984e-013 m
Information								
Time	6. s							
Load Step	6							
Substep	1							
Iteration Number	8							
Integration Point Results								
Display Option		Averaged						
Average Across Bodies		No						

FIGURE 4
Model (A4) > Static Structural (A5) > Solution (A6) > Total Deformation

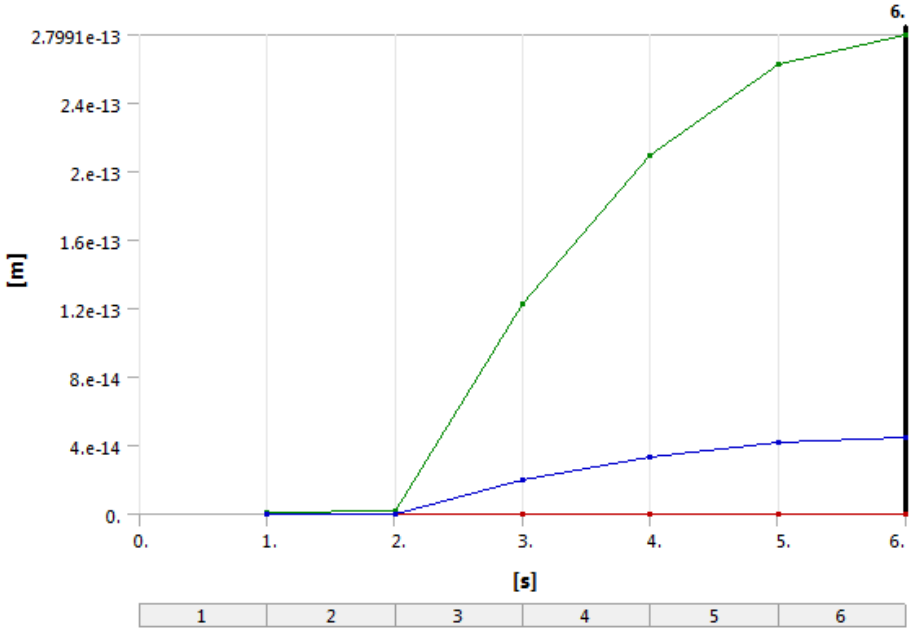

TABLE 14
Model (A4) > Static Structural (A5) > Solution (A6) > Total Deformation

Time [s]	Minimum [m]	Maximum [m]	Average [m]
1.	0.	1.1143e-015	1.7814e-016
2.		2.2286e-015	3.5628e-016
3.		1.2245e-013	1.9575e-014
4.		2.0992e-013	3.3559e-014
5.		2.6242e-013	4.1951e-014
6.		2.7991e-013	4.4747e-014

FIGURE 5
Model (A4) > Static Structural (A5) > Solution (A6) > Total Deformation > Total Deformation

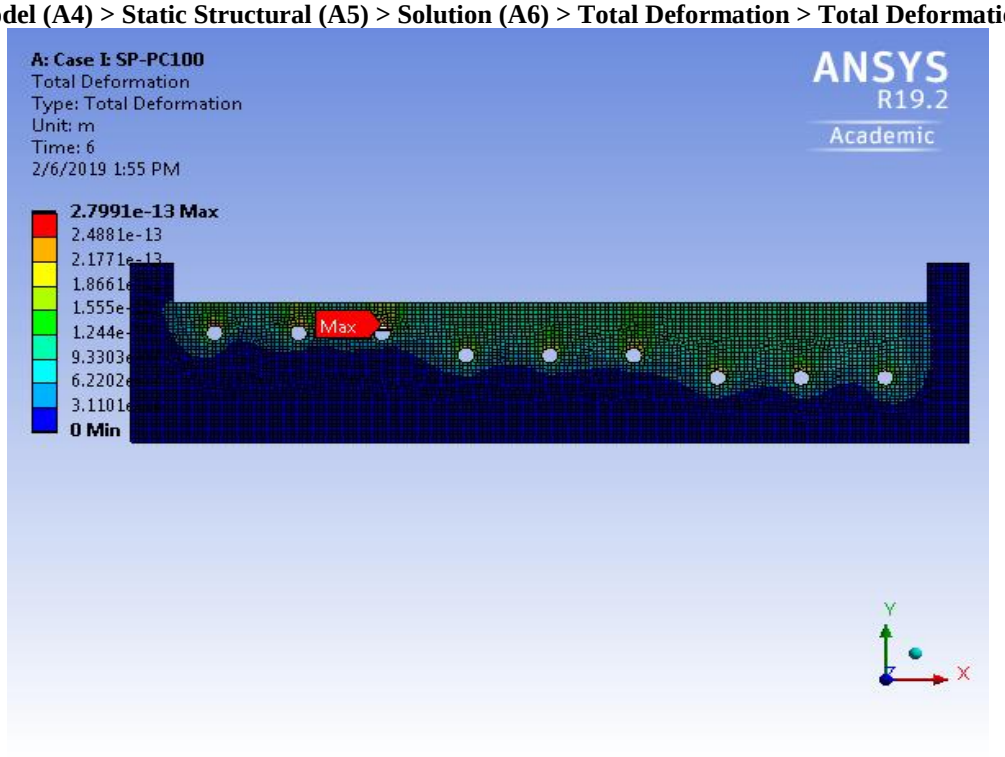

FIGURE 6
Model (A4) > Static Structural (A5) > Solution (A6) > Equivalent Stress

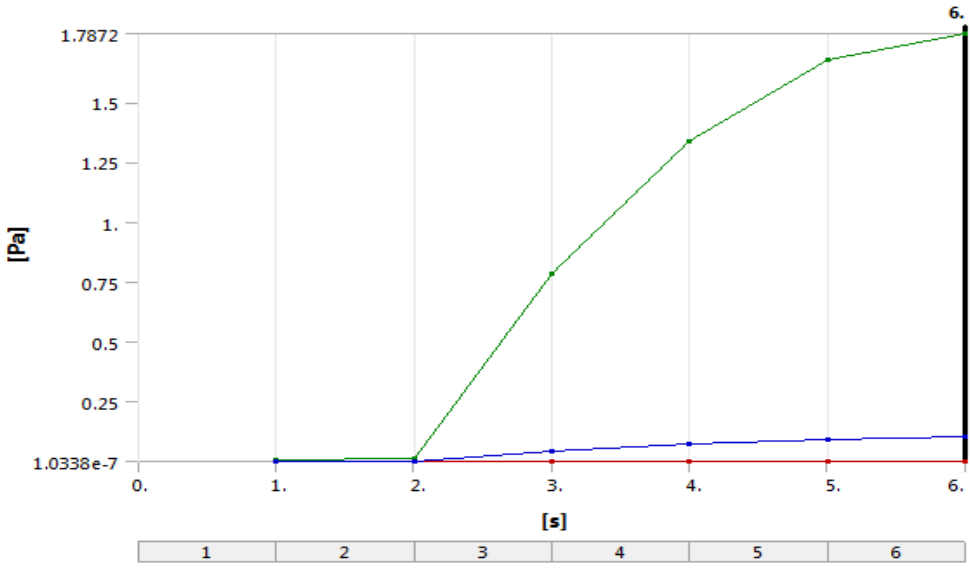

TABLE 15
Model (A4) > Static Structural (A5) > Solution (A6) > Equivalent Stress

Time [s]	Minimum [Pa]	Maximum [Pa]	Average [Pa]
1.	1.0338e-007	7.115e-003	3.9969e-004
2.	2.0676e-007	1.423e-002	7.9938e-004
3.	1.136e-005	0.78186	4.3921e-002
4.	1.9476e-005	1.3404	7.5297e-002
5.	2.4346e-005	1.6756	9.4127e-002
6.	2.5969e-005	1.7872	0.1004

FIGURE 7
Model (A4) > Static Structural (A5) > Solution (A6) > Equivalent Stress > Equivalent Stress

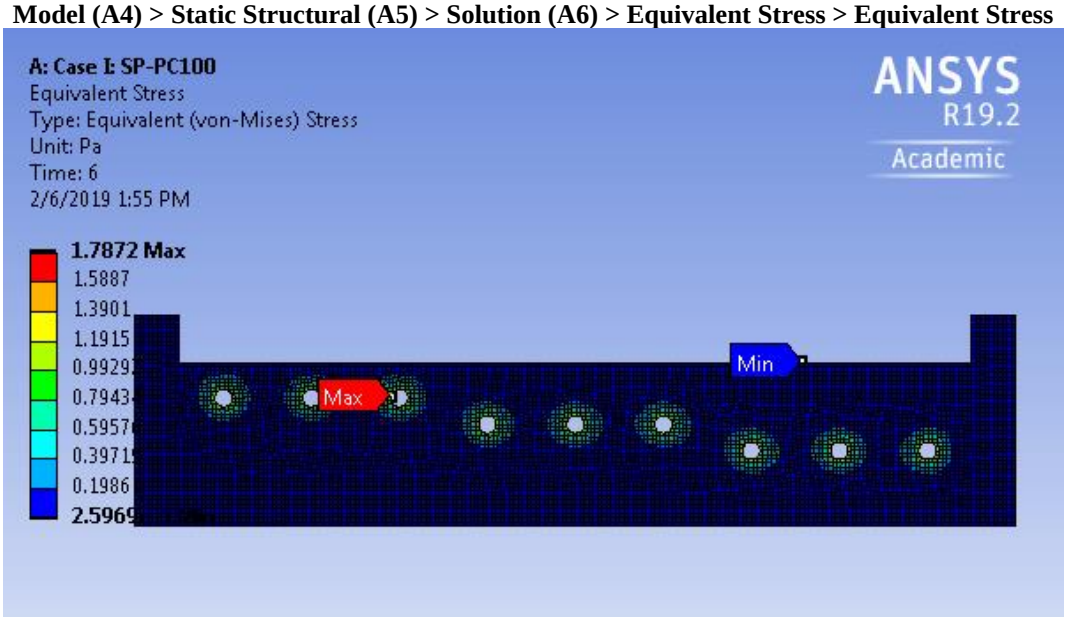

FIGURE 8
Model (A4) > Static Structural (A5) > Solution (A6) > Maximum Principal Stress

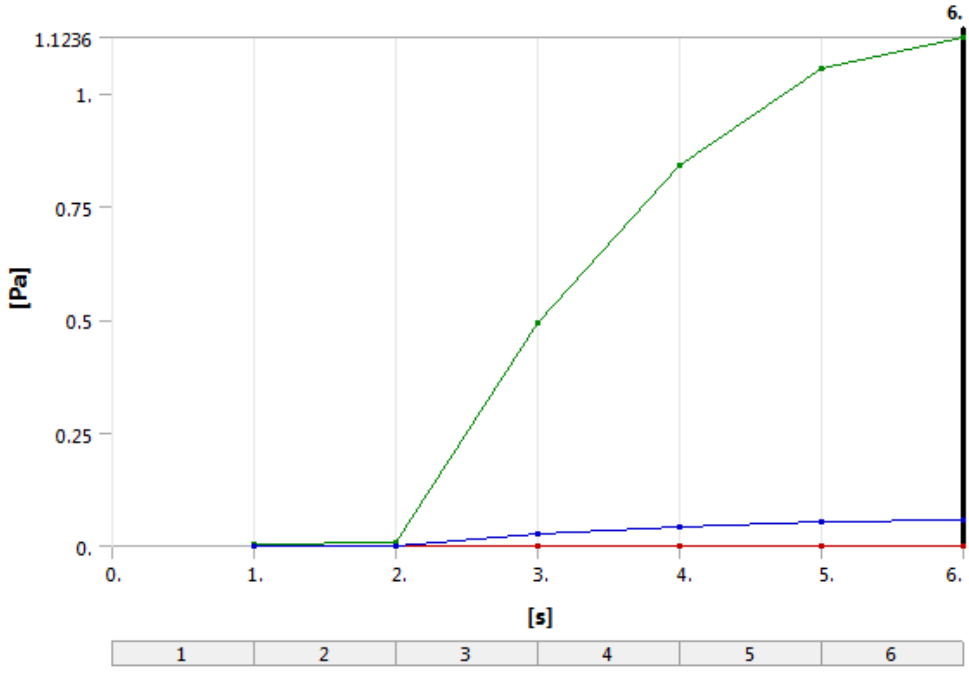

TABLE 16
Model (A4) > Static Structural (A5) > Solution (A6) > Maximum Principal Stress

Time [s]	Minimum [Pa]	Maximum [Pa]	Average [Pa]
1.	0.	4.4729e-003	2.2712e-004
2.		8.9458e-003	4.5424e-004
3.		0.49152	2.4958e-002
4.		0.84265	4.2787e-002
5.		1.0534	5.3487e-002
6.		1.1236	5.7051e-002

FIGURE 9
Model (A4) > Static Structural (A5) > Solution (A6) > Maximum Principal Stress > Maximum Principal Stress

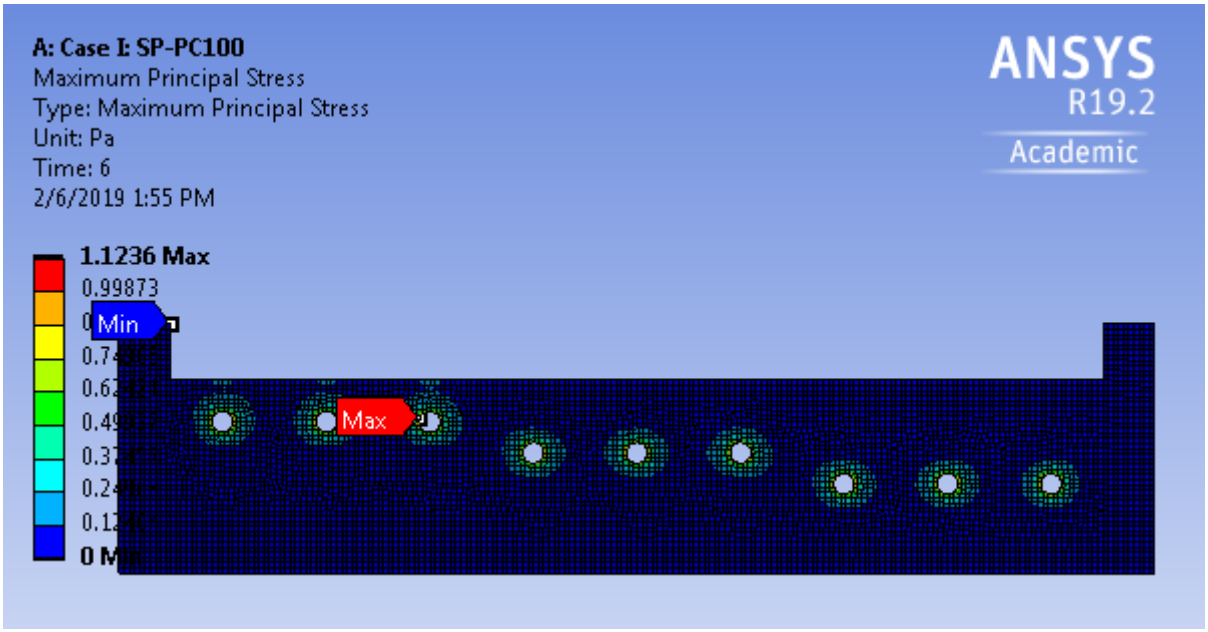

FIGURE 10
Model (A4) > Static Structural (A5) > Solution (A6) > Normal Stress

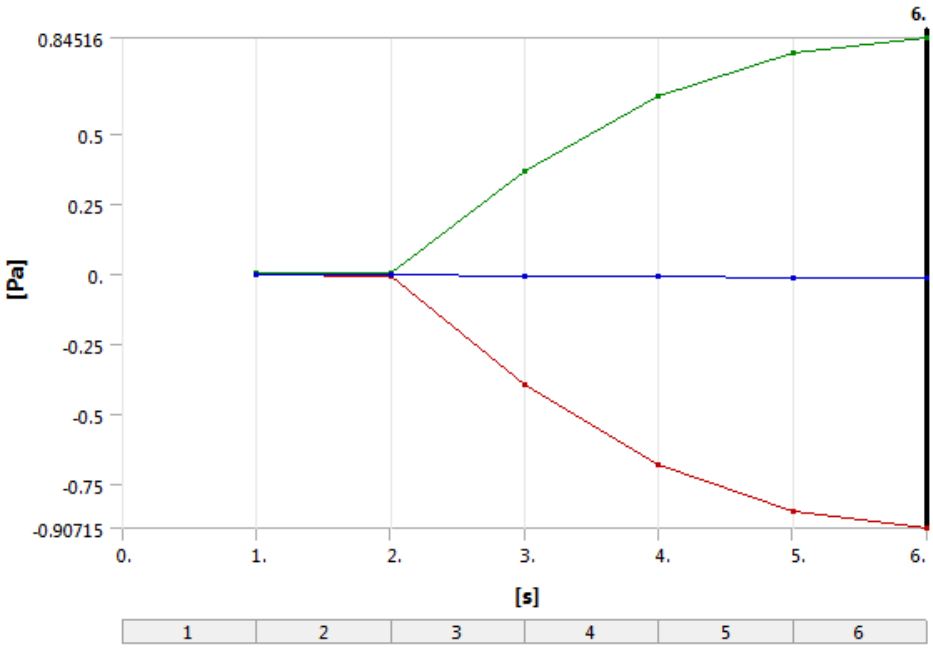

TABLE 17
Model (A4) > Static Structural (A5) > Solution (A6) > Normal Stress

Time [s]	Minimum [Pa]	Maximum [Pa]	Average [Pa]
1.	-3.6113e-003	3.3646e-003	-5.2463e-005
2.	-7.2227e-003	6.7292e-003	-1.0493e-004
3.	-0.39685	0.36973	-5.7651e-003
4.	-0.68034	0.63385	-9.8835e-003
5.	-0.85047	0.79236	-1.2355e-002
6.	-0.90715	0.84516	-1.3178e-002

FIGURE 11
Model (A4) > Static Structural (A5) > Solution (A6) > Equivalent Elastic Strain

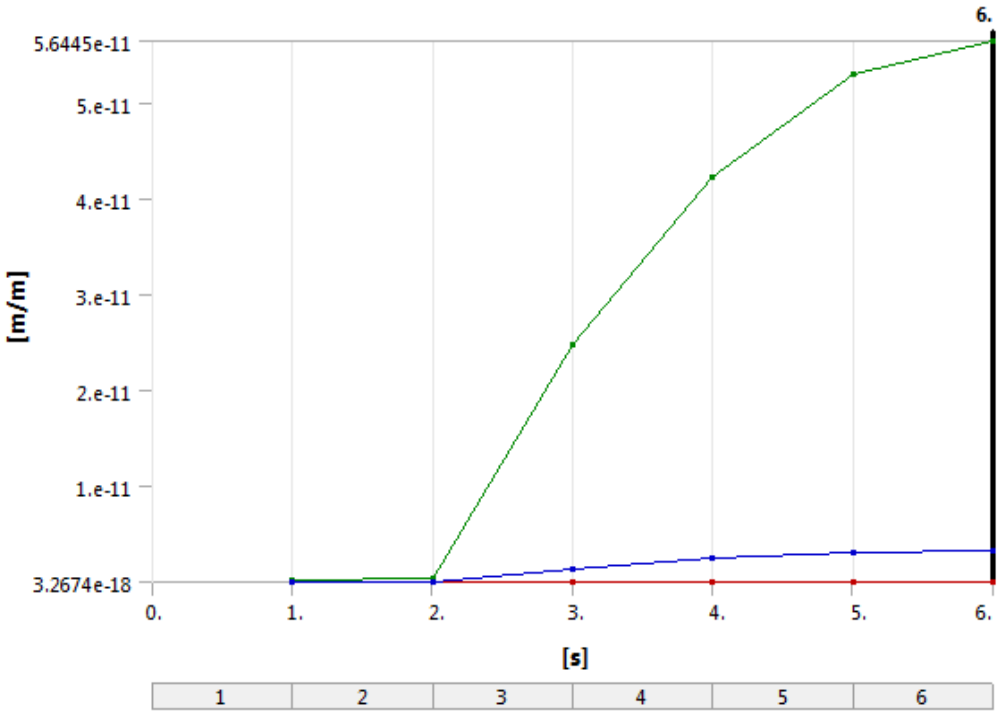

TABLE 18
Model (A4) > Static Structural (A5) > Solution (A6) > Equivalent Elastic Strain

Time [s]	Minimum [m/m]	Maximum [m/m]	Average [m/m]
1.	3.2674e-018	2.2471e-013	1.2832e-014
2.	6.5347e-018	4.4941e-013	2.5665e-014
3.	3.5905e-016	2.4693e-011	1.4101e-012
4.	6.1553e-016	4.2332e-011	2.4175e-012
5.	7.6946e-016	5.2919e-011	3.0221e-012
6.	8.2074e-016	5.6445e-011	3.2235e-012

FIGURE 12
Model (A4) > Static Structural (A5) > Solution (A6) > Maximum Principal Elastic Strain

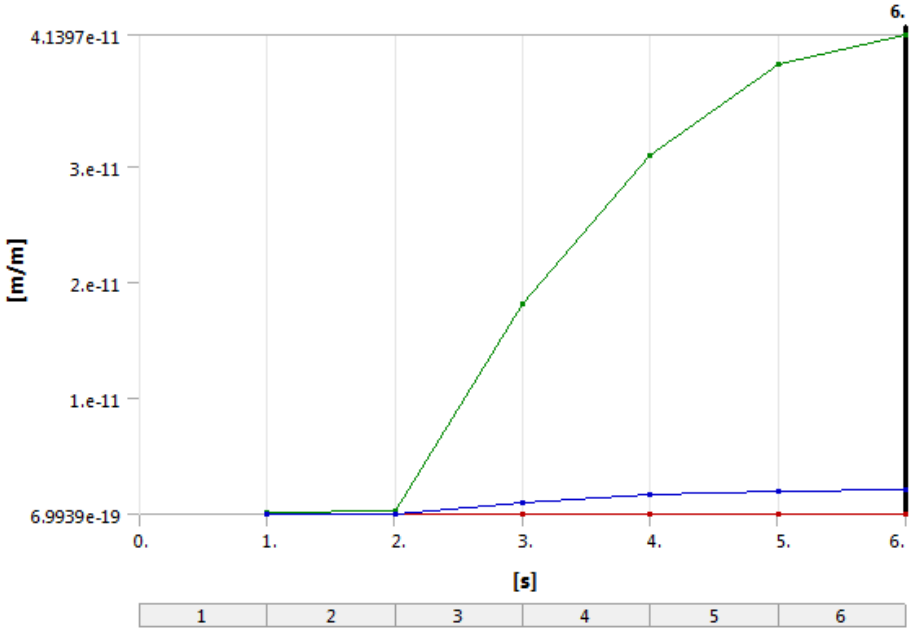

TABLE 19
Model (A4) > Static Structural (A5) > Solution (A6) > Maximum Principal Elastic Strain

Time [s]	Minimum [m/m]	Maximum [m/m]	Average [m/m]
1.	6.9939e-019	1.648e-013	8.6365e-015
2.	1.3988e-018	3.296e-013	1.7273e-014
3.	7.6855e-017	1.811e-011	9.4905e-013
4.	1.3176e-016	3.1047e-011	1.627e-012
5.	1.6471e-016	3.8811e-011	2.0339e-012
6.	1.7568e-016	4.1397e-011	2.1694e-012

FIGURE 13
Model (A4) > Static Structural (A5) > Solution (A6) > Normal Elastic Strain

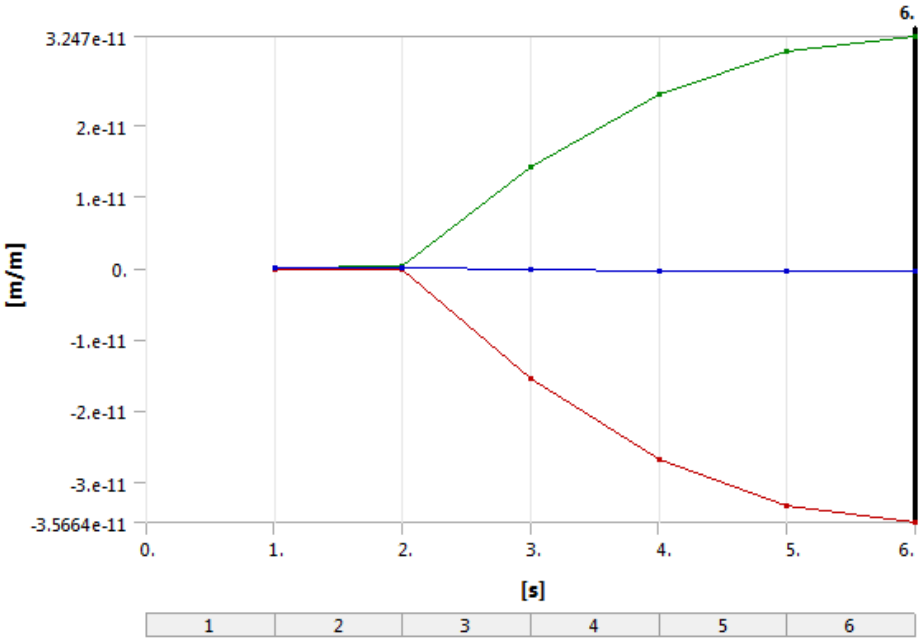

TABLE 20
Model (A4) > Static Structural (A5) > Solution (A6) > Normal Elastic Strain

Time [s]	Minimum [m/m]	Maximum [m/m]	Average [m/m]
1.	-1.4198e-013	1.2926e-013	-1.9572e-015
2.	-2.8396e-013	2.5852e-013	-3.9143e-015
3.	-1.5602e-011	1.4204e-011	-2.1507e-013
4.	-2.6747e-011	2.4351e-011	-3.6871e-013
5.	-3.3436e-011	3.0441e-011	-4.6091e-013
6.	-3.5664e-011	3.247e-011	-4.9163e-013

FIGURE 14
Model (A4) > Static Structural (A5) > Solution (A6) > Directional Deformation

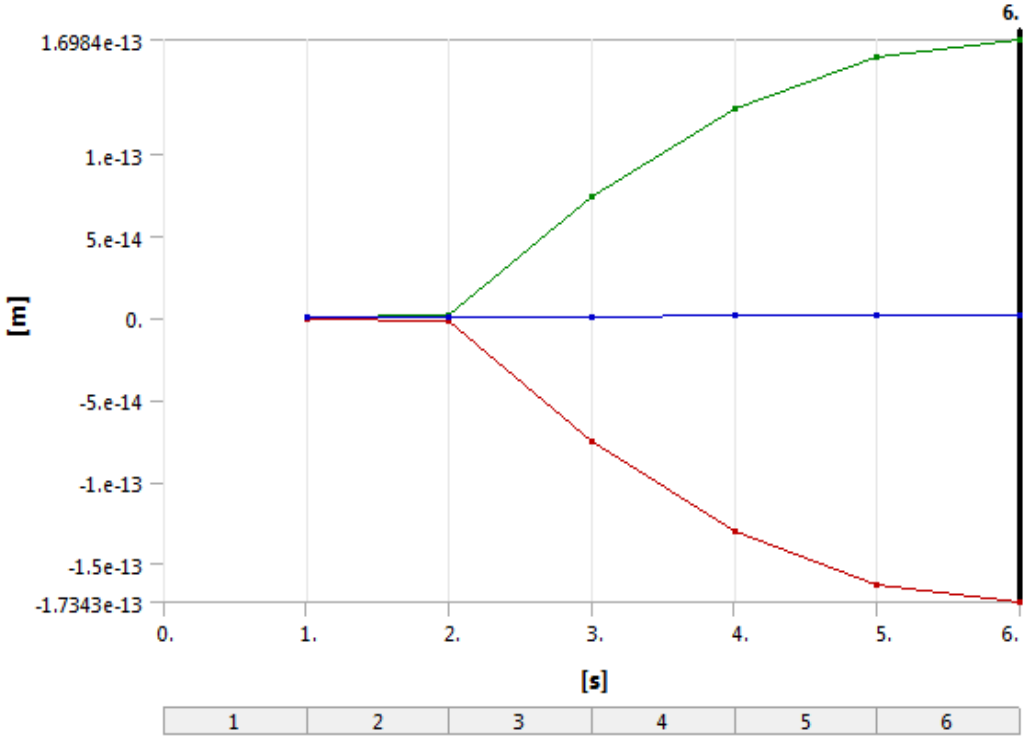

TABLE 21
Model (A4) > Static Structural (A5) > Solution (A6) > Directional Deformation

Time [s]	Minimum [m]	Maximum [m]	Average [m]
1.	-6.9044e-016	6.7613e-016	7.9516e-018
2.	-1.3809e-015	1.3523e-015	1.5903e-017
3.	-7.5871e-014	7.4299e-014	8.738e-016
4.	-1.3007e-013	1.2737e-013	1.498e-015
5.	-1.626e-013	1.5923e-013	1.8726e-015
6.	-1.7343e-013	1.6984e-013	1.9974e-015

Total Deformation (Max) vs Applied Pressure

FIGURE 15
Model (A4) > Total Deformation (Max) vs Applied Pressure

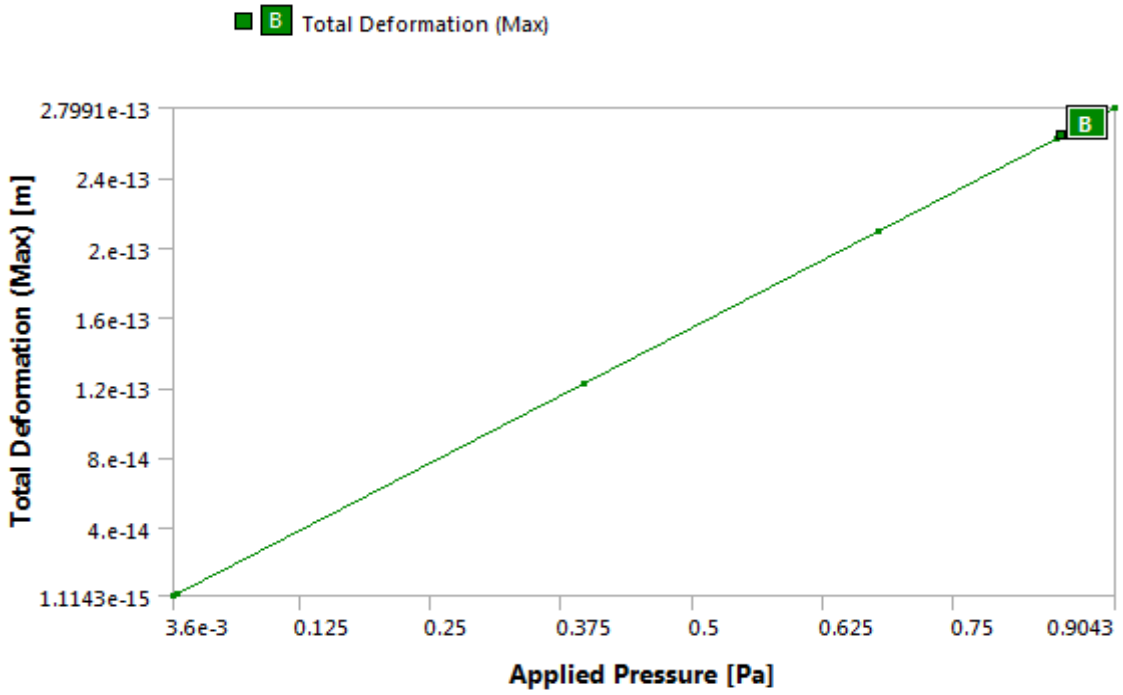

Equivalent Stress (Max) vs Equivalent Elastic Strain (Max)

FIGURE 16
Model (A4) > Equivalent Stress (Max) vs Equivalent Elastic Strain (Max)

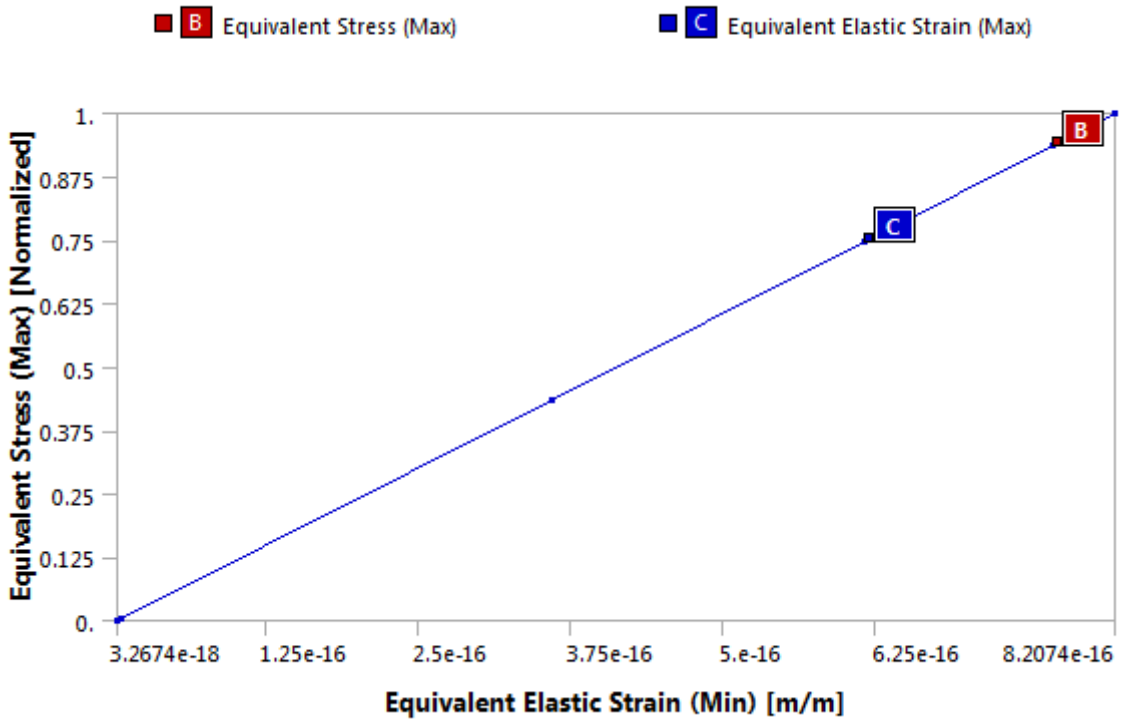

Maximum Principal Stress (Max) vs Maximum Principal Elastic Strain (Max)

FIGURE 17
Model (A4) > Maximum Principal Stress (Max) vs Maximum Principal Elastic Strain (Max)

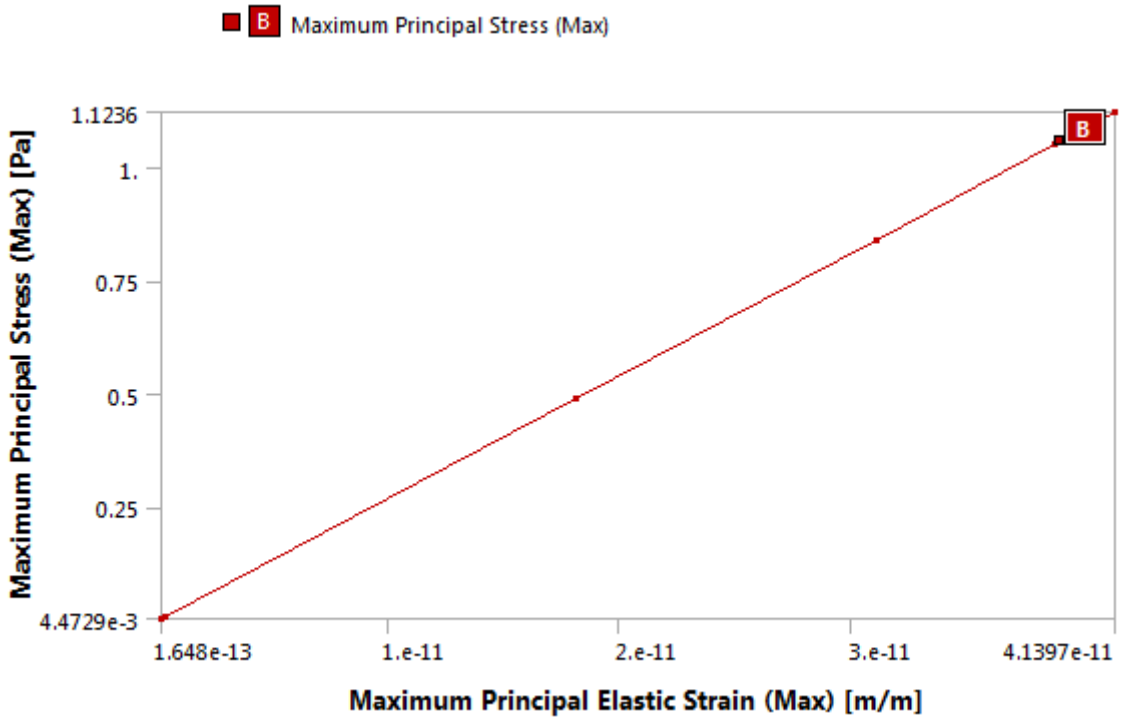

Normal Stress (Max) vs Normal Elastic Strain (Max)

FIGURE 18
Model (A4) > Normal Stress (Max) vs Normal Elastic Strain (Max)

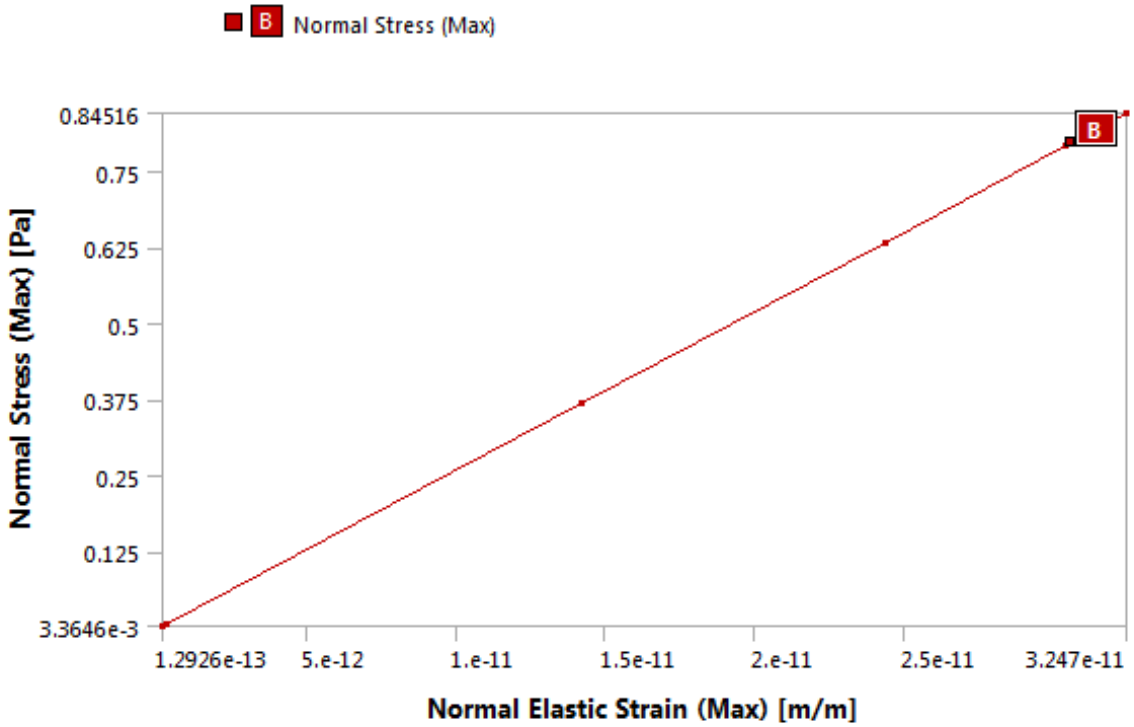

Material Data

Concrete NL

TABLE 22
Concrete NL > Constants

Density	2434.4 kg m^-3

TABLE 23
Concrete NL > Drucker-Prager Strength Piecewise

Pressure P Pa	Yield Stress Y Pa
-4.e+006	0
0	1.e+007
1.5e+007	4.e+007
5.e+007	4.4e+007

TABLE 24
Concrete NL > Tensile Pressure Failure

Maximum Tensile Pressure Pa
-4.e+006

TABLE 25
Concrete NL > Crack Softening Failure

Fracture Energy Gf J m^-2
100

TABLE 26
Concrete NL > Isotropic Elasticity

Young's Modulus Pa	Poisson's Ratio	Bulk Modulus Pa	Shear Modulus Pa	Temperature C
3.167e+010	0.2	1.7594e+010	1.3196e+010	

TABLE 27
Concrete NL > Color

Red	Green	Blue
181	155	130

TABLE 28
Concrete NL > Tensile Ultimate Strength

Tensile Ultimate Strength Pa
4.4e+006

TABLE 29
Concrete NL > Compressive Ultimate Strength

Compressive Ultimate Strength Pa
4.3e+007